

# **Unravelling the precipitation pathway of biorelevant minerals: from fundamental studies to biomedical applications**

THÈSE N° 8691 (2018)

PRÉSENTÉE LE 29 JUIN 2018

À LA FACULTÉ DE L'ENVIRONNEMENT NATUREL, ARCHITECTURAL ET CONSTRUIT

GRUPE LUDWIG

PROGRAMME DOCTORAL EN SCIENCE ET GÉNIE DES MATÉRIAUX

ÉCOLE POLYTECHNIQUE FÉDÉRALE DE LAUSANNE

POUR L'OBTENTION DU GRADE DE DOCTEUR ÈS SCIENCES

PAR

**Agnese CARINO**

acceptée sur proposition du jury:

Prof. F. Nüesch, président du jury

Prof. C. Ludwig, directeur de thèse

Dr V. Buscaglia, rapporteur

Dr B. Lothenbach, rapporteuse

Prof. P. Bowen, rapporteur



ÉCOLE POLYTECHNIQUE  
FÉDÉRALE DE LAUSANNE

Suisse  
2018





*To my family...*



# Acknowledgements

This thesis is part of the outcome of the research performed at the Paul Scherrer Institut, in the Laboratory for Bioenergy and Catalysis, in the framework of an interdepartmental project, 'CROSS', between the Energy and Environment and the Photon Science divisions. I would like to thank Prof Alexander Wokaun and Prof Oliver Kröcher to give me the opportunity to learn and work in such a stimulating environment. Thanks for support and availability.

I would like to express my deepest gratitude to my doctoral father, Prof Christian Ludwig, for his patience, support, and to providing me with an excellent atmosphere for my research.

I would like to acknowledge Dr Antonio Cervellino, Dr Elisabeth Mueller, Dr Davide Ferri for their time and the knowledge that they shared with me. My thesis would have been completed without the numerous meetings and discussions organised by Prof Paul Bowen and his great group at EPFL.

I would like to thank SNI for their financial support, together with the industrial partner Medicoat AG, and the co-workers of FHNW in Basel.

I am very grateful to Prof Frank Nüesch (EPFL/EMPA), Dr Vincenzo Buscaglia (CNR Genova), Dr Barbara Lothenbach (EMPA), Prof Paul Bowen (EPFL) for agreeing to be members of my PhD examination committee, their valuable time, careful and meticulous corrections of my thesis, and for the discussion, feedbacks, and precious suggestions that I received during the oral examination.

I thank the PSI Technology Transfer team for their support and encouragement in the last months of my PhD.

## Acknowledgements

---

I would like to thank the family of OLI System, Inc. in the US. I had a very nice introduction to the thermodynamic modelling and a very nice time with them at the beginning of my PhD.

Also, I would like to thank the wonderful people of our group at PSI (CPM) and EPFL. Some people left and some more joined. Thank you for all your help and telling me that everything will be alright. I would like to thank Dr Frank Pilger, Mr Reza Andalibi, Mr Ahmed Mohammad, Miss Silvia Vita, and Dr Mattia Lucchini for the good time spent together, despite the night-shift, the tiredness, and my mood swings.

Furthermore, I would like to thank all the people who joined the lab and my office making such a pleasant environment to work in and with.

Moreover, I cannot forget to thank all the friends met at the PhD Winter School and the Hercules school. In particular, I would like to thank Sasha, Berta, Ludovico; I had a very great time with you in Grenoble and Hamburg.

Warmest thanks are reserved for my friends and family. I want to thank my sisters, brother, and brothers-in-law for their help and advice. I missed you tremendously and felt sorry I could not always be there when you needed me. A special thanks go to my beautiful nephews, Caterina, Pietro, Giacomo, and Benedetta; although I know you didn't understand my decision to leave home, you supported me all the way with your smiles, hugs, and Skypes, despite you missed me. I miss you tremendously. I want to profoundly thank my dad and my mum for their help, support, and our talks. And last but not least, I owe deepest gratitude to Andrea, my biggest support during this PhD. Thanks for what you teach me, for your infinite patience, and your constant support, which gave me the strength to carry on.

This thesis would probably never have been completed without their support, and it is therefore dedicated to them.

*Villigen, 16 June 2018*

Agnese Carino

# Abstract

The formation pathway of biominerals archetypes, namely calcium carbonate (CaC) and calcium phosphates (CaPs), was investigated using a multidisciplinary approach. The time-resolved analytical data were collected using a controlled-composition method and interpreted using a computational tool. Some basic-science questions were identified arising from long-lasting debates on the details about the solid formation mechanism. Some of these questions are here addressed by the accurate experimental data collection, the application of new cutting-edge techniques, and the development of a rigorous thermodynamic-kinetic model for the entire solid formation process from solution.

The time-resolved data were collected analysing the aqueous species *in-situ*. In parallel, the amount of chemicals added into the reactor, to maintain iso-*pH* conditions, was mathematically correlated to the bonded carbonate or phosphate ions, allowing the collection of two independent series of data and the assessment of both the cation and the anion during the solid formation process. This analytical approach went beyond the state-of-the-art.

The complex mechanism was partitioned into its sub-processes, and a new strategy was identified to indirectly disclose the nature of the building units involved in the solid growth. Some assumptions embedded in the derivation of the nucleation theory did not compromise the theoretical validity of the framework, and the thermodynamic quantities expressed in the formulation have to be properly related to the nucleating phase and not extended as intensive properties of the solid.

As main scientific results, for both CaC and CaPs systems, the experimental data are consistent with a classical nucleation and crystallisation mechanism, where primary, secondary, and diffusion limited growth are taken into account. The associated thermodynamic and kinetic quantities, such as the surface energy for primary and secondary nucleation as well as the nucleation and growth rate are reported and critically discussed in this dissertation.

The models allowed detailed investigations in the pre-nucleation zone with the aim of

## Abstract

---

evaluating the presence of clusters at controlled T, pH ionic strength, and cation/anion ratio against saturation level. An experimental setup was developed to study clusters *in-situ*: a reactive horizontal micrometric pulsation-free liquid jet was investigated with a focused synchrotron X-ray beam, and the small angle scattering signals were collected for both CaC and CaPs systems.

Preliminary results confirm the presence of clusters and attempts to identify their size distribution are ongoing. The agreement between experimental data, standard and cutting-edge analytical investigations, and modelling results allowed the definition of a plausible solid formation pathway, for both the investigated systems, based on the nucleation theory framework, in which the plausible influence of clusters was assessed.

Beside the basic-science activities, some applications in the biomedical field were also evaluated. Among them, the controlled growth of CaPs phase on pre-treated Ti implants, *e.g.*, dental implants, was achieved. This application opened exciting perspectives toward the production and the commercialisation of implants characterised by a faster healing time and improved stability.

The scientific results were published in peer-reviewed papers and an international patent application; two additional papers are currently under finalisation.

Keywords: calcium carbonate; calcium phosphate; controlled composition approach; potentiometric measurements; precipitation modelling; thermodynamic-kinetic model; population balance modelling; classical nucleation; diffusion- limited growth; non-classical precipitation; small-angle X-ray scattering (SAXS).

# Riassunto

I processi di formazione di carbonato (CaC) e fosfati di calcio (CaPs), archetipi di biominerali, sono stati investigati con un approccio multidisciplinare.

I dati cinetici – raccolti impiegando un metodo che permette il controllo composizionale – sono stati interpretati e modellizzati.

Sono state identificate alcune domande fondamentali associate ai dettagli del meccanismo della formazione del solido da soluzione. In questa dissertazione, ho cercato di rispondere a queste domande basandomi sull'accurata raccolta di dati sperimentali, la comprensione dei dettagli matematici dei modelli utilizzati, l'applicazione di tecniche sperimentali innovative, la letteratura e lo sviluppo di un modello termodinamico-cinetico rigoroso del processo.

I dati cinetici sono stati raccolti analizzando la speciazione chimica *in-situ*. Parallelamente, la quantità di reagenti aggiunti nel reattore, per mantenere le condizioni di iso-*pH*, è stata correlata con gli ioni carbonato e fosfato legati; questo ha permesso la raccolta di due serie di dati indipendenti durante il processo di formazione del solido. L'approccio rappresenta un'innovazione rispetto allo stato dell'arte.

Il processo è stato deconvolto nei suoi sotto processi e la dimensione delle unità di crescita coinvolta nella formazione del solido è stata stimata. Alcune assunzioni utilizzate nella derivazione matematica della teoria di nucleazione classica sono emerse influenti sulla validità matematica del modello. Tuttavia, le quantità termodinamiche derivate dal calcolo devono essere propriamente associate alla fase nucleante e non al solido ottenuto.

Come risultati scientifici principali, per entrambi i sistemi CaC e CaPs, i dati sperimentali sono coerenti con meccanismi di nucleazione classica e cristallizzazione. Le quantità termodinamiche e cinetiche associate sono riportate e discusse in dettaglio in questa tesi.

I modelli permettono di investigare con dettaglio la zona di prenucleazione allo scopo di identificare la presenza di cluster a costante temperatura, *pH*, forza ionica, e rapporto catione/anione ma variando in modo controllato la sovrassaturazione del

## Riassunto

---

sistema.

Inoltre, è stato costruito un setup sperimentale per investigare *in-situ* i cluster: un getto liquido, reattivo, orizzontale, micrometrico e privo di pulsazioni è stato sottoposto all'analisi di luce di sincrotrone (X-ray) ed è stato raccolto il segnale di scattering a basso angolo per entrambi i sistemi CaC e CaP.

La corrispondenza tra dati sperimentali, ottenuti tramite analisi standard e avanzate, e i risultati del modello, hanno permesso di definire un percorso plausibile di formazione del solido basato sulle teorie classiche ed individuando il plausibile ruolo dei cluster.

Oltre alle attività scientifiche fondamentali, sono stati svolti studi di tipo applicativo, mirati all'impiego dei CaPs in campo biomedico. In particolare, è stato ottimizzato il controllo della crescita di CaPs sulla superficie di Ti per impianti dentali.

Questa applicazione ha aperto interessanti prospettive indirizzate alla produzione e commercializzazione di impianti caratterizzati da un minore tempo di guarigione e di immobilizzazione dell'impianto oltre ad una sua migliorata stabilità nell'osso mandibolare.

I risultati del mio lavoro di dottorato sono pubblicati in forma di articoli scientifici (peer-reviewed) ed un brevetto internazionale. Altri due articoli sono in via di conclusione.

Parole chiave: calcio carbonato; calcio fosfato; metodo a composizione controllata; misure potenziometriche; modello descrittivo sulla precipitazione; modello termodinamico-cinetico; modello di bilanci di popolazione; nucleazione classica; crescita limitata dalla diffusione; precipitazione non classica; X-ray scattering a basso angolo (SAXS).



# Contents

<b>Acknowledgements</b>	<b>v</b>
<b>Abstract</b>	<b>vii</b>
<b>List of figures</b>	<b>xiv</b>
<b>List of tables</b>	<b>xvii</b>
<b>Introduction</b>	<b>1</b>
Motivation . . . . .	1
Objectives . . . . .	3
Thesis outline . . . . .	5
My contributions . . . . .	5
<b>1 Experimental</b>	<b>7</b>
1.1 Materials investigated . . . . .	7
1.1.1 Calcium carbonate system . . . . .	7
1.1.2 Calcium phosphate system . . . . .	9
1.2 Experimental and setups . . . . .	11
1.2.1 Solution preparation . . . . .	11
1.2.2 Controlled composition approach . . . . .	13
1.2.2.1 Titration setup . . . . .	13
1.2.2.2 Calibration of the electrodes . . . . .	13
1.2.2.3 A typical precipitation experiment . . . . .	14
1.2.2.4 CaC experiments . . . . .	18
1.2.2.5 CaP experiments . . . . .	20
1.3 Computational model: basis, and system-specific details. . . . .	24
1.3.1 Calcium carbonates . . . . .	26
1.3.1.1 Preliminary thermodynamic calculations (OLI software)	26

## Contents

---

1.3.1.2	Comprehensive thermodynamic model . . . . .	27
1.3.1.3	Kinetic model . . . . .	31
1.3.2	Calcium phosphates . . . . .	35
1.3.2.1	Speciation Model . . . . .	35
1.3.2.2	Thermodynamic and Kinetic models . . . . .	39
1.4	Automatisation method . . . . .	39
1.5	Constant saturation approach: setups & experiments . . . . .	40
1.6	Liquid jet setup . . . . .	41
<b>2</b>	<b>Precipitation</b>	<b>45</b>
2.1	Basis of the solid formation process from solution . . . . .	45
2.1.1	Driving force for the solid formation . . . . .	48
2.2	Elementary processes of solid formation . . . . .	52
2.2.1	Nucleation . . . . .	54
2.2.2	Growth . . . . .	61
2.2.3	Aggregation . . . . .	66
2.3	Alternative pathways of solid formation . . . . .	67
2.3.1	Spinodal decomposition . . . . .	67
2.3.2	Aggregation of Stable or Metastable Particles . . . . .	68
2.3.3	Multi-step Pathways . . . . .	71
2.3.4	Oriented attachment and mesocrystal formation . . . . .	71
2.4	<i>Classical</i> and <i>non-classical</i> concepts: milestones of understanding . . . . .	73
<b>3</b>	<b>CaCs &amp; CaPs studies</b>	<b>77</b>
3.1	A Case Study: The Amorphous Calcium Carbonate (ACC) Precipitation Pathway Unravelling. . . . .	79
3.1.1	Abstract . . . . .	80
3.1.2	Introduction . . . . .	80
3.1.3	Experiment and modelling . . . . .	82
3.1.4	Results and discussion . . . . .	84
3.1.5	Conclusion . . . . .	94
3.2	Formation and Transformation of Calcium Phosphate Phases under Biologically Relevant Conditions: Experiments and Modelling . . . . .	99
3.2.1	Abstract . . . . .	100
3.2.2	Introduction . . . . .	100

3.2.3	Material, methods, and model . . . . .	102
3.2.4	Results . . . . .	105
3.2.5	Discussion . . . . .	112
3.2.6	Conclusions . . . . .	119
3.3	In-situ liquid WAXS and SAXS studies on the early stage of amorphous calcium carbonate (ACC) formation . . . . .	121
3.3.1	Abstract . . . . .	122
3.3.2	Introduction . . . . .	122
3.3.3	Material and methods . . . . .	125
3.3.4	Preliminary data analysis . . . . .	126
3.3.4.1	Evaluation of the scale factor . . . . .	126
3.3.4.2	Fitting approaches . . . . .	128
3.3.4.3	Bimodal approach . . . . .	129
3.3.5	Preliminary results and discussion . . . . .	131
<b>4</b>	<b>Investigation methods</b>	<b>135</b>
4.1	Infra-Red and Raman spectroscopy . . . . .	135
4.2	Imaging techniques . . . . .	136
4.2.1	Optical Microscopy . . . . .	136
4.2.2	Scanning Electron Microscopy with Focus Ion Beam system . . . . .	136
4.2.3	Transmission Electron Microscopy . . . . .	140
4.3	Dynamic light scattering . . . . .	141
4.4	Titration . . . . .	142
4.4.1	Potentiometric measurements . . . . .	142
4.5	Investigation using X-rays . . . . .	144
4.5.1	X-ray scattering and diffraction . . . . .	144
4.5.2	Rietveld analysis . . . . .	146
4.5.3	Synchrotron radiation . . . . .	147
4.5.4	Small Angle X-Ray Scattering at the Material Science beamline X04SA (SLS-Villigen PSI) . . . . .	148
4.6	Thermal analyses . . . . .	149
<b>5</b>	<b>Concluding remarks</b>	<b>153</b>
<b>A</b>	<b>Appendix A</b>	<b>161</b>
A.1	TD and K results for all datasets . . . . .	161
A.2	Additional figures . . . . .	182

---

## Contents

---

A.3	Additional tables . . . . .	184
A.4	Additional notes . . . . .	184
A.5	Evaluation of the term $\left[Ca_{surf}^{2+}\right]$ . . . . .	185
A.6	Equations for $\Delta G_h^*$ and $\Delta G_s^*$ and critical size . . . . .	187
<b>B</b>	<b>Appendix B</b>	<b>189</b>
B.1	Additional Characterization analyses . . . . .	189
B.1.1	IR and Raman spectroscopy . . . . .	189
B.1.2	SEM and EDX analyses . . . . .	190
B.2	Additional table and figure . . . . .	192
B.3	Complete datasets . . . . .	193
<b>C</b>	<b>Appendix C</b>	<b>197</b>
C.1	CerInk project . . . . .	199
C.1.1	Introduction . . . . .	199
C.1.2	Results . . . . .	200
C.1.3	Conclusion . . . . .	202
C.1.4	SNI successful story 2017 . . . . .	202
C.2	Patent application . . . . .	207
C.2.1	Abstract . . . . .	207
C.2.2	Introduction . . . . .	208
C.2.3	Objectives . . . . .	210
C.2.4	Preferred embodiments . . . . .	211
C.2.5	Patent claims . . . . .	218
C.3	Continuous synthesis of gold nanoparticles using the segmented flow tubular reactor (SFTR) . . . . .	221
<b>D</b>	<b>Appendix D</b>	<b>223</b>
D.1	Size Control of Pt Clusters on CeO <sub>2</sub> Nanoparticles via an Incorporation- Segregation Mechanism and Study of Segregation Kinetics . . . . .	225
D.2	Hydrothermal Synthesis of SrTiO <sub>3</sub> : Role of Interfaces . . . . .	239
	<b>List of publications</b>	<b>255</b>
	<b>Curriculum Vitae</b>	<b>257</b>
	<b>Bibliography</b>	<b>259</b>
	<b>Acronyms</b>	<b>280</b>

# List of Figures

1	Amazing Nature! . . . . .	2
1.1	Typical calcium related experimental curves. . . . .	15
1.2	Typical NaOH experimental curve. . . . .	17
1.3	Block diagram of the Metrohm method to run the precipitation experiments. . . . .	40
1.4	Liquid jet setup. . . . .	42
1.5	Liquid jet setup mounted at the MS beamline (SLS). The 4 pumps and the Coriolis flowmeters are visible in the front. . . . .	43
2.1	Classical nucleation theory landscape: free energy vs nuclei size. . . . .	55
2.2	Schematic representation of Gibbs free energy landscapes. . . . .	57
2.3	Energy landscape for homogeneous and “true” secondary nucleation. . . . .	60
2.4	Growth regimes for BaSO <sub>4</sub> precipitation. . . . .	63
2.5	Schematization of the concentration profile in the diffusion-limited growth. . . . .	66
2.6	Phase diagram. . . . .	69
2.7	Free energy profile of nucleation of calcium carbonate. . . . .	70
2.8	Pathways to crystallisation by particle attachment. . . . .	73
3.1	TD curves for ACC experiments at T=298.15 K and pH=9.00. . . . .	83
3.2	Gibbs free energy of formation for CaCO <sub>3</sub> <sup>0</sup> and {CaCO <sub>3</sub> <sup>0</sup> · CO <sub>3</sub> <sup>2-</sup> }. . . . .	87
3.3	$K_{sp}$ versus ( CO <sub>3</sub> <sup>2-</sup> / Ca <sup>2+</sup> -1 ). . . . .	88
3.4	$pK_{sp}$ of ACC against temperature at pH= 9.00. . . . .	89
3.5	Calculated kinetic data on particle evolution. . . . .	90
3.6	Primary particles size distribution against time. . . . .	91
3.7	ACC surface energy, cohesion energy, and the derived surface energy for secondary nucleation. . . . .	93
3.8	Schematization of the precipitation pathway of ACC. . . . .	95
3.9	TD curves for H- and L-IS. . . . .	108

## List of Figures

---

3.10 K data for H-IS experiments. . . . .	109
3.11 XRD data for H-, C-, and L-IS experiments. . . . .	109
3.12 SEM micrographs, samples H- and L-IS. . . . .	110
3.13 TEM micrographs, samples H- and L-IS. . . . .	111
3.14 Chemical potential plot of CaP system from the literature. . . . .	114
3.15 Chemical potential plot of for series H-IS (A), and for series L-IS (B). . .	115
3.16 The SAXS data in the angular range for condition levels $C_2$ , $C_4$ , $C_8$ . . . .	127
3.17 Best fitting for condition levels $C_2$ , $C_4$ , $C_8$ . . . . .	130
3.18 Number and mass distribution for condition levels $C_2$ , $C_4$ , $C_8$ . . . . .	132
3.19 Preliminary interpretation of the experimental data. . . . .	133
4.1 A schematic illustration of the interactions between a beam of high energy electrons and a sample. . . . .	138
A.1 TD curves experiments at $T=278.35$ K. . . . .	162
A.2 Kin curves experiments at $T = 278.35$ K. . . . .	163
A.3 TD curves experiments at $T = 288.15$ K. . . . .	164
A.4 Kin curves experiments at $T = 288.15$ K. . . . .	165
A.5 TD curves experiments at $T = 298.15$ K. . . . .	166
A.6 Kin curves experiments at $T = 298.15$ K. . . . .	167
A.7 TD curves experiments at $T = 308.15$ K. . . . .	168
A.8 Kin curves experiments at $T = 308.15$ K. . . . .	169
A.9 TD curves experiments at $T = 318.15$ K. . . . .	170
A.10 Kin curves experiments at $T = 318.15$ K. . . . .	171
A.11 TD curves experiments at $T = 298.15$ K. . . . .	172
A.12 Kin curves experiments at $T = 298.15$ K. . . . .	173
A.13 TD curves experiments at $T = 298.15$ K. . . . .	174
A.14 Kin curves experiments at $T = 298.15$ K. . . . .	175
A.15 TD curves experiments at $T = 298.15$ K. . . . .	176
A.16 Kin curves experiments at $T = 298.15$ K. . . . .	177
A.17 TD curves experiments at $T = 298.15$ K. . . . .	178
A.18 Kin curves experiments at $T = 298.15$ K. . . . .	179
A.19 Example of carbonate-to-calcium ratio against time in the solid phase for the experiment at $T = 318.15$ K and $pH = 9.00$ . . . . .	180
A.20 Values of $pK_{sp}$ of ACC calculated from both OLI and the model devel- oped for the experiments at $T = 298.15$ K and $pH$ in the range between 9.00 to 10.00. . . . .	180

---

A.21 Cluster concentration and average cluster-cluster distance for the experiment done at $T = 298.15$ K and $pH = 9.00$ . . . . .	181
A.22 Experiments at constant $S$ . . . . .	182
A.23 Primary particles calculations. . . . .	183
A.24 Primary particles calculations. . . . .	183
B.1 IR and Raman spectra for H- and L-IS experiments. . . . .	190
B.2 Particles of H-IS experiment (A) reported with its corresponding EDX spectrum (B). . . . .	191
B.3 Surface energy for L, H, C-IS experiments reported as a function of ionic strength (IS). . . . .	192
B.4 Constant Ionic Strength (C-IS) experimental (black) and calculated (red) data. (A) calcium ion activity and (B) NaOH volume added into the system for iso-pH condition. . . . .	193
B.5 Ionic Strength of H-IS, C-IS experiments (A), and of L-IS (B). . . . .	193
B.6 Chemical speciation of calcium (A, C, E), and of phosphorous (B, D, F) for C-IS, H-IS, and L-IS, respectively. . . . .	194
B.7 Kinetic data for H-, C-, L-IS. . . . .	195
B.8 Chemical potential plot for C-IS series. . . . .	196
C.1 Ceramic body with density gradient. . . . .	206
C.2 Compression strength (CS) and density of sintered samples. . . . .	206
C.3 Characterization analyses of Au NPs. . . . .	221





# List of Tables

1.1	Calcium phosphate phases and their molar ratio . . . . .	9
1.2	CaCs equilibrium constants. . . . .	31
1.3	Ionic size for CaC model. . . . .	32
1.4	Ionic size for CaP model. . . . .	38
1.5	CaPs equilibrium constants. . . . .	39
A.1	TD regressed quantities for ACC and $\text{CaCO}_3^0$ . . . . .	184
A.2	Calculated ( $\text{CO}_3^{2-}/\text{Ca}^{2+}$ ) ratio . . . . .	184
B.1	Surface energy values vs the ionic strength. . . . .	192



# Introduction

## Motivation

The ability to synthesise in the laboratory biominerals, inorganic substances produced in nature by a living organism, tailoring their physicochemical properties, such as shape and phase, is an ambitious scientific target with paramount implications in several fields. Biominerals formation occurs in very different environments, from normal temperature and pressure (NTP) conditions to very harsh circumstances, such as those in deep-sea hydrothermal vents. These materials show an incredible variety of morphologies from the amazing micrometric calcium carbonate structures produced by microorganisms to bones and teeth in the higher animals, which are mainly made of calcium phosphate (figure 1). Indeed, calcium carbonate and phosphate are biominerals archetypes and therefore selected as the primary subjects of my scientific activity, keeping in mind that *the comprehension of the solid formation pathway is the way to achieve the control over the solid physicochemical properties and morphology*.

Nowadays, the scientific community aims to improve the understanding of the solid formation pathway from solutions, with the target to achieve better control over materials produced in large quantiles at the industrial level as well as to develop new advanced materials mimicking what nature is doing since millions of years. *In-situ* techniques, such as cryogenic transmission electron microscopy, liquid phase electron microscopy, liquid phase atomic force microscopy, together with analytical ultra-centrifugation, synchrotron-based analyses, molecular dynamics simulations (MDS), and density functional theory (DFT) calculations, seem the most promising tools to analyse and characterize the evolution of a system during the crystallization processes. Despite that, the understanding of the mineral formation mechanisms from solution is only partially disclosed, and it is still a challenging task. Recent results obtained using the aforementioned techniques, together with the identification

## Introduction

---

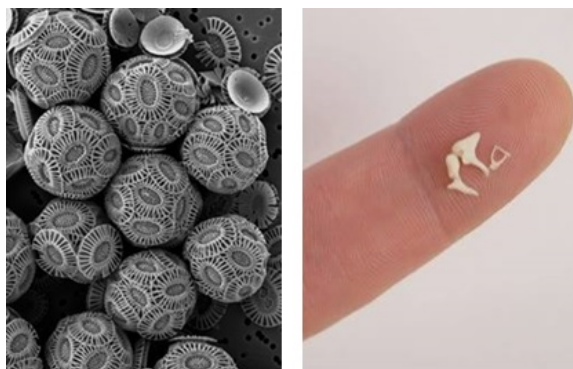


**Figure 1** – Amazing Nature! (Left)  $\text{CaCO}_3$  microalgae skeleton; (Right) the smallest bones in the human body, the malleus (hammer), the incus (anvil), and the stapes (stirrup) in the middle human ear.

of mesocrystalline materials, *i.e.*, crystalline structures composed by a periodically arranged sub-crystals with similar size and crystal structure, paved the way to new perspectives in search of the definition of a new solid formation mechanism. These results led the scientists to question the solid formation mechanism according to the “classical” view that is based on the nucleation theory, which Gibbs (1877) proposed since the XIX century, and later Nielsen disseminated (1964). In the debate, the significant assumptions and approximations made in the mathematical derivations of the theory were discussed, and some new “non-classical” views were proposed in which the participation of sub-critical clusters in the solid formation processes was invoked [2–6]. A large number of new results were obtained in that direction, but ambiguities on definitions, concepts, and difficulties to compare or understand experimental data were generated as well.

A fundamental point concerns the data collection method; it is particularly challenging because the system is evolving, the object under investigation is often a transient phase, and modifications can be induced by sampling and characterisation. Therefore, *in-situ* time-resolved non-invasive investigations are the most promising techniques to collect suitable data to study the precipitation pathway. *Ex-situ* characterisation on the final product, only allow speculation. Moreover, slight changes in the experimental conditions can vary the precipitation process significantly, with dramatic effect on the experiments reproducibility. In this context, my activity was focused on the definition of an appropriate method suitable to collect reproducible kinetic data on precipitation reactions in order to address scientific questions about the solid formation mechanism.

Among them:

- *If clusters are present before the nucleation stage, are they involved in the calcium carbonate and calcium phosphate crystallisation pathways?*
- *In which elementary process do they take part and, consequently, how does the Gibbs free energy landscape of the solid formation look like?*
- *Is it still possible to describe the experimental data in the presence of clusters using the classical approach?*

The experimental data were collected using state-of-the-art analytical tools, and a computational model was applied to identify the details of most plausible precipitation pathway. The model deals simultaneously with the thermodynamic and kinetic aspects of the process, and it is based on the classical nucleation and growth framework. Such an approach was applied to calcium carbonate (CaC) and calcium phosphate (CaP) systems, and the results are discussed in this dissertation.

## Objectives

The objective of this work was mainly focused on experimental activities and data analysis. A rigorous method was applied firstly to collect experimental data on homogeneous precipitation reactions of calcium carbonate and calcium phosphate, and secondly, a computational thermodynamic-kinetic model was used to regress the experimental data, to retrieve unknown key parameters, and to describe the details of the most plausible precipitation pathway. Calcium phosphate (CaP) is the main constituent of bone and used as a biocement as well as being used as a bioactive coating for medical devices such as prosthesis and implants. The understanding of the details of the CaP formation mechanism is of high importance in the biomedical field, and it represents the primary applied objective of this doctoral work. The final target was achieved finalising a sequence of milestones. The first one was the study of calcium carbonate (CaC) being an optimal candidate as a model system and one of the most studied minerals in geoscience and biochemistry. Moreover, CaC and CaP share the same cation, and they precipitate under similar conditions. The appropriate experimental protocol was developed starting from the literature [6–8]. The experimental data were collected *in-situ* and time-resolved using a controlled composition approach to get kinetic information suitable for the computational model. In fact,

## Introduction

---

the process is influenced by several parameters, and it is mandatory to reduce the number of variables in order to have a problem computationally solvable with a limited number of independent datasets. Moreover, the experimental setup should be automatized to collect reproducible data and reduce the measurement incertitude. Initially, the unknown thermodynamic quantities of aqueous and solid species were regressed from the experimental data using the commercial software OLI Studio [9]. Afterwards, a system-specific code was produced and combined with a previously developed general core code [10], which deals with the classical nucleation and growth theoretical equations and using the population balance approach. The results of such initial research were finalised in a scientific publication in which the details of the precipitation pathway of amorphous calcium carbonate were disclosed. Even more relevant for my target, such achievements paved the way towards my second milestone: the formation mechanism of calcium phosphate. In fact, following a similar approach, a complete thermodynamic-kinetic model for the formation and transformation of calcium phosphate phase under biomimetic conditions was accomplished and published. It is worth noting that the obtained results, even when in excellent agreement with literature data, are specific for the experimental conditions applied and does not affect the validity of alternative theories or pathways active under other experimental conditions.

The optimised thermodynamic-kinetic models were used for more advanced studies. For instance, the early stage of the precipitation, for both CaC and CaP systems, was investigated using liquid jet equipment at the Material Science beamline (X04SA, SLS). Thanks to the models, the measurements were carried out at known and constant saturation levels.

The model predictions were applied to study the heterogeneous precipitation of CaP using different materials as seeds, such as hydroxyapatite (HA) nanopowders, and titanium dioxide. These studies were done to achieve the control over the heterogeneous nucleation of calcium phosphate, in particular of HA and octacalcium phosphate (OCP) on passivated Ti discs. Titanium represents the most used metallic material for the biomedical implants. In this field, the calcium phosphate coating would represent a promising feature to decrease healing time and osseointegration with the natural bones. Thanks to the method and the developed model, titanium screws used for dental implants were efficiently coated with thin layer of OCP. These results were disclosed in a patent application and led to a new – currently running – project in which industrial partners are involved.

## Introduction

---

The knowledge on how to control the calcium phosphate growth can be used as a starting point in the preparation of bioceramics, scaffolds, and composites. In fact, the nano and micro-structured surface, combined with optimal bulk porosity, represents the biggest challenge in the fabrication of CaP bone grafts, implants, and prosthesis with excellent osteoinductive properties. With this ambitious perspective, I worked on a parallel application-oriented activity. The latter aims to prepare 3D printed porous ceramic scaffolds, characterised by a biomimetic density gradient, and mechanical stability close to those of human bones. Ceramic processes were applied to achieve such a target starting from a well-developed 3D printing procedure [11, 12] and materials with controlled density were prepared.

## Thesis outline

This dissertation introduces the systems studied and setups used in chapter 1. In chapter 2, the solid formation theories, fundamental concepts, and definitions are summarised. The scientific outcomes are reported in chapter 3. The applied analytical methodologies are reported in chapter 4. Conclusions and perspectives are summarised in chapter 5. In appendices A and B are reported the details of the results and supporting materials for the CaC and CaP systems, respectively. The application-oriented activities are described in appendix C, and the scientific contributions as co-author are reported in appendix D.

## My contributions

All the experimental work done is attributable to me, under the supervision of Dr Andrea Testino and Prof Christian Ludwig. The synchrotron experiments were carried out by me and done in collaboration with Mr Mohammed Ahmed Shaban Abdelfadil, Mr Mohammad Reza Andalibi, and coordinated by Dr Andrea Testino and Dr Antonio Cervellino. The chemical analyses were done by Dr Mohamed Tarik. IR and Raman analyses were performed by Dr Davide Ferri and Dr Adrian Marberger, respectively, in cooperation with me. Prof Takashi Ishikawa and Dr Elisabeth Müller collected the electron micrographs in cooperation with me. Ceramic inks preparation and characterisations were done by Silvia Vita, in the framework of her master thesis project, under my supervision; the 3D printing of the ceramic samples was done by Adrian Rohner at the Fachhochschule Nordwestschweiz FHNW in Basel, while the

## Introduction

---

porous ceramic processing was done by me, coordinated by Dr Andrea Testino.

The analytical method that I developed and used for experiments automatisation was distributed to different internal and external collaborators. In the co-authorship works reported in appendix D, I contributed in the samples preparations for the synchrotron experiments, and I have carried out the experiment during the assigned shifts of the beam time. Moreover, I compiled four new thermodynamic databases using OLI ESP [9] for the systems CaC, CaP, calcium silicate hydrate (CSH), and  $\text{SrTiO}_3$  in solvothermal conditions.



# 1 | Materials, experimental, modeling, and setups

## 1.1 Materials investigated

This section introduces the chemical systems studied in this doctoral work. Aqueous calcium carbonate and phosphate systems represent the most studied biominerals because of their relevance in the biological and environmental fields. A general overview about them is given in sections 1.1.1, and 1.1.2 for carbonate and phosphate, respectively.

### 1.1.1 Calcium carbonate system

Calcium carbonate (CaC) is the major source of water hardness, one of the most studied minerals, scientifically relevant in biomineralisation [13] and geosciences, and is forming enormous scales of biological (reefs, ocean sediments) and geological origin. Crystalline  $\text{CaCO}_3$  is produced for many industrial applications, (*e.g.*, pharmaceuticals, dental care products, cleaning agents). Precipitation of calcium carbonate from relatively concentrated solutions ( $>0.02 \text{ mol L}^{-1}$ ) involves the formation of an initial “precursor”, a gel phase of amorphous calcium carbonate (ACC), which transforms into a mixture of both calcite and/or vaterite [14–17], even in the presence of additives [18]. The vast amount of literature on the calcium carbonate system provides extensive information on the solubility and kinetic parameters of its dissolution. However, the understanding of the precipitation mechanism is still lacking. The formation, stabilisation, and crystallisation of ACC is controlled by various factors including temperature, *pH* and dopants (*e.g.*,  $\text{Mg}^{2+}$ , organics, or seeds [14]). However, the mechanisms of ACC formation are poorly understood because its transformation can be rapid and may proceed *via* intermediate phases [19]. These factors made

## 1. Experimental

---

time-resolved observations by usual off line techniques difficult.

Early models applied to describe the precipitation pathway consider the nucleation of different polymorphs and hydrates, which then transform into more stable modifications [20, 21] that can also be influenced by the presence of additives [22, 23]. New characterisation tools such as cryogenic-TEM (cryo-TEM) or X-ray microscopy demonstrate that precipitation starts with particles  $\approx 30$  nm in size, which then transform into calcite or vaterite phases [24–26]. That precipitation probably proceeds *via* agglomeration mechanisms involving ACC pre-nucleation clusters [6].

Recently, the early formation of vaterite in the presence of stearic acid [27] has been studied by cryo-TEM. In such studies, the initial formation of vaterite and the eventual transformation into calcite is difficult to control, leading to an inhomogeneous solid in term of shapes and with a broadsize distributions [28, 29]. Other instrumental evidence by *in-situ* small and wide-angle X-ray scattering (SAXS/WAXS) [30] show that ACC crystallises into vaterite *via* a three-stage process. First, hydrated and disordered ACC forms, then rapidly transforms to more ordered and dehydrated ACC; in conjunction with this, vaterite forms *via* a spherulitic growth mechanism. Second, when the supersaturation of the solution with respect to vaterite decreases sufficiently, the mechanism changes to ACC dissolution and vaterite crystals grow [30]. The Ostwald ripening of vaterite particles controls the third stage. This pathway is proposed as the underlying abiotic mechanism for calcium carbonate mineralisation from ACC. The transformation from vaterite to calcite proceeds *via* dissolution-reprecipitation, the kinetics of which depends on solution composition. There is little evidence yet whether this crystallisation mechanism is the same for all carbonates, and if it is the same for pure  $\text{CaCO}_3$  and its solid solutions with other cation (such as solid solution between  $\text{CaCO}_3$  and  $\text{MgCO}_3$  end-members).

Recently, Verch *et al.* [31] reported that, if a mixed calcium and magnesium solution is brought in contact with carbonate ions, mixed pre-nucleation clusters form, in which Ca gets enriched over Mg. It is particularly intriguing in the case of  $(\text{Ca}, \text{Sr})\text{CO}_3$  aqueous-solid solution system because pure strontianite ( $\text{SrCO}_3$ ) crystallises in aragonite structure, while  $\text{CaCO}_3$  with trace Sr usually forms calcite structure. According to thermodynamic predictions [32], at about equal Ca and Sr amounts in the system, two phases (Sr-calcite and Ca-strontianite) should form. However, usually one “disordered” mixed carbonate phase forms during laboratory reaction times [33].

Despite a large number of papers on  $\text{CaCO}_3$  crystallisation, only few deal with the first solid product (ACC), and there is no rigorous model describing its formation.

## 1.1. Materials investigated

### 1.1.2 Calcium phosphate system

The calcium orthophosphates are salts of the tribasic phosphoric acid,  $\text{H}_3\text{PO}_4$  (table 1.1). Those containing  $\text{H}_2\text{PO}_4^-$  ions only form under rather acidic conditions, therefore are not typically found in biological systems. However, both  $\text{HPO}_4^{2-}$  and  $\text{PO}_4^{3-}$  ions occur in the mineral of bones and teeth and various pathological calcifications. Some calcium phosphates are hydrated, and those that belong to the basic apatitic calcium phosphate family contain  $\text{OH}^-$  ions. Most are sparingly soluble in water, and some are very insoluble, but all dissolve in acids.

**Table 1.1** – Calcium phosphate phases and their molar ratio

Calcium phosphates	Abbreviation	Chemical formula	Ca/P molar ratio (theoretical)
Amorphous calcium phosphate	ACP	$\text{Ca}_3(\text{PO}_4)_2 \cdot n\text{H}_2\text{O}$	1.5
Biphasic calcium phosphate	BCP	HA and $\beta$ -TCP (in phase)	Dependent on ratio of HA and $\beta$ -TCP
Carbonate hydroxyapatite	Carbonate HA	$\text{Ca}_{10}(\text{PO}_4)_6(\text{CO}_3)_2(\text{OH})_2$	Nonstoichiometric
Dicalcium phosphate anhydrous (Monetite)	DCPA	$\text{CaHPO}_4$	1.0
Dicalcium phosphate dihydrate (Brushite)	DCPD	$\text{CaHPO}_4 \cdot 2\text{H}_2\text{O}$	1.0
Hydroxyapatite	HA	$\text{Ca}_{10}(\text{PO}_4)_6(\text{OH})_2$	1.67
Octacalcium phosphate	OCP	$\text{Ca}_8\text{H}_2(\text{PO}_4)_6 \cdot 5\text{H}_2\text{O}$	1.33
$\alpha$ -Tricalcium phosphate	$\alpha$ -TCP	$\text{Ca}_3(\text{PO}_4)_2$	1.5
$\beta$ -Tricalcium phosphate	$\beta$ -TCP	$\text{Ca}_3(\text{PO}_4)_2$	1.5

Calcium hydroxyapatite (HA,  $\text{Ca}_{10}(\text{PO}_4)_6(\text{OH})_2$ ) is the main inorganic phase in bone and other hard tissues of vertebrates. Apatites are an important class of minerals with the generalized formula  $\text{M}_{10}(\text{XO}_4)_6\text{L}_2$  where M is a bivalent cation (such as  $\text{Mg}^{2+}$ ,  $\text{Ca}^{2+}$ ,  $\text{Sr}^{2+}$ ,  $\text{Ba}^{2+}$ ,  $\text{Cd}^{2+}$ ,  $\text{Zn}^{2+}$ ,  $\text{Pb}^{2+}$  and some other mono and trivalent cations); X is usually P, V, As or Si, possibly also C and S; L is a monovalent anion such as,  $\text{OH}^-$ ,  $\text{F}^-$ ,  $\text{Cl}^-$ ,  $\text{Br}^-$  [34]. For instance is possible to synthesise compositions as Sr, Ca, Mg fluorohydroxyapatite  $(\text{Mg,Ca,Sr})_{10}(\text{PO}_4)_4(\text{OH,F})_2$  [35–37], as well as find an even more complex composition in natural samples. Thus, several isomorphous substitutions on the three sites are allowed, and they are kinetically possible even at room temperature, or under physiological conditions.

Pure HA crystallises in the monoclinic space group  $P2_1/b$ . However, the presence of

## 1. Experimental

impurities stabilises the hexagonal structure at room temperature. The hexagonal structure, space group  $P6_3/m$ , exhibits lattice parameters of about  $a = 9.43 \text{ \AA}$  and  $c = 6.88 \text{ \AA}$ , with two formula units per cell.

Octacalcium phosphate (OCP),  $\text{Ca}_8(\text{HPO}_4)_2(\text{PO}_4)_4 \cdot 5 \text{ H}_2\text{O}$ , is a biologically important compound. Its crystalline structure belongs to the triclinic system, with the space group  $P\bar{1}$  and lattice parameters of about  $a = 19.69 \text{ \AA}$ ,  $b = 9.52 \text{ \AA}$ ,  $c = 6.83 \text{ \AA}$ ,  $\alpha = 90.15^\circ$ ,  $\beta = 92.54^\circ$  and  $\gamma = 108.65^\circ$ , and two formula units per unit cell. The structure consists of two alternating layers, parallel to (100) plane: one (of about 1.1 nm) with apatitic structure and a second one (of about 0.8 nm) more hydrated as in the DCPD. This particularity generates a periodicity perpendicular to the (100) plane at a relatively large distance (about 1.9 nm, corresponding to  $a$ ), which generates a characteristic high intensity (100) diffraction peak at a low angle. In a standard laboratory instrument, equipped with a Cu  $K_\alpha$  source, this feature appears at about  $5^\circ 2\theta$ ; thus, it is not easy to detect. The presence of the apatitic layer explains the often reported epitaxy between OCP and HA as well as the coexistence of HA-OCP in synthetic and natural samples.

CaP powders can be synthesised with high temperature processes (solid-state reaction), wet chemical routes (precipitation, hydrolysis, sol-gel, hydrothermal), or mechanochemical methods [38, 39]. Porous CaP ceramics are widely used as a synthetic bone [40–43]. For this application, the most commonly applied are composed of sintered HA,  $\beta$ -TCP, and mixture thereof [44]. When CaP powders are produced by solid-state reactions, the particles are agglomerated, characterised by a low aspect ratio and with a broad size distribution [45]. Conversely, when synthesised by precipitation, higher aspect ratios can be achieved (acicular, sheets), but still a high degree of agglomeration and large size and geometry variations are observed [46]. Less agglomeration is reported for hydrothermally produced CaP particles. Needles or whiskers are commonly observed, but the particle size distribution remains quite broad. The understanding of the solid formation mechanism of CaP has significant applications in dentistry, orthopaedics, and reconstructive surgery, as well as in the nutrient cycle in the environment. The crystallisation of CaP from aqueous solutions is reported to proceed *via* the formation of amorphous precursors which fits with the concept of multistage crystallisation, in agreement with the Ostwald step rule [47, 48]. The investigations carried out at the early stage of the solid formation indicated the presence of a precursor with Ca/P ratio of 1.5, which was postulated to consist of several  $\text{Ca}_9(\text{PO}_4)_6$  clusters (Posner's clusters, [49]). Although these observations

## 1.2. Experimental and setups

were met with scepticism, recent reports seem to indicate that the precipitation of calcium phosphate involves the formation of nanometer-sized building blocks. Using AFM (Atomic Force Microscopy), Wang *et al.* [50] observed the calcite surface-induced formation of an apatitic phase through the nucleation and aggregation of nanosized clusters, which subsequently form stable ACP plates prior to the transformation to the final crystalline HA phase. Wang *et al.* [51] observed the crystallisation of CaPs precursors and finally HA inside nanoparticles of ACP formed by the aggregation of Posner's clusters. Other studies report the involvement of octacalcium phosphate as the first phase in the mineralisation process of bone and tooth tissues. Detailed kinetic studies of non-classical CaP crystallisation have been performed using a modified route, in which  $\text{Ca}(\text{NO}_3)_2$  have been replaced with a  $\text{CaCl}_2$  solution [51, 52]. DCPD was reported to be present in the early stage of the calcium phosphate precipitation as well [53].

## 1.2 Experimental and setups

Time-resolved data need to be collected to study the solid formation pathway. In the framework of my studies, the precipitation reactions were followed using a constant composition approach, similar to the system developed by Kazmierczak and Thomson [7, 8] in the investigation of crystal morphology and later adapted by Gebauer [6]. Indeed, this method allows the collection of experimental data maintaining constant some parameters, such as *pH*, specific ionic species concentration, ionic strength, and – provided that a thermodynamic model is available – even the supersaturation. In a later experimental activity, the early stages of precipitation were studied *in-situ* at the synchrotron, under constant supersaturation, temperature, and *pH*. In these experiments, the efforts were devoted towards the detection of entities – and their size distribution – with higher electron density with respect to the liquid phase before the critical saturation point. The systems were studied with a setup developed *ad-hoc*, a contactless reactive pulsation-free liquid jet setup, which is described in section 1.6.

### 1.2.1 Solution preparation

All solutions were prepared using demineralised water further purified using a MilliQ system (Sartorius arium<sup>®</sup> pro VF Ultrapure Water System, resistivity  $>18.2 \text{ M}\Omega \text{ cm}$  at  $25^\circ\text{C}$ ), equipped with UV lamp and ultrafilter, and finally boiled to strip  $\text{CO}_2$ . Mother

## 1. Experimental

---

solutions of HCl and NaOH were prepared by 1:10 dilution from certified  $1 \text{ mol L}^{-1}$  standard solutions (Fluka n. 38210 and n. 38280, respectively). All other chemicals were purchased from Sigma Aldrich (analytical grade ReagentPlus<sup>®</sup>, BioUltra<sup>®</sup>, BioXtra<sup>®</sup>). HCl and NaOH solutions were adjusted to  $10 \text{ mmol L}^{-1}$  from mother solutions. These were used to attain iso-*pH* conditions during the precipitation reactions for both CaC and CaP.

For the calcium carbonate (CaC) system, calcium chloride dihydrate ( $\text{CaCl}_2 \cdot 2 \text{ H}_2\text{O}$ , n. C3881, 99.0%), sodium bicarbonate ( $\text{NaHCO}_3$ , n. 223484, 99.95-100.05%), and sodium carbonate ( $\text{Na}_2\text{CO}_3$  n. S8875,  $\geq 99.5\%$ ) were used. The carbonate buffer solution (*pH*=9.23, at  $25^\circ\text{C}$ ) was prepared from  $\text{NaHCO}_3$  and  $\text{Na}_2\text{CO}_3$  ( $0.732 \text{ g L}^{-1}$  and  $0.106 \text{ g L}^{-1}$ , respectively). The  $\text{CaCl}_2$  solution ( $10 \text{ mmol L}^{-1}$ ) was prepared directly weighing the salt.

In the precipitation study of calcium phosphate (CaP) system, calcium chloride dihydrate ( $\text{CaCl}_2 \cdot 2 \text{ H}_2\text{O}$ , n.C3881, 99.0%), disodium hydrogen phosphate dihydrate ( $\text{Na}_2\text{HPO}_4 \cdot 2 \text{ H}_2\text{O}$ , n. 71643,  $\geq 99.0\%$ ), sodium dihydrogen phosphate dihydrate ( $\text{NaH}_2\text{PO}_4 \cdot 2 \text{ H}_2\text{O}$ , n.71505,  $\geq 99.0\%$ ), and sodium chloride ( $\text{NaCl}$ , n.S7653,  $\geq 99.5\%$ ) were used. The phosphate buffer solution (*pH*= 7.43, at  $25^\circ\text{C}$ ) was prepared from  $\text{Na}_2\text{HPO}_4 \cdot 2 \text{ H}_2\text{O}$  and  $\text{NaH}_2\text{PO}_4 \cdot 2 \text{ H}_2\text{O}$  ( $0.4290 \text{ g L}^{-1}$  and  $1.3082 \text{ g L}^{-1}$ , respectively). When needed, the ionic strength of the different precursor solutions, such as  $\text{CaCl}_2$ , NaOH,  $\text{CH}_3\text{COOH}$ , and  $\text{Na}_2\text{HPO}_4/\text{NaH}_2\text{PO}_4$  buffer, was adjusted to 0.154 by addition of NaCl.

For the liquid jet experiments, the solution concentrations were defined based on the model indication as described later, in order to obtain the wanted *pH*, IS, Ca/C (or Ca/P) ratio, and saturation.

The exact concentration of solutions was double checked by titration (conductometric and acidimetric methods or by ICP-MS); the same stock solutions were used in all calibration and precipitation experiments. Additionally, the concentration of carbonate ions in the NaOH solution was determined weekly by acidimetric titration and OLI [9] modelling.

## 1.2.2 Controlled composition approach

### 1.2.2.1 Titration setup

The precipitation reactions were performed with a setup composed of different commercial titrator devices, electrodes, and reactor supplied by Metrohm AG [54]. The devices are controlled by the dedicated software *tiamo*<sup>TM</sup> 2.4 (full version). Reactions were performed in a closed double-walled water-jacketed Pyrex titration vessel (6.1418.220), connected with an external thermostatic bath (Isotemp, Fisher Scientific), equipped with a five openings lid, and kept under constant stirring (magnetic bar size 15 mm, mixing speed level 11 of the Metrohm AG stirrer device). The gas atmosphere in the reactor was flushed with  $\approx 2 \text{ mL min}^{-1}$  of air, which was pre-conditioned in a Drechsel bottle containing the same carbonate buffer solution at the same temperature and *pH* of the precipitation experiment. Thus, the  $\text{CO}_2$  partial pressure of the air (and humidity) in the reactor was controlled and kept constant.

The use of a small batch reactor allows the collection of kinetic data from the chemical species in solution which reflect the evolution of the solid formation; these data are the fundamental input in the computational model. To preserve the same conditions during the whole precipitation, *pH* and *T* were kept constant. Two 907 Titrandos and one 809 Titrandos devices, controls four dosing devices 800 Dosinos, that operate 807 Dosing Unit. The latter is equipped with a 10 mL glass cylinder, whose volume is divided into 10000 steps resulting in a minimum addition volume of 1.0  $\mu\text{L}$ . Four burettes with anti-diffusion valve tips (6.2726.090) were used to dispense the solutions inside the reactor and were immersed in the liquid phase. Calcium concentration and *pH* were monitored using two calcium sensitive electrodes (Ca-ISE, 6.0510.100) and two *pH* glass electrodes (Unitrode Pt 1000, 6.0258.600) connected to the titrator devices. The temperature was controlled using the Pt 1000 sensors of the *pH* electrodes. The titration system was completed with the 856 Conductivity Module, equipped with a 5-rings conductivity measuring cells (cell  $c = 0.7 \text{ cm}^{-1}$  with Pt 1000, 6.0915.100); further to monitoring the crystallisation process, a photometric sensor Optrode (6.1115.000) was used at one of its six possible wavelengths.

### 1.2.2.2 Calibration of the electrodes

All electrodes were calibrated before each precipitation experiment. The *pH* electrodes were calibrated at the same temperatures and stirring rate of the precipitation

## 1. Experimental

experiments using a 3-points calibration method (pH 4.00, 7.00, 10.00). For the Ca-ISEs, 10 mmolL<sup>-1</sup> CaCl<sub>2</sub> stock solution was added to 35 mL CO<sub>2</sub>-free MilliQ water. During their calibration pH ( $\pm 0.02$ , by addition of NaOH or HCl diluted solution), temperature, ionic strength (IS), stirring rate, as well as electrodes positions into the reactor were maintained at the level of the precipitation experiments. Conductivity cell was calibrated with a 100 mScm<sup>-1</sup> standard solution. No calibration was needed for the optical electrode. Before each use, the electrodes were rinsed several times with MilliQ water and dried with a filtered air stream. The Ca-ISEs were pre-conditioned for 30 min in a similar environment of the initial experimental conditions before each calibration or experiment, to ensure that negligible amount of Ca<sup>2+</sup> was released by the polymeric membranes in the solution. These conditioning procedures were defined by conductometric measurements. After each experiment, all electrodes were washed with acetic acid 10 wt%, rinsed several times with MilliQ water. When not used, the pH electrodes were stored in 3 molL<sup>-1</sup> KCl, whereas the Ca-ISEs, Optrode electrode, and conductivity cell were stored dried.

### 1.2.2.3 A typical precipitation experiment

All precipitation reactions were done at constant temperature ( $\pm 0.2$  °C) and constant pH ( $\pm 0.02$ ). The pH was automatically controlled at a constant value during the entire experiment by titration with acidic or alkaline solutions. In a typical precipitation experiment, 35 mL of buffer solution (carbonate or phosphate; in the following example, the carbonate case is discussed) was poured into the reactor. The solution was pre-titrated with NaOH and HCl to set the defined experimental pH. Once temperature and pH were constant, the calcium solution was added into the reactor at 30  $\mu\text{L min}^{-1}$ . Figure 1.1 represents a schematisation of the calcium amount in the reactor over time. Due to the constant flow rate of CaCl<sub>2</sub> solution added into the reactor, the overall amount of calcium (black line) rises linearly. The coloured lines represent (after the appropriate data treatment) the amount of Ca<sup>2+</sup> measured by the ISEs. In a first stage (figure 1.1, blue line), the amount of Ca<sup>2+</sup> increases over time. Here there is no solid precipitate yet and all chemical species in solution attain the thermodynamic equilibrium (aqueous speciation). The difference between the black line and the blue line represents the amount of Ca that is “bonded”, that is, not in the “free” form as in the calibration experiments, in which no carbonate was present (calibration done at T, pH, and IS equal to the experiment). Thus, this difference must be associated to a Ca-carbonate species, *i.e.*, a “bonded” Ca species, such as CaCO<sub>3</sub><sup>0</sup> ion pair. From these



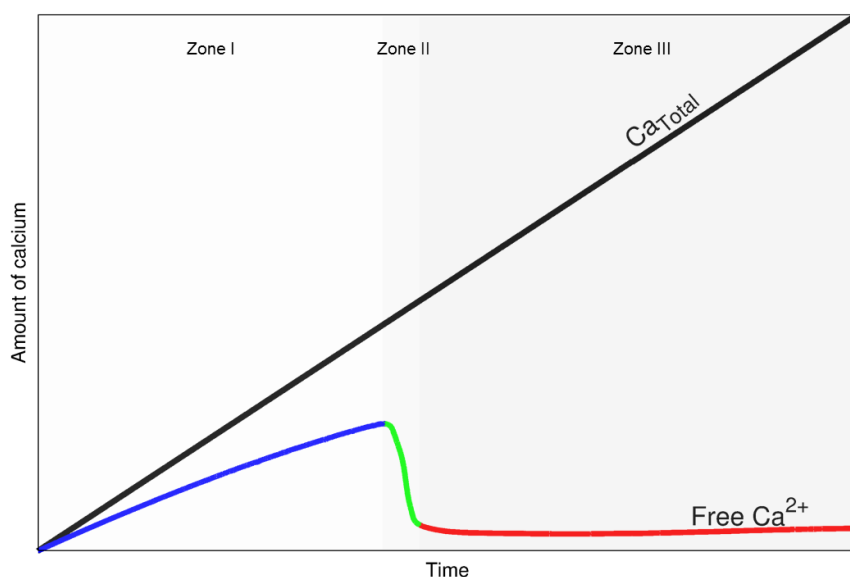


**Figure 1.1** – Calcium added into the reactor. The total amount of calcium (black line) and the amount of  $\text{Ca}_{\text{free}}^{2+}$  (coloured lines) are reported over time.

data, the thermodynamic model of the aqueous species can be refined, and unknown thermodynamic quantities regressed.

The amount of Ca in the system increases up to a maximum value where the precipitation occurs. Nucleation and growth processes govern the following second stage (green line), which is under kinetic control. These data are those of fundamental relevance in the kinetic model. Here the growth rate is fast and limited by the growth kinetics.

The amount of  $\text{Ca}^{2+}$  in solution decreases up to a rather constant value (red line). In this third stage, the aqueous species are again at the thermodynamic equilibrium (as in the first stage), now with both aqueous and solid species. Due to the continuous addition of  $\text{CaCl}_2$  the solid grows, but the growth rate is now limited by the addition of  $\text{CaCl}_2$  and is not limited by the growth kinetics. Thus, the experimental data in this stage have no kinetic relevance, but they are fundamental to assess the solubility of the solid phase in those specific experimental conditions. The resulting solubility product defines the saturation value during the entire precipitation. In this stage, a slightly positive slope is attained because of the depletion of carbonate ions in the reactor due to the solid formation.

The  $\text{CaCl}_2$  solution flow rate (and its optimal concentration) can be varied in the experiments within a range. If the flow rate (or the concentration) is too high, a local increase of  $\text{Ca}^{2+}$  concentration can be established at the burette tip where the pre-

## 1. Experimental

---

cipitation could occur. In this condition, the experiments are poorly reproducible. Moreover, if the  $\text{Ca}^{2+}$  molar flux ( $\text{mols}^{-1}$ ) is overly high, in the last stage of the precipitation the equilibrium at the slow-growing stage of the solid is not attained and, the resulting calculated solubility is wrong, and the kinetic stage (green line) might be too fast and too influenced by the dynamic addition of the chemicals. On the other side, if the flow rate is overly slow, the experiment could last too long, generating a considerable amount of data to treat. Finally, if the concentration is too low, the overall added volume could exceed the reactor capacity. Thus, an experimental trade-off on the concentration and the flow rate of the chemicals needs to be found.

A typical experiment lasts for 3 h to 12 h in a 50 mL reactor. In the precipitation experiments, two Ca-ISEs and two pH electrodes are used, because the solid could interfere with the sensitive elements of the electrodes. If this happens, the signals between the electrodes of the same type are not consistent, and the experiment and calibration need to be repeated. Only when the signals of the electrodes are consistent over the entire experiment timeframe, the data acquisition is considered valid, and the signals averaged, after appropriate data treatment and standard deviation calculated. Moreover, the position of the electrodes in the reactor is maintained as constant as possible. All these little cares were systematically applied in order to have a high reproducibility of the experimental results.

At least three valid repetitions of the data per experimental condition were collected. Each dataset consists of about 3000 data points. Each experimental dataset consists of two independent series of data against time: the first one is the activity of  $\text{Ca}^{2+}$ , as aforementioned discussed, and the second one is the amount of NaOH to add into the system to attain iso-pH conditions. This series corresponds to the amount of carbonate (or phosphate) bonded (chemical derivation in sections 1.2.2.4 and 1.2.2.5). Figure 1.2 represents a typical curve of the NaOH amount added into the system, which is composed of three (almost) linear segments. From the first segment, the amount of bonded carbonate to form aqueous species (including clusters) can be argued. In the second segments, a relatively high amount of carbonate is bonded due to the fast precipitation of the solid phase, while the last segment refers to the carbonate bonded in the slow growth stage (ion pairs and solid phase). Of course, first and third segments have different slopes which can be ascribed to the formation of the solid phase only. In the case of CaC, if only  $\text{CaCO}_3^0$  ion pair is considered and just one stoichiometry for the solid ( $\text{Ca}:\text{CO}_3=1$ ) is allowed, the calculated values for free  $\text{Ca}^{2+}$  and bonded carbonate should be consistent with the experimental data. On the contrary, if a discrepancy

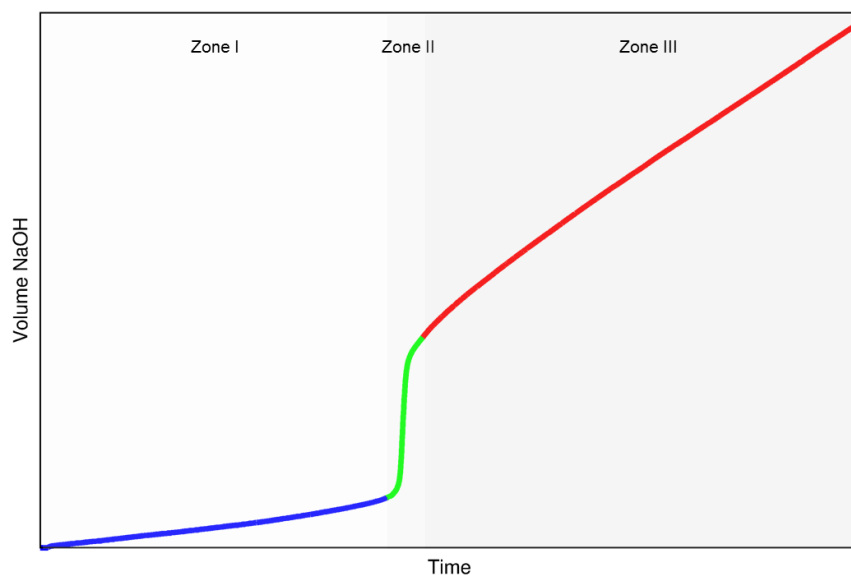


**Figure 1.2** – NaOH added into the reactor to keep  $pH$  constant during the precipitation reaction. The total amount of calcium is reported over time.

is highlighted, a different stoichiometry can be considered. Indeed, in the case of CaC, an interaction between  $\text{CaCO}_3^0$  and  $\text{CO}_3^{2-}$  as well as an interaction between ACC and  $\text{CO}_3^{2-}$  were assessed (section 3.1). It is worth mentioning that such considerations cannot be argued without the simultaneous evaluation of the two independent series of data. If only free  $\text{Ca}^{2+}$  data are considered, the formation constant of the ion pair and the solubility constant of the solid phase can be estimated through a speciation model (as done in the literature, [6]), but no clue on their stoichiometry can be argued. On the other side, if the free  $\text{Ca}^{2+}$  data are combined with the bonded carbonate data, the stoichiometry of the ion pair and the solid phase can be evaluated as well. This kind of approach is one of the strengths of my scientific outcomes, beyond the state-of-the-art. In the case of CaP, this particular feature is of fundamental relevance. In fact, different stoichiometry for the clusters (Posner's clusters), as well as for the solid phase (Ca/P ratio from 1 (DCPD) to 1.66 (HA)) are possible. To each composition a different amount of bonded phosphate corresponds therefore different slopes of the first and the third segments results. Thus, the analytical information of both  $\text{Ca}^{2+}$  free and bonded phosphate, in the two segments where the thermodynamic equilibrium is attained, allows the regression of the thermodynamic quantities of the known species (*e.g.*, stoichiometry and formation constant of the Posner's clusters and stoichiometry and solubility of the solid phase). The analytical derivation of bonded carbonate or phosphate ions will be described in the following session, in the framework of

## 1. Experimental

the system specific particularities of the two investigated processes (section 1.2.2.4 and 1.2.2.5, for CaC and CaP, respectively).

### 1.2.2.4 CaC experiments

Precipitation experiments were performed at five different temperatures at constant pH (9.00), namely 6.2 °C, 15.0 °C, 25.0 °C, 35.0 °C and 45.0 °C. An additional set of four experiments at constant temperature (25.0 °C) were carried out at pH of 9.25, 9.50, 9.75 and 10.00. As introduced in section 1.2.2, the amount of bonded carbonate can be analytically evaluated from the amount of NaOH added into the system to maintain the pH constant. In the case of the formation of  $\text{CaCO}_3^0$  ion pair, it is possible to calculate the amount of bonded carbonate applying the following reasoning.

The second protonation reaction of carbonic acid is



The associate equation reads

$$K_{H2} = \frac{a_{\text{CO}_3^{2-}} \cdot a_{\text{H}^+}}{a_{\text{HCO}_3^-}} \quad (1.2)$$

If  $\text{Ca}^{2+}$  ions are added in a system containing a carbonate buffer, both carbonic species can react to form bound carbonate (*e.g.*  $\text{CaCO}_3^0$  ion pair). In the following scheme, the initial stage represents the system when the reaction between the indicated ions has not yet occurred. The final stage represents the equilibrium after Ca bonding.

(A)	$\text{HCO}_3^-$	+	$\text{Ca}^{2+}$	$\xrightleftharpoons{K_1}$	$\text{CaCO}_3^0$	+	$\text{H}^+$
Initial	$n$		$m$		–		$l$
Final	$n - \alpha$		$m - \alpha - \beta$		$\alpha + \beta$		$l + \alpha - \xi$

(B)	$\text{CO}_3^{2-}$	+	$\text{Ca}^{2+}$	$\xrightleftharpoons{K_2}$	$\text{CaCO}_3^0$
Initial	$p$		$m$		–
Final	$p - \beta$		$m - \alpha - \beta$		$\alpha + \beta$

where  $n$ ,  $m$ ,  $l$ , and  $p$  are the activities for bicarbonate, calcium, hydronium, and

## 1.2. Experimental and setups

carbonate ions, respectively, in the system at the initial stage, before the ion pairs formation. After adding  $\text{Ca}^{2+}$  ions, a fraction  $\alpha$  reacts with bicarbonate ion, and a fraction  $\beta$  reacts with carbonate ions to form  $\text{CaCO}_3^0$ . Thus, the activities of all chemical species are reported in the final stage. In particular,  $\xi$  represents the amount of  $\text{H}^+$  that need to be “removed” from the system to keep constant pH. In the system, “removed” means adding an amount of  $\text{OH}^-$  into the system equivalent to  $\xi$ .

Thus, to keep pH constant, the amount of  $\text{H}^+$  in the initial  $l$  and final  $(l + \alpha - \xi)$  stage need to be constant. Thus

$$\alpha = \xi \quad (1.3)$$

where  $\xi$  is the activity of  $\text{OH}^-$  added. Rewriting (1.2) with the symbols for the initial and final stage, including (1.3), we obtain

$$K_{H2} = \frac{p \cdot l}{n} \quad (1.4)$$

and

$$K_{H2} = \frac{(p - \beta) \cdot l}{n - \alpha} \quad (1.5)$$

From the equivalence of eqs. (1.4) and (1.5) can be obtained

$$\frac{p - \beta}{n - \alpha} = \frac{p}{n} \quad (1.6)$$

The numerator at the left-hand-side of eq. (1.6) represents the amount of carbonate ion which remains in solution after the formation of carbonate-bound species (*i.e.*,  $\text{CaCO}_3^0$ ). Similarly, the denominator is the amount of bicarbonate ion. Since the pH is constant, the carbonate-to-bicarbonate ratio remains constant in the whole process. From eq. (1.6), we obtain:

$$n = \frac{p \cdot \alpha}{\beta} \quad (1.7)$$

which combined with eq. (1.6) and eq. (1.4), gives

$$\beta = \alpha \cdot \frac{K_{H2}}{l} = \alpha \cdot \frac{a_{\text{CO}_3^{2-}}}{a_{\text{HCO}_3^-}} \quad (1.8)$$

## 1. Experimental

---

The amount of bound carbonate to form the ion pair represented as  $\text{CO}_3^{2-}$  bound, can be defined as

$$[\text{CO}_3^{2-}]_{\text{bound}} = [\text{CaCO}_3^0] = \alpha + \beta \quad (1.9)$$

Combining eq. (1.9) with eq. (1.8)

$$[\text{CO}_3^{2-}]_{\text{bound}} = \alpha \cdot \left( 1 + \frac{a_{\text{CO}_3^{2-}}}{a_{\text{HCO}_3^-}} \right) = \alpha \cdot \left( 1 + \frac{K_{\text{H2}}}{a_{\text{H}^+}} \right) \quad (1.10)$$

Thus, considering eqs. (1.3) and (1.4)

$$[\text{CO}_3^{2-}]_{\text{bound}} = \xi \cdot \left( 1 + \frac{K_{\text{H2}}}{a_{\text{H}^+}} \right) \quad (1.11)$$

In conclusion, recalling the meaning of  $\xi$

$$[\text{OH}^-]_{\text{to add}} = \frac{a_{\text{H}^+} \cdot [\text{CO}_3^{2-}]_{\text{bound}}}{a_{\text{H}^+} + K_{\text{H2}}} \quad (1.12)$$

which represents the analytical link between the amount of NaOH added into the system and the bonded carbonate ion. When also ACC is formed, the amount of NaOH needed to keep the pH constant is due to both species ( $\text{CaCO}_3^0(\text{aq})$ ,  $\text{CaCO}_{3(\text{s, am})}$ ) which explain the slope difference of the first and third segments.

### 1.2.2.5 CaP experiments

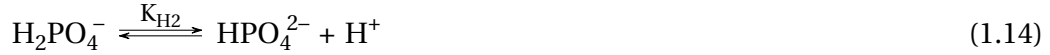
The precipitation experiments were done under biologically relevant conditions, such as 37.0 °C and pH 7.40, and at different ionic strength (IS), which is controlled by the addition of NaCl in the precursor solutions. The first series of experiments were carried out at low IS (L-IS, 0.024 to 0.017, *i.e.*, without the addition of NaCl into the initial solutions). The second series at high IS (H-IS, 0.149 to 0.088, *i.e.*, adding NaCl in the phosphate buffer only). The third series at constant IS (0.154, *i.e.*, adding NaCl in every solution used during the precipitation). In the L-IS and H-IS, the IS strength drifted during the precipitation, mainly because of the dilution due to the addition of  $\text{CaCl}_2$  and NaOH solutions; in the C-IS, the IS was maintained at a constant level, *i.e.*, that of physiological conditions.

As discussed in section 1.2.2, the amount of bonded phosphate can be analytically evaluated from the amount of NaOH added into the system to maintain the pH

## 1.2. Experimental and setups

constant, applying the reasoning here developed in the case of the formation of the  $\text{CaHPO}_4$  ion pair. The derivation of other species can be done in the same way and their final derivations is summarised at the end.

The protonation equilibria of phosphoric acid are:



The associated equations are:

$$K_{H1} = \frac{a_{\text{H}_2\text{PO}_4^-} \cdot a_{\text{H}^+}}{a_{\text{H}_3\text{PO}_4}} \quad (1.16)$$

$$K_{H2} = \frac{a_{\text{HPO}_4^{2-}} \cdot a_{\text{H}^+}}{a_{\text{H}_2\text{PO}_4^-}} \quad (1.17)$$

$$K_{H3} = \frac{a_{\text{PO}_4^{3-}} \cdot a_{\text{H}^+}}{a_{\text{HPO}_4^{2-}}} \quad (1.18)$$

If  $\text{Ca}^{2+}$  ions are added in a system containing phosphate ions, a fraction of phosphate ions can react to form bound phosphate species. For instance, in the case of the formation of the ion pair  $\text{CaHPO}_4$  the associated equilibrium reactions are:

<hr/>					
(A)	$\text{H}_3\text{PO}_4$	+	$\text{Ca}^{2+}$	$\xrightleftharpoons{K_1}$	$\text{CaHPO}_4^0$ + $2\text{H}^+$
Initial	$q$		$m$		– $l$
Final	$q - \gamma$		$m - \alpha - \beta - \gamma - \delta$		$\alpha + \beta + \gamma + \delta$ $l + 2\gamma + \beta - \delta - \xi$
<hr/>					
(B)	$\text{H}_2\text{PO}_4^-$	+	$\text{Ca}^{2+}$	$\xrightleftharpoons{K_2}$	$\text{CaHPO}_4^0$ + $\text{H}^+$
Initial	$q$		$m$		– $l$
Final	$p - \beta$		$m - \alpha - \beta - \gamma - \delta$		$\alpha + \beta + \gamma + \delta$ $l + 2\gamma + \beta - \delta - \xi$
<hr/>					
(C)	$\text{HPO}_4^{2-}$	+	$\text{Ca}^{2+}$	$\xrightleftharpoons{K_3}$	$\text{CaHPO}_4^0$
Initial	$n$		$m$		–
Final	$n - \alpha$		$m - \alpha - \beta - \gamma - \delta$		$\alpha + \beta + \gamma + \delta$
<hr/>					

## 1. Experimental

(D)	$\text{PO}_4^{3-}$	+	$\text{Ca}^{2+}$	+	$\text{H}^+$	$\xrightleftharpoons{K_4}$	$\text{CaHPO}_4^0$
Initial	$r$		$m$		$l$		–
Final	$r - \delta$		$m - \alpha - \beta - \gamma - \delta$		$l + 2\gamma + \beta - \delta - \xi$		$\alpha + \beta + \gamma + \delta$

where  $q$ ,  $p$ ,  $n$ ,  $r$ ,  $m$ , and  $l$  are the activities for phosphates, calcium and hydronium ions in the system in the initial stage, respectively, before the ion pair formation. After adding  $\text{Ca}^{2+}$  ions, a fraction of phosphates ions reacts forming the ion pair  $\text{CaHPO}_4$ . Thus, the activities of all chemical species are reported in the final stage. In particular,  $\xi$  represents the amount of  $\text{H}^+$  that needs to be “removed” from the system to keep constant pH. In the system, “removed” means adding an amount of  $\text{OH}^-$  into the system to attain iso-pH conditions. Thus Initial = Final,

$$\begin{aligned} l &= l + 2\gamma + \beta - \delta - \xi \\ 2\gamma + \beta - \delta &= \xi \end{aligned} \quad (1.19)$$

where  $\xi$  is the amount of  $\text{OH}^-$  added. Rewriting eqs. (1.16)-(1.18) with the symbols for the initial and final stage (Scheme 1), they give

$$K_{H1} = \frac{(p - \beta) \cdot l}{q - \gamma} = l \cdot \frac{p}{q} \quad (1.20)$$

$$K_{H2} = \frac{(n - \alpha) \cdot l}{p - \beta} = l \cdot \frac{n}{p} \quad (1.21)$$

$$K_{H3} = \frac{(r - \delta) \cdot l}{n - \alpha} = l \cdot \frac{r}{n} \quad (1.22)$$

which can be rewritten as

$$\gamma = \frac{\alpha \cdot l^2}{K_{H1} \cdot K_{H2}} \quad (1.23)$$

$$\beta = \frac{\alpha \cdot l}{K_{H2}} \quad (1.24)$$

$$\delta = \frac{\alpha K_{H3}}{l} \quad (1.25)$$

Combining eq. (1.25) with eq. (1.24), the amount of  $\text{OH}^-$  to add for the iso-pH condition gives

$$[\text{OH}^-]_{\text{to add}} = \xi = \alpha \cdot \left( \frac{2 \cdot l^2}{K_{H1} \cdot K_{H2}} + \frac{l}{K_{H2}} - \frac{K_{H3}}{l} \right) \quad (1.26)$$



## 1.2. Experimental and setups

The amount of  $\text{CaHPO}_4$  ion pair formed, which corresponds to the bonded phosphate for the formation of that specific ion pair, is

$$\begin{aligned} [\text{PO}_4^{3-}]_{(\text{CaHPO}_4^0)} &= \alpha + \beta + \gamma + \delta \\ &= \alpha \cdot \left( 1 + \frac{l}{K_{H2}} + \frac{l^2}{K_{H1} \cdot K_{H2}} + \frac{K_{H3}}{l} \right) \end{aligned} \quad (1.27)$$

Combining eq. (1.26) and eq. (1.27) the amount of  $\text{OH}^-$  to add to keep iso-pHcondition because of the formation of the ion pair  $\text{CaHPO}_4$  is

$$[\text{OH}^-]_{\text{to add}} = [\text{PO}_4^{3-}]_{(\text{CaHPO}_4^0)} \cdot \frac{\left( \frac{l}{K_{H2}} + \frac{2l^2}{K_{H1} \cdot K_{H2}} - \frac{K_{H3}}{l} \right)}{\left( 1 + \frac{l}{K_{H2}} + \frac{K_{H3}}{l} + \frac{l^2}{K_{H1} \cdot K_{H2}} \right)} \quad (1.28)$$

The same procedure can be reformulated for all considered calcium-phosphate species that are formed during the addition of  $\text{Ca}^{2+}$  ion into the phosphate buffer, kept at iso-pHconditions. Thus,

$$[\text{OH}^-]_{\text{to add}} = [\text{PO}_4^{3-}]_{(\text{CaH}_2\text{PO}_4^+)} \cdot \frac{\left( \frac{l}{K_{H1}} - \frac{K_{H2}}{l} - \frac{2K_{H2} \cdot K_{H3}}{l^2} \right)}{\left( 1 + \frac{K_{H2}}{l} + \frac{l}{K_{H1}} + \frac{K_{H2} \cdot K_{H3}}{l^2} \right)} \quad (1.29)$$

$$[\text{OH}^-]_{\text{to add}} = [\text{PO}_4^{3-}]_{(\text{CaPO}_4^-)} \cdot \frac{\left( \frac{3 \cdot l^3}{K_{H1} \cdot K_{H2} \cdot K_{H3}} + \frac{2 \cdot l^2}{K_{H2} \cdot K_{H3}} + \frac{l}{K_{H3}} \right)}{\left( 1 + \frac{l}{K_{H3}} + \frac{l^2}{K_{H2} \cdot K_{H3}} + \frac{l^3}{K_{H1} \cdot K_{H2} \cdot K_{H3}} \right)} \quad (1.30)$$

For solid phases formation, the same consideration can be applied.

For HA ( $\text{Ca}_5(\text{PO}_4)_3\text{OH}$ )

$$[\text{OH}^-]_{\text{to add}} = [\text{PO}_4^{3-}]_{\text{HA}} \cdot \frac{\left( 10 \frac{l}{K_{H1}} + 7 + 4 \cdot \frac{K_{H2}}{l} + \frac{K_{H2} \cdot K_{H3}}{l^2} \right)}{\left( \frac{K_{H2}}{l} + 1 + \frac{l}{K_{H1}} + \frac{K_{H2} \cdot K_{H3}}{l^2} \right)} \quad (1.31)$$

For OCP ( $\text{Ca}_4\text{H}(\text{PO}_4)_3$ )

$$[\text{OH}^-]_{\text{to add}} = [\text{PO}_4^{3-}]_{\text{OCP}} \cdot \frac{\left( 8 \frac{l}{K_{H1}} + 5 + 2 \cdot \frac{K_{H2}}{l} + \frac{K_{H2} \cdot K_{H3}}{l^2} \right)}{\left( \frac{K_{H2}}{l} + 1 + \frac{l}{K_{H1}} + \frac{K_{H2} \cdot K_{H3}}{l^2} \right)} \quad (1.32)$$

Finally, for a generic  $\text{Ca}_x(\text{PO}_4)_y\text{OH}_{(2x-3y)}$  Posner's cluster containing  $x$  calcium ions and  $y$  phosphate ions, and eventually neutralized by  $\text{OH}^-$  (or  $\text{H}^+$ ), *e.g.*,  $\text{Ca}_6(\text{PO}_4)_3$ ,

## 1. Experimental

$Ca_5(PO_4)_3OH$ ,  $Ca_4(PO_4)_3H$ , *etc.*

$$[OH^-]_{\text{to add}} = [PO_4]_{Ca_x(PO_4)_y} \cdot \frac{\left(2 \cdot \frac{l}{K_{H1}} + (2x - y) + (2x - 2y) \frac{K_{H2}}{l} + (2x - 3y) \frac{K_{H2} \cdot K_{H3}}{l^2}\right)}{\left(\frac{K_{H2}}{l} + 1 + \frac{l}{K_{H1}} + \frac{K_{H2} \cdot K_{H3}}{l^2}\right)} + (2x - 3y) \quad (1.33)$$

The overall amount of  $OH^-$  to add in solution to keep iso-*pH* conditions is the summation of eqs. (1.28)–(1.33) where the corresponding bonded phosphate species is calculated by the speciation model in the case of aqueous species or by the kinetic model in the case of solid species.

### 1.3 Computational model: basis, and system-specific details.

In this doctoral work, a computational model has been applied to understand the precipitation process of both calcium carbonate (CaC) and calcium phosphate (CaP) systems. The central core code was already developed in the group. Thus, in the framework of this work, only the system-specific part (for CaC and CaP systems) of the code was developed and implemented. Specifically, the speciation equations and the mass balance equations, described in sections 1.3.1 and 1.3.2, were implemented. In the original code version, Testino *et al.* [10] have shown how the analysis of kinetic data using the Population Balance Equation (PBE) may help to understand the precipitation pathway and the elementary processes of the aqueous  $BaTiO_3$  system [55]. The crystallisation curves (amount of solid *vs* time) display a sigmoidal shape and show a significant induction time, which was ascribed by several authors [56–58] to be due to a dissolution-precipitation mechanism. Nevertheless, the theoretical interpretation based on the Johnson-Mehl-Avrami equations in solution is questionable. These equations have rigid boundary conditions and provide macroscopic kinetic parameters that cannot be easily correlated with fundamental properties that describe supersaturation, interfacial tension, and diffusion transport.

The PBE approach offered an alternative way to correlate measured particle size distributions and their evolution over time to the CNT parameters. PBE describes the evolution of size distribution and statistical moments of an ensemble of particles

### 1.3. Computational model: basis, and system-specific details.

simultaneously undergoing nucleation, growth, coalescence, and disruption. This approach may be used to discern between specific classical and non-classical crystallisation pathways, if based on a specific set of models describing the experimental data vs time, namely, mass balance, primary and secondary particle size, evidence on pre-nucleation clusters, amorphous phases, crystalline or non-crystalline intermediates, induction time, *etc.* This set of models can be associated with the most plausible crystallisation pathway for the system under investigation, while other mechanisms may be excluded. The PBE links the experimental data and the kinetic rate equations that mathematically describe a specific crystallisation pathway. In such studies, the acquisition of the high-quality time-resolved kinetic data plays a crucial role. Rate laws for dissolution, nucleation, and growth depend on aqueous speciation, *pH*, water and ions activities, saturation, ionic strength, and so forth. Therefore, modelling the kinetics of mineral-water reactions is hardly possible without the computer-aided thermodynamic speciation software [59]. The model can run different models for the different elementary processes of precipitation, such as nucleation, growth, and aggregation. In the nucleation part, it is possible to choose between 4 models:

- homogeneous nucleation
- 2D secondary nucleation
- 3D secondary nucleation
- heterogeneous nucleation

The growth process can be simulated in two regimes:

- constant rate growth
- diffusion limited growth

For the aggregation, two models are implemented:

- constant kernel
- constant Brownian

## 1. Experimental

---

The used code is based on the discretised population balance approach, where the continuum of size is divided into classes. Each class is associated with a differential equation, and the system of ordinary differential equations is solved at every time step. The kinetic solver is used to compute the amount of solid phase formed, where the particles are considered as spheres. This limitation is due to the applied population balance approach being monovariate. Thus only one internal parameter (*i.e.*, the particle equivalent diameter) can be considered. Within this constraint, the applied approach can correctly calculate at least the first four moments of the particles population [10]. Moreover, since the measurement of the particle size distribution was not experimentally achievable in the case of calcium carbonate and phosphate systems, the computation code was used to solve the mass balance equations. Nucleation and growth rates, as well as, the particle size represent some of the computation output. Different combinations were applied to interpret the experimental precipitation curves. The kinetic package is combined with a thermodynamic package that solves the aqueous system speciation.

### 1.3.1 Calcium carbonates

#### 1.3.1.1 Preliminary thermodynamic calculations (OLI software)

Preliminary thermodynamic modelling was carried out using OLI software (v. 9.2) in order to identify all relevant chemical species and calculate some equilibrium constants (such as  $K_w$ ,  $K_{H2}$ ), for the comprehensive thermodynamic model (1.3.1.2). The considered aqueous chemical species, within the experimental conditions, are the following:  $\text{Ca}^{2+}$ ,  $\text{CO}_3^{2-}$ ,  $\text{HCO}_3^-$ ,  $\text{H}^+$ ,  $\text{OH}^-$ ,  $\text{CaCO}_3^0$ ,  $\text{Na}^+$ ,  $\text{Cl}^-$ ,  $\text{Ca}(\text{HCO}_3)^+$ ,  $\text{CaCl}_2^0$ ,  $\text{CaCl}^+$ ,  $\text{CaOH}^+$ ,  $\text{NaCO}_3^-$ ,  $\text{HCl}^0$ ,  $\text{NaHCO}_3^0$ , and  $\text{CO}_2$ . The solid phase ACC ( $\text{CaCO}_{3(s, \text{am.})}$ ) was introduced into the species database using the thermodynamic properties of  $\text{CaCO}_{3(s, \text{aragonite})}$  as starting point and then refined as ACC.

For these preliminary thermodynamic calculations the experimental data were spilt into two sections generating two sub-datasets, namely before the maximum and at the plateau of the  $\text{Ca}^{2+}$  ion signal (Figure 3.1 p. 83, Zone I and IV), excluding the sigmoidal parts of the signal in between. In fact, within the former two segments, pseudo equilibrium conditions might be assumed, namely before the precipitation (where only ionic or molecular species equilibria were considered) and in the presence of the precipitated solid phase (where the chemical species in solution might be considered in equilibrium with the solid phase which undergoes precipitation, *i.e.*, saturation is

### 1.3. Computational model: basis, and system-specific details.

supposed to be equal to 1), respectively; the implication of the latter assumption is discussed in chapter 3, section 3.1.

All the experimental data at  $pH=9$  in the explored temperature range (from 279.35 K to 318.35 K, *i.e.*, 10 sub-datasets of 25 points each, equally distributed over the whole segment) were used to regress the thermodynamic quantities for the chemical species  $\text{CaCO}_3(\text{s, am.})$  and  $\text{CaCO}_3^0(\text{aq.})$ . Table A.1 summarizes the results. A similar approach was used at  $T=298.15$  K and the different  $pH$ s but the regression of the thermodynamic values based on the two sub-datasets for each  $pH$  value were carried out at each  $pH$  value independently.

Based on the regressed data and assuming the pseudo equilibrium of the chemical species with the solid phase, the solubility of the  $\text{CaCO}_3^0(\text{aq.})$  was estimated against  $T$  and  $pH$ . These values were used as starting points in the comprehensive thermodynamic-kinetic model.

#### 1.3.1.2 Comprehensive thermodynamic model

The comprehensive thermodynamic model was developed to compute the relevant features of the speciation, as well as additional quantities, in a code implementable in the kinetic model (appendix A, section A.1). The preliminary calculation showed that only the first eight of the aforementioned aqueous chemical species were relevant for the thermodynamic modelling; all the others species containing Ca or C were a least two orders of magnitude lower in concentration and thus not considered relevant in the comprehensive model. The considered aqueous species and equations in the speciation model are:

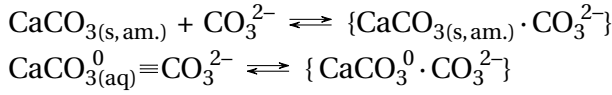


The considered solid species are (ACC)  $\text{CaCO}_3 \rightleftharpoons \text{CO}_3^{2-} + \text{Ca}^{2+}$ ;  $K_{sp}(1)$

Their equilibrium constants are reported in table 1.2. Two additional interactions were considered, one between carbonate ion and the ACC phase,  $\text{CaCO}_3(\text{s, am.})$ , and

## 1. Experimental

a second one between carbonate ion and the ion pair  $\text{CaCO}_3^0_{(\text{aq})}$ , according to the chemical reactions:



and associated with the equations:

$$a_{\text{CaCO}_{3(\text{s, am.})}} \cdot a_{\text{CO}_3^{2-}} \cdot K_{\alpha 1} = a_{\{\text{CaCO}_{3(\text{s, am.})} \cdot \text{CO}_3^{2-}\}} \quad (1.39)$$

$$a_{\text{CaCO}_3^0_{(\text{aq})}} \cdot a_{\text{CO}_3^{2-}} \cdot K_{\alpha 2} = a_{\{\text{CaCO}_3^0 \cdot \text{CO}_3^{2-}\}} \quad (1.40)$$

where  $K_{\alpha 1}$  and  $K_{\alpha 2}$  represent the equilibrium constants and  $a_x$  the activity of the species  $x$ .

In this thesis, the chemical species with graph brackets notation have a meaning which is defined for every case. In the previous chemical reactions, graph brackets identify complex chemical species with a defined ratio between the indicated species. For instance  $\{\text{CaCO}_3^0_{(\text{aq})} \cdot \text{CO}_3^{2-}\}$  identifies a chemical species where the ratio between the ion pair and the carbonate ion is 1:1. Thus, it is a schematisation of an ionic aqueous species composed by one  $\text{Ca}^{2+}$  ion, two  $\text{CO}_3^{2-}$  ions, an undefined number of  $\text{HCO}_3^-$  ions and most probably neutralized by  $\text{Na}^+$  ions. Similarly, the chemical species  $\{\text{CaCO}_{3(\text{s, am.})} \cdot \text{CO}_3^{2-}\}$  represents the interaction between the amorphous phase and carbonate ions with the indicated stoichiometric ratio; again bicarbonate ions and counter ions might be, plausibly, involved. This species can be considered as ionic since it represents the dynamic chemisorption interaction between carbonate ions and the amorphous phase. It is plausible that in a carbonate buffer, each calcium ion could interact with more than one carbonate ion, as indicated by atomistic simulations [60]. Similarly, the ACC phase can bind carbonate ions on its “surface” changing the overall carbonate-to-calcium ratio ( $\text{CO}_3^{2-}/\text{Ca}^{2+}$ ) in the solid phase. The introduction of these species, formally allows tuning the  $\text{CO}_3^{2-}/\text{Ca}^{2+}$  between 1 (no interaction) to 2 (complete formation of such species) before and after the formation of ACC. The introduction of these entities were justified by the depletion of carbonate ions from the solution, experimentally correlated to the amount on hydroxide ions added in to the system in order to maintain the  $\text{pH}$  constant. In fact, the amount of

### 1.3. Computational model: basis, and system-specific details.

bound carbonate ions is experimentally accessible from the equation:

$$\{OH^-\}_{to\ add} = \frac{a_{H^+} \cdot \{CO_3^{2-}\}_{bound}}{a_{H^+} + K_{H2}} \quad (1.41)$$

which is derived as described in section 1.2.2.4. In eq. 1.41, the graph brackets for  $\{CO_3^{2-}\}_{bound}$  identify all species where carbonate ions is bound, *i.e.*, not as ionic species in solution:

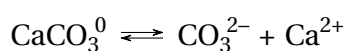
$$\{CO_3^{2-}\}_{bound} = CaCO_3(s, am.) + CaCO_3^0 + 2\{CaCO_3(s, am.) \cdot CO_3^{2-}\} + 2\{CaCO_3^0(aq) \cdot CO_3^{2-}\} \quad (1.42)$$

and  $\{OH^-\}_{to\ add}$  is the amount of hydroxide ions to add into the system in order to keep the  $pH$  constant. In this latter case, graph brackets are used to consider that  $OH^-$  and  $H^+$ , have a different activity coefficient: as discussed and demonstrated deriving the equations in section 1.2.2.4, the amount of hydroxide ions added into the system corresponds to the activity of the hydrogen ion needed to neutralize the system. Thus, the difference between the activity coefficients of these two species needs to be taken into account.

In eq. 1.41,  $K_{H2}$  is the second carbonic acid protonation constant:



It is worth noting that, contrary to the bound carbonate ion, the amount of bound bicarbonate ion is not experimentally accessible. Thus, the chemical interaction between bicarbonate ions and or  $CaCO_3^0$  is plausible as well, but not relevant for modelling. The ion pair  $CaCO_3^0$  formation reaction is:



and the associated equilibrium constant,  $K_{AS}$ , is defined as:

$$a_{CaCO_3^0} \cdot K_{AS} = a_{CO_3^{2-}} \cdot a_{Ca^{2+}} \quad (1.44)$$

Saturation,  $S$ , is defined as:

$$S = \frac{a_{CO_3^{2-}} \cdot a_{Ca^{2+}}}{K_{sp}} \quad (1.45)$$

## 1. Experimental

where  $K_{sp}$  is the solubility product of the solid phase which undergoes precipitation, namely  $\text{CaCO}_{3(s, am.)}$ . Of course, the ionic product of water is also considered:

$$K_w = a_{H^+} \cdot a_{OH^-} \quad (1.46)$$

Since  $\text{CaCl}_2$  solution is added into the system, the total concentration of  $\text{Cl}^-$ ,  $\text{Cl}_T$ , is computed as:

$$[\text{Cl}_T] = 2 [\text{Ca}_T] \quad (1.47)$$

where  $[\text{Ca}_T]$  is the overall concentration of Ca in the system. The amount of  $\text{Na}^+$  is that required to attain the electro neutrality condition:

$$\sum [i] c_i = 0 \quad (1.48)$$

where  $[i]$  is the molar concentration of the chemical aqueous species  $i$  and  $c_i$  is its ionic charge.

It is worth noting that the overall amount of  $\text{Na}^+$ , subtracted by the amount of  $\text{Na}^+$  introduced with the initial carbonate buffer solution, can be compared to  $V_T(\text{OH}_{\text{to add}}^-)$ , since NaOH is added into the system to keep the pH constant. Thus, considering that  $\text{Na}^+$  and  $\text{OH}_{\text{to add}}^-$  are independently computed, their calculated molar equivalence represents an internal consistency proof. In this calculation the amount of carbonate ions that contaminated the NaOH solution need to be considered.

Two additional mass balance equations must be included for total Ca,  $\text{Ca}_T$ , and total C,  $\text{C}_T$ , respectively.

$$\begin{aligned} \text{Ca}_T = & \text{Ca}^{2+} + \text{CaCO}_3^0_{(aq)} + \text{CaCO}_{3(s, am.)} \\ & + \{ \text{CaCO}_{3(s, am.)} \cdot \text{CO}_3^{2-} \} + \{ \text{CaCO}_3^0_{(aq)} \cdot \text{CO}_3^{2-} \} \end{aligned} \quad (1.49)$$

$$\begin{aligned} \text{C}_T = & \text{CO}_3^{2-} + \text{HCO}_3^- + \text{CaCO}_3^0 + 2 \{ \text{CaCO}_{3(s, am.)} \cdot \text{CO}_3^{2-} \} \\ & + 2 \{ \text{CaCO}_3^0_{(aq)} \cdot \text{CO}_3^{2-} \} \end{aligned} \quad (1.50)$$

The overall amount of Ca and C are known parameters. Finally, pH is fixed to a defined value:

$$\text{pH} = -\log(a_{H^+}) \quad (1.51)$$



### 1.3. Computational model: basis, and system-specific details.

**Table 1.2** – Equilibrium constants for the equation considered in the model(25 °C, pH 9.00).

Equilibrium constant	Value	Source
$K_{H2}$	$4.68 \times 10^{-11}$	OLI <sup>1</sup>
$K_w$	$1.0 \times 10^{-14}$	OLI
$K_{AS}$	$3.32 \times 10^2$	Regressed
$K_{sp}$	$3.55 \times 10^7$	Regressed
$K_{\alpha 1}(2)$	$2.8 \times 10^3$	Regressed
$K_{\alpha 2}(3)$	$4.2 \times 10^{10}$	Regressed

The eqs. 1.39-1.51, combined with the thermodynamic constants  $K_{sp}$ ,  $K_{AS}$ ,  $K_{\alpha 1}$ , and  $K_{\alpha 2}$  and the known values for  $K_w$ ,  $K_{H2}$ , pH,  $Ca_T$ , and  $C_T$  allow the calculation of the chemical speciation (eight chemical species and two complex species) as well as  $S$ ,  $\{CO_3^{2-}\}_{bonded}$ , and  $\{OH^-\}_{toadd}$  for a given amount of  $CaCO_{3(s,am.)}$ . The latter species is the objective of the mass balance equation included in the kinetic model (1.3.1.3). Without computing the kinetics, the system of equations can be solved with the constraint  $CaCO_{3(s,am.)} = 0$  to describe the first sub-dataset of the experimental data, *i.e.*, before the solid formation (Figure 1, Zone I). The activity coefficient  $\gamma_i$  for the aqueous chemical species  $i$  are calculated using the Debye-Hückel equation for long range interaction [61] (chapter 2, section 2.1.1, eq. (2.13)).

The activity coefficients for the two complex chemical species  $\{CaCO_{3(s,am.)}^0 \cdot CO_3^{2-}\}$  and  $\{CaCO_{3(aq)}^0 \cdot CO_3^{2-}\}$  are set to 1, making the thermodynamic constants  $K_{\alpha 1}$  and  $K_{\alpha 2}$  constrained and valid for  $IS \approx 0.01$ .

Eqs. (1.39)-(1.51) and (2.13)-(2.14) are efficiently computed by means of a FORTRAN code using the subroutine **c05qbf** for systems of non-linear equations of the NAG library [62, 63]. In the code, the activity coefficients and the chemical speciation are computed in a loop until constant  $IS$  is attained. The code is integrated into the kinetic model as described in the following section and solved for every  $CaCO_{3(s,am.)}$  value.

#### 1.3.1.3 Kinetic model

The kinetic model developed for crystalline materials [10], is here applied for the ACC precipitation. Two nucleation elementary processes, namely primary homogeneous nucleation and secondary 3D nucleation, and diffusion-limited growth are considered. Nucleation is computed according to the classical equations described by Nielsen [1].

<sup>1</sup>OLI Studio 9.5 OLI Systems, Inc. <https://www.olisystems.com/>

## 1. Experimental

**Table 1.3** – Ionic size for the considered species used in the CaC model [64].

Species	Ionic size (Å)
OH <sup>-</sup>	3.5
Ca <sup>2+</sup>	6.0
CO <sub>3</sub> <sup>2-</sup>	4.5
HCO <sub>3</sub> <sup>-</sup>	4.2
H <sup>+</sup>	9.0
Cl <sup>-</sup>	3.0
Na <sup>+</sup>	4.2

Briefly, the primary homogeneous nucleation rate,  $B_h$ , is:

$$B_h = \frac{2D}{d^5} \exp\left(-\frac{\Delta G_h^*}{k_B T}\right) \quad (1.52)$$

where  $D$  is the diffusion coefficient of the solute,  $\Delta G_h^*$  is the Gibbs free energy barrier for homogeneous nucleation, and  $d$  can be approximated with the molecular diameter of the solute (taken here as the cubic root of the CaCO<sub>3</sub> molecular volume,  $v$ ). Similarly, the secondary nucleation rate,  $B_s$ , is:

$$B_s = \frac{2D}{d^4} \exp\left(-\frac{\Delta G_s^*}{k_B T}\right) A_T \quad (1.53)$$

where  $\Delta G_s^*$  is the Gibbs free energy barrier for secondary nucleation and  $A_T$  is the overall particle surface available for secondary nucleation. The equations for  $\Delta G_h^*$  and  $\Delta G_s^*$  and the corresponding critical size (diameter) are recalled in the appendix A, in the section A.5.

It is worth noting that only two quantities, *i.e.* the surface tension  $\Gamma$  for the primary homogeneous nucleation and the equivalent surface tension  $\Gamma_{eq}$  for the secondary nucleation, define the two nucleation rates. Moreover,  $\Gamma_{eq}$  is defined as [10]:

$$\Gamma_{eq} = \frac{\Gamma}{6} \left(6 - \frac{\beta}{\Gamma}\right) \quad (1.54)$$

where  $\beta$  is the cohesion energy, which can vary in the range 0 to  $2\Gamma$ .

Due to the cohesion energy contribution, secondary nucleation occurs at lower supersaturation with respect to the homogeneous nucleation but cannot take place if not preceded by homogeneous nucleation events since  $A_T$  is zero (eq.1.53). Thus, primary

### 1.3. Computational model: basis, and system-specific details.

homogeneous nucleation is defined by the value of  $\Gamma$  whereas secondary nucleation is defined by the value of  $\beta$ .

The model includes a Brownian diffusion-controlled growth rate contribution. Growth is assumed to occur by incorporation of  $\text{Ca}^{2+}$  and  $\text{CO}_3^{2-}$  ions onto the solid phase particles of diameter  $L$ . The linear growth rate term is:

$$G = \frac{dr}{dt} = J_N \cdot v_m \quad (1.55)$$

where  $t$  is time,  $r$  the solid particle radius,  $J_N$  is the molecular flux of the chemical species on the solid surface and  $v_m$  is the molar volume of the solid phase. The molecular flux can be calculated as:

$$J_{\text{Ca}^{2+}} = \frac{2D_{\text{Ca}^{2+}}}{L} \left( [\text{Ca}_{\text{bulk}}^{2+}] - [\text{Ca}_{\text{surf}}^{2+}] \right) \quad (1.56)$$

where  $D_{\text{Ca}^{2+}}$  is the diffusion coefficient for  $\text{Ca}^{2+}$  and  $[\text{Ca}_{\text{bulk}}^{2+}]$  and  $[\text{Ca}_{\text{surf}}^{2+}]$  are the concentrations of  $\text{Ca}^{2+}$  in the liquid bulk (*i.e.*, far from the particle surface and corresponds to the measured concentration of  $\text{Ca}^{2+}$  ion) and close to the particle surface (*i.e.*, where the local solubility equilibrium with the solid phase is assumed), respectively.

The value of  $[\text{Ca}_{\text{surf}}^{2+}]$  is computed as a function of the diffusion and activity coefficient of  $\text{Ca}^{2+}$  and  $\text{CO}_3^{2-}$ , the solubility product  $K_{sp}$ , and the supersaturation  $S$ , as derived in annexe A resulting in the equation A.12.

The diffusion coefficient for  $\text{Ca}^{2+}$  and  $\text{CO}_3^{2-}$  are assumed to be  $7 \times 10^{-10}$  and  $8 \times 10^{-10} \text{ m}^2 \text{ s}^{-1}$  respectively [65], *i.e.*, those commonly considered for ionic species in aqueous dilute solutions. Temperature dependence of diffusion coefficients are computed according to the Stokes-Einstein equation:

$$\frac{D_{T_1}}{D_{T_2}} = \frac{T_1 \mu_{T_2}}{T_2 \mu_{T_1}} \quad (1.57)$$

where  $D$  are the diffusion coefficients and  $\mu$  are the dynamic viscosity of water at the absolute temperatures  $T_1$  and  $T_2$ . Thus, the diffusion controlled growth has neither quantities nor parameters to be set.

The computation of  $\text{CaCO}_{3(\text{s,am.})}$  is carried out by applying the discretized population balance approach, which is described in detail in a previous work [10]. Shortly, the discretisation allows the computation of the particle size distribution using conventional finite differences techniques. The population of particle is fractionated in a

## 1. Experimental

---

limited number of classes. If  $N_i$  is the number of particles in the  $i^{th}$  class, the variation  $dN_i/dt$  can be split into different contributions related to the elementary processes that are influencing the particle size distribution itself. In the present case, the considered elementary processes are the primary homogeneous nucleation, the secondary nucleation, and the diffusion controlled growth. Thus, the numerical variation of particles in each class can be written as:

$$\frac{dN_i}{dt} = \left( \frac{dN_i}{dt} \right)_{prim. \text{ nucl.}} + \left( \frac{dN_i}{dt} \right)_{sec. \text{ nucl.}} + \left( \frac{dN_i}{dt} \right)_{growth} \quad (1.58)$$

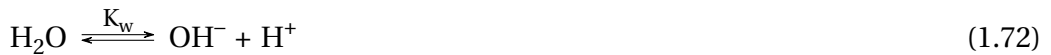
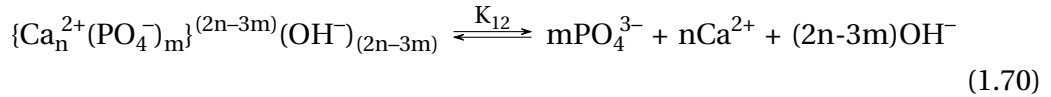
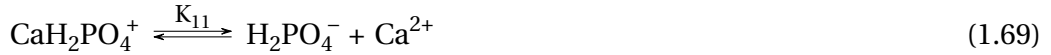
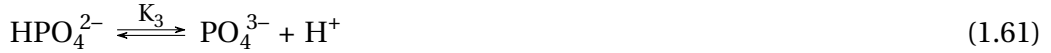
The expressions for the three terms of the right-hand side of eq. 1.58 are reported elsewhere [10]. In particular, the growth algorithm is computed using  $M = 4$ , which means that the first four moments ( $m_0$ : total number;  $m_1$ : total length;  $m_2$ : total surface;  $m_3$ : total volume) of the particle size distribution are correctly calculated. At every time step, the amount of the solid phase formed,  $\text{CaCO}_{3(s,am.)}$ , is calculated as a consequence of simultaneous events of primary nucleation, secondary nucleation and diffusion limited growth. Moreover, the chemical speciation is computed as described in the section 1.3.1.2.

The value of  $\Gamma$  and  $\beta$  for the kinetic model and the thermodynamic constants  $K_{sp}$ ,  $K_{AS}$ ,  $K_{\alpha 1}$ , and  $K_{\alpha 2}$  are the only quantities of the entire thermodynamic-kinetic model to be refined based on the nine experimental precipitation experiments of two series of independent data ( $\text{Ca}^{2+}$  in solution and NaOH added). Moreover, those quantities have a well-defined physical meaning and their values should agree with available estimations in the literature. The kinetic model code is developed in FORTRAN and the system of ordinary differential equations derived by eq. 1.58 (one differential equation per size class, about 30-50 classes are needed) is solved with the subroutine LSODE [66]. The overall computational time for the thermodynamic-kinetic model is about 5-10 s with a modern standard PC.

## 1.3.2 Calcium phosphates

### 1.3.2.1 Speciation Model

The considered aqueous species and equations in the speciation model are



where (1.70) considers the Posner's clusters of variable stoichiometry.

Ca mass (mol) balance:

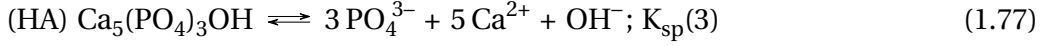
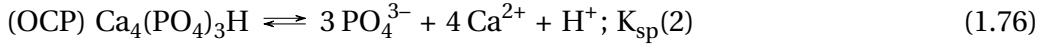
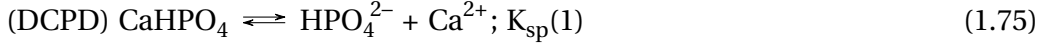
$$\begin{aligned} Ca_T = & Ca^{2+} + CaH_2PO_4^- + CaPO_4^- + CaHPO_4 \\ & + n\{Ca_n^{2+}(\text{PO}_4^-)_m\}^{2n-3m} + DCPD + 4OCP + 5HA \end{aligned} \quad (1.73)$$

P mass (mol) balance:

$$\begin{aligned} P_T = & CaH_2PO_4^- + CaPO_4^- + CaHPO_4 + m\{Ca_n^{2+}(\text{PO}_4^-)_m\}^{2n-3m} \\ & + DCPD + 3OCP + 3HA + \text{H}_3\text{PO}_4 + \text{H}_2\text{PO}_4^- + \text{HPO}_4^{2-} + \text{PO}_4^{3-} \\ & + 2\text{P}_2\text{O}_7^{4-} + 2\text{HP}_2\text{O}_7^{3-} + 2\text{H}_2\text{P}_2\text{O}_7^{2-} + 2\text{H}_3\text{P}_2\text{O}_7^- + 2\text{H}_4\text{P}_2\text{O}_7 + \text{NaHPO}_4^- \end{aligned} \quad (1.74)$$

## 1. Experimental

The considered solid species are



Known quantities:  $\text{H}^+$ ,  $\text{P}_T$ ,  $\text{Ca}_T$ ,  $\text{DCPD}^2$ ,  $\text{HAP}$ ,  $\text{OCP}$ . 22 species, 16 equations, 6 known quantities: the problem can be solved. The system of 16 non-linear equations is reduced to two analytical equations by means of symbolic solver software (Maple 18). The two molar balance equations read:

$$\begin{aligned} & \frac{K_{eq}(12) \cdot a_{\text{Ca}}^n \cdot a_{\text{PO}_4}^m \cdot \left(\frac{K_w}{a_{\text{H}}}\right)^z \cdot n}{\gamma_{\text{Ca}_n\text{P}_m}} + \frac{a_{\text{Ca}}}{\gamma_{\text{Ca}}} \\ & + \frac{K_{eq}(11) \cdot a_{\text{Ca}} \cdot a_{\text{PO}_4} \cdot a_{\text{H}}^2}{K_{eq}(3) \cdot K_{eq}(2) \cdot \gamma_{\text{CaH}_2\text{PO}_4}} + \frac{K_{eq}(9) \cdot a_{\text{Ca}} \cdot a_{\text{PO}_4} \cdot a_{\text{H}}}{K_{eq}(3) \cdot \gamma_{\text{CaHPO}_4}} \\ & + \frac{K_{eq}(10) \cdot a_{\text{Ca}} \cdot a_{\text{PO}_4}}{\gamma_{\text{CaPO}_4}} + 5\text{HA} + 4\text{OCP} = \text{Ca}_T \end{aligned} \quad (1.78)$$

<sup>2</sup>DCPD (Brushite,  $\text{CaHPO}_4 \cdot 2 \text{H}_2\text{O}$ ) or DCPA (Monetite,  $\text{CaHPO}_4$ ) are equivalent at this level being the water of crystallization not influent in the mass balances.

### 1.3. Computational model: basis, and system-specific details.

$$\begin{aligned}
& \frac{K_{eq}(12) \cdot a_{Ca}^n \cdot a_{PO_4}^m \cdot \left(\frac{K_w}{a_H}\right)^z \cdot n}{\gamma_{Ca_nP_m}} + \frac{K_{eq}(11) \cdot a_{Ca} \cdot a_{PO_4} \cdot a_H^2}{K_{eq}(3) \cdot K_{eq}(2) \cdot \gamma_{CaH_2PO_4}} \\
& + \frac{K_{eq}(9) \cdot a_{Ca} \cdot a_{PO_4} \cdot a_H}{K_{eq}(3) \cdot \gamma_{CaHPO_4}} + \frac{K_{eq}(10) \cdot a_{Ca} \cdot a_{PO_4}}{\gamma_{CaPO_4}} \\
& + \frac{2 \cdot a_{PO_4}^2 \cdot a_H^4}{K_{eq}(3)^2 \cdot K_{eq}(8) \cdot K_{eq}(7) \cdot K_{eq}(6) \cdot \gamma_{H_2P_2O_7}} + \frac{a_{PO_4} \cdot a_H^2}{K_{eq}(3) \cdot K_{eq}(2) \cdot \gamma_{H_2PO_4}} \\
& + \frac{2 \cdot a_{PO_4}^2 \cdot a_H^5}{K_{eq}(3)^2 \cdot K_{eq}(8) \cdot K_{eq}(7) \cdot K_{eq}(6) \cdot K_{eq}(5) \cdot \gamma_{H_3P_2O_7}} \\
& + \frac{a_{PO_4} \cdot a_H^3}{K_{eq}(3) \cdot K_{eq}(2) \cdot K_{eq}(1) \cdot \gamma_{H_3PO_4}} \\
& + \frac{2 \cdot a_{PO_4}^2 \cdot a_H^6}{K_{eq}(3)^2 \cdot K_{eq}(8) \cdot K_{eq}(7) \cdot K_{eq}(6) \cdot K_{eq}(5) \cdot K_{eq}(4) \cdot \gamma_{H_4P_2O_7}} \\
& + \frac{2 \cdot a_{PO_4}^2 \cdot a_H^3}{K_{eq}(3)^2 \cdot K_{eq}(8) \cdot K_{eq}(7) \cdot \gamma_{HP_2O_7}} + \frac{a_{PO_4} \cdot a_H}{K_{eq}(3) \cdot \gamma_{HPO_4}} \\
& + \frac{K_{eq}(13) \cdot a_{Na} \cdot a_{PO_4} \cdot a_H}{K_{eq}(3) \cdot \gamma_{NaHPO_4}} \\
& + \frac{2 \cdot a_{PO_4}^2 \cdot a_H^2}{K_{eq}(3)^2 \cdot K_{eq}(8) \cdot \gamma_{P_2O_7}} + \frac{a_{PO_4}}{\gamma_{PO_4}} + 3OCP + 3HA = P_T
\end{aligned} \tag{1.79}$$

which are included in the FORTRAN code and numerically solved for  $Ca^{2+}$  and  $PO_4^{3-}$  by a specific high precision subroutine. The amount of solid phases formed is calculated by the kinetic package as a consequence of nucleation and growth events and, whereas necessary, an empiric equation for transformation among solid phases (*e.g.*, OCP to HA).

$$\frac{dHA}{dt} = k_1 \cdot OCP \tag{1.80}$$

Equations 17 and 18 reports the case of OCP (OCP variable) precipitation and recrystallization towards HA phase (HAP variable). On a standard PC the full speciation iteration run, up to self-consistent results, is solved in a fraction of a second. Since the speciation needs to be calculated at every time step, simultaneously to the ODE system associated to the population balance equations, a fast speciation solver is of primary relevance.

## 1. Experimental

**Table 1.4** – Ionic size for the considered species in the CaP model [64].

Species	Ionic size diameter (Å)
$\text{OH}^-$	3.5
$\text{Ca}^{2+}$	6.0
$\text{PO}_4^{3-}$	4.0
$\text{H}_2\text{PO}_4^-$	4.2
$\text{H}_3\text{PO}_4^0$	4.5
$\text{CaHPO}_4^0$	4.5
$\text{CaPO}_4^-$	4.2
$\text{CaH}_2\text{PO}_4^+$	4.5
$\text{P}_2\text{O}_7^{4-}$	4.5
$\text{HP}_2\text{O}_7^{3-}$	4.5
$\text{H}_2\text{P}_2\text{O}_7^{2-}$	4.4
$\text{H}_3\text{P}_2\text{O}_7^-$	4.5
$\text{H}_4\text{P}_2\text{O}_7$	4.5
$\text{HPO}_4^{2-}$	4.5
$\text{NaHPO}_4^-$	4.5
$\text{H}^+$	9.0
$\text{Cl}^-$	3.0
$\text{Na}^+$	4.2



## 1.4. Automatisisation method

**Table 1.5** – Equilibrium constants for the equation considered in the model.

Equilibrium constant	Value	Source
$K_{eq}(1)$	$5.7900 \times 10^{-3}$	OLI <sup>3</sup>
$K_{eq}(2)$	$6.5174 \times 10^{-8}$	OLI
$K_{eq}(3)$	$5.8416 \times 10^{-13}$	OLI
$K_{eq}(4)$	$2.5173 \times 10^{-2}$	OLI
$K_{eq}(5)$	$4.3652 \times 10^{-3}$	OLI
$K_{eq}(6)$	$2.5573 \times 10^{-7}$	OLI
$K_{eq}(7)$	$5.1127 \times 10^{-10}$	OLI
$K_{eq}(8)$	$4.4610 \times 10^3$	OLI
$K_{eq}(9)$	$3.1365 \times 10^2$	OLI
$K_{eq}(10)$	$5.3696 \times 10^6$	OLI
$K_{eq}(11)$	4.1668	OLI
$K_{eq}(12)$	$1.3 \times 10^{21}$	regressed
$K_{eq}(13)$	6.8923	BRGM <sup>4</sup>
$K_w$	$2.3720 \times 10^{-14}$	OLI
$K_{sp}(1)$	$2.19 \times 10^{-7}$	[67]
$K_{sp}(2)$	$2.00 \times 10^{-49}$	[68]
$K_{sp}(3)$	$2.35 \times 10^{-59}$	[69]

### 1.3.2.2 Thermodynamic and Kinetic models

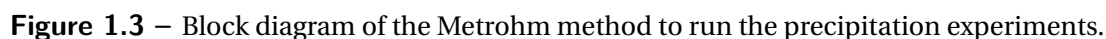
The applied models, unless for the system specific equations summarized in this section 1.3.2.1, are the same of those used for ACC precipitation. Thus, the reader can refer to the CaC section (1.3.1) replacing the mass balance for CaC eqs. (1.49)-(1.50) with the respective eqs. (1.78)-(1.79) specific for CaP.

## 1.4 Automatisisation method

The measuring method consisted of a main track, and different side-operation tracks. pH value, calcium potential, conductivity, and optical signals are monitored by the tiamo<sup>TM</sup> software and the collected data are then stored in the tiamo<sup>TM</sup> database. A special method has been build up for the unseeded crystallisation experiments to automatically control every single command required to carry out the precipitation reaction.

<sup>3</sup>OLI Studio 9.5 OLI Systems, Inc. <https://www.olisystems.com/>

<sup>4</sup>Bureau de Recherches Géologiques et Minières, BRGM, <http://www.brgm.eu/>



## 1.5 Constant saturation approach: setups & experiments

In the framework of my studies, CaC and CaP system were investigated using synchrotron - based scattering techniques. Two experimental setups were used for these studies, a reactive pulsation-free horizontal liquid jet and the acoustically levitated drop. Figure 1.4 reports an example of the liquid jet and the suspended drop. Both setups are contactless, *i.e.*, there is no solid surface on which heterogeneous nucleation can occur. Moreover, the absence of a confinement media does not add a scattering contribution due to the amorphous material (glass or polymer) of the confinement itself. The two setups are radically different. The suspended drop has a spherical

## 1.6. Liquid jet setup

geometry, and the scattering data should be more conveniently collected using a Pilatus 2D detector positioned perpendicular to the axis of the X-ray beam. Moreover, if a process evolves in the droplet, time-resolved data can be collected; because of the high energy beam the droplet temperature can increase, and the droplet can shrink because of the liquid evaporation. Nevertheless, using a chamber with the controlled atmosphere, the evaporation can be controlled, and if an undersaturated droplet is suspended, due to controlled evaporation, precipitation can be studied.

The horizontal liquid jet has a cylindrical geometry, as a capillary. Thus, the Mythen strip detector is the optimal configuration. The liquid is constantly renovated, and temperature, evaporation, and beam damage is not an issue. Time resolution can be studied by varying the delay between the mixing point and the measuring point. Nevertheless, heterogeneous nucleation in the delay loop can occur. The two setups are entirely complementary, but the liquid jet setup is much more complicated and delicate to handle than the suspended drop. Even if both systems were initially investigated, for the specific questions and features of the system in the framework of my thesis, the liquid jet setup was the best choice. In the following chapter, some details of this set up are described. It is worth mentioning that such a set up was explicitly designed and realised in the framework of my doctoral program, firstly in the laboratory and then optimized during long-term experiments composed of 5 beamtimes of about one week each (about 100 shifts in total).

## 1.6 Liquid jet setup

The horizontal liquid micro-jet is generated using 4 HPLC pumps connected to a PEEK micromixer and equipped with a capillary exit. Moreover, an additional HPLC pump is connected to the mixer and used to deliver a washing chemical (*e.g.*, diluted acetic acid). The internal capillary diameter defines the liquid jet size and can be tuned between 25  $\mu\text{m}$  and 1 mm. Also, the material of the capillary can be varied, from PEEK, PTFE, stainless steel, or quartz but other options are possible. Each pump is equipped with a pulsation damper loop, a back pressure regulator valve, and a high precision Coriolis flow meter (figure 1.5). A digital signal feedback loop from the flow meter to the pump ensure an optimal flow rate control in the range  $0 \text{ mL min}^{-1}$  to  $10 \text{ mL min}^{-1}$  per channel with an error of  $\pm 0.01 \text{ mL min}^{-1}$ . The pulsation needs to be entirely dumped because the four liquid are then mixed and a periodic variation of the flow is not acceptable. The delivering tubes before the mixer were thermostated using

## 1. Experimental

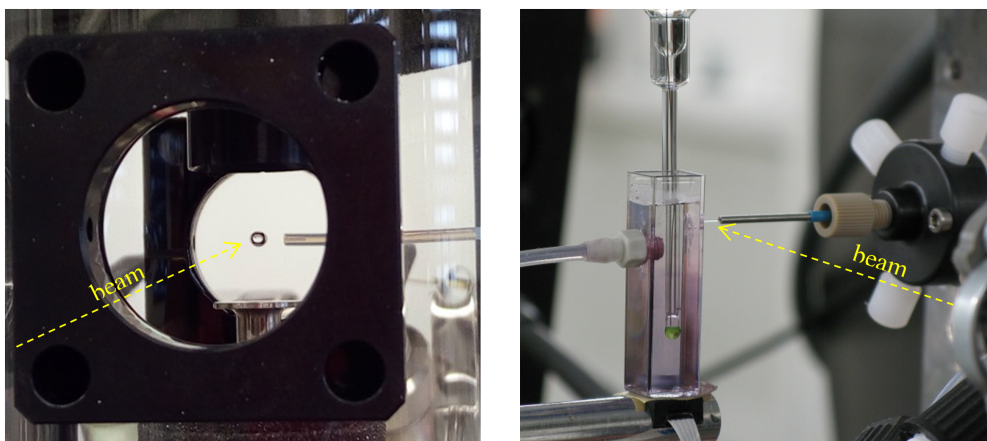


**Figure 1.4** – Contactless devices in use at the X04SA beamline: on the left, a 2.5 mm diameter droplet suspended by acoustic waves is shown. The Teflon tubing on the right side of the picture serves as the droplet injector. The X-ray beam is interacting with the droplet while the wide- and small- angle X-ray patterns are collected on a 2D detector (Pilatus). On the right, a 250  $\mu\text{m}$  horizontal pulsation-free liquid jet generated out of a stainless steel capillary is shown. The jet is accumulated in a mechanically stirred cuvette (catcher) in which pH and temperature are monitored on-line, and the liquid is continuously drained. The liquid jet is produced by mixing five liquids delivered by HPLC pumps, each remotely controlled by high precision Coriolis flow meters. Small- and wide- angle X-ray patterns are collected on a high- resolution strip detector (Mythen).

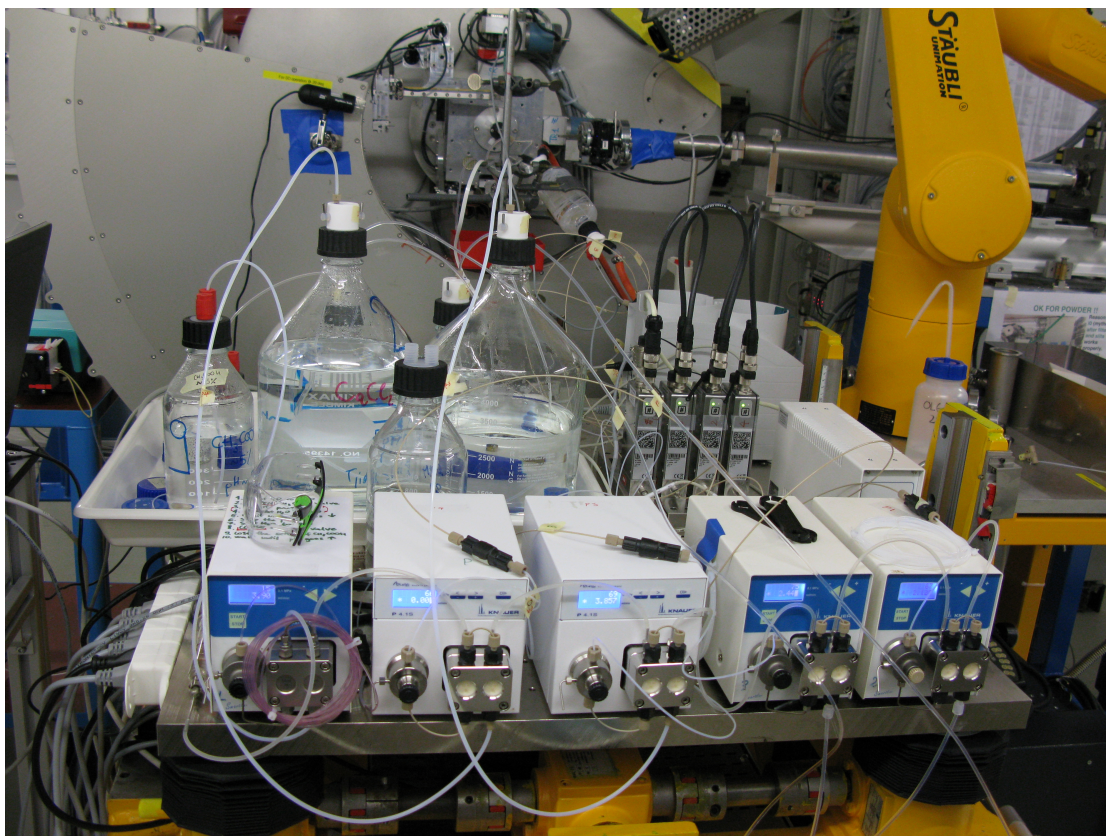


**Figure 1.5** – Liquid jet setup mounted at the MS beamline (SLS). The 4 pumps and the Coriolis flowmeters are visible in the front.

a double-walled water-jacketed tubing system. A liquid jet of  $250\ \mu\text{m}$  was used at an overall flow rate of  $8\ \text{mL}\cdot\text{min}^{-1}$ . The X-ray beam was focused on the liquid jet,  $250\ \mu\text{m}$  height and  $2\ \text{mm}$  wide. The liquid was collected in a catcher, where  $T$  and  $p\text{H}$  of the solution, under stirring, were monitored on-line (figure 1.4, right). The experiments were carried out at constant  $T$ ,  $p\text{H}$  and at different saturation levels, which were calculated using the developed thermodynamic model. Preliminary measurements were carried out with colloidal gold suspension produced and characterised in-house, with known particle size distribution and shapes C.3. The preliminary outcomes of such experiments are summarised in chapter 3, section 3.3.

## 1. EXPERIMENTAL

## 2 | Solid formation from solution

### 2.1 Basis of the solid formation process from solution

Crystallisation and precipitation from solution refer to chemical processes where a solid is formed from supersaturated solution. The main differences between the two processes can be just defined as semantics, but it reflects the background of the scientist involved in the discussion and the nature of the product obtained. The term ‘crystallisation’ is preferentially used by crystallographers, with a physics background. The product of such a process should be inherently crystalline; the process is slow enough to allow the solid to grow to a certain extent, and the dissolution of the solid might be studied as well, being the reverse process of the crystal growth. Often, the term ‘precipitation’ is used in chemistry and engineering, and it refers to a relatively fast irreversible process where a sparingly soluble solid is formed. Regardless of its crystalline nature, the product of the precipitation is a solid in the size range from few nm to some  $\mu\text{m}$ . The product of precipitation might be complicated to handle, in particular when composed of amorphous or poorly crystalline nanoparticles with a metastable nature. Despite the most appropriate definition, precipitation might be designated as a “rapid crystallisation”. In industry precipitation processes are used since many decades; for instance, they are applied in the production of advanced products such as catalysts and their metal oxide supports, as well as for the preparation of salts at colossal scale – millions of metric tons – such as sodium bicarbonate according to the well-known *Solvay* process.

Söhnel and Garside presented precipitation mathematics and principles in the late 80s [70]. The solid formation process consists of different sub-processes, called elementary processes (such as nucleation, growth, aggregation, agglomeration, *etc.*; section 2.2), which can occur on the same temporal scale (in parallel or convoluted) or considered as consecutive events (serial). Nucleation and growth occur at the

## 2. Precipitation

---

beginning of the solid formation, and they are strongly convoluted (*i.e.*, they influence each other). In some cases, aggregation and agglomeration occur at a later stage and can be considered as a subsequent transformation. Other elementary processes such as ripening, ageing, and cementing are considered active on a more extended temporal scale and not directly convoluted with nucleation and growth.

Besides the temporal synchronisation of the elementary processes, another critical feature need to be addressed, which affects the solution where the precipitation occurs. When some of the aforementioned elementary processes take place, they promote the depletion of chemicals from the solution in a characteristic manner, whereas others do not. In a batch reactor where nucleation or growth events are active, the concentration of the chemical species in solution decreases over time; on the contrary, if in the same system only aggregation occurs, the concentration of the chemical species in solution, except for specific cases [71], does not change.

The precipitation occurs if the solution is supersaturated. The supersaturation  $S$ , or more rigorously  $\ln(S)$ , is the driving force for the phase transition (2.1.1). Nucleation and growth are strongly affected by  $S$ , but with a very different dependence. Supersaturation value has a much stronger influence on nucleation than on growth. For instance, growth can occur at relatively low  $S$  values (*e.g.*, at  $S = 1.1$ ) when nucleation is negligible. Furthermore, if the  $S$  level in a batch system is rapidly increased, a large number of nuclei will be generated, the  $S$  level will rapidly decrease, and the available species in solution for the growth will be in a limited amount. In this case, a relatively high amount of species in solution are consumed by nucleation; as a consequence, the solid will be composed of small particles. On the contrary, if the  $S$  value is raised gradually, a limited number of nuclei will be initially generated, and most of the aqueous species will be consumed by the growth: few particles can grow to a large extent, and the final solid will be composed by relatively large particles. It is clear that nucleation and growth are temporarily convoluted through the instantaneous  $S$  level.

The supersaturation in a system can be induced in several ways, for instance by a change of the temperature, of the solvent kind or properties (*e.g.*, in supercritical conditions), as a consequence of a chemical reaction, or by mixing of solutions. Thus, the experimental setup used to study the precipitation processes and the strategy followed to induce the supersaturation, with particular care on the speed with which the supersaturation increases, is of fundamental relevance. Attention needs to be paid to avoid the contamination of the reactors, equipment, and solutions with organic



## 2.1. Basis of the solid formation process from solution

and inorganic compounds, and even gaseous species, such as CO<sub>2</sub>, as well as foreign solids, which could trigger heterogeneous nucleation.

The study of solid evolution can be combined with the depletion of chemical species from solution over time, and the characteristic effect of the elementary processes active during the evolution of solid formation be disclosed. Therefore, if an appropriate computation tool is applied, the entire precipitation process can be de-convoluted into the elementary processes, and the precipitation pathway can be identified.

In the literature, different models exist for the computation of nucleation and growth. The solid formation process is complicated; this complexity is mainly due to the simultaneity of the elementary processes and the mathematics associated with elaborate models. Selecting an appropriate combination of nucleation and growth mechanisms, it is possible to compose a model which describe the experimental results without setting or calculating quantities in contradiction with experimental evidence or without physical consistency. Within these constraints, the obtained model can be defined as *a plausible interpretation of the process, i.e., able to explain the experimental results. In parallel, alternative pathways may be considered inconsistent.*

The concepts introduced until now will be elaborated in depth within this chapter. The different aspects of the so-called classical nucleation theory are presented in sections 2.1.1– 2.2; the contemporary alternative “non-classical” theories, recently introduced in the literature concerning nucleation and precipitation mechanisms in general, are presented in section 2.3. In fact, in recent years, the identification of mesocrystals (2.3.4) opened the way toward a new non-classical interpretation of the solid formation mechanisms, and the literature reports different hypotheses regarding these alternative pathways. Nevertheless, the classical view remains the most used for the interpretation of the experimental data because it is supported by a mathematical framework and well-defined equations. Moreover, together with the new approaches, confusion has been created regarding the concept and the application of non-classical mechanisms; often it is not clear if “non-classical” refers to nucleation process or to the entire crystallisation pathway.

The classical nucleation theory (section 2.2.1) is based on a defined Gibbs free energy landscape. The non-classical nucleation theories define alternative landscapes arguing that the one assumed in the classical approach is a too simplistic view. The alternative energy landscapes of the non-classical approaches are associated to the concept of the existence and stabilisation of pre-nucleation entities (clusters): some-

## 2. Precipitation

---

times they are considered to influence the nucleation mechanism itself, sometimes their role is claimed in the solid growth mechanism, instead. The precipitation pathway is different if their involvement is considered one way or another. However, another case is even plausible: clusters are present in the system, and they act as spectator species along the solid formation pathway. The involvement of such entities in the precipitation pathway triggered my curiosity and the scientific questions posed in the motivations of this dissertation.

In the following sections, the basic concepts of the solid formation are presented (2.1.1). Moreover, some of the elementary processes are introduced (2.2). Then, in the section (2.3), the new pathways and theories on the precipitation are briefly presented. In the last part, the classical and non-classical pathways are summarized emphasising differences, limitations, and some milestones of understanding.

### 2.1.1 Driving force for the solid formation

The precipitation is a phase transformation; the Gibbs free-energy of variation ( $\Delta G$ ), at constant temperature and pressure, associated to a phase transformation can be described by the equation 2.1 and it refers to the overall volume (mass) of the substance, named as “bulk contribution”.

$$\Delta G_V = \Delta n(\mu_2 - \mu_1) \quad (2.1)$$

where the  $\Delta n$  is the amount of solid phase formed, starting from the phase with chemical potential  $\mu_1$  to the phase with chemical potential  $\mu_2$ . As an intensive quantity, the molar affinity,  $\varphi$ , is the driving force of the transformation process.

$$\varphi = \frac{\Delta G_V}{\Delta n} = (\mu_1 - \mu_2) = -\Delta\mu \quad (2.2)$$

Introducing the chemical potential definition, the eq. (2.2) reads

$$\varphi = -\Delta\mu = k_B T \ln \left( \frac{a_1}{a_2} \right) \quad (2.3)$$

where  $\Delta\mu$  is the change in chemical potential or change in free energy per mass,  $k_B$  the Boltzmann constant,  $T$  the temperature,  $a_1$  and  $a_2$  the activities of the two phases. In a system under equilibrium,  $\varphi = 0$  and the chemical activities of the two phases are equal. If we consider that  $a_1$  is related to the dissolved phase ( $a_{aq}$ ), and  $a_2$  is the

## 2.1. Basis of the solid formation process from solution

solute in equilibrium with the macroscopic crystal ( $a_{eq}$ ), it is possible to rewrite  $\varphi$  as

$$\varphi = k_B T \ln \left( \frac{a_{aq}}{a_{eq}} \right) = k_B T \ln(S) \quad (2.4)$$

where  $S$  is the (super)saturation

$$S = \frac{a_{aq}}{a_{eq}} \quad (2.5)$$

Thus, the driving force towards the solid formation ( $\varphi$ ) from supersaturated solution is proportional to  $\ln(S)$ . In the example of the following precipitation reaction



the saturation ratio is given by

$$S = \frac{[a_A]^\alpha [a_B]^\beta}{K_{sp}} \quad (2.7)$$

where  $K_{sp}$  is the solubility product of the macroscopic crystal

$$K_{sp} = [a_{A,eq}]^\alpha [a_{B,eq}]^\beta \quad (2.8)$$

When  $S > 1$ , the solution is supersaturated. The supersaturation is directly related to the solubility product of the solid under formation (2.8), and it implies that at any given concentration there is a specific driving force to toward the formation of different polymorphs. It is worth noting that supersaturation can be written differently:

$$S = \frac{IAP}{K_{sp}} \quad (2.9)$$

where  $IAP$  represent the generic ion activity product of the species considered in the solid formation process ((2.7) and (2.9) are equivalent). The same species and reaction need to be considered in the expression of the  $K_{sp}$ . Thus, every arbitrary reaction can be defined in the solid formation, without affecting the  $S$  value. In this dissertation, the saturation is expressed as in equation (2.9). The saturation of a system can be expressed as saturation index,

$$SI = \log_{10} \left( \frac{IAP}{K_{sp}} \right) \quad (2.10)$$

## 2. Precipitation

In this case,  $SI = 0$  represents the solubility equilibrium. Moreover, it is possible to calculate the saturation index of the system using the equation

$$SI = \log_{10} \left( \frac{IAP}{K_{sp}} \right)^{v^{-1}} \quad (2.11)$$

where  $v$  correspond to the sum of the stoichiometric coefficient of the reagents ( $v = \alpha + \beta$  in case of eq. 2.6). This equation is often used in engineering approaches.

In an ideal solution, the activity of a chemical species can be approximated by its concentration. The ideal conditions correspond to very diluted solutions. As soon as ions interact with each other, this approximation is no longer appropriate, and the activity needs to be considered. The activity coefficients take into account the solution non-ideality.

$$a_i = \gamma_i c_i \quad (2.12)$$

where  $a_i$ ,  $\gamma_i$ , and  $c_i$  represent the activity, the activity coefficient, and the concentration of the specie  $i$ , respectively. Conveniently, the concentration is expressed as molality (mole/kg), such as the moles of the considered species  $i$  per  $kg$  of solvent. The activity coefficient is influenced by

- the charge of the species considered;
- the effective hydrated size of the ion;
- the ionic strength;
- the temperature;
- the dielectric constant of the solvent.

The activity coefficient for the aqueous chemical species  $i$  may be calculated using the extended Debye-Hückel equation for long-range interaction [61], which has validity for  $IS < 10^{-1}$  M.

$$-\log \gamma_i = \frac{z_i^2 \cdot A \cdot T \cdot \sqrt{IS}}{1 + d_i \cdot B \cdot T \cdot \sqrt{IS}} \quad (2.13)$$

where  $z_i$  is the charge of the ion  $i$ ,  $A$  and  $B$  are the Debye-Hückel parameters, whose values depend on the dielectric constant of the solvent and the temperature,  $T$  is the

## 2.1. Basis of the solid formation process from solution

temperature,  $d_i$  is the ionic diameter in [cm], and  $IS$  the ionic strength, calculated as

$$IS = \frac{1}{2} \sum_{i=0}^n c_i \cdot z_i^2 \quad (2.14)$$

where  $c_i$  is the molality and  $z_i$  is the charge of the ion  $i$ . The Debye-Hückel parameters for water can be approximated with virial equations

$$A = 5.154210 \cdot 10^{-06} T^2 + 6.5023 \cdot 10^{-04} T + 4.9190 \cdot 10^{-01} \quad (2.15)$$

$$B = 8.8160 \cdot 10^{-07} T^2 + 1.5206 \cdot 10^{-04} T + 3.2479 \cdot 10^{-01} \quad (2.16)$$

The second contribution to the overall Gibbs free energy of the solid formation process is expressed by the surface energy term,  $\Delta G_S$ . The free energy of the substance forming the surface layer is greater than the free energy of the bulk material: molecules or ions on the surface layer are in a state of higher potential energy (less, and weaker bonds) than internal molecules. This excess of free energy can be expressed by the surface tension,  $\Gamma$  (energy per unit area). The expression of the Gibbs free energy, including the surface contribution, becomes:

$$\Delta G = \Delta G_V + \Delta G_S = -\frac{V_n}{v} \cdot k_B \cdot T \cdot \ln(S) + \oint \Gamma \cdot A \cdot dA \quad (2.17)$$

where  $V_n$  is the particle volume,  $v$  is the molecular volume,  $\Gamma$  is the surface tension (energy per unit area). The graphical representation of equation (2.17) depicts the Gibbs free-energy landscape (figure 2.1).

Decreasing the size of the solid, the definition of ‘surface’ and its properties are somewhat ambiguous. Moreover, the equations (2.1)–(2.9) consider the equilibrium of the chemical species in solutions with the macroscopic crystals. In a macroscopic crystal ( $> 1 \mu\text{m}$ ), the number of atoms that defined a surface is negligible with respect to the ones that constitute the volume. If the size decreases, the contribution of the atoms on the surface becomes more and more critical, and the solid size has to be considered. The Gibbs-Thomson (Kelvin) equation (2.18) expresses the relationship between the activity of the species in solution at the equilibrium ( $a_1$  and  $a_2$ ), the size of the solid considered (of radius  $r_1$  and  $r_2$ ), the molecular volume of solid that compose the crystal ( $v$ ), and the liquid-solid interfacial tension ( $\Gamma_{l,s}$ )

$$k_B \cdot T \cdot \ln\left(\frac{a_2}{a_1}\right) = 2 \cdot v \cdot \Gamma_{l,s} \left(\frac{1}{r_2} - \frac{1}{r_1}\right) \quad (2.18)$$

## 2. Precipitation

---

Rewriting the equation in terms of solubility products, it results that small crystals are more soluble than the bigger ones,

$$\ln \frac{K_{sp_r}}{K_{sp}} = 2 \frac{v \cdot \Gamma_{l,s}}{k_B \cdot T \cdot r} \quad (2.19)$$

where  $K_{sp_r}$  is the solubility product of a crystal with radius  $r$ . As a consequence of the different solubility between small and large particles, a system composed by a population of particles with a specific distribution in size will spontaneously evolve: the smaller particles will dissolve, and the larger particle will grow. This process is called Ostwald ripening and is influencing the particle size distribution over time. It is particularly active at the nanoscale since the solubility of nanoparticles is much larger than the solubility of microparticles.

A further consequence is discussed in section 2.4, and it is associated with the definition of ‘stability’; since the solubility changes with the particle size, a small particle can be defined stable with respect to its local environment (and thus at its solubility equilibrium), even if the resulting solution is supersaturated with respect to larger particles (which have a lower solubility).

In the equations (2.17)–(2.19), the surface tension is considered independent of the solid size, or more rigorously independent to the surface curvature. This approximation (called the *capillary approximation*) allows some simplification, not only on the equations here described in this section but more relevantly on the derivation of the classical nucleation theory, as discussed in the following.

## 2.2 Elementary processes of solid formation

As shortly introduced in section 2.1.1, the precipitation process includes a phase transition. In the cases discussed in this dissertation, a supersaturated homogeneous solution evolves toward the formation of a solid, generating a multiphase system. The overall process can be partitioned according to sub-processes, called *elementary processes*. Each elementary process takes into account well-defined events in the solid evolution, and a specific combination of the elementary processes defines a peculiar precipitation pathway. Several elementary processes can be active during the precipitation; some of them overlap and strongly influence each other on the same timescale. During the entire precipitation, the relative role of each elementary

## 2.2. Elementary processes of solid formation

process changes over time, making the understanding of the precipitation pathway complicated. The final product reflects the whole precipitation process, and it is not possible to retrieve the specific pathway by analysing the final product only since several different pathways can be postulated by convoluting a set of elementary processes. Also, subsequent processes, such as Ostwald ripening, cementing, or recrystallisation may completely mask the nature of the precipitated solid [71, 72]. A way to study a plausible pathway includes the deconvolution of the entire precipitation into its elementary processes (*deconvolution approach*), each of them needs to be well-defined and described in mathematically.

In this dissertation, the primary emphasis is paid on those processes that reflect a change in the solution composition during their contribution to the precipitation, *i.e.*, nucleation and growth. Other processes such as aggregation, agglomeration, ripening, cementing, *etc.* may occur on a time scale beyond the investigation windows discussed here and their contribution to the solid evolution is not recognisable from the solution viewpoint. Moreover, the object of this work is to try to evaluate the initial stage of the solid formation, where the solid undergoes rapid change under kinetic control.

It is also worth mentioning that the particle “enlargement” process due to the growth is very often confused with the particle “enlargement” because of aggregation. The terminology is fundamental: primary particle growth and the formation of secondary particles (composed of primary particles) are two distinct processes, described by a very different mathematical framework. As discussed in section 2.2.3, secondary particles can be formed as a consequence of secondary nucleation events or aggregation events, whereas primary particles growth required the incorporation of building units into the primary particle itself.

The mathematical description of the elementary process may be based on simplified empirical equations or in a more complex form in which each parameter has a well-defined physical meaning. The latter approach typically generates a more complicated mathematical framework, but offers significant advantages:

1. Since the quantities involved in the model have a definite physicochemical meaning, their values have to be consistent with the literature which reports reference values experimentally obtained with other methods or from other calculations.
2. If the regressed quantity is unknown, the calculated values should be consistent

## 2. Precipitation

with similar systems and the results will then be useful to the community for further investigations.

3. A model based on physical quantities offers more robust extrapolation capabilities toward unexplored conditions. A model with prevision capability is a high-value tool.

Since a comprehensive description of every possible precipitation pathway largely exceeds the objective of this dissertation, in the following sections the concept and the mathematical description of the considered elementary processes are described, with particular emphasis to nucleation and grow.

### 2.2.1 Nucleation

Nucleation is the first step of the solid formation that can occur in a supersaturated solution. It is an activated process, *i.e.*, an energy barrier needs to be overcome. The energy barrier is the consequence of the change of the two free energy contributions against the size of the solid matter being formed, eq. (2.17): a negative contribution due to the volume of the solid (bulk or volume contribution) and a positive contribution due to its surface (interfacial or surface contribution). The sum of these two terms against the size of the solid matter defines the Gibbs free energy landscape. In the most simplified view, both volume and surface contribution have a monotonic behaviour against size. Figure 2.1 graphically represents such a case. The resulting curve identifies a maximum, whose coordinates correspond to the energy barrier ( $\Delta G^*$ ) to overcome to promote a nucleation event and the critical size ( $r^*$ ) of the solid at that moment. The value of  $r^*$  (or  $r_{crit}$ ) formally divides the solid entities undergo formation in two ranges. Before the critical size the solid entities, defined as “embryos”, are considered unstable, *i.e.* they have a larger probability to decrease than increase in size or, in other words, they have a formation constant lower than the unity. The solid entities larger than the critical size are defined “nuclei”. These nuclei are considered stable and spontaneously increase their size by incorporation of ion or molecules. The formation of a nucleus can be formally described as a ‘chemical reaction’ in which an embryo of size  $r_{n-1}$ , composed by  $n - 1$  molecules  $M$ , increases in size because of the addition of one more molecules to reach the critical size ( $r_n^*$ ),





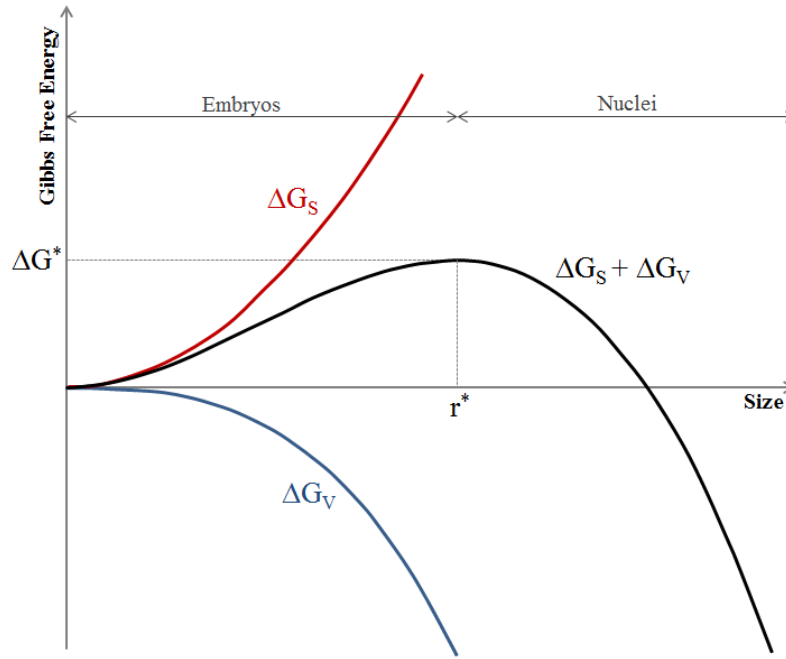


**Figure 2.1** – Classical nucleation theory landscape: free energy vs nuclei size.

The associated kinetic equation can be formulated as

$$\frac{dN(r^*)}{dt} = k_1 \cdot N(M) \cdot N(r_{n-1}) - k_{-1} \cdot N(r_n^*) \quad (2.21)$$

where  $\frac{dN(r^*)}{dt}$  is the numerical rate of nuclei generated per unit of volume,  $k_1$  and  $k_{-1}$  are the kinetic constants for the forward and backward reaction, respectively, and  $N(M)$ ,  $N(r_{n-1})$ ,  $N(r_n^*)$  are the number of molecules, embryos, and nuclei per unit of volume in the system, respectively.

After some elaboration, the nucleation rate – generally indicated as  $J_N$  – can be expressed in term of an Arrhenius equation, in which the activation energy appears as an exponential factor. The pre-exponential term derives from the Einstein equation for molecular diffusion,

$$J_N = \frac{2D}{d^5} \cdot e^{-\frac{\Delta G^*}{k_B T}} \quad (2.22)$$

where  $D$  is the diffusion coefficient,  $d$  the molecular diameter of the structural unit of the solid,  $k_B$  the Boltzmann constant, and  $T$  the temperature. This equation is commonly used to evaluate the number of nuclei generated per unit of time and unit

## 2. Precipitation

---

of volume. The term  $\Delta G^*$  reads

$$\Delta G^* = \varepsilon \cdot \frac{v^2 \cdot \Gamma^3}{k_B^2 \cdot T^2 \cdot \ln^2(S)} \quad (2.23)$$

where  $\varepsilon$  is a dimensionless geometrical factor of the considered embryo (i.e.,  $\frac{16\pi}{3}$  for a sphere),  $v$  is the molar volume of the structural unit,  $\Gamma$  is the surface energy (or surface tension), and  $S$  is the supersaturation. The critical size ( $r^*$ , radius) corresponds to

$$r^* = \frac{v \cdot \Gamma}{k_B \cdot T \cdot \ln(S)} \quad (2.24)$$

In a homogeneous solution, if  $S$  is gently increased, the average statistical size of the embryo grows. In the proximity of  $r^*$ , because of local stochastic thermal and density fluctuation, nucleation events occur, and the solid formation process starts. The formulation above is the base of the so-called *classical nucleation theory* (CNT), which was postulated by Gibbs (1876), with a thermodynamic approach, considering the droplet formation due to water condensation in a humid air environment. Gibbs demonstrated that even if the overall variation of the chemical potential is negative, the process does not evolve spontaneously and a free-energy barrier has to be overcome, introducing the concept of activation energy. After Gibbs, the nucleation theory was formulated by Volmer and Weber (1925) and corrected by Becker and Döring (1935) as a phenomenological approach, including some limitations and approximations. The theory was completed by Zeldovich (1943), disseminated by Nielsen (1964) and, nowadays it is largely applied.

Apart from details associated to the derivation of CNT, which are described in detail by Nielsen [1], in the framework of this dissertation, it is worth mentioning that one of the most relevant criticisms to the CNT concerns the *capillary approximation*. For the sake of brevity, this approximation makes the surface tension,  $\Gamma$ , independent of the embryo (nuclei) size. Moreover, it is assumed that the value for  $\Gamma$  in the nano-regime corresponds to that of the macroscopic (larger than  $1 \mu\text{m}$ ) solid. The first consequence is that the surface energy contribution has the monotonic behaviour depicted in figure 2.1 and, consequently, the overall Gibbs free energy has only one point where the derivative is zero. Introducing in the derivation an arbitrary  $\Gamma = \Gamma(r)$ , the capillary approximation is excluded. Thus, a different Gibbs free energy landscape is obtained, which can have more than one point where the derivative is zero, e.g. a minimum before the critical size, as depicted in figure 2.2, leading to a different

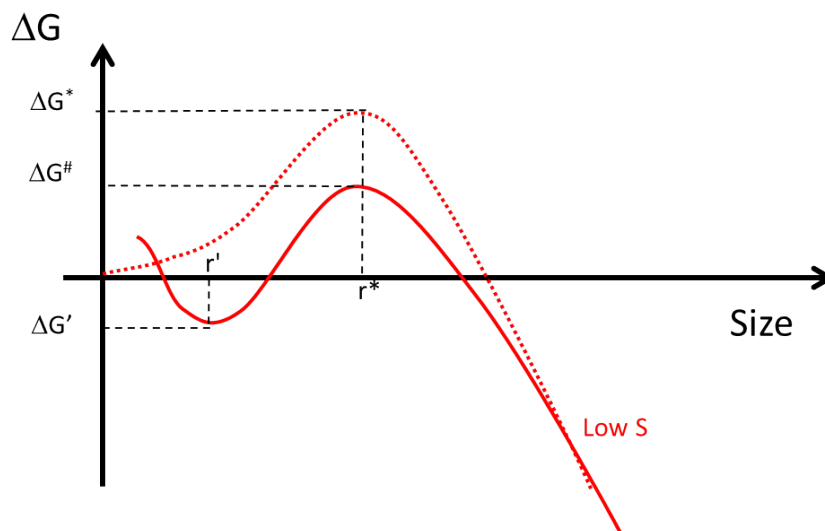


**Figure 2.2** – Schematic representation of Gibbs free energy landscapes. In case of relatively low  $S$  (continuous line, NCNT) a relative minimum may be depicted. The critical size and the size of metastable embryos are indicated as  $r^*$  and  $r'$ , respectively. The dotted line depicts the Gibbs free energy profile according to the CNT.

landscape and, thus defining a *non-classical nucleation theory* (NCNT). Therefore, it can be generalised that, in the CNT, the Gibbs free energy landscape corresponds to that depicted in figure 2.2 (dotted line); every different landscape may be directly associated with the NCNT framework. The CNT may be considered too simplified and not capable of describing quantitatively experimental crystallisation data. Moreover, when the existence at the macroscopic scale of intermediate and amorphous phases, precursors of the thermodynamically stable crystalline phase have been experimentally detected, this criticism about CNT become more important. The presence of sub-critical species gave rise to the possibility of various energy landscapes able to describe their existence and their contribution to the nucleation mechanism. Several NCNT can be argued; some of them will be discussed in section 2.3, with particular emphasis on the studies carried out on calcium carbonate (CaC) and calcium phosphate (CaP) systems.

A way to investigate the details of the nucleation process is to study the function  $\Gamma = \Gamma(r)$ . Attempts were done using Monte Carlo simulations, and Molecular Dynamics (MD) simulations trying to calculate the free energy of cluster formation with molecular approaches [60]. A general overview on classical and non-classical theories are reported in the review of Karthika and co-workers [73]. Nevertheless, it is relevant to underline that

## 2. Precipitation

---

- the equation (2.22), used in the kinetic calculations, is independent of every landscape before  $\Delta G^*$  but it only depends on the energy barrier to overcome;
- if the nucleation events occur in a timeframe in which  $S$  is almost constant, the critical size (eq. (2.24)) is almost constant; thus  $\Gamma(r)$  is also almost constant, and the capillary approximation has no consequences on the theoretical framework. However, the estimated value for  $\Gamma$  from nucleation rate refers to that specific size ( $r^*$ ) and that specific nucleating material and cannot be addressed as a property of the solid obtained as the final product of the precipitation.

It can be concluded that, in the specific conditions where nucleation occurs at almost constant  $S$ , the equation (2.22) can be applied, and the meaning of  $\Gamma$  needs to be correctly interpreted and communicated.

The nucleation mechanism so far described defines the homogeneous nucleation. The “homogeneity” refers to the physical status of the system before that the nucleation events occur. When the system is composed of a homogeneous (single phase) solution, the nucleation events are equally probable in each partition of the entire volume considered. Nevertheless, each tiny solid in suspension induces a local inhomogeneity; this can locally promote nucleation. In fact, unless the system is exceptionally pure, very often the nucleation is triggered by heterogeneities. Depending on the nature of the considered inhomogeneity, different kind of nucleation can be formulated. Furthermore, according to the traditional schematisation, the nucleation can be primary or secondary.

The primary and secondary definition recall a “temporal meaning”. The secondary nucleation can occur only after primary nucleation. The primary nucleation refers to a process that is not influenced by the solid undergoing formation. The primary nucleation can be classified into homogeneous and heterogeneous. The mechanism described previously in this section can be rigorously defined as primary homogeneous nucleation. Instead, in the primary heterogeneous nucleation, the new solid-phase forms thanks to the presence of a foreign pre-existing solid. The pre-existing solid can be present in the reactor as unwanted solid impurities, the reactor wall, the stirrer, or foreign seeds added into the system on purpose.

The secondary nucleation is triggered and self-catalysed by the same solid that is formed during the precipitation and can be divided into different sub-classes. “True” secondary nucleation occurs when new nuclei form onto the pre-generated nu-

clei suspended into the solution. “Apparent” secondary nucleation takes into account for small fragment detached from the pre-generated particles because of the fluid-dynamic stress of the system. “Contact” secondary nucleation is due to fragments of pre-existing particles formed because of the impact and adhesion onto the reactor wall, stirrer, *etc.*

Each described nucleation process is associated with its specific activation energy. The primary homogeneous nucleation is the most energetically demanding. Nevertheless, primary heterogeneous nucleation occurs if the substrate offers some affinity to the nucleating solid. In this context, affinity means that the nucleating phase gains a surface energy contribution (lowering the surface energy curve in figure 2.1) as a consequence of the contact with the heterogeneity. The cohesion energy quantifies this energy gain contribution  $\beta$  [70]. Rigorously,  $\beta$  should be defined as cohesion energy when a perfect match between the embryo-particle is attained and adhesion energy when a mismatch between the entities involved in the process remains. This mismatch may be due to crystallographic reasons or because of adsorbed additives (or even because of the solvent is not desorbed) at the interface.

With the primary homogeneous nucleation process, the “true” secondary nucleation is considered of particular relevance in the context of this dissertation and is described in detail. In this mechanism, 3D embryos are incorporated on the surface of the same solid phase which is precipitating [70]. Three constraints have to be satisfied to justify the occurrence of these events; the presence of 3D embryos in solution; the presence of a solid phase with the same nature as that of the precipitating material; a convenient cohesion energy contribution associated with the interaction between the already present solid phase and embryos. Secondary nucleation is an activated process (figure 2.3, green lines). It is similar to homogeneous primary nucleation (figure 2.3, red lines) but less energetically demanding ( $\Delta G_h^* < \Delta G_s^*$ ) because of the energy gain  $\beta$  due to the embryo-particle cohesion. In principle, it is almost the same process as heterogeneous nucleation yet involving a surface of the same nature as that of the embryo. By definition, secondary nucleation needs to be preceded by primary homogeneous nucleation and growth events (in the absence of seeds in suspension), which have to generate enough solid surfaces to allow the secondary nucleation itself. The secondary nuclei grow as well as the primary ones. These events generate more and more surface that further promotes additional secondary nucleation events and growth, according to a self-catalytic behaviour. As a consequence, the saturation level – in a batch reactor – rapidly decreases.

## 2. Precipitation

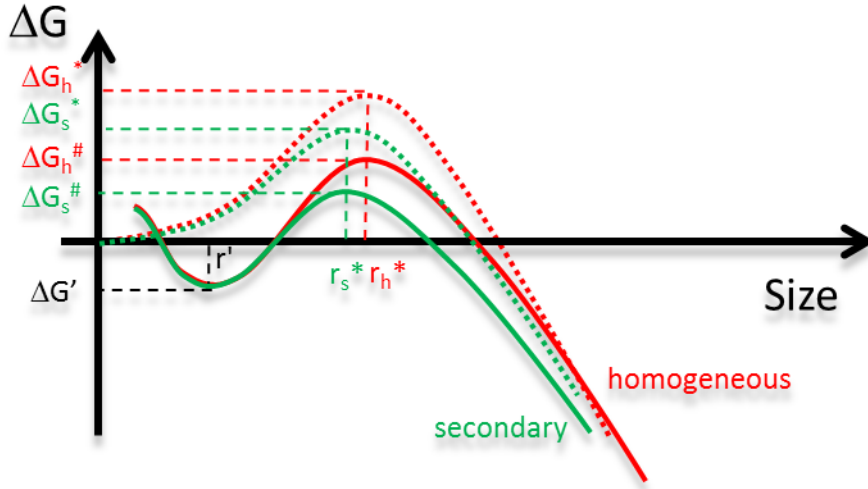


**Figure 2.3** – Schematic representation of Gibbs free energy landscapes for homogeneous and “true” secondary nucleation Gibbs free energy landscapes. In the case of secondary nucleation, the coordinate of the critical size corresponds to a lower size and lower activation energy concerning the homogeneous nucleation due to the contribution of the energy of cohesion. Dotted and continuous lines depict the CNT and NCNT, respectively.

The equations for the “true” secondary nucleation can be derived as those of the homogeneous nucleation. Thus,

$$J_s = \frac{2 \cdot D}{d^4} e^{-\frac{\Delta G^*}{k_B T}} \quad (2.25)$$

$$\Delta G^* = \varepsilon \frac{v^2 \cdot \Gamma_{eq}^3}{(k_B)^2 \cdot T^2 \cdot \ln^2(S)} \quad (2.26)$$

$$r^* = \frac{v \cdot \Gamma_{eq}}{k_B \cdot T \cdot \ln(S)} \quad (2.27)$$

$$\Gamma_{eq} = \frac{\Gamma}{6} \left( 6 - \frac{\beta}{\Gamma} \right) \quad (2.28)$$

where  $\Gamma_{eq}$  includes the cohesion energy  $\beta$  and the secondary nucleation rate,  $J_s$  ( $\# L^{-2} t^{-1}$ ), refers to the surface of the solid on which the events occur.

The mechanism of the “true” secondary nucleation, and the influence of  $\beta$  can be understood in the following manner: an embryo is metastable in solution and in equilibrium with its environment (section 2.1.1, eq. (2.19)). Because of the cohesion energy gain, when the embryo comes into contact with a solid surface, the surface contribution of its Gibbs free energy decreases and it is incorporated into the solid

## 2.2. Elementary processes of solid formation

surface (figure 2.3, dotted green lines). If the precipitating solid has a crystalline nature, it may expose solid faces with different surface energies, eventually influenced by the presence of additives (or the solvent itself). This anisotropy plays a relevant role in the case of moderate cohesion energy since the embryo can be preferentially incorporated in a defined direction, resulting in a polycrystalline material with oriented-attachment ordering [74, 75]. Instead, when several directions (faces) are energetically equivalent, such as in a cubic crystal with a cubic habit, 3D mesocrystals might be obtained. Finally, if the cohesion energy is high, the embryo incorporation is isotropic, and the obtained material is a disordered polycrystalline material with an equiaxed shape, *i.e.*, a secondary particle composed of primary particles (raspberry-like secondary particles). Often such secondary particles are addressed as “aggregates”, but in fact, they are not necessarily produced by an aggregation mechanism [10].

Figure 2.3 allows further discussion of possible reaction pathway scenarios. Assuming the two red lines (primary nucleation) continuous (NCNT) and dotted (CNT) and considering – for the sake of simplicity – the condition where  $\Delta G_s^* = \Delta G_s^\# + \Delta G'$  and the same value of  $r_h^*$ . This defines the energy barrier to overcome is the same for both landscapes, regardless of the existence or not of a relative minimum before  $r_h^*$ , the nucleation rate, which depends only on the energy barrier to overcome, gives the same result for both scenarios. The energy of activation can be derived from studies of the nucleation event, but events before the critical size is reached are not attainable. Similar considerations can be drawn for the secondary nucleation as well (green lines). Therefore, as previously discussed, the derived equation for both primary and secondary nucleation rates can be used independently to the specific landscape, provided that nucleation occurs at almost constant supersaturation, and analysis of the nucleation rate cannot help us understand the details of the Gibbs free energy landscape.

### 2.2.2 Growth

The growth process occurs by incorporation of a building unit on the solid surface. The building unit can be an ion, a molecule, an ion pair, or a cluster composed of several ions or molecules and it must be transported through the solution up to the solid surface. Once on the surface, the building unit releases the solvation molecules, and then can be incorporated in an appropriate site. Therefore, the incorporation pathway is defined by several successive steps; the slowest one controls the entire growth rate. Each step in the incorporation pathway characteristically depends on supersaturation.

## 2. Precipitation

Thus, since in a batch reactor the supersaturation changes over time, the growth rate controlling mechanism can change during the solid formation. Figure 2.4 is a classical representation of the growth regime change over time, where the growth process of  $\text{BaSO}_4$  in a supersaturated solution is schematised. In the starting point conditions, a large number of nuclei are generated, and they increase in size up to the point Z (vertical line). The value of  $S$  is not influenced because of the limited overall mass of the nucleated matter. At point Z, these nuclei grow under a diffusion-limited regime (zone G) and,  $S$  decreases of one order of magnitude along the horizontal dashed line before that the regime changes, becoming limited by the surface incorporation. Considering the overall growth process reported in the example, 90% of the solid grows under a diffusion-limited regime since  $S$  decreases of a factor of 10.

In principle, if the transport through the solution controls the growth rate, both diffusion and convection may play a role. When the solid particles are smaller than  $10\text{ }\mu\text{m}$ , convection can be neglected because the velocity of the solid through the solution at standard stirring rates is very low. Thus, a stationary diffusional concentration field is set up around the crystal faster than the liquid in the close vicinity of the solid is renewed. In this condition, the transport is purely diffusion-limited. As in the example of figure 2.4, the most relevant kinetic data on the precipitation process are collected where the  $S$  rapidly drops. Thus, the diffusion limited growth regime is of particular relevance in the framework of this dissertation.

### Diffusion-limited growth

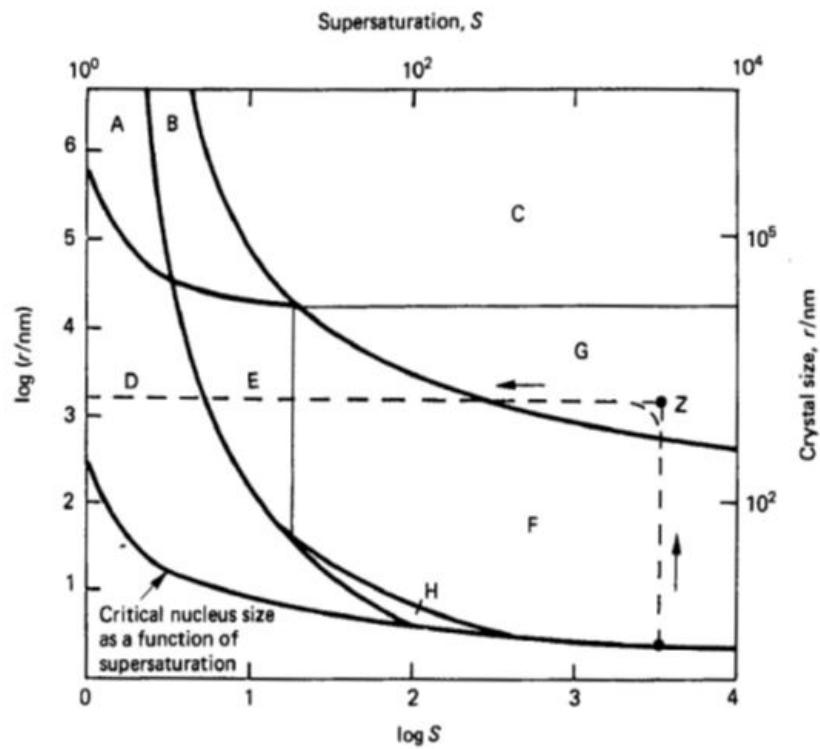
In general, the molar transport of matter (flux,  $J_D$ ) per unit of solid surface and time that reach the particle of solid in movement in a supersaturated solution under the diffusion and convective regime, can be derived by Fick's first law

$$J_D = K_C(C_{\text{bulk}} - C_{\text{surf}}) \quad (2.29)$$

where  $K_C$  ( $\text{Lt}^{-1}$ ) represents the transport coefficient and  $C_{\text{bulk}}$ , and  $C_{\text{surf}}$  are the concentration ( $\text{molL}^{-3}$ ) of the solute far from and close to the surface of the solid, respectively. When the regime is purely diffusional, the transport coefficient can be approximated by  $D/\delta$ , where  $D$  is the diffusion coefficient, and  $\delta$  is the thickness stagnant superficial film (figure 2.5). If the relative speed of a sub-micrometric particle with respect to the solution is small (*slip velocity*), the Brownian motion limits its diffusion, and  $\delta$  can be approximated with the particle radius,  $r$ . Thus, the



## 2.2. Elementary processes of solid formation



- |  |  |
|--|--|
| <i>A</i> – mononuclear or convection;        | <i>E</i> – polynuclear or screw dislocation; |
| <i>B</i> – polynuclear or convection;        | <i>F</i> – polynuclear;                      |
| <i>C</i> – convection;                       | <i>G</i> – diffusion;                        |
| <i>D</i> – mononuclear or screw dislocation; | <i>H</i> – mononuclear.                      |

**Figure 2.4** – Schematization of  $\text{BaSO}_4$  precipitation and the growth regime variation along the solid formation [1].

## 2. Precipitation

---

diffusive flux reads

$$J_D = \frac{D}{r} \cdot (C_{\text{bulk}} - C_{\text{surf}}) \quad (2.30)$$

The corresponding linear growth rate,  $G_D$  ( $\text{ms}^{-1}$ ) of the particle reads

$$\begin{aligned} G_D &= \frac{dr}{dt} = J_D \cdot v \\ &= \frac{D \cdot v}{r} (C_{\text{bulk}} - C_{\text{surf}}) \end{aligned} \quad (2.31)$$

where  $v$  is the molecular volume of the growth unit. If more than one chemical species have to reach the solid surface, such as the case of the schematic reaction



then the condition

$$\begin{aligned} \frac{J_A}{n} &= \frac{J_B}{m} = \frac{D_A (A_{\text{bulk}} - A_{\text{surf}})}{n r} \\ &= \frac{D_B (B_{\text{bulk}} - B_{\text{surf}})}{m r} \end{aligned} \quad (2.33)$$

needs to be satisfied.

Thus, the general equation (2.33) reduced to  $A_{\text{surf}}$ , reads

$$\frac{D_A}{D_B} \cdot \frac{n}{m} \cdot \frac{\gamma_A}{\gamma_B} \cdot (A_{\text{bulk}} - A_{\text{surf}}) = \left( \frac{S \cdot K_{sp}}{\gamma_A^n \cdot \gamma_B^m \cdot A_{\text{bulk}}^n} \right)^{\frac{1}{m}} - \left( \frac{K_{sp}}{\gamma_A^n \cdot \gamma_B^m \cdot A_{\text{surf}}^n} \right)^{\frac{1}{m}} \quad (2.34)$$

where  $n$  and  $m$  are the stoichiometry coefficients,  $\gamma_A$  and  $\gamma_B$  are the activity,  $D_A$  and  $D_B$  are the diffusion coefficient for the chemical species  $A$  and  $B$ , respectively,  $K_{sp}$  is the solubility product,  $S$  is the saturation,  $A_{\text{bulk}}$  is the concentration of the chemical species  $A$  in the solution bulk (far from the solid and experimentally accessible), and  $A_{\text{surf}}$  is the concentration of the chemical species  $A$  on the surface of the solid. In this full form, this equation has no analytical solution, and it is numerically solved for  $A_{\text{surf}}$ . Nevertheless, some simplification may be done. In the case of  $\text{CaCO}_3$

## 2.2. Elementary processes of solid formation

precipitation,  $n = m = 1$  and the analytical solution of equation (2.34) become

$$Ca_{\text{surf}} = \frac{a_{Ca}^2 \cdot h \cdot Ca_{\text{bulk}}^2 + K_{sp} \cdot S}{2 \cdot a_{Ca}^2 \cdot h \cdot Ca_{\text{bulk}}} + \frac{\sqrt{h^2 \cdot Ca_{\text{bulk}}^4 \cdot a_{Ca}^4 + 2 \cdot K_{sp} \cdot S \cdot h \cdot Ca_{\text{bulk}}^2 \cdot a_{Ca}^2 - 4 \cdot K_{sp} \cdot h \cdot Ca_{\text{bulk}}^2 \cdot a_{Ca}^2 + K_{sp}^2 \cdot S^2}}{2 \cdot a_{Ca}^2 \cdot h \cdot Ca_{\text{bulk}}} \quad (2.35)$$

where  $Ca_{\text{surf}}$  is the concentration of  $Ca^{2+}$  on the surface of the solid,  $Ca_{\text{bulk}}$  is the concentration of  $Ca^{2+}$  in the solution.

Furthermore, if one of the components is considered at a concentration much higher than the other and its concentration can be considered constant and equal to the bulk value ( $B_{\text{surf}} \approx B_{\text{bulk}}$ ), equation (2.34) can be simplified. For instance, for the formation of octacalcium phosphate and considering the reaction



The equation (2.35) reads

$$Ca_{\text{surf}} = \left( \frac{K_{spOCP}}{\gamma_{Ca}^4 \gamma_{PO_4}^3 \gamma_H} \right)^{4^{-1}} \quad (2.37)$$

The building unit can be an ion, a molecule, an ion pair, a cluster composed of several ions or molecules. In a regime where the growth mechanism is limited by the diffusion of the building unit, the value of the diffusion coefficient (equation (2.31)) of the building unit itself can reveal its size using the Stokes-Einstein equation (2.38).

$$D = \frac{k_B \cdot T}{6\pi \cdot \eta \cdot r} \quad (2.38)$$

The evaluation of the size of the building unit allows the discrimination between classical (where ions or molecules are the building unit of the solid phase) or non-classical crystallisation pathway (where clusters are considered as the building unit). The use of this indirect method to discriminate which crystallisation pathway is the most plausible is one of the originalities of my scientific achievement.

## 2. Precipitation

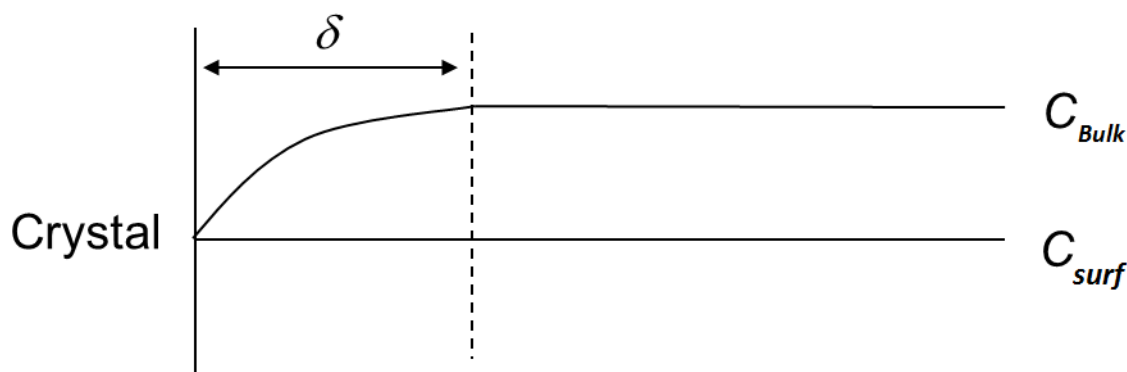


**Figure 2.5** – Schematization of the concentration profile in the diffusion-limited growth.

### 2.2.3 Aggregation

Aggregation is the mechanism by which secondary particles are formed as a result of effective collisions among primary (or smaller secondary) particles. By definition, the interacting particles are larger than the critical size and cannot be defined as embryos. In this process, the energy barrier to overcome is associated with the balance between attractive (van der Waals) and repulsive (electrostatic) forces, and it is much less energetically demanding than secondary nucleation events, that is, the other elementary process able to promote secondary particle formation. After effective collisions, primary particles can find an energetically convenient orientation and a mesocrystalline structure might be attained. The obtained secondary particles can then be appropriately addressed as “aggregates” since aggregation events produced them. Again, any additives on the particles’ surface might be able to promote or inhibit aggregation as well as particle-particle preferred orientation.

In the framework of this dissertation, aggregation was not considered for two main reasons. Firstly, to study aggregation time-resolved data on the evolution of the solid phase are needed. In fact, aggregation cannot be reflected by the concentration of chemical species in solution because it is a process that does not involve any variation of the solid amount in the system; thus, the concentration of the chemical species in solution is not affected by aggregation. Moreover, due to the limited concentration of the solid product in diluted solution (and concentration cannot be increased because it is limited by the solubility of the solid under observation), the on-line time-resolved data collection on the evolution of the solid phase was not experimentally accessible.

## 2.3. Alternative pathways of solid formation

Nevertheless, aggregation occurs as experimentally detected by electron microscopy investigations. It is merely a process not detectable in the experimental investigation carried out and does not influence the nucleation and growth processes. This statement, rigorously, cannot be generalised. In fact, if a sort of re-crystallisation follows aggregation, the overall specific surface area of the solid may change, and thus influence the secondary nucleation and growth (which are surface-dependent). Nevertheless, considering the timescale of the process under analysis, it is plausible to assume that aggregation occurs on a time scale that does not influence the overall surface area of the solid, at least in the time frame where the precipitation is under kinetic control (figure 1.1, section 1.2.2.3).

Secondly, the kinetic model is based on a monovariate population balance approach. Monovariate means that only one internal coordinate can be considered, that is the particle size (radius or diameter). Such a particle size can be that of the primary particles, which are those generated by primary homogeneous and “true” secondary nucleation, or that of the secondary particle, which are those particles formed by several primary particles produced by a series of secondary nucleation events or aggregation. This limitation to only one internal coordinate forces the code to be focused either on primary or on secondary particle size. Thus, if secondary nucleation is included in the model, the internal coordinate has to be the primary particle size, because it is a process occurring on the surface of primary particles; if aggregation is included, the internal coordinate has to be the secondary particle size. As a consequence, a monovariate population balance approach is not able to deal simultaneously with secondary nucleation and aggregation on the same timescale.

## 2.3 Alternative pathways of solid formation

### Non-classical nucleation and non-classical crystallisation.

#### 2.3.1 Spinodal decomposition

The spinodal decomposition (SD) mechanism is a first-order phase transition. Generally, it refers to metals or polymers solidification from melts or solid protein formation from solution. This process has been proposed as an alternative pathway to the nucleation mechanism described by the CNT. The spinodal decomposition differs from nucleation in both thermodynamics and kinetics aspects, and it can follow multistage

## 2. Precipitation

---

pathways during the solid formation.

In the spinodal regime, the system is thermodynamically unstable and suddenly separates into two phases of different composition. Contrary to nucleation, the spinodal decomposition is an energy barrier-free process because the energy surface term is absent; the two phases are connected to them and interconnected within themselves. The interface between the two phases is widespread, and there is no interfacial tension between them. Figure 2.6 represents a phase diagram, where different areas are depicted. In the inner zone (SD) spinodal decomposition occurs, whereas nucleation and growth dominate the zones between the dotted and the continuous lines (N+G). The two liquid phases generated by spinodal decomposition are inherently unstable, and thus they can change composition over time. The microscopic composition fluctuations can lead to the solid formation.

The spinodal decomposition mechanism is not so often reported for the electrolyte solutions. Despite that, recently in the literature, the spinodal decomposition has been applied in the description of calcium carbonate (CaC) and calcium phosphate (CaP) precipitation from solution.

In 2013, Wallace and co-workers [60] predicted the appearance of polymeric species of small size ( $<10$  ion pairs) in the precipitation process of a moderately concentrated  $\text{CaCO}_3$  solution. Using molecular dynamics (MD) simulations, they reported the continuous growth of these entities into a compact cluster, with little or no free-energy barrier. Since the authors claimed that the process was not activated, they invoked a spinodal decomposition process for that system. Because the result of the clusters growth process gave a bimodal distribution, the authors depicted it as consequence of monomer addition and particle-particle coalescence. Moreover, they proposed that the presence of multi-ion clusters, as reported in the previous literature [6], is in agreement with the particle distributions obtained as results of the liquid-liquid phase separation as shown by their computational dynamic simulation results.

### 2.3.2 Aggregation of Stable or Metastable Particles

One of the alternative theories to CNT considers the solid formation from solution via a nucleation mechanism promoted by aggregation of species in solution. These species can be ion complexes or multi-ion clusters; they are defined as “pre-nucleation clusters” because of their presence in solution before the nucleation process. This mechanism has been proposed principally for sparingly soluble salts precipitation, such

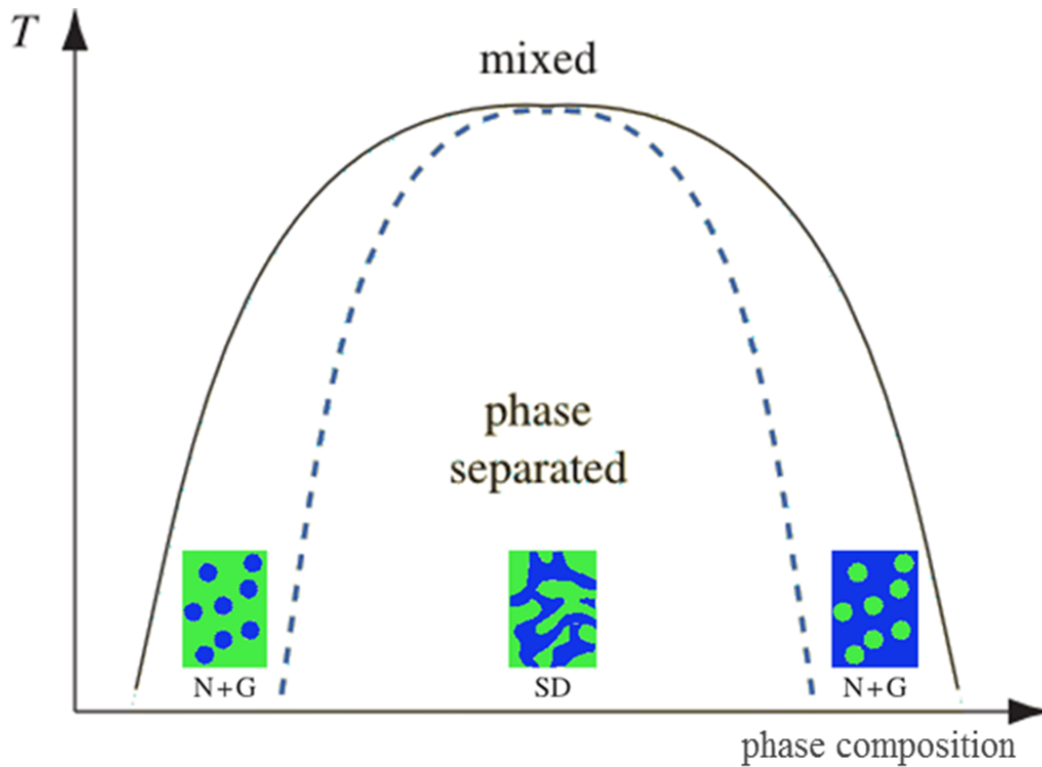


**Figure 2.6** – Phase diagram. In the tangent region, the mixed state is thermodynamically stable. Inside the dotted line, the mixture will separate by spinodal decomposition (SD); between the dotted and solid lines there is a kinetic barrier, and the system evolves through nucleation and growth.

as calcium carbonate (CaC) [6, 27] and calcium phosphate (CaP) [76] systems. For CaC system, Gebauer *et al.* [6] proposed a multi-ion binding model to explain the  $\text{Ca}^{2+}$  ion complexation during calcium solution addition in carbonate buffer solution and the detection of species larger than ions,  $\approx 2$  nm in size, using the analytical ultracentrifugation (AUC). Moreover, Demichelis *et al.* [77] predicted using MD simulations the involvement of dynamic polymeric structures, small clusters, in the CaC precipitation pathway. Because of the prenucleation clusters present in solution in equilibrium with the monomeric species, the authors defined them as thermodynamically *stable* species. The nucleation mechanism proposed by them has an alternatives Gibbs free energy landscape (figure 2.7) since it considers the clusters aggregation as a barrier-free process. The same authors [78], more recently, showed that the prenucleation clusters are stable relative to monomers because they formation is favoured above dissolution, even in undersaturated conditions. Moreover, Pouget *et al.* [27] detected

## 2. Precipitation

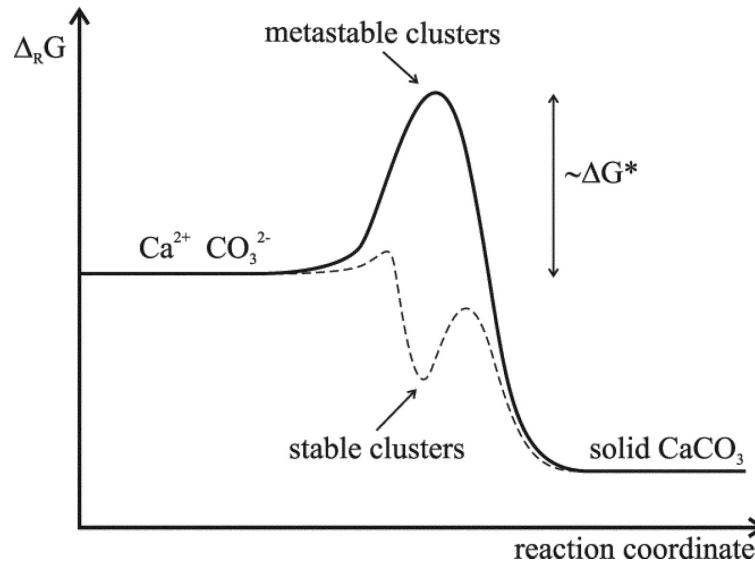


**Figure 2.7** – Free energy profile of nucleation of calcium carbonate. From [6]. Reprinted with permission from AAAS.

the prenucleation clusters of  $\text{CaCO}_3$  with an average size of about 0.7 nm using cryo-TEM analyses. The authors interpreted the observations considering these clusters within the size range predicted by the classical nucleation theory (CNT), that means they deemed the prenucleation clusters as thermodynamically metastable species. Hu *et al.* calculated the nucleation rate of calcite via aggregation of precritical clusters, which occupy a minimum of free-energy barrier *vs* size, using the equation of CNT. Here, they estimate the dependency of the energy barrier on supersaturation and bulk interfacial free energy as reported in equation (2.39)

$$\Delta G^* = B \frac{\Gamma^3}{(\ln(S) \pm C)^2} \quad (2.39)$$

where  $C$  is a constant that depends on the shape factor, the particle radius, and the free energy excess of the particles. If the energy excess refers to a local minimum, then the sign is positive, while if the minimum refers to the global process, the sign is negative. The supersaturation is influenced by the presence of these particles, when they are stable or metastable with respect to the free ions the probability of nucleation events decrease or increase, respectively.

The cryo-TEM method was also applied to study CaP system by Dey and co-workers [79]. They observed the formation of amorphous calcium phosphate (ACP) particles,



## 2.3. Alternative pathways of solid formation

which later transforms into oriented apatite crystals. As a further result, they proposed that calcium phosphate nucleates via aggregation of pre-nucleation clusters mechanism. Habraken and coworker [76] carried out a more detailed experimental study on the same system, based on analytical and cryo-TEM analyses, together with *ab-initio* calculations. The complete picture led to the interpretation of a multistage pathway: first, calcium triphosphate complexes aggregate in a polymeric network forming the amorphous phase, then, octacalcium phosphate (OCP), and finally re-crystallises as hydroxyapatite (HA). The authors consider these prenucleation clusters as metastable species with respect to monomeric species; they are in a local free-energy minimum but at a higher energetic state compare to monomers.

*“Although cryo-TEM data was initially interpreted as evidence for  $\text{CaCO}_3$  pre-nucleation clusters averaging about 0.7 nm in size [27], subsequent analysis led to the conclusion that these features were below the direct interpretable size range of the measurement, and that the observations also could be reconciled with a distribution of cluster sizes as predicted by classical nucleation models.”[80]*

### 2.3.3 Multi-step Pathways

The multi-step crystallisation pathway has been introduced as an alternatives mechanism to classical nucleation theory (CNT) following the observation of the precipitated solid. In the case of sparsely soluble salts, the first solid formed is a metastable polymorph. Habraken and coworkers [76] argued that the formation of the metastable phase can be related to kinetic limitations. Navrotsky [81] proposed the formation of a metastable phase as a consequence of an “inversion in phase stability”: the bulk phase becomes less stable because of the increased surface free energy at the nucleation stage promoting the formation of particles with the smaller size. The dissolution-recrystallisation process was observed for calcium carbonate [30, 82, 83], and it was described as an indirect multistep nucleation pathway. In these studies, the amorphous phase nucleates and grows until the most stable phase appears, thus the amorphous dissolves back into solution.

### 2.3.4 Oriented attachment and mesocrystal formation

The oriented attachment mechanism is a particle-mediated process and involves a mesoscopic transformation [84, 85]. The peculiarity of such a process is the formation

## 2. Precipitation

---

of a product composed by sub-units that present single crystal characteristics. Its driving force is the reduction of the surface Gibbs free energy contribution. Van der Waals forces start to act between all particles in solution and therefore play a role in the aggregation of nanocrystallites. The primary particles generated by nucleation arrange into an iso-oriented crystal. Because of their subsequent fusion, the iso-crystal evolves through a single crystal structure. The stable primary particles, called “sub-units”, are the key point of the oriented attachment mechanism. Indeed, the final structure is due to the particles rearrangement, promoted by their thermal energy (vibration), toward a lower energy configuration, usually represented by a coherent particle-particle interface. The presence of additives can stabilise the formed nuclei allowing the control over their aggregation mechanisms, towards their iso-oriented assembling. The additives may also reduce the energy barrier for nucleation influencing the surface energy contribution. The structured crystals generated by oriented attachment mechanism are called mesocrystals. With this term, the scientists wanted to emphasise the structure of a material, rather than its mechanism of formation [86]. The existence of such crystals opened the debate about NCNT and particle-attachment mechanism, trying to find alternative energy pathways to explain the formation of the mesocrystals instead of a bulk crystal. Penn and Banfield [75] observed the oriented attachment mechanism during the synthesis of nanocrystalline titania, under hydrothermal conditions. Li *et al.* [87], during the formation of iron oxyhydroxide particle, observed the continuous rotation and highly direction-specific interaction until they match in the crystalline lattice. Concerning sparingly soluble salts, like CaC or CaP, the particle based mechanism has been invoked to explain the formation of an amorphous phase as first precipitation process. In 2015 the crystallisation by particle attachment mechanism was reported for different environments, such as synthetic, biogenic, and geologic [88]. Moreover, the authors consider the different nature of the particles involved in the particle-mediated growth, *i.e.* multi-ion complexes [76], oligomers (or clusters) [77], and nanoparticles - whether crystalline [87], amorphous [89], or liquid [90], as schematically represented in figure 2.8.

## 2.4. Classical and non-classical concepts: milestones of understanding

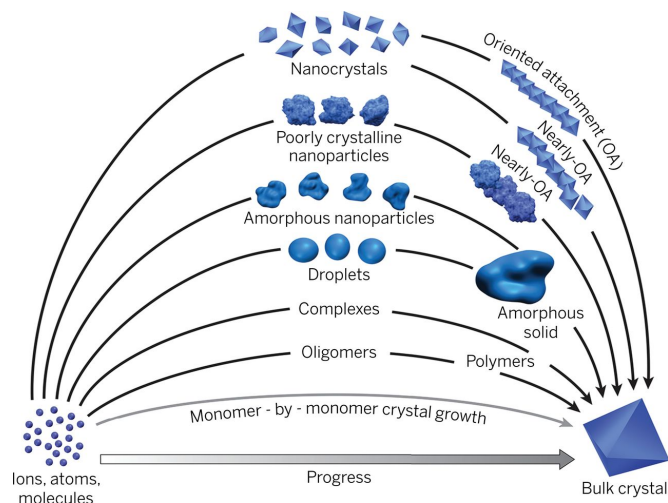


**Figure 2.8** – Pathways to crystallisation by particle attachment. From [88]. Reprinted with permission from AAAS.

## 2.4 Classical and non-classical concepts: milestones of understanding

*In this short section, the concepts regarding classical and non-classical theories are summarised and discussed in a general view. The aim is to mitigate some confusion in the terminology as well as to highlight the scientific background of my entire work which represents my starting point of understanding.*

The classical nucleation theory is the most applied theory to describe the crystallisation processes. The term non-classical was introduced in the sixties. This term is somewhat ambiguous, and its meaning has changed in the recent years relative to the original concept. Cahn and Hilliard, in 1959, associated the term to the nucleation mechanism [91] (section 2.2.1). Their investigation considered two partially miscible components. The authors postulated the formation of nuclei with a compositional gradient. The concept of the nucleus itself, characterised by the solid-liquid interface, was questioned as a function of saturation level. This concept was re-discussed by Nielsen [1], in a context where the description of the energetics of small particles using the surface energy ( $\Gamma$ ) was addressed as one of the weak points of the entire nucleation theory (2.1.1). An additional contribution was reported by Larson and Garside [92]; the non-classical nucleation theory was again properly invoked in the context of the size-dependent surface energy as the particle size approaches the nano-regime.

## 2. Precipitation

---

Nowadays, very often, the definition of non-classical is associated with the “particle-based” solid formation concept [2, 4], which is different to the original concept introduced by Cahn and Hilliard. In fact, one of the standard experimental evidence of a non-classical pathway is the formation of a solid with a mesocrystalline nature [3]. Mesocrystals are three-dimensional crystalline entities (secondary particles) composed of crystalline subunits (primary particles), that self-organise themselves in an ordered fashion (see section 2.3.4). The mechanism proceeds via attachment of building or growth units of the solid being formed, such as multi-ions, particles, and so forth, according to the so-called particle-based reaction. Therefore, the term “non-classical” is associated with the whole precipitation pathway and not any more to a defined elementary process (*i.e.*, nucleation).

When alternative theories to the classical one are introduced, it is essential that they clarify the characteristics of the microscopic species involved, and which elementary process is deemed to imply such species. Unfortunately, there is no quantitative theory for solid formation mechanism *via* aggregation of stable or meta-stable particles. The intermediated entities involved in the oriented attachment process are named and defined in very different manners, mainly regarding their stability and their density, generating misunderstanding. These entities are invoked as evidence of non-classical mechanisms since they are not being involved as stable entities by the classical view. Indeed, the classical theory includes the presence of embryos. In that framework, they have a higher probability to dissolve than to grow for thermodynamic reasons. It is worth noting that the thermodynamic equilibrium refers to macroscopic solids; yet, by definition, embryos have a size even smaller than the critical size. Thus, recalling the Kelvin equation (2.24), which correlates the solubility with the size of the solid particles (or, more rigorously, with the curvature of the particle), the embryos have a solubility higher than the critical nucleus, thus the solution is indeed supersaturated with respect to the macroscopic solid [93, 94]. However, considering the solubility of the embryos, they are not in a supersaturated environment. That means, the overall system is out of equilibrium, but the embryos are in stable equilibrium with the solution, even if the embryos themselves are not stable with respect to a macroscopic solid of the same nature.

The system reacts rapidly to any variation of saturation, setting a new solid-liquid equilibrium level. Because of local speciation and temperature fluctuations, the embryo population is characterised by particular size distribution. If the supersaturation increases, embryos grow to a larger size, and simultaneously their solubility decreases. If the supersaturation decreases, they partially dissolve to a smaller size with a further

#### 2.4. *Classical and non-classical concepts: milestones of understanding*

increase of their solubility. If the system is not perturbed, embryos remain at constant size and at that saturation level (between 1 and the critical value) for an indefinite period. This indefinite quiescence could be maintained if the embryos do not interact with any solid interface, which includes the reactor wall, dust, or any other surfaces that could eventually serve as a heterogeneous nucleation substrate.

To summarise, the presence of entities of *subcritical* size (embryos) is described in the CNT. The embryos are metastable with respect to the solid that forms but in thermodynamic equilibrium with respect to the species in solution. Their size depends on the saturation level, or more rigorously, on the value of their bulk and surface Gibbs free energy, and the local chemical speciation in solution. Experimental identification of embryos is very demanding as any alteration of the solution implies, at least, a change in their size. For instance, it is not possible to separate them from the mother solution, modify the solution temperature, add any chemicals [95] to stabilise them, change solvent [76], or dry the suspension [95].

In the framework of NCNT, some authors [6, 77] defined such intermediate clusters “stable” with respect to ions. They described this stability, as a local minimum in the Gibbs free energy landscape. The existence of a minimum identifies a metastable state, which might be associated to clusters of a preferential size.

The particle-based pathway postulates a direct contribution of the metastable embryo into the solid formation mechanism of the secondary particles. Nevertheless, the formation of a mesocrystalline solid, as well as the oriented attachment mechanism, does not necessitate of a new pathway to interpret their formation mechanism. A possible pathway is explicitly included in the classical process, where the three-dimensional “true” secondary nucleation or aggregation processes are included in the precipitation mechanism. Both of these elementary processes generate secondary polycrystalline particles.

A clarification has to be made on the “primary” and “secondary” terms combined with “nucleation” or “particles”:

- a primary particle is considered a single entity, such as a crystallite;
- a secondary particle is an entity composed by several primary particles;
- primary nucleation identifies a process that generates particle without the influence of the solid that is precipitating;
- secondary nucleation identifies a process that is triggered by the solid that is

## 2. Precipitation

---

precipitating.

As a consequence:

- primary and secondary nucleation can generate primary particles;
- when secondary nucleation occurs, a secondary particle is obtained, which is composed of a primary particle produced by primary nucleation and several primary particles produced by secondary nucleation.

As introduced in section 2.1.1, precipitation is a relatively fast process that occurs when a solid phase is separated from solution; crystallisation is an analogous process, but it is accepted that it refers to the formation of a crystalline phase. To achieve such ordering, a relatively long time to allow the incorporation of the crystal building units may be necessary. However, precipitation does not necessarily involve the formation of an ordered structure, and the process can be much faster than crystallisation.

In the classical precipitation pathway, there is no restriction whatsoever on the nature of the precipitated solid phase. More specifically, it could be an amorphous phase, which might dissolve and crystallise, or it may undergo some other processes, either concurrent or after precipitation, leading to a more thermodynamically stable phase [96]. In fact, according to Ostwald's step rule, the first phase formed is the less ordered and less dense phase, which is often an amorphous phase, which subsequently can dissolve or transform into a more stable phase. The system naturally evolves toward an increased thermodynamic stability; even so, not all the polymorphs of a specific system have necessarily to appear along the precipitation pathway. Despite this simple reasoning, the presence of an amorphous intermediate phase as a first product of the solid formation process was used as an indication of a non-classical pathway [6, 84].

A very last consideration of fundamental relevance: most of the alternative pathways proposed in the literature based on experimental observation lack of an appropriate mathematical framework. Therefore, the description of the precipitation mechanism was merely qualitative. Thus, a computational model able to describe such pathways was not achievable due to the missing mathematical description, and these alternative pathways cannot even be compared, on a quantitative basis, to the classical framework.

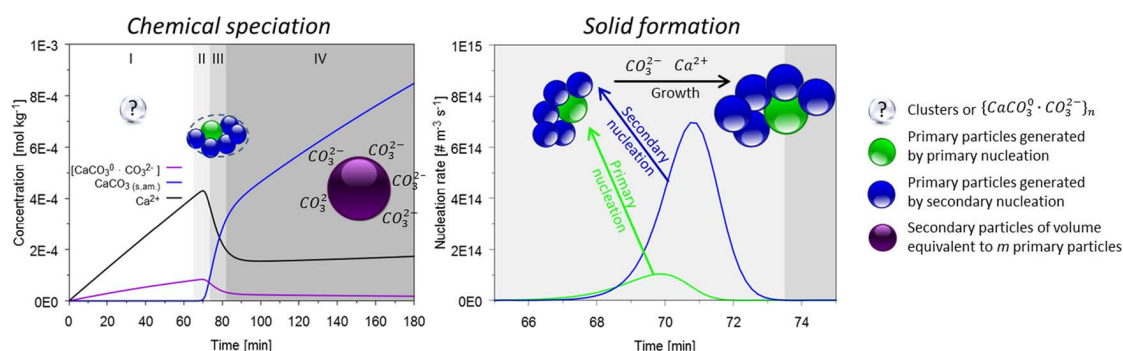
### **3 | Calcium carbonate and phosphate systems precipitation studies**





### 3.1. A Case Study: The Amorphous Calcium Carbonate (ACC) Precipitation Pathway Unravelled.

## 3.1 A Case Study: The Amorphous Calcium Carbonate (ACC) Precipitation Pathway Unravelled.



Author's contribution to this publication:

- experimental data collection;
- data analysis;
- regression of TD data;
- thermodynamic model;
- model refinement

This chapter is adapted from **A. Carino et al.**, Thermodynamic-Kinetic Precipitation Modeling. A Case Study: The Amorphous Calcium Carbonate (ACC) Precipitation Pathway Unravelled. From Cryst. Growth Des., **2017**, 17 (4), pp 2006-2015,[97].

### 3. CaCs & CaPs studies

---

#### 3.1.1 Abstract

Nine accurate experimental data sets on amorphous calcium carbonate (ACC) formation in dilute solution were collected varying temperature and pH. The entire precipitation process is described using a complete thermodynamic-kinetic model. The thermodynamic model includes two new complex chemical interactions whereas the kinetic model is based on the discretised population balance approach. Saturation, primary particles size distribution, average secondary particles size, nucleation, and growth rates, as well as a number of additional parameters on the ACC precipitation reaction, are reported. The excellent agreement among experiments, calculated results, and literature data demonstrates that a complete thermodynamic-kinetic model can significantly contribute toward the understanding of a plausible pathway for precipitating systems. In this case study, the classical nucleation theory, which includes homogeneous nucleation, “true” secondary nucleation, and diffusion limited growth events, is able to completely describe the entire precipitation process. The calculated surface ( $\Gamma$ ) and cohesion ( $\beta$ ) energies range from  $28 \text{ mJ m}^{-2}$  to  $35 \text{ mJ m}^{-2}$  and  $30 \text{ mJ m}^{-2}$  to  $42 \text{ mJ m}^{-2}$ , respectively, as a function of pH and temperature. Clusters or pre-nucleation entities act as spectators and are not directly involved in the solid formation pathway. The general methodological approach presented can be readily applied to other solid phase formation processes.

#### 3.1.2 Introduction

Precipitation is a complex event, being a convolution of several elementary processes, such as nucleation, growth, aggregation, disruption, ripening, cementing, *etc.* These processes may be also further classified: nucleation might be homogeneous, secondary, or heterogeneous; growth might be limited by the diffusion of chemical species or mediated by the incorporation of the solid building unit on the surface. The particular combination of the aforementioned elementary processes, and their relative contribution to the overall precipitation process, defines the solid formation pathway that has been a matter of intense scientific debate over recent years. Two pathways are mainly discussed, the classical one, corresponding to the so-called classical nucleation theory (CNT) described in detail by Nielsen [1], and the non-classical pathway [91, 92], mainly invoked wherever some morphological features of the precipitated solid phase do not seem interpretable through the classical theory framework. Because of the variety and the huge amount of publications on this topic, a rather

### 3.1. A Case Study: The Amorphous Calcium Carbonate (ACC) Precipitation Pathway Unravelled.

comprehensive description of the terms used in the field is reported in section 2.4 and might be useful to clarify important concepts and to corroborate our findings.

Several systems can be selected as a model to study the precipitation process. Among them, our effort was devoted to study the formation pathway of amorphous calcium carbonate (ACC) which is often considered as an ideal example of non-classical precipitation [2, 85, 98]. Despite being studied for several decades, there are still more than 200 scientific contributions per year published over the last 10 years just on its precipitation kinetics, demonstrating that there are still several unanswered questions.

Nowadays, it is widely accepted that the initial step of calcium carbonate crystallization is often the formation of ACC [14, 27, 77, 96, 99–102]. Depending on the experimental conditions, crystalline polymorphs are then formed, ideally until the most stable phase (calcite). Thus, a number of papers deal with the formation or recrystallization of crystalline phases, such as vaterite, aragonite and calcite from ACC [30, 82, 95, 100, 101, 103, 104]. Often, experimental studies are focused on the solid phases, their relative composition, and the obtained particles size or morphology. Despite the numbers of contributions in the literature, a detailed study on ACC precipitation able to describe the full precipitation pathway considering both the thermodynamic and the kinetic aspects is missing. Here, we present for the first time, to the best of our knowledge, a rigorous thermodynamic-kinetic model able to describe the complete ACC precipitation process.

Nine accurate experimental data sets on the precipitation process were collected in a relatively wide range of temperature and pH. The associated plausible precipitation pathways were studied applying an exhaustive speciation model merged with a precipitation kinetic model, based on the discretized population balance approach, without introducing any adjustable parameters. The speciation model is based on the state of the art thermodynamic quantities for the system under investigation. Moreover, ionic interactions between the ion pair  $\text{CaCO}_3^0$  and the carbonate ions as well as the interactions between ACC with the latter were taken into account. The kinetic model considers a double nucleation process, primary (homogeneous) and “true” secondary nucleation [1] combined with a diffusion limited growth mechanism. The concept used to model the formation of the amorphous solid is very similar to the one applied in the case of  $\text{BaTiO}_3$  precipitation from solution [10], where polycrystalline secondary particles formation was studied.

We demonstrate that the classical theory described by Nielsen is able to elucidate the details of ACC formation in the whole range of the experimental conditions investi-

### 3. CaCs & CaPs studies

---

gated. Moreover, new thermodynamic quantities associated with the formation of the ion pair  $\text{CaCO}_3^0$ , ACC, and the considered complex species, were regressed. The complex species might be responsible for the formation of entities in suspension, which are often addressed in literature as pre-nucleation clusters. Thanks to the rigorous approach, experimentally inaccessible data such as primary and secondary nucleation rate, surface and cohesion energies, critical primary and secondary nucleation size, linear growth rate, average secondary particle size, and primary particle size distribution over time are calculated. As discussed in this case study, the applied approach can be easily generalized and extended to other solid formation processes in particular when some fundamental kinetic data, thermodynamic quantities, or the properties of the early stage precipitation products are not experimentally accessible [76, 95, 105].

#### 3.1.3 Experiment and modelling

The precipitation reaction was studied using a constant composition approach and potentiometric titration method, as proposed by Kazmierczak *et al.* [7], Tomson and Nancollas [8], and Gebauer *et al.* [6, 106]. Specifically, the system saturation level was slowly increased by means of  $\text{CaCl}_2$  addition in a buffered carbonate/bicarbonate solution while temperature and pH were kept constant. Experimental data were collected at a fixed temperature ( $T = 298.15 \text{ K}$ ) varying pH from 9.00 to 10.00, as well as at a fixed pH ( $\text{pH} = 9.00$ ), while varying the temperature in the range between 279.35 K to 318.15 K. An exhaustive description of the experiments is reported as section 1.2. In the thermodynamic model, the state-of-the-art quantities for ACC and  $\text{CaCO}_3^0$  were refined and two additional interactions among chemical species included. The kinetic model, based on classical nucleation theory equations, includes homogeneous and “true” secondary nucleation, and diffusion limited growth processes [1, 10]. An extended section dedicated to the thermodynamic and kinetic models are included in sections 1.3.1.2 and 1.3.1.3, respectively. Briefly, the model for ACC formation embraces a comprehensive thermodynamic-kinetic code developed in FORTRAN. The thermodynamic code is able to solve the chemical speciation, as well as the calculation of some fundamental quantities for the kinetic code, such as the supersaturation and ionic strength. It is based on a set of nonlinear equations which are describing the mass, molar and charge balances among the considered chemical species. In addition to the most relevant chemical species, two complex species were considered, namely,  $\{\text{CaCO}_3^0 \cdot \text{CO}_3^{2-}\}$  and  $\{\text{CaCO}_3(\text{s, am}) \cdot \text{CO}_3^{2-}\}$ , which are a simplified representation of the interaction between the ion pair and ACC with carbonate ions,

### 3.1. A Case Study: The Amorphous Calcium Carbonate (ACC) Precipitation Pathway Unravelled.

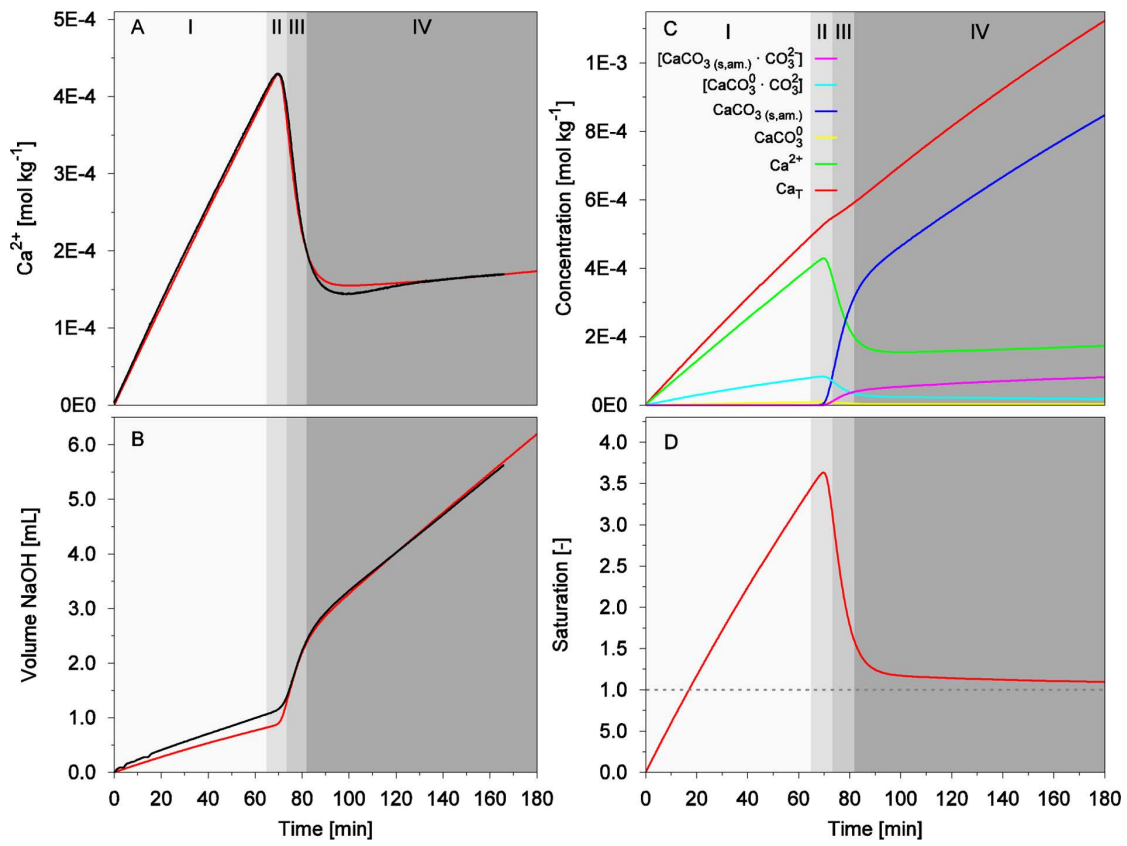


**Figure 3.1** – Experimental (black) and calculated (colored) data for the experiment at  $T=298.15\text{ K} \pm 0.2\text{ K}$  and  $\text{pH} = 9.00 \pm 0.02$  against time. (A)  $\text{Ca}^{2+}$  molality in solution, derived from the ISEs electrodes; (B) volume of NaOH added into the system to achieve iso- $\text{pH}$  conditions; (C) relevant chemical species, as extensively described in section 1.3.1.2; (D) calculated saturation. The horizontal dotted line highlights the condition  $S = 1$ . The Roman numerals refer to the zones associated with the precipitation evolution, identified by shaded greys.

respectively. They were implemented into the model to take into account the amount of bound carbonate ions, which is correlated to the amount of NaOH added into the system and to compute the value of  $\text{CO}_3^{2-}/\text{Ca}^{2+}$  for the species ion pair  $\{\text{CaCO}_3^0 \cdot \text{CO}_3^{2-}\}$  and in the solid phase  $\{\text{CaCO}_3(\text{s, am.}) \cdot \text{CO}_3^{2-}\}$ .

The kinetic code is based on the discretized population balance approach which is mathematically described by a system of ordinary differential equations. The equations for the classical nucleation theory were implemented. A diffusion controlled growth mechanism was considered and an algorithm able to correctly compute the first four moments of the particle size distribution was used [10]. The computed amount of solid is used to solve the mass balance equations of the thermodynamic code until self-consistency is reached at every time step.

#### 3.1.4 Results and discussion

A complete model, consisting of both thermodynamic and kinetic parts, was developed and specifically applied to describe the ACC full precipitation pathway. As a preliminary thermodynamic study, the experimental data have been regressed using OLI software (version 9.2, Studio and ESP packages [9]). The chemical speciation of the system was defined and thermodynamic quantities refined for both  $\text{CaCO}_3^0$  and ACC (table A.1).

In the following figures, the experiment carried out at  $T = 298.15 \text{ K}$  and  $p\text{H} = 9.00$  are discussed in detail. All the other data sets are reported in appendix A. Experimental data and some of the computational results are reported as black and colored curves, respectively. Zero on the time axis corresponds to the start of  $\text{CaCl}_2$  solution addition into the reactor. In figure 3.1 the two independent series of as-recorded experimental data are plotted, namely the concentration of  $\text{Ca}^{2+}$  in solution (figure 3.1A) and the volume of  $\text{NaOH}$  added into the system to keep iso- $p\text{H}$  conditions (figure 3.1B). The concentration of  $\text{Ca}^{2+}$  in solution initially rises almost linearly and proportionally to  $\text{CaCl}_2$  added into the system ( $\text{CaT}$ ) up to a maximum; it decreases down to a minimum following a sigmoidal shaped curve and finally an almost constant value is obtained. This trend allows the formal splitting of the entire experiment into four zones which are related to the elementary processes occurring during the precipitation. This division in zones is extended to all figures in order to simplify the precipitation description. Zone I refers to the pre-nucleation region; in zone II the precipitation starts. The concentration of  $\text{Ca}^{2+}$  rapidly decreases in zone III until an almost steady-state value in zone IV is reached. At the end of zone III the experimental data show a lower minimum with respect to the calculated value. This discrepancy is more evident in some cases or absent in other cases, for instance  $p\text{H} = 9.25$ ,  $T = 298.15 \text{ K}$ , and  $p\text{H} = 9.00$ ,  $T = 288.15 \text{ K}$  (appendix A), respectively. If a fraction of a less soluble solid phase would be formed, lower solubility equilibrium could be achieved, which might be reflected with a transient lower minimum in the  $\text{Ca}^{2+}$  concentration (see later). In zone IV, further solid phase is formed resulting in a stable plateau. The slightly positive slope is due to ACC formation and the associated  $\text{CO}_3^{2-}$  depletion: a higher calcium concentration is allowed at a fixed saturation level if the concentration of the carbonate ions decreases. In some other experimental conditions, this positive slope is even more evident (*e.g.*,  $p\text{H} = 9.00$ ,  $T = 279.35 \text{ K}$ , appendix A).

In the model, the level of the red curve in zone IV is refined optimizing the value of  $K_{sp}$ , that is, the solubility product of ACC for those experimental conditions. It is worth

### 3.1. A Case Study: The Amorphous Calcium Carbonate (ACC) Precipitation Pathway Unravelled.

noting that the chemical speciation in solution is influenced by the most soluble solid phase in suspension; the presence of less soluble solid phases might be hidden and cannot be excluded from the speciation data. Nevertheless, the presence of more than one solid phase would result in a mass unbalance in the thermodynamic-kinetic model, which is not the case here (see eqs. (1.49) and (1.50), section 1.3.1.2).

Solubility fluctuations were detected in the experiment carried out at  $pH = 10.00$  and  $T = 298.15\text{ K}$  ( $\text{Ca}^{2+}$  signal in zone IV, figure A.17), which can be associated with some solid phase transformations, as also reported elsewhere [6, 76, 107], but this behavior is beyond the scope of the work presented here. Figure 3.1B represents the graphical results of eqs. (1.41) and (1.42) (section 1.3.1.2) and has to be discussed in combination with figure 3.1C, which reports the concentration of calcium species against time. According to the model, a rather high value for the equilibrium constant of formation for  $\{\text{CaCO}_3^0 \cdot \text{CO}_3^{2-}\} (K_{\alpha 2})$  was calculated (*i.e.*, almost all the  $\text{CaCO}_3^0$  ion pairs are combined with carbonate ions to form the complex species  $\{\text{CaCO}_3^0 \cdot \text{CO}_3^{2-}\}$  ((1.40), section 1.3.1.2). Accordingly, a rather low Gibbs free energy of formation (figure 3.2, gray dots) for  $\{\text{CaCO}_3^0 \cdot \text{CO}_3^{2-}\}$  was estimated. This complex species formation is able to explain the experimental data in zone I of figure 3.1B, where ACC has not yet formed (blue curve, figure 3.1C). The amount of NaOH needed to maintain a constant  $pH$  (eq. (1.41), 1.3.1) depends on the amount of bound carbonate ((1.42), section 1.3.1.2).  $\text{CaCO}_3^0$  cannot be considered as the only depletion source for carbonate ions because the resulting values in zone I (figure 3.1B) would be only about one-half of the experimental ones. Thus, a species with a higher carbonate-to-calcium ratio ( $\text{CO}_3^{2-}/\text{Ca}^{2+}$ ) has to be considered. Among several options, the simplest hypothesis was assumed here, that is the formation of the complex species  $\{\text{CaCO}_3^0 \cdot \text{CO}_3^{2-}\}$ , thus fixing the  $\text{CO}_3^{2-}/\text{Ca}^{2+}$  ratio. This ratio is in excellent agreement with the value calculated by molecular dynamic simulations [60]. Even including this interaction, some discrepancies between the experimental and calculated values remain (figure 3.1B, zone I) which might be due to a more complex interaction, *i.e.*, the presence of species with an even higher  $\text{CO}_3^{2-}/\text{Ca}^{2+}$  ratio. In some other cases (appendix A) the amount of bound carbonate is perfectly described by the model. Thus, fixing  $\text{CO}_3^{2-}/\text{Ca}^{2+} = 2$  for that complex species was considered as an appropriate compromise between the experimental data description and the model complexity.

Figure 3.2 reports the calculated Gibbs free energies of formation for  $\text{CaCO}_3^0$  (red points) as well. The optimized values for its equilibrium constant of formation ( $K_{AS}$ , (1.44), section 1.3.1.2) are several orders of magnitude higher than those calculated

### 3. CaCs & CaPs studies

---

for the considered complex species (grey points). On the contrary, the preliminary model based on the OLI software, where only  $\text{CaCO}_3^0$  was considered as ion pairing, shows regressed values for  $\text{CaCO}_3^0$  (green points) in agreement with the literature data (at least for  $T \geq 298.15 \text{ K}$ ). In fact in the OLI model, as well as in the literature (blue and orange points), the amount of bound carbonate was not considered as an input dataset (figure 3.1B) and the definition of species with a higher  $\text{CO}_3^{2-}/\text{Ca}^{2+}$  ratio cannot be computed. Both the preliminary and the complete thermodynamic-kinetic model are able to correctly estimate the amount of bound Ca but only the latter can cope with the amount of bound carbonate as well.

The species  $\{\text{CaCO}_3^0 \cdot \text{CO}_3^{2-}\}$  and  $\text{CaCO}_3^0$  might form clusters. From the speciation point of view, they represent bound calcium and carbonate ions which do not contribute to the saturation level, irrespectively of whether they are of monomeric or polymeric nature (*i.e.*, embryos or metastable particles according to the classical or non-classical nucleation theories, respectively). Such embryos could coalesce to larger entities of super-critical size, causing a homogeneous nucleation event via embryo-embryo interaction instead of gradual growth of the embryo by incorporation of molecular or ionic species [108–110] (also introduced in 2.3). In this paper the formation of critical nuclei by embryo-embryo coalescence is neglected. This simplification might be supported considering that such entities are plausibly carbonate-rich. Thus, they should have a relatively high negative charge, which could prevent their coalescence by electrostatic repulsion [60, 77, 111]. Moreover, specific experiments were carried out interrupting the  $\text{CaCl}_2$  addition into the system (appendix A, figure A.22) in order to maintain the supersaturation constant and monitoring the amount of  $\text{Ca}^{2+}$  in solution over time. In the case of random coalescence events among embryos, the precipitation should start anyway, revealed by a calcium ion signal decrease. Instead, the calcium concentration remains constant over time. If the  $\text{CaCl}_2$  addition restarts, the calcium concentration in solution increases again until a critical value where the precipitation occurs. Nevertheless, the embryo-embryo coalescence cannot be excluded *a priori* since the population of embryos and their size should increase with the supersaturation and a certain threshold might be required to promote embryo-embryo coalescence, but at the supersaturation level of this study, molecular dynamic simulation showed that these are expected to be rare events [60]. The mathematical expression for nucleation mediated by embryo-embryo coalescence is rather complicated to implement but it is currently the objective of a further study, in order to include these events into an even more general approach.



### 3.1. A Case Study: The Amorphous Calcium Carbonate (ACC) Precipitation Pathway Unravelled.

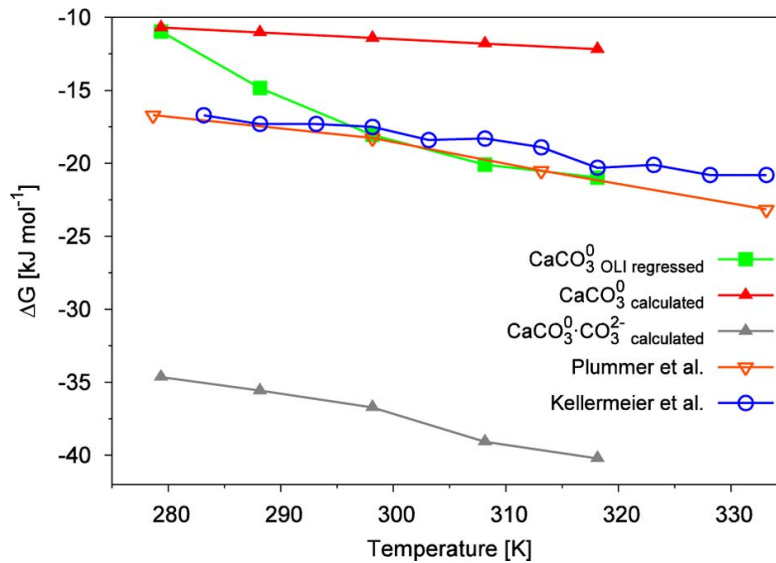


**Figure 3.2** – Calculated and literature [107, 110] values for the Gibbs free energy of formation (from aqueous calcium and carbonate ions) for the indicated chemical species against temperature. The green points represent the values regressed using the OLI software. The red and gray points represent the Gibbs free energy of formation for  $\text{CaCO}_3^0$  and  $\{\text{CaCO}_3^0 \cdot \text{CO}_3^{2-}\}$ , respectively, calculated using the complete model. The blue and orange points report the literature values. The plotted lines are guides for the eye.

The complex interaction  $\{\text{CaCO}_3(\text{s, am}) \cdot \text{CO}_3^{2-}\}$  (1.3.1.2) can be included to take discrepancies between calculated and experimental values in figure 3.1B into account, zone IV, *i.e.*, when ACC is present in suspension. This interaction computes the  $\text{CO}_3^{2-}/\text{Ca}^{2+}$  in the solid phase (as done for the previously discussed complex species) which was 1.08 at the end of the computational time. Table A.2 in appendix A summarizes the calculated  $\text{CO}_3^{2-}/\text{Ca}^{2+}$  values for all the datasets. At  $T \leq 298.15 \text{ K}$  and  $\text{pH} \leq 9.25$  the calculated  $\text{CO}_3^{2-}/\text{Ca}^{2+}$  is close to 1. For higher temperatures and higher  $\text{pH}$  the ratio was calculated to be progressively higher, up to 1.64. Moreover, figure A.19 shows an example of the behaviour of the  $\text{CO}_3^{2-}/\text{Ca}^{2+}$  in the solid phase as a consequence of the interaction of ACC with carbonate ions.

The ACC interaction with carbonate ions helps to understand some relevant points. For instance, in figure 3.3 the calculated value for  $K_{sp}$  is plotted against  $(\text{CO}_3^{2-}/\text{Ca}^{2+} - 1)$  for all the experiments. Because of such an interaction, the ACC solubility is shown to be  $\text{pH}$ -dependent. A similar trend is shown against temperature (figure 3.3B).

Here, a solubility decrease against temperature might be explained with the positive change of entropy of formation (table A.1). Nevertheless, because of the ACC interaction with carbonate ions, an influence on the Helmholtz free energy of formation

### 3. CaCs & CaPs studies

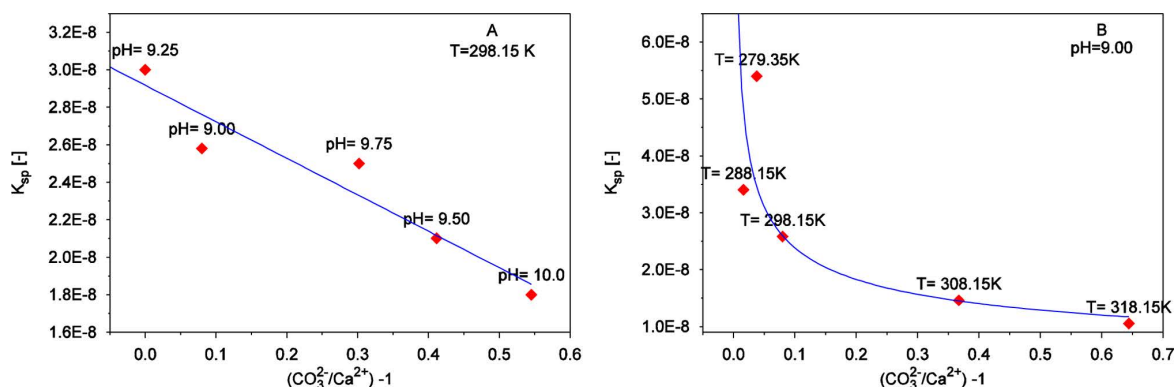


**Figure 3.3** –  $K_{sp}$  versus  $(\text{CO}_3^{2-}/\text{Ca}^{2+}) - 1$  in the solid phase (A) for  $T = 298.15 \text{ K}$  and different pH and (B) for  $\text{pH} = 9.00$  at different temperatures. The lines represent the fitting curves.

cannot be excluded.

Our findings – which are purely based on thermodynamic-kinetic modelling – are in agreement with the recent literature, where the existence of different ACCs, called proto-crystalline phases, is supported by spectroscopic studies [112, 113]. However, the estimation of  $\text{CO}_3^{2-}/\text{Ca}^{2+}$  in the solid phase was not reported. At this stage, we could speculate that ACC have different  $\text{CO}_3^{2-}/\text{Ca}^{2+}$  as a function of pH and temperature, and the solid phase eventually obtained by crystallization is a consequence of that ratio.

Figure 3.1D reports on the evolution of the calculated supersaturation: it rises up to a maximum value of about 3.6 in zone I; then it drops relatively quickly (20 min) to about 1.19 at the end of zone III; finally decreases slowly to about 1.09 at the end of the computational time (180 min) in zone IV. This residual supersaturation is due to the continuous addition of  $\text{Ca}^{2+}$  solution into the reactor (where carbonate and bicarbonate ions are still in large excess with respect to  $\text{Ca}^{2+}$ ) and the solid formation continues by particles growth (as discussed later). Thus, the assumption of  $S = 1$ , which is commonly applied to calculate the value of  $K_{sp}$  from the experimental data (e.g., from figure 3.1A, zone IV) as done in our preliminary thermodynamic calculation and in literature [107], might introduce an overestimation error of 10 % to 20 % on the solubility product. In this work the residual supersaturation was taken into account and the corrected  $K_{sp}$  values as a function of temperature are reported in figure 3.4. The equivalent plot against pH is reported in figure A.20. The calculated ionic strength (IS) (eq. (2.14), 2.1.1) is changing with time constantly with the progress of the reaction: it rises in zone I because of the amount of  $\text{CaCl}_2$  and  $\text{NaOH}$  solution added; it reaches a maximum value in zone II and it rapidly decreases in zone III due to the

### 3.1. A Case Study: The Amorphous Calcium Carbonate (ACC) Precipitation Pathway Unravelled.

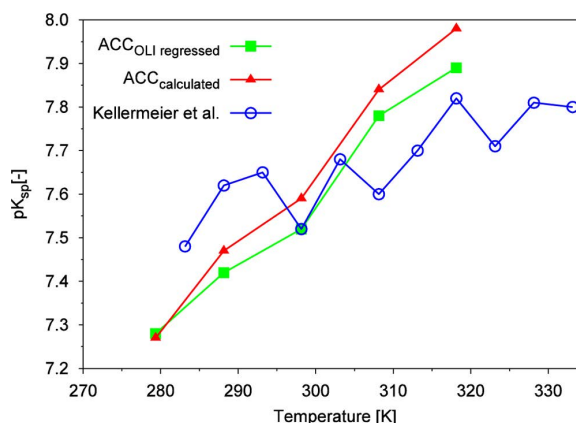


**Figure 3.4** – Solubility product (plotted as  $pK_{sp}$ ) of ACC against temperature at  $pH=9.00$ . Blue points: Literature values [107]. Green points: Preliminary calculation performed with OLI [9] software. Red points: Data calculated using the complete thermodynamic-kinetic model. The plotted lines are guides for the eye.

precipitation, followed by a slower decrease in zone IV due to the incorporation of ions into the growing solid phase (figure A.5). The ionic strength is rather low ( $\approx 0.01$ ) and its variation is rather limited ( $\pm 10\%$ ); as a consequence the activity coefficients (eq. (2.13), 2.1.1) are almost constant in the full experimental range (about 0.89 to 0.90 and 0.65 to 0.67 for mono-charged and bi-charged species, respectively). As a self-consistency test, the total solution volume and the overall amount of Ca (CaT) in the reactor were calculated (figure A.5). Moreover, figure A.5 shows the calculated amount of  $Na^+$  and  $OH^-$  added into the reactor, which are independently calculated from equation eq. (1.48), and eq. (1.41) (1.3.1.2), respectively. The two curves slightly diverge because of the carbonatation of the NaOH solution, which is experimentally determined (1.2).

Figure 3.5 shows the calculated kinetic data on particle evolution. In figure 3.5A, the primary (green curve) and secondary (blue curve) nucleation rates are shown in the time frame where these events occur, namely between 65 min to 73 min; the value of supersaturation is reported (red curve) as well. It can be argued that more than 90 % of the nucleation events (both homogeneous and secondary) occur at  $3.5 < S < 3.7$ , that is, at almost constant  $S$ . As a consequence, the equations describing the nucleation rate according to the classical nucleation theory are justified as the dependency of the surface energy on nuclei size (*i.e.*, saturation level) can be neglected. In figure 3.5B, C, and D, the growth rate, average (number) primary particle size, and number of particles, respectively, are plotted (on the same time scale starting from  $t = 60$  min). Moreover, the aforementioned slight discrepancy between the experimental and cal-

### 3. CaCs & CaPs studies

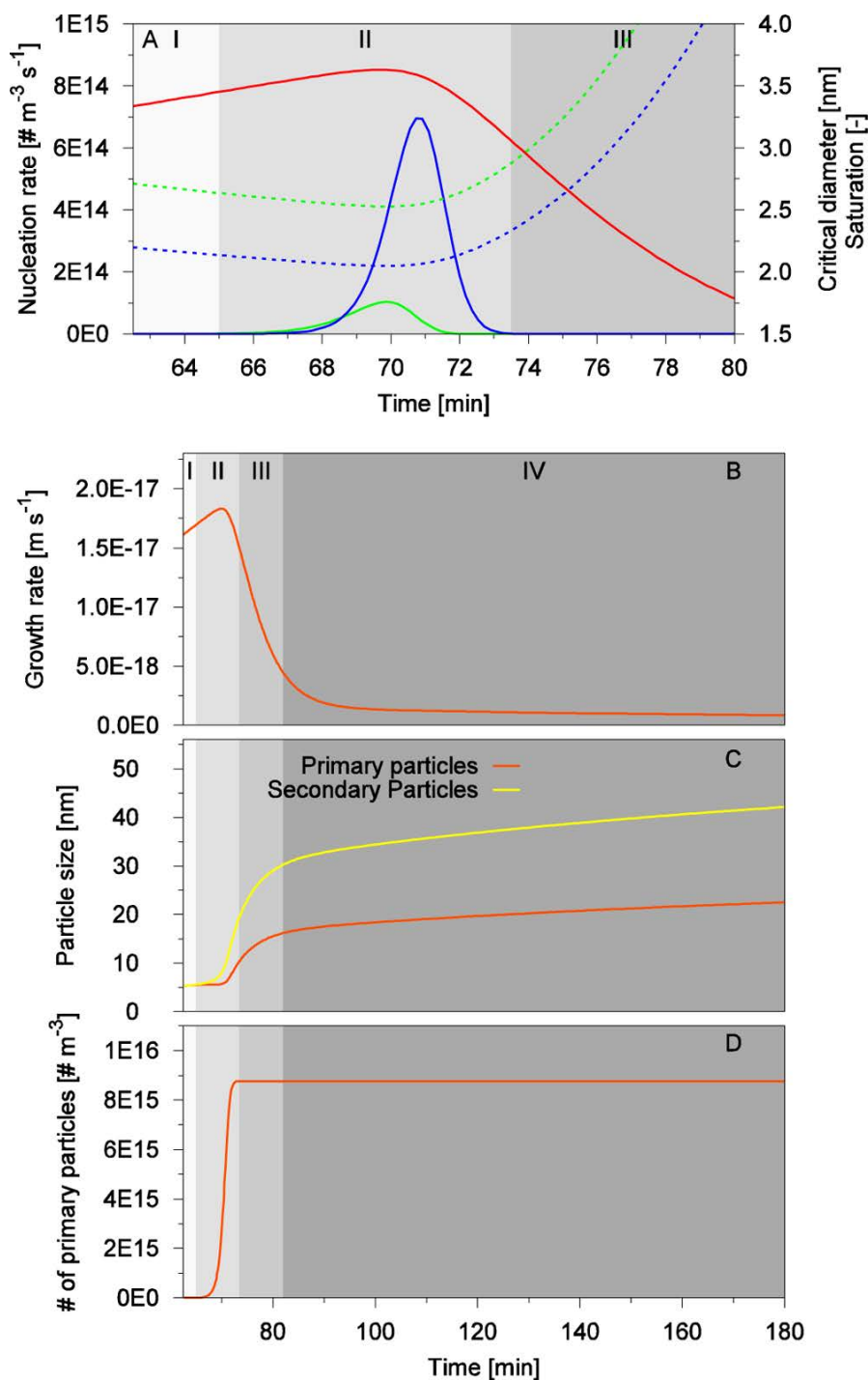


**Figure 3.5** – Calculated kinetic data on particle evolution. (A) Primary (green) and secondary (blue) nucleation rates, saturation (red), and critical nucleation size for primary homogeneous (dashed green) and “true” secondary nucleation (dashed blue) against time; (B) linear growth rate; (C) averaged primary (orange) and secondary (yellow) particles size, calculated as described in the text; and (D) number of primary particles.

### 3.1. A Case Study: The Amorphous Calcium Carbonate (ACC) Precipitation Pathway Unravelled.

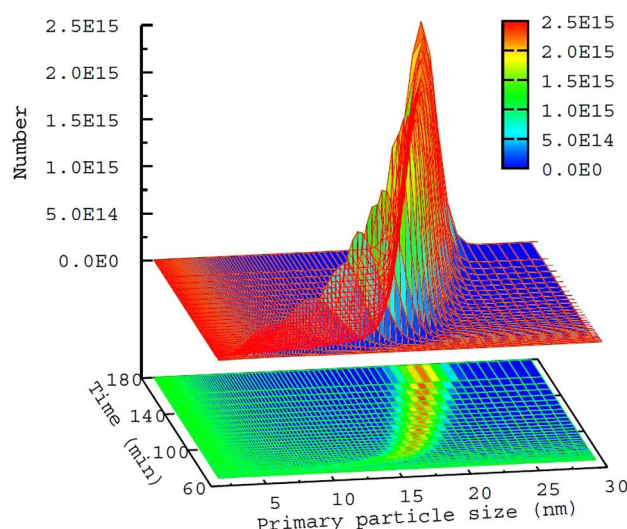


**Figure 3.6** – Primary particles size distribution against time. Nucleation starts at about  $t = 68$  min and the primary particles grow during the entire experimental time according to a log-normal distribution. The surface plot (top) is also represented as 2D map at the bottom.

culated data at the end of zone III (figure 3.1A) could be explained as a transient lower ACC. Moreover, figure 3.6 shows the detailed primary particle size distribution against time. From figure 3.5, the split of the overall precipitation in zones can be clearly argued. In Zone I (figure 3.5A), before primary nucleation, no particles are present in the system. As previously discussed, this zone is dominated by ionic and molecular species and embryos. Zone II identifies the timeframe where nucleation occurs. At  $S \approx 3.5$  primary nucleation starts and the maximum nucleation rate is attained for the maximum  $S$  value ( $S \approx 3.7$ ). The primary nucleation starts before the maximum in  $S$  and before the calcium ion (figure 3.1A) or dosed NaOH (figure 3.1D) signals are affected by the solid formation. In figure 3.5A the critical size for nucleation is also reported, which corresponds to about 2.6 nm for primary nucleation.

In literature it is reported that an embryo should be composed of 22 formula units and a volume of  $6.5 \text{ nm}^3$  which corresponds to a cluster density of about  $1350 \text{ kg m}^{-3}$ , a water-to- $\text{CaCO}_3$  molar ratio of about 4.3 and a diameter of about 2.3 nm [60]. This value is coherent with the calculated critical size (figure 3.5A). Moreover, if all  $\{\text{CaCO}_3^0 \cdot \text{CO}_3^{2-}\}$  and  $\text{CaCO}_3^0$  species are in form of clusters, it is possible to estimate the cluster concentration and the average cluster-cluster distance (figure A.21). The maximum cluster concentration ( $\approx 2.5 \times 10^{18} \text{ m}^{-3}$ ) corresponds to the maximum supersaturation. The average cluster-cluster distance would be about 100 nm during most of the precipitation, depicting a situation coherent with molecular dynamic

### 3. CaCs & CaPs studies

simulations for low supersaturation levels [60]. At  $t = 68$  min, primary particles, even if in limited number (figure 3.5D), can grow with a certain speed (figure 3.5B) and the overall solid surface increases (figure A.23E). Secondary nucleation is then possible (figure 3.5A, zone II) and occurs at relatively high speed with respect to the primary nucleation, since a lower energy barrier has to be overcome; the maximum rate of secondary nucleation is about 6.5-folds that of the primary ones. The calculated critical size resulted to be about 2 nm (figure 3.5A), *i.e.*, smaller than the primary nucleation because of the cohesion energy contribution (as discussed in section 2.2, figure 2.3). At  $t = 71$  min primary nucleation is almost concluded whereas secondary nucleation is still close to the maximum. At  $t = 74$  min, when  $S$  is about 3.2, secondary nucleation becomes negligible as well. The overall number of particles attain a constant value (figure 3.5D) and primary particles grow (figure 3.5C) relatively fast in the whole zone III, from the initial size of about 5 nm to about 15 nm. Finally, in zone IV, the primary particles grow at  $S \approx 1.09$  (figure 3.1D), where their size attains the final size of about 21 nm (figure 3.5C). Thus, zones III and IV identify two different growth regimes: zone III is diffusion limited while in zone IV it is limited by the amount of Ca added into the system. The calculated ACC surface energy (or ACC/water interfacial energy,  $\Gamma$ ) against  $pH$  and temperature is reported in figure 3.7. The cohesion energy ( $\beta$ ), which defines the secondary nucleation rate (eq. (1.54), 1.3.1.2), is reported as well. At  $T = 298.15$  K on average they correspond to  $32.5 \text{ mJ m}^{-2}$  ( $\pm 5 \%$ ) and  $37 \text{ mJ m}^{-2}$  ( $\pm 5 \%$ ), respectively. The estimated surface energy is in agreement with the value reported for low concentration precipitation experiments [114]. However, in the literature very a broad range for surface energy is reported (ranging from about  $20 \text{ mJ m}^{-2}$  to  $280 \text{ mJ m}^{-2}$ ) which is strongly dependent on the experimental conditions [114, 115]. It is worth mentioning that the calculated  $\Gamma$  values reported here were calculated from the nucleation rate, thus they refer to ACC particles of about 2 nm (figure 3.5A) and not to the bulk value.

A clearer trend can be estimated from values of  $\Gamma$  and  $\beta$  against temperature, where both quantities increase with  $T$ . Higher values of  $\Gamma$  can be again associated with lower solubility against temperature (figure 3.3) [115], supporting the fact that the ACC thermodynamic properties might be influenced by the  $\text{CO}_3^{2-}/\text{Ca}^{2+}$  ratio. The estimated cohesion energy value (which can vary between 0 and  $2\Gamma$ , section 1.3.1.3) is close to the  $\Gamma$  value and indicates a relatively high energy gain for true secondary nucleation events. However, texturing or any kind of oriented attachment events are not possible, being the solid phase of amorphous nature. The particle size reported in figure 3.5C refers to the averaged primary particle size. As extensively discussed in section 2.2.1,

### 3.1. A Case Study: The Amorphous Calcium Carbonate (ACC) Precipitation Pathway Unravelled.

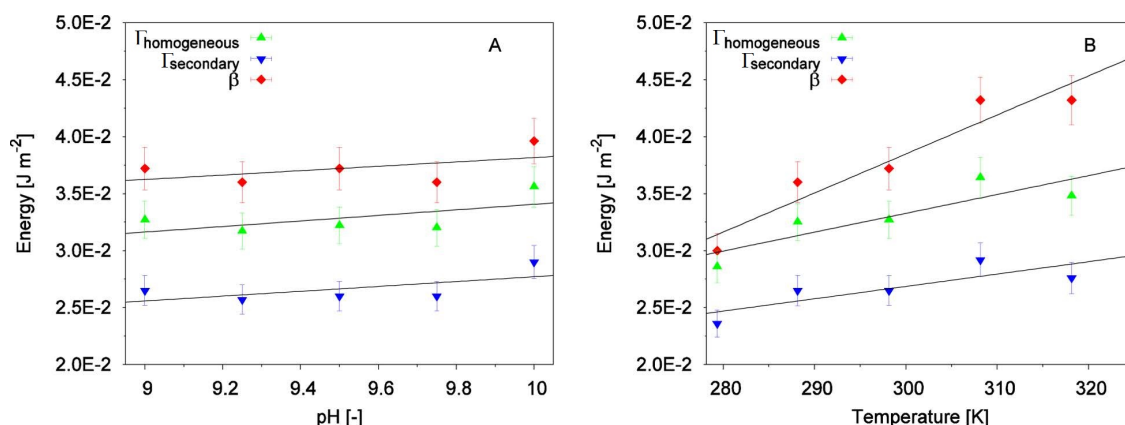


**Figure 3.7** – ACC surface energy ( $\Gamma_{\text{homo}}$ , green points), cohesion energy ( $\beta$ , red points), and the derived (eq. (1.54), 1.3.1.2) surface energy for secondary nucleation ( $\Gamma_{\text{sec}}$ , blue points) (A) against pH at  $T=298.15$  K and (B) against temperature at  $pH=9.00$ . The continuous lines represent the best linear fit among the experimental values. The vertical bars represent the estimated error.

primary particles are those produced by nucleation and growth events. Secondary nucleation events occur on the surface of a primary particle, produced by primary nucleation (figure 3.8). The obtained secondary particle is composed of two kinds of primary particles: the first kind produced by primary nucleation and the second kind produced by secondary nucleation. If several secondary nucleation events occur, each secondary particle will be composed of several primary particles; among them, by definition, only one had been produced by primary nucleation. Thus, considering that the overall amount of primary particles produced by primary nucleation is about  $1.5 \times 10^{15} \text{ m}^{-3}$  (which can be calculated from the integral of the green curve in figure 3.5A) and the overall amount of primary particles produced by secondary nucleation is about  $9.8 \times 10^{15} \text{ m}^{-3}$  (which can be calculated from the integral of the blue curve in figure 3.5A) and considering that each secondary particle is generated by one primary particle produced by primary nucleation, each secondary particle is in average composed of 7.5 primary particles (figure 3.8). Therefore, assuming that secondary particles are spherical with a volume equivalent to 7.5 primary particles, at the final computational time ( $t=180$  min) the averaged secondary particles size is about 42 nm (figure 3.5C). This hypothesis may be justified considering that the solid phase has an amorphous nature and the secondary particles might minimize the liquid-solid interface, assuming a quasi-spherical shape. The calculated results on the produced secondary particles size might be compared with data available in literature. For instance, Pouget *et al.* reported that under similar experimental conditions, the ACC particle size, before phase transformation towards more stable crystalline phases,



### 3. CaCs & CaPs studies

---

is in the range of 20 nm to 70 nm [27]. Figure A.24 in appendix A reports the calculated averaged secondary particle size as a function of  $pH$  and temperature: smaller secondary particles are obtained increasing either  $pH$  or temperature.

The agreement between the experimental data and the calculated values is shown in figure 3.1A, B as well as for all the experimental datasets (A.1). This agreement with literature data obtained by experiments and our simulations strongly suggests that the discussed model is able to describe the details of the precipitation pathway. It is worth emphasizing that the growth model – zones II, III, and IV – considers diffusion coefficients which are those typical for ionic species in diluted solution. Therefore, in our experimental conditions, the growth building units are of the size of ions and not clusters of much larger size and therefore with a much smaller diffusion coefficient. These facts strongly support that the precipitation mechanism can be represented as a particle based mechanism but the secondary particles are generated as a consequence of secondary nucleation events and the growth of primary particles is dominated by diffusion of ionic species (calcium and carbonate ions) and not by incorporation of larger entities. Clusters or pre-nucleation particles might be present in suspension over the complete precipitation process but they are spectator entities and not directly involved in the solid formation. Thus, the classical nucleation theory and the classical precipitation pathway are obeyed. Here the aggregation process, which occurs as a consequence of collisions among secondary particles, is not considered. In fact, aggregation is a process that has no influence on the chemical speciation and cannot be evaluated if the data analysis is limited to the “liquid side” of the precipitation process. Thus, to be able to evaluate the occurrence of aggregation, experimental data on the evolution of the solid phase, *i.e.*, the particle size distribution, needs to be collected. Assuming that reliable experimental data on the particle size distribution of ACC over time could be collected, the associated mathematical problem would be more complicated since a bivariate population balance approach would be needed because two internal coordinates would be necessary: one for primary the particles and one for the secondary particles. Nowadays, such an approach was developed only for the quadrature method of moments (QMOM) [116, 117].

#### 3.1.5 Conclusion

Nine experimental datasets on ACC precipitation were collected following a rigorous experimental protocol, with state-of-the-art equipment and an accurate and reproducible procedure, at  $T = 298.15$  K and a  $pH$  from 9.00 to 10.00 and at  $pH = 9.00$  in the



### 3.1. A Case Study: The Amorphous Calcium Carbonate (ACC) Precipitation Pathway Unravelled.

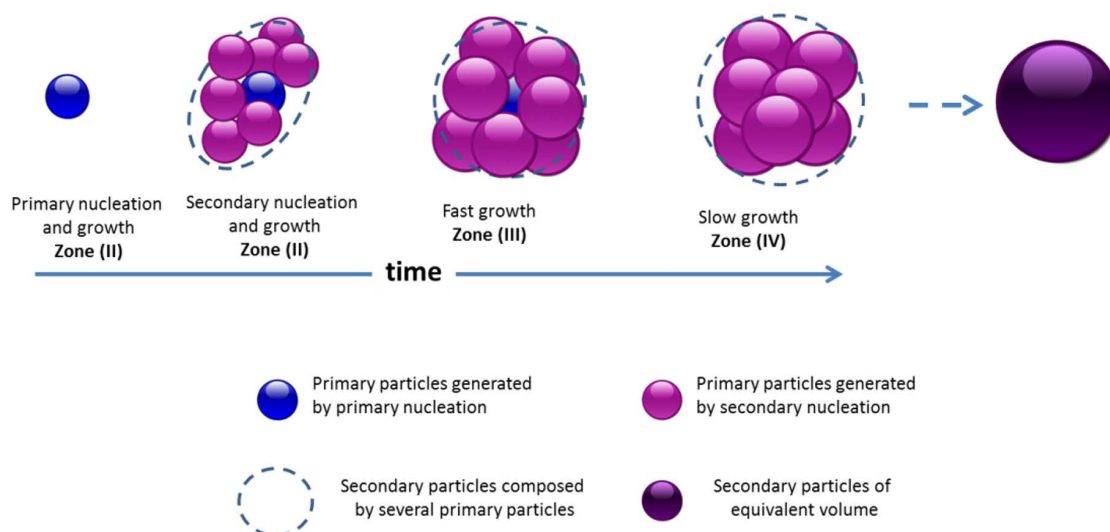


**Figure 3.8** – Schematization of the precipitation pathway. In zone II, primary and secondary nucleation events occur in combination with growth. Because of secondary nucleation events, secondary particles are formed (dashed lines). In zone III, nucleation events are no longer possible and primary particles rapidly grow by incorporation of calcium and carbonate ions. In zone IV, a slow growth process governs the solid formation as a consequence of the continuous feeding of the system with calcium ions. The secondary violet particle has a volume equivalent to the sum of the volumes of the primary particles of which it is composed.

### 3. CaCs & CaPs studies

---

temperature range between 279.35 K to 318.15 K.

A comprehensive model for ACC formation was developed. The model embraces a comprehensive thermodynamic – kinetic code developed in FORTRAN. The thermodynamic code is able to solve the chemical speciation, as well as the calculation of some fundamental quantities for the kinetic code, such as the supersaturation and ionic strength. It is based on a set of non-linear equations which are describing the mass, molar and charge balances among the considered chemical species. In addition to the most relevant chemical species, two complex species were considered, namely  $\{\text{CaCO}_3^0 \cdot \text{CO}_3^{2-}\}$  and  $\{\text{CaCO}_{3(s, am)} \cdot \text{CO}_3^{2-}\}$ , which are a simplified representation of the interaction between the ion pair and ACC with carbonate ions, respectively. They were implemented into the model to take into account the amount of bound carbonate ions, which is correlated to the amount of NaOH added into the system and to compute the value of for the ion pair and in the solid phase. The kinetic code is based on the discretized population balance approach which is mathematically described by a system of ordinary differential equations. The equations for the classical nucleation theory, as described by Nielsen, were implemented. A diffusion controlled growth mechanism was considered and an algorithm able to correctly compute the first four moments of the particle size distribution was used. The computed amount of solid is used to solve the mass balance equations of the thermodynamic code until self-consistency is reached at every time step.

As a result, for the first time the complete description of the precipitation pathway was obtained by the regression of just a few quantities with a well-defined physico-chemical meaning, such as the ACC surface and cohesion energies, the ACC solubility product, and the formation constants for  $\text{CaCO}_3^0$  and for the two complex species considered. Moreover, the ACC's primary particle size distribution, the average secondary particle size, the primary and secondary nucleation rate and the linear growth rate were calculated over time, temperature, and pH. The same model was applied to the nine experimental datasets and the values of the aforementioned quantities were estimated over the whole experimental range. The calculated ACC's secondary particle size and solubility are in excellent agreement with the most recent estimation in the literature. In addition, most of the other calculated thermodynamic and kinetic quantities are not reported in the literature.

The agreement between the calculated results with the experimental data as well as with the literature values show that the precipitation pathway can be described by a combination of primary nucleation, secondary nucleation and diffusion controlled growth, according to the classical nucleation theory and a classical precipitation path-

### 3.1. A Case Study: The Amorphous Calcium Carbonate (ACC) Precipitation Pathway Unravelled.

way. The use of equations derived from the classical nucleation theory was justified because the nucleation events occur in a limited timeframe at almost constant supersaturation and the dependency of surface energy upon the critical size can be neglected. Secondary particles were formed as a consequence of secondary nucleation events and all primary particles (both those generated by primary and those generated by secondary nucleation events) grow incorporating  $\text{Ca}^{2+}$  and  $\text{CO}_3^{2-}$  ions. In fact, in the growth algorithm the quantities which are controlling the growth rate are the diffusion coefficients of the building or growth units. In the model, a diffusion coefficient typical for ionic species in diluted aqueous solution are considered and the results were fully consistent with the experimental values. On the other hand, in the case where clusters are considered as building unit of the solid formation, a relatively low diffusion coefficient (at least 1 or 2 orders of magnitude smaller) should be considered in the growth algorithm, which was not consistent with the experimental results. We demonstrate that the deconvolution of the whole precipitation pathway into the elementary processes by means of the thermodynamic-kinetic modelling, allows the evaluation of the building unit diffusion coefficient, which discloses the classical precipitation pathway. In a more extended view, ACC is indeed formed by “particle incorporation” but these events have to be more properly identified with the elementary process “secondary nucleation”. After primary nucleation and growth events, which generate particles of about 5 nm, secondary nucleation occurs and secondary nuclei are stabilized on the surface of the growing solid phase. Primary particles grow up to tens of nanometers, firstly rather rapid and then slowly at almost constant supersaturation during the extended period of continuous feeding of the system with  $\text{CaCl}_2$  into the carbonate rich suspension. The presence in suspension of the complex species  $\{\text{CaCO}_3^0 \cdot \text{CO}_3^{2-}\}$  is supported by the experiments and it represents a chemical species with a  $\text{CO}_3^{2-}/\text{Ca}^{2+}$  close to 2, in agreement with the most recent molecular dynamic simulations; plausibly, the complex species  $\{\text{CaCO}_3^0 \cdot \text{CO}_3^{2-}\}$  might be responsible for embryos or pre-nucleation cluster formation. Nevertheless, this entity seems not to be directly involved in the precipitation pathway as a building unit for the ACC formation.

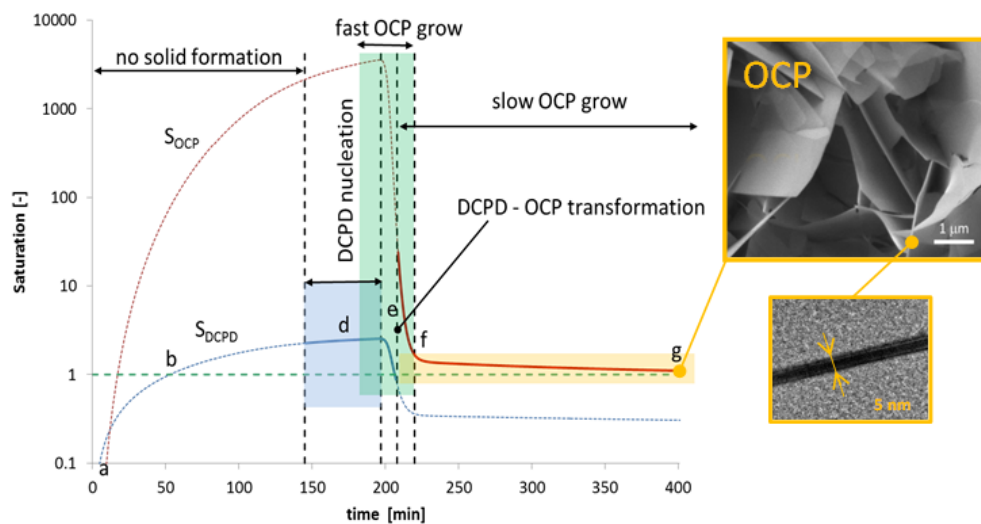
A thermodynamic-kinetic model, able to describe the details of the whole precipitation pathway and to estimate the physicochemical quantities that are governing each elementary process, is a fundamental approach to define a plausible precipitation pathway. The described model can be readily applied to other systems. Additional experimental data on the formed solid phase may further support the modelling results presented here. Nevertheless, data collection should be carried out with *in-*

### 3. CaCs & CaPs studies

---

*situ* time-resolved techniques, without system perturbation, and able to selectively evaluate at least the average particle size of the ACC phase, *e.g.*, by synchrotron based experiments. To the best of our knowledge, such experimental data are not available yet and are an objective of our current research.

## 3.2 Formation and Transformation of Calcium Phosphate Phases under Biologically Relevant Conditions: Experiments and Modelling



Author's contribution to this publication:

- i. experimental data collection;
- ii. data analysis;
- iii. thermodynamic model;
- iv. model refinement.

This chapter is adapted from **A. Carino** *et al.*, Formation and Transformation of Calcium Phosphate Phases under Biologically Relevant Conditions: Experiments and Modelling. Accepted by Acta Biomaterialia, [118].

### 3. CaCs & CaPs studies

---

#### 3.2.1 Abstract

The experimental data on calcium phosphates formation were collected in dilute solution at constant  $pH$  (7.40) and temperature (37.0 °C) at different levels of ionic strength (IS). The evolution of the solid phase formation is described in detail using a thermodynamic-kinetic model. The thermodynamic model takes into account all relevant chemical species as well as Posner's clusters; the kinetic model, based on the discretized population balance approach, accounts for the solid formation of solution. The experimental data are consistent with an initial formation of dicalcium phosphate dihydrate (DCPD, brushite), which dominates the nucleation rate, and its rapid transformation into octacalcium phosphate (OCP) or hydroxyapatite (HA), which dominates the growth rate. Depending on the experimental conditions and, including the influence of the IS level, OCP may be further transformed into apatite. The classical nucleation theory is able to describe the experimental results very well, and the solid phase growth is limited by the diffusion of  $Ca^{2+}$  ions. The precipitation pathway described by a complete thermodynamic-kinetic model is expected to contribute to the understating of the *in vivo* osteogenesis.

#### 3.2.2 Introduction

Calcium phosphates are largely studied in many fields, such as chemistry, material science, and geology, as well as in biomedical applications, in which they are used to coat metallic implants [119] and as biocements [120]. Calcium phosphates include a large group of biomaterials [121]. Among them, the apatite,  $Ca_{10}(PO_4)_6X_2$ , where X corresponds to  $OH^-$  in hydroxyapatite (HA), and those related to apatite-like structures, such as the octacalcium phosphate,  $Ca_8(HPO_4)_2(PO_4)_4 \cdot 5 H_2O$  (OCP), are the most relevant in natural bone formation. Nowadays, OCP is considered the *in vivo* precursor of the thermodynamically stable calcium phosphate form, HA, which is the main mineral constituent of bone and teeth. The role of OCP in the osteogenesis was the object of debate since Brown *et al.* [40–43] suggested that this mineral is the intermediary phase in the biological calcification process, being present as a transient phase in hard tissues. The authors identified several lines of evidence to support their conclusions. One of the most relevant observations was related to the peculiar platy shape morphology of OCP, which is conserved after *in vitro* hydrolysis to HA crystals whereas needle-like morphology would be expected if HA had precipitated directly from solution [122]. OCP surrounded by HA was detected by HRTEM (High-

### 3.2. Formation and Transformation of Calcium Phosphate Phases under Biologically Relevant Conditions: Experiments and Modelling

Resolution Transmission Electron Microscopy) in the dentin of aborted fetuses [123] and the hypothesis that OCP is the crystalline phase occurring in young bones got more and more support. *In vivo* experiments have shown that OCP is rapidly converted to HA, *i.e.*, within 7 to 10 days after implantation and, interestingly, the rate of new bone formation on apatite converted from OCP was faster than that on both calcium-deficient HA and stoichiometric HA implanted directly [124–126]. The effect of calcium phosphates on the osteoblastic activity and bone regeneration, with particular emphasis on OCP activity, has been recently reviewed [127] concluding that, *in vivo*, OCP seems more bioactive than other calcium phosphate phases.

The synthesis of OCP in solution and its bioactivity is relatively well reported in the literature [127]. According to the opinion of present authors, the most relevant studies on OCP and HA were carried out by Nancollas *et al.* [8, 23] and by Iijima *et al.* [128]; in these studies, the constant composition approach was applied. Such a method is particularly suitable to study the details of the precipitation pathway.

The formation mechanism of calcium phosphate - and, in general, that of all sparsely soluble inorganic salts - is also a matter of debate. In the particular case of calcium phosphate, the presence of nanometric size clusters (Posner's clusters [49]), and their involvement in the solid formation mechanism has been suggested [76, 129–132]. Posner's clusters were experimentally detected by cryo-HRTEM [79] (cryogenic-HRTEM) and AFM [50] (Atomic Force Microscopy) and their involvement in the solid growth process was proposed, paving the way to the so-called non-classical precipitation theory [4], in which nanometer-size building blocks are considered as the growth unit of the solid. A similar debate is currently ongoing on  $\text{CaCO}_3$  whereas the most recent literature is in favour of the classical view, in which the solid grows by incorporation of ions, while larger clusters act as spectator species [97, 133].

Despite a considerable number of papers on calcium phosphate precipitation, to the best of our knowledge, a complete mathematical description based on a thermodynamic-kinetic model, which is able to simultaneously solve the chemical speciation and the details of the nucleation and growth pathway, is still missing [134]. In a comprehensive paper [51], Wang L. and Nancollas G.H. highlighted some open key questions about the formation mechanism of calcium phosphates. In particular, they focused their studies on the driving force for the solid formation, stating, "*Nucleation and growth may follow different mechanisms across the continuum of driving force*". In this paper, we address some of the aforementioned open questions, shedding some light on the precipitation mechanism. Here, the applied approach is similar to that followed in the study of the amorphous calcium carbonate (ACC) precipitation pathway [97], and

### 3. CaCs & CaPs studies

---

we demonstrate that, in our experimental conditions, the experimental data are fully consistent with a classical precipitation pathway. The mechanism involves the initial formation of a solid phase with  $\text{Ca/P} = 1$  and its rapid transformation into OCP or HA. Such a pathway was already postulated by Francis and Webb [53]. In this paper, we present the detailed mathematical description. Moreover, the solid formation driving force changes during the precipitation pathway in a rather complex manner. The described mechanism may be replicated, under similar physicochemical conditions, in biological systems during osteogenesis or pathological mineralization and can contribute to the understanding of biomineralization-biodesmineralization processes. Furthermore, the knowledge of the solid formation driving force will allow the *in vitro* controlled deposition of calcium phosphate bioceramics on implants and prostheses.

#### 3.2.3 Material, methods, and model

The precipitation reaction was studied using a controlled composition approach and potentiometric titration method [97]. Specifically, the system saturation level was slowly increased by means of  $\text{CaCl}_2$  addition ( $30 \mu\text{L min}^{-1}$ ) in a  $\text{Na}_2\text{HPO}_4/\text{NaH}_2\text{PO}_4$  solution. Experimental data were collected at a fixed temperature, initial concentration of phosphate buffer, and  $\text{pH}$  ( $T = 37.0^\circ\text{C} \pm 0.2^\circ\text{C}$ , total  $\text{P} = 10.0 \text{ mmol kg}^{-1}$ ,  $\text{pH} = 7.40 \pm 0.03$ ). The  $\text{pH}$  was monitored and adjusted at the pre-set value via counter-titration with  $\text{NaOH}$  or  $\text{HCl}$  solutions. The precipitation was studied at different ionic strength (IS), which is controlled by the addition of  $\text{NaCl}$  in the precursor solutions. The first series of experiments were carried out at low IS (0.024 to 0.017, *i.e.*, without the addition of  $\text{NaCl}$  into the initial solutions). The second series at high IS (0.149 to 0.088, *i.e.*, adding  $\text{NaCl}$  into the phosphate buffer only). The third series at constant IS (0.154, *i.e.*, adding  $\text{NaCl}$  in every solution used during the precipitation). In the first and second series, hereafter called L-IS and H-IS, during the precipitation the IS strength drifted, mainly because of the dilution due to the addition of  $\text{CaCl}_2$  and  $\text{NaOH}$  solutions; in the third series, hereafter named C-IS, the IS was maintained at a constant level, *i.e.*, the physiologically relevant conditions. Each series consists of at least 3 repetitions. The precipitated solids were separated from the solution by centrifugation and thus, washed in milliQ water, acetone and stored dry. For morphological studies, the solid was re-dispersed in isopropanol. Additional details on the experimental protocol are reported in section 1.2.

The mathematical model is developed in FORTRAN, and it is composed of two main



### 3.2. Formation and Transformation of Calcium Phosphate Phases under Biologically Relevant Conditions: Experiments and Modelling

packages: the thermodynamic speciation solver and the solid kinetic solver. Both packages are cyclically called until self-consistency at every time step is reached [10, 97].

The thermodynamic model is based on the chemical equations reported in section 1.3.2.1. In particular, 22 chemical species are considered: 19 aqueous species and three solid phases namely dicalcium phosphate dihydrate (DCPD), OCP and HA. Additional to the system of 14 equations associated with the chemical equations reported in section 1.3.2.1, two mass balance equations for total Ca and total P are included. Thus, the problem can be solved if six quantities are known, namely the  $pH$  value, total Ca, total P, and the quantities of the three solid phases. The amounts of solid phases are computed by the kinetic solver whereas the other three quantities are given. The system of 16 equations is analytically reduced to 2 equations only, which are efficiently numerically solved at every call of the speciation package (1.3.2, eqs. (1.78)-(1.79)).

The kinetic package includes the equations for primary nucleation, secondary nucleation and diffusion limited growth. The evolution of the solid particles is computed by means of a discretised population balance approach, where the continuum of size is divided into classes. Each class is associated with a differential equation, and the system of ordinary differential equations is solved at every time step. The details of the population balance approach are described elsewhere [10]. At this level, the kinetic solver is used to compute the amount of solid phase formed, where the particles are considered as spheres. Since the experimental evidence shows that particles are not equiaxed, no information on particle size distribution can be argued, unless a defined particle thickness is set. This limitation is due to the applied population balance approach being monovariate. Thus only one internal parameter (*i.e.*, the particle equivalent diameter) can be considered. Within this constraint, the applied approach is able to correctly calculate at least the first four moments of the particles population [10]. The implication of the assumed particle shape is discussed later.

Because of the addition of  $\text{CaCl}_2$  into the reactor, both the activity of  $\text{Ca}_{(\text{aq})}^{2+}$  and  $pH$  change. In order to attain iso- $pH$  conditions, a diluted  $\text{NaOH}$  solution was added into the reactor. Thus, two independent datasets were collected against time: (i) the activity of  $\text{Ca}_{(\text{aq})}^{2+}$  and (ii) the amount of  $\text{NaOH}$  added into the reactor. It is worth mentioning that the needed amount of  $\text{NaOH}$  is due to the formation of calcium-phosphate species such as  $\text{CaPO}_4^-(\text{aq})$ ,  $\text{CaHPO}_4^0(\text{aq})$ ,  $\text{CaH}_2\text{PO}_4^+(\text{aq})$ , Posner's clusters, and

### 3. CaCs & CaPs studies

---

the solid phases DCPD, OCP, and HA. The amount of NaOH added can be analytically calculated, provided that the formation constants of the aforementioned species are known. Among them, only the formation constant of Posner's clusters is unknown and can be regressed from the experimental data. The considered parameters in the model are the surface energy for primary and secondary nucleation, the stoichiometry and formation constant for the Posner's clusters, the stoichiometry of the solid phases formed and their solubility, the transformation rate from OCP to HA, and the diffusion coefficient of the chemical species involved in the molecular growth. At every set of parameters, the calculated evolution of  $\text{Ca}_{(\text{aq})}^{2+}$  activity and the amount of NaOH added into the reactor against time are compared with the respective experimental curves. The model is considered appropriate when the calculated curves are able to correctly describe the experimental data in the full timeframe and either the regressed parameters are consistent with the literature values (if available), or they correspond to reasonable values.

The collected powders were fully characterised. The chemical analyses were performed by ICP- MS (Agilent 7700x) (Inductively Coupled Plasma Mass Spectrometry), after digestion of the samples and dilution in Milli-Q water, and using external standard calibration.

Synchrotron X-ray Powder Diffraction (SXRPD) patterns were collected at the X04SA-Materials Science beamline, Swiss Light Source (SLS), Paul Scherrer Institut (PSI). The X-ray beam energy was set to 22 keV, and the powders were confined in 0.1 mm rotating glass capillaries in Debye-Scherrer geometry.

Morphology and composition of the samples were analyzed by a scanning electron microscopy (Zeiss NVision40,) equipped with energy-dispersive spectroscopy (EDX, Oxford). High-resolution electron microscopy (TEM) and high-angle annular dark field (HAADF) scanning transmission electron microscopy (STEM) images were acquired with a Talos F200X (FEI) microscope being operated at an acceleration voltage of 200 kV. The powders for SEM and STEM characterization were dispersed in isopropanol and then deposited onto carbon-coated or holey carbon-coated copper grids, allowing the solvent to evaporate in air.

The infrared spectra were collected in the ATR-IR mode using a Vertex 80V spectrometer (Bruker) equipped with a Platinum ATR unit by accumulating 100 interferograms at  $4\text{ cm}^{-1}$  resolution.

The Raman spectra were acquired on dried powder samples using a Raman spectrometer (RamanRXN1 Analyzer supplied with Invictus<sup>TM</sup> 785-nm laser; Kaiser Optical

### 3.2. Formation and Transformation of Calcium Phosphate Phases under Biologically Relevant Conditions: Experiments and Modelling

Systems) equipped with a CCD camera (1024x256 EEC MPP Type, Kaiser Optical Systems) with collimated incident radiation and a probe size of 2 mm. Spectra were collected at ambient conditions by averaging 300 scans with 2 s time exposure at  $2\text{ cm}^{-1}$  spectral resolution and at an average power of 300 mW.

#### 3.2.4 Results

Figure 3.9 shows the experimental, and the calculated results for the  $\text{Ca}^{2+}$  activity (A, C) and the amount of NaOH (B, D) added into the system for the series H-IS and L-IS. The results obtained for H-IS are almost identical to those for C-IS (appendix B.3). The experimental data collected for the series H-IS and C-IS showed a high reproducibility, whereas the experimental data for the series L-IS were much more scattered and several repetitions were required in order to identify an appropriate variability range. The experimental and calculated curves are reported as black and coloured lines, respectively. In all figures, zero on the time axis corresponds to the addition start of calcium chloride solution into the reactor. The activity of  $\text{Ca}^{2+}$  in solution rises almost linearly and proportionally to  $\text{CaCl}_2$  added into the system ( $\text{Ca}_T$ , 1.3.2.1, addition rate of  $30\text{ }\mu\text{L}$ ) up to a maximum; it decreases down to a minimum following an (inversed) sigmoidal shaped curve, and finally, an almost constant value is reached. The slightly positive slope at the plateau is due to the depletion of  $\text{PO}_4^{3-}$  ions from solution and the speciation equilibrium with the formed solid. In parallel, NaOH is added into the system, and a three-linear-segments-shaped signal is acquired; the steepest segment corresponds to the rapid solid formation whereas the first and last segments identify the two equilibrium stages before precipitation and in the presence of the solid, respectively.

The maximum  $\text{Ca}^{2+}$  activity in figure 3.9A (H-IS) is higher than that in figure 3.9C (L-IS), but the same initial slope and almost the same final plateau levels are attained. Since the experiments refer to the different IS levels, they can be compared in terms of  $\text{Ca}^{2+}$  activity, provided that the appropriate activity coefficient calculation model is applied [97].

The chemical speciation of Ca and P species is reported in figure B.6 in section B.3. The predominant Ca species in solution are  $\text{Ca}^{2+}$ ,  $\text{CaHPO}_4^0$ ,  $\text{CaPO}_4^-$  and Posner's clusters. The stoichiometry of the latter and their stability constants are regressed from the experimental data. In the model, every stoichiometry for Posner's clusters is possible, such as  $\text{Ca}_x(\text{PO}_4)_y\text{OH}_n\text{H}_m\text{Na}_i\text{Cl}_j^{k+}$ . The best fitting is obtained considering the stoichiometry as  $\text{Ca}_6(\text{PO}_4)_4$  (6:4 clusters) for L-IS series and  $\text{Ca}_9(\text{PO}_4)_6(\text{OH})_4^{4-}$  (9:6

### 3. CaCs & CaPs studies

clusters) for H-IS, and C-IS. The estimated stability constant (conditioned, *i.e.*, valid in the specified IS) of these clusters resulted to be  $3.0 \times 10^{46}$  for L-IS, and  $2.5 \times 10^{95}$  to  $4.0 \times 10^{95}$  for H-IS and C-IS.

The predominant P species are  $\text{HPO}_4^{2-}$ ,  $\text{H}_2\text{PO}_4^-$ , and  $\text{NaHPO}_4^-$ . The concentrations of pyrophosphate-related ions (*e.g.*,  $\text{HP}_2\text{O}_7^{3-}$ ,  $\approx 10^{-6} \text{ mol l}^{-1}$ ) is at least three orders of magnitude lower than those related to orthophosphate ions (*e.g.*,  $\text{NaHPO}_4^-$ ,  $\approx 10^{-3} \text{ mol l}^{-1}$ ) but their consideration into the speciation model is required to attain a relative mass balance error at the limit of the computational error ( $< 5 \times 10^{-10}$ ) and an overall charge unbalance lower than  $5 \times 10^{-17} \text{ mol kg}^{-1}$ .

For series L-IS and H-IS, the concentration of  $\text{Na}^+$  and  $\text{Cl}^-$  decrease (as well as IS) because of the dilution of the system due to the addition of  $\text{CaCl}_2$  and  $\text{NaOH}$ . For the series C-IS,  $\text{Na}^+$ ,  $\text{Cl}^-$ , and IS are constant during the entire experimental timeframe (figure B.5).

Figure 3.10 reports on the calculated primary and secondary nucleation rate and the critical size for primary and secondary nucleation, in the supersaturation range where such events occur, for H-IS series.

The critical supersaturation value from the regressed model was found to be 2.53 (2.28) for the H-IS (C-IS) series, and 3.45 for the L-IS series (figure B.7). As discussed later, the critical supersaturation refers to the solid phase responsible for nucleation, *i.e.* DCPD. It is worth mentioning that in this paper supersaturation ( $S$ ) is defined as  $IAP/K_{sp}$ , (where  $IAP$  is the Ion Activity Product calculated from the speciation model), without any exponential normalization for the solid phase stoichiometry, according to the classical nucleation theory described by Nielsen [1].

Since the nucleation is governed by the formation of DCPD (see section 3.2.5), the calculated surface energy for primary ( $\Gamma$ ) and secondary ( $\Gamma_{eq}$ ) nucleation, refers to that phase and not to OCP (or HA) which is the final product of the precipitation. The secondary nucleation takes into account for the generation of new primary nuclei on the surface of the already formed solid [10, 97], thus for the self-catalytic behaviours of the precipitation. Among the three series of experiments, the calculated surface energy almost scaled linearly with the IS in the nucleation range (figure B.3, B.2). For instance  $\Gamma$  resulted to be  $42.5 \text{ mJ m}^{-2}$ ,  $35.5 \text{ mJ m}^{-2}$  and  $32.8 \text{ mJ m}^{-2}$  for C-IS ( $IS = 0.154$ ), H-IS ( $IS = 0.125$ ), and L-IS ( $IS = 0.022$ ), respectively. The adhesion energy ( $\beta$ ) [10, 97] is estimated to be  $69\% \pm 1\%$  of the maximum theoretical value ( $2\Gamma$ ) for all the experiments. The estimated size-averaged maximum linear growth rate during the fast growth stage (point *d*, figure 3.9) is  $6.5 \times 10^{-9} \text{ ms}^{-1}$  ( $7.1 \times 10^{-9} \text{ ms}^{-1}$ ) for H-IS (C-IS)

### 3.2. Formation and Transformation of Calcium Phosphate Phases under Biologically Relevant Conditions: Experiments and Modelling

series and  $5.6 \times 10^{-9} \text{ m s}^{-1}$  for the L-IS series. These values are reasonable for sparsely soluble salts. In the following stage (*f-g*, figure 3.9) the growth is limited by the  $\text{Ca}^{2+}$  addition into the reactor and the estimated size-averaged linear growth rate ranges (for all experiments) from  $4.0 \times 10^{-11} \text{ m s}^{-1}$  (in *f*, figure 3.9) to  $2.0 \times 10^{-11} \text{ m s}^{-1}$  (in *g*). The diffusion coefficient is estimated to be  $3.1 \times 10^{-10} \text{ m}^2 \text{ s}^{-1}$  which is substantially lower than that calculated for  $\text{Ca}^{2+}$  ions ( $1.08 \times 10^{-9} \text{ m}^2 \text{ s}^{-1}$ ) at the experimental condition of temperature (37.0 °C) and dynamic viscosity ( $6.85 \times 10^{-4} \text{ kg m}^{-1} \text{ s}^{-1}$ ).

The precipitated solids were characterized by IR and Raman spectroscopy, high-resolution X-ray diffraction (XRD), electron microscopy, and chemical analysis, and both OCP and HA were detected.

The clearest evidence for phase composition is given by the collected high-resolution X-ray diffraction patterns (figure 3.11) because of the intense characteristic peak (100) of OCP at a low angle.

As reported in the literature, maturation time, *pH* value, temperature, and the way of addition of reactants influences the precipitated solid phase [135, 136]. These results were confirmed by our experiments. In particular, in the series H-IS, the solid collected for short ageing time (450 min) contains an high amount of OCP, but it evolves towards HA if calcium solution addition is suspended and the solid is aged for several hours (figure 3.11, pattern H-IS, aged). Nevertheless, in the series C-IS, OCP seems more stable, and the evolution toward HA was not clearly detected during the experimental timeframe. Nevertheless, both OCP and HA phases are present in the collected solid phase. Here, Rietveld refinement is used to evaluate the lattice parameters of the solid phases, but the quantitative evolution of the solid composition is questionable since not all the peak intensities can be properly fitted, most probably because of the particle shape and incertitude on the solid phase stoichiometry. For the L-IS series, the obtained solid phase was HA even for short ageing time. Thus, a trend between IS and OCP stabilization can be speculated.

The unit cell parameters obtained by Rietveld refinement for the L-IS series samples collected for both short (250 min) and long maturation time (600 min) (figure 3.11) were  $a = 9.451 \text{ \AA} \pm 0.002 \text{ \AA}$  and  $c = 6.875 \text{ \AA} \pm 0.002 \text{ \AA}$ . Similar values are reported for freshly precipitated HA [137]. Instead, for the samples of the series H-IS and C-IS (figure 3.11), the diffraction patterns show clearly the intense characteristic peak (100) of OCP at a low angle. The refined OCP cell parameters are  $a = 19.713 \text{ \AA} \pm 0.002 \text{ \AA}$ ,  $b = 9.525 \text{ \AA} \pm 0.002 \text{ \AA}$ ,  $c = 6.840 \text{ \AA} \pm 0.002 \text{ \AA}$ ,  $\alpha = 90.12^\circ \pm 0.01^\circ$ ,  $\beta = 92.53^\circ \pm 0.01^\circ$ , and  $\gamma = 108.30^\circ \pm 0.01^\circ$ .

### 3. CaCs & CaPs studies

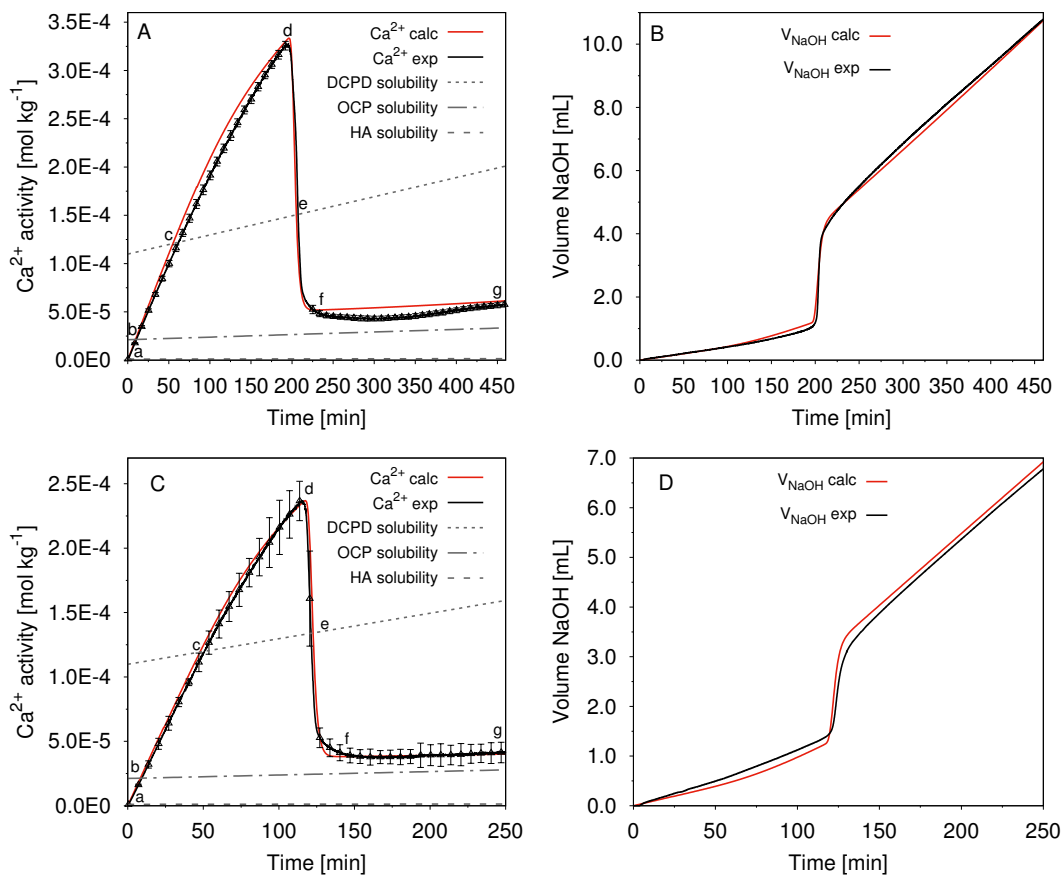


**Figure 3.9** – Experimental (black) and calculated (red) data. (A,C)  $\text{Ca}^{2+}$  molal activity in solution, derived from the ISEs electrodes for H-IS and L-IS experiments, respectively; (B, D) volume of NaOH added into the system to keep iso- $p\text{H}$  conditions for H-IS and L-IS experiments, respectively. The letters (a-g) in A and C are discussed in the text.

### 3.2. Formation and Transformation of Calcium Phosphate Phases under Biologically Relevant Conditions: Experiments and Modelling

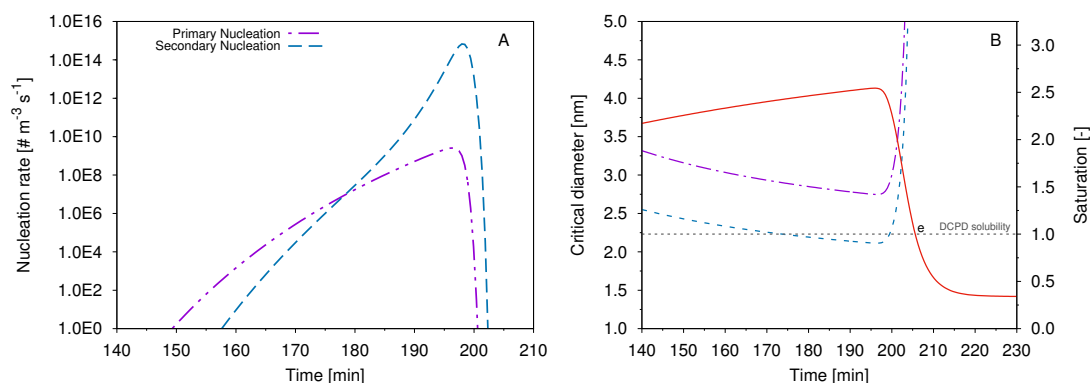


**Figure 3.10** – Calculated kinetic data for H-IS series. (A) Primary (purple,  $\cdots$ ) and secondary (blue,  $\cdots$ ) nucleation rates; (B) critical nucleation size for primary homogeneous (purple,  $\cdot - \cdot$ ) and "true" secondary nucleation (blue,  $\cdot -$ ) at the DCPD supersaturation level (red line).

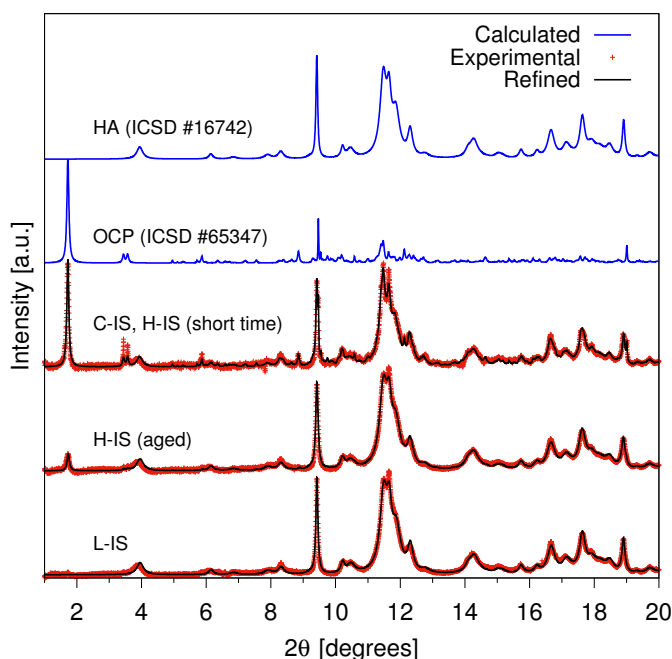


**Figure 3.11** – Diffraction patterns, after background subtraction, collected on dry powders. From top to down: reference pattern for HA (ICSD 16742); reference pattern for OCP (ICSD 65347); samples of the series C-IS (which shows equivalent results to samples of the series H-IS collected for short ageing time); sample of the series H-IS (aged); sample of the series L-IS. For experimental patterns, the experimental data (red points) and the Rietveld refinements (black lines) are reported. Energy: 22 keV,  $\lambda=0.56433 \text{ \AA}$ .

### 3. CaCs & CaPs studies

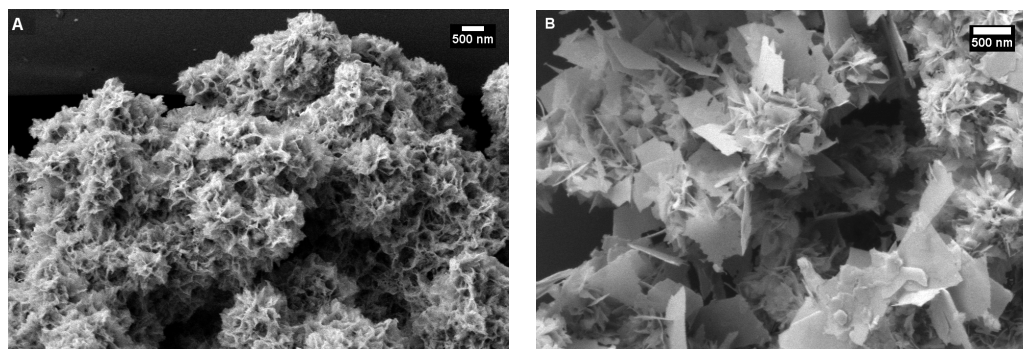


**Figure 3.12** – SEM micrograph of (A) particles of L-IS experiments, scale 500 nm; (B) particles of C-IS experiments, scale 250 nm.

Ca/P molar ratio measured by chemical analysis was 1.43 and 1.50 for L-IS and H-IS (C-IS) experiments, respectively. These values are below the 1.67 expected in case of crystalline apatite and above 1.33 expected for OCP phase, which is in agreement with the co-existence of both phases.

Figure 3.12 shows representative images of C-IS and L-IS series samples, corresponding to the diffractograms of figure 3.11. The sample of the series C-IS (figure 3.12B), in which the OCP phase is present in a relevant amount, show well-developed platy-like crystals of  $1\text{ }\mu\text{m}$  to  $3\text{ }\mu\text{m}$  and  $5\text{ nm}$  to  $10\text{ nm}$  thickness, which are commonly associated to the OCP phase [121], together with needle-like crystals, generally associated to HA phase [138]. The sample of L-IS series (figure 3.12A) show a less developed structure, with smaller crystals when compare to the other series, together with a sponge-like structure, which is commonly present in HA samples [139].

TEM micrographs allow further insight of the nanostructure (figure 3.13). First of all, the thin crystals are very sensitive to the electron beam, and artefacts can be easily generated during the observation. Secondly, the fringes associated with the most intense OCP peak ( $1.87\text{ nm}$ ) were not detected since most platy crystallites were preferentially lying with their (100) plane on the carbon support. Difficulties to identify such a planar distance were reported in the literature [140] even because the material is very sensitive to electron bombardment and rapidly recrystallize [141]. Thirdly, only crystalline particles were detected. Figure 3.13(B, D) shows the large and thin OCP crystals whereas smaller acicular crystallites were detected in the case of HA (figure 3.13A, C). However, few large platy-like crystals were detected in the HA samples as well, probably as a memory of an OCP transient phase.

Raman and IR spectroscopies confirmed the co-existence of both phases, in agreement with diffraction results (section B.1.1) and the absence of carbonate contamina-



### 3.2. Formation and Transformation of Calcium Phosphate Phases under Biologically Relevant Conditions: Experiments and Modelling

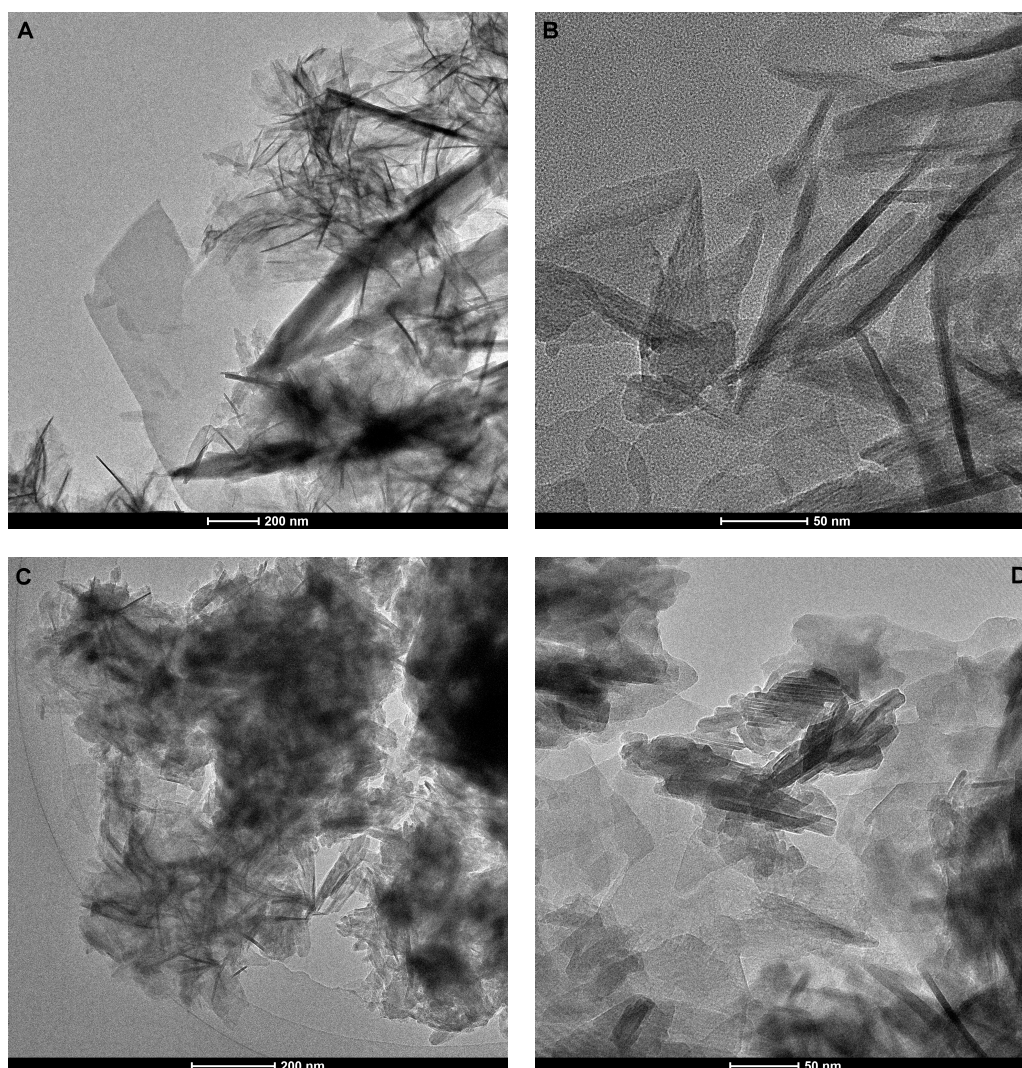


**Figure 3.13** – TEM micrographs of (A,B) L-IS sample and (C,D) C-IS sample.

### 3. CaCs & CaPs studies

---

tion.

#### 3.2.5 Discussion

Several combinations of nucleation and growth models were considered in the code, but only one of them was able to describe all the experimental results exhaustively, with full agreement with the literature and with the characterizations of the solid. In particular, every attempt to simulate the direct nucleation of OCP or HA fails, resulting in inconsistent nucleation and growth parameters, supersaturation level, and solubility of the solid phases. Instead, if only a solid phase with  $\text{Ca/P} = 1$  is considered, the model is able to describe the evolution of the  $\text{Ca}_{(\text{aq})}^{2+}$ , but it is not able to cope with the amount of NaOH added into the reactor for iso-*pH* condition, nor, with the experimental results about the crystal phase collected and its solubility.

The best description of the precipitation pathways is obtained by hypothesizing that primary and secondary nucleation [10, 97] are driven by the formation of DCPD, which is rapidly transformed to OCP (or HA depending on the experimental conditions). Growth is diffusion limited, under the driving force of the solubility of OCP (or HA). According to this assumption, every detail of the precipitation is described, and every parameter of the model is completely consistent with the literature. The calculated critical supersaturation, which triggers primary nucleation, is relatively low since DCPD is accounted as the nucleating phase and has a much higher solubility than OCP or HA. The considered DCPD solubility is  $2.19 \times 10^{-7}$  in all experimental conditions [67]. Otherwise, if OCP (or HA) is considered as nucleating phase, the critical supersaturation value would correspond to about  $4 \times 10^3$  (or  $2 \times 10^4$ , respectively), resulting in inconsistent low surface energy values associated to the corresponding solid phases and an unreasonably high nucleation rate. According to our model, the critical supersaturation with respect to DCPD is in the range of 2.5 to 3.5, which is in line with values reported for other sparsely soluble inorganic compounds. The involvement of an intermediate solid phase in the formation of OCP was already postulated being amorphous calcium phosphate, ACP [51], or DCPD [53, 142]. Despite the absence of a long-range periodic order, ACP appears to have a relatively constant composition, with a Ca/P of about 1.5 [143, 144] or as low as 1.15 [145]; the latter is very unstable and it rapidly re-crystallizes into crystalline DCPD. Our experimental evidence is consistent with an intermediate nucleating phase with a Ca/P ratio = 1, but, to date, we cannot speculate if it is crystalline or not. Both DCPD and dicalcium phosphate

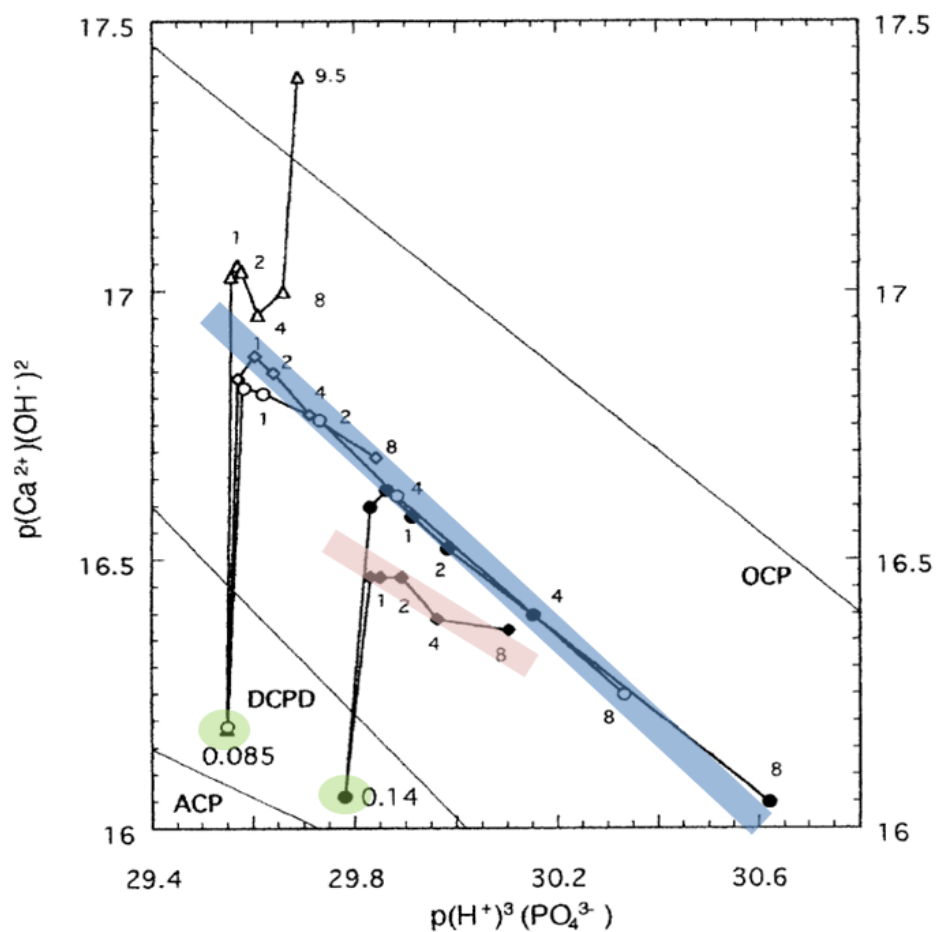
### 3.2. Formation and Transformation of Calcium Phosphate Phases under Biologically Relevant Conditions: Experiments and Modelling

anhydrous DCPA (monetite) are plausible: DCPA is thermodynamically slightly more stable than DCPD, but the hydrated form is considered the kinetic product, having lower surface energy [146], and its formation is consistent with the Ostwald's empirical rule of states. In the proposed precipitation pathway, OCP can be considered as the natural intermediate between DCPD and HA since it is composed of apatitic and hydrated layers. The apatitic layers are structurally related to HA whereas the hydrated layers are compositionally related to DCPD.

An additional line of evidence to support the involvement of DCPD instead of ACP is given by the fact that in the nucleation conditions the system is supersaturated with respect to DCPD but undersaturated with respect to ACP [136]. Figure 3.14 represents the chemical potential plots of the experimental data obtained by Iijima *et al.* [121, 136], and the experimental data of the current work (figures 3.15A and 3.15B for H-IS and L-IS, respectively).

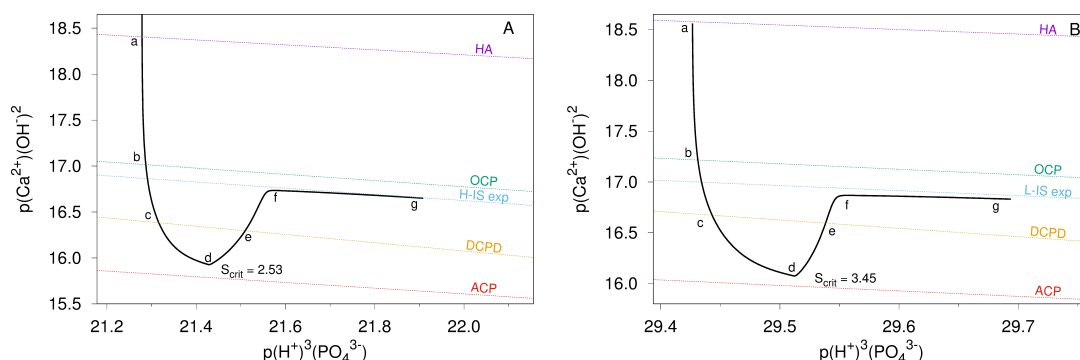
In Iijima's work (figure 3.14), the initial conditions are indicated as shaded green points, and the system evolves towards the formation of OCP or HA (blue and pink shaded points, respectively) depending on the experimental conditions. In parallel, Figure 3.15A represents the precipitation pathway for the H-IS series where OCP is obtained. At position *a* in figure 3.15A the addition of  $\text{Ca}^{2+}$  starts, and the system is immediately supersaturated with respect to HA. The addition of  $\text{CaCl}_2$  proceeds and from position *c* the system is supersaturated even with respect to DCPD. Around point *d* nucleation occurs when the system remains undersaturated with respect to ACP. Thus, ACP precipitation does not occur. At point *e* the system becomes undersaturated with respect to DCPD but still supersaturated with respect to both OCP and HA. According to our calculation, at this point, primary and secondary nucleation events are already negligible (figure 3.10), whereas the growth rate is still close to its maximum rate. Plausibly, DCPD is rapidly dehydrated and re-crystallized in a more stable solid phase (figure 3.10B, point *e*). The latter becomes the predominant phase in the section *f* and in equilibrium with the solution in section *g*. The same points (*a-g*) are represented in figure 3.9A. That solubility equilibrium does not correspond to the literature value of OCP but, in the diagram of figure 3.15, a line parallel to that of OCP equilibrium is identified, *i.e.* the precipitated solid phase has the Ca/P ratio of about 1.33. Similar results are reported in figure 3.14 (blue-shaded points). The presence of OCP in the collected solid phase was confirmed by XRD (figure 3.11).

Figure 3.15B reports on the precipitation pathway for the L-IS series where HA is obtained (XRD, figure 3.11) and the slope in the region where the equilibrium with the



**Figure 3.14** – Chemical potential plot of literature data [136]. The shaded blue area identify sample with OCP structure whereas the pink shade area identify samples with HA structure. Reprinted from [136], with permission from Elsevier.

### 3.2. Formation and Transformation of Calcium Phosphate Phases under Biologically Relevant Conditions: Experiments and Modelling



**Figure 3.15** – Chemical potential plot of for series H-IS (A), and for series L-IS (B).

solid phase is attained, is equivalent to that of HA. Again, similar results are reported in figure 3.14, where the pink shaded area identifies the formation of a solid phase with a crystal structure and Ca/P ratio of HA. The obtained solid phase in figure 3.14 was driven by different Ca/P ratio in the initial solution (shaded green points) and the  $\text{Ca}^{2+}$  addition rate into the reactor. It was also reported that OCP is transformed to HA as soon as  $\text{Ca}^{2+}$  addition is suspended; stirring has a relevant influence as well [121, 136]. According to our experimental results, also IS influences the selection of the formed solid phase. All these evidences indicate that the solubility of the solid phases obtained in such *in vitro* conditions is higher than those reported for OCP and HA. In particular, the solubility constant of OCP (as  $\text{Ca}_4(\text{PO}_4)_3\text{H}$ ) corresponds to  $2 \times 10^{-48}$  and that for HA (as  $\text{Ca}_5(\text{PO}_4)_3\text{OH}$ ) corresponds to  $2 \times 10^{-51}$ . In the literature a wide range of solubility is reported for apatitic calcium phosphates, ranging from  $10^{-42.5}$  to  $10^{-66}$  [147–153]. This considerable variability is ascribed to the possible incorporation of foreign ions into the structure.

Our experiments are conducted in a carbonate-free environment (and spectroscopic evidences confirm the absence of carbonates in the structure), but the incorporation of chloride or sodium ions is plausible, even if not EDX detectable (figure B.2). Similarly, the experimental results of figure 3.14 are collected in a carbonate- and chloride-free environment and relatively high solubility for the formed solid phases is reported, too. The solubility values for OCP and HA are very close to each other, and their coexistence is plausible. Our diffraction and spectroscopic characterizations also confirm the coexistence of both phases (figure 3.11 and B.8). Moreover, the structural similarities between OCP and HA allow the epitaxial growth of HA on OCP [154] (see refined lattice parameters  $b$  and  $c$ , Section 3), and they further, suggesting that OCP is a plausible precursor of HA in the early stage of bone and teeth formation.

### 3. CaCs & CaPs studies

---

The modelling results are consistent with the solid phase obtained. If OCP is set at solid phase formed for L-IS series - as well as if HA is set as the solid phase for H-IS or C-IS - the experimental data for  $\text{Ca}^{2+}$  activity might be somehow reproduced, but the amount of NaOH needed is mostly inconsistent with the experimental results.

In the H-IS series, a slow transformation of OCP to HA is also included in the model, using an empirical equation (section 1.3.2.1, eq. (1.80)). Thus, 300 minutes after the nucleation stage, the model calculates that about 20 mol% of OCP is transformed to HA. This transformation takes into account the experimental slope of the NaOH added volume against time in the segment *f-g* in figure 3.9B. This transformation is also supported by XRD results, even if diffraction patterns show a higher amount of HA with respect to the model prediction. Nevertheless, since a single solid phase can be included in the population balance modelling, only an empirical equation was considered to take into account the solid-solid OCP-HA transformation. According to the modelling results, the existence of DCPD as the transient phase is plausible, but its direct identification is very difficult. This intermediate phase may exist only in a limited time frame (few minutes, from point *d* to point *e* in figure 1) and at very low concentration since only nuclei are produced. They become rapidly undersaturated and, according to the model, have to disappear in *e*. Therefore, DCPD should not present in the final product. Even in the case where DCPD does not recrystallize towards OCP or HA, its fractional amount is too low to be detected (<0.1 wt%).

In the C-IS series, no transformation towards HA was introduced to fit the experimental data, in agreement with diffraction results, where a high amount of OCP is detected. It is also worth mentioning that the time-resolved experimental data collected in solution are used to calculate the solid phase composition at the end of the precipitation, but the characterized solid was collected, washed and dried: some modification of the solid phase due to these operations cannot be excluded. Thus, honestly speaking, the quantitative analysis obtained by Rietveld refinement on the OCP/HA ratio evaluated on the collected solid phases, as well as the other characterizations on the solids, can only partially be called as experimental validation of the modelling results. The final model validation can be obtained by *in-situ* time-resolved characterization of the solid in the section *d-f* of figure 3.15, which is the objective of our current research. To date, only the trend in the experimental result can be outlined. In the L-IS, HA is obtained even for short ageing times; in H-IS, OCP is obtained, and it is transformed to HA during the experimental time frame of some hours; in C-IS, OCP appears stable during the experimental time frame and in coexistence with HA.

### 3.2. Formation and Transformation of Calcium Phosphate Phases under Biologically Relevant Conditions: Experiments and Modelling

Considering that temperature,  $pH$  value, phosphate concentration, as well as  $Ca^{2+}$  activity in the range ( $f$ - $g$ ) (figure 3.9A,C, B.4) are constant among all the experiments and the fact that IS has an influence, it could be concluded that the activity of phosphate ions plays a role, being the activity coefficient of such species influenced by the IS. The activity coefficient for  $PO_4^{3-}$  corresponds to 0.06, 0.06 to 0.10, and 0.25 to 0.30, for C-IS, H-IS and L-IS, respectively. Thus, according to this interpretation, it can be speculated that the activity of phosphate ions – and their local speciation – is determining the osteogenesis thermodynamics whereas  $Ca^{2+}$  ions diffusion is controlling the osteogenesis kinetics.

Beside the solid phase obtained, the modelling results can suggest a possible growth mechanism, and some indication about the nature of the building unit deduced. In the region ( $f$ - $g$ ), the solid growth is limited by  $Ca^{2+}$  addition [97], thus under thermodynamic control. Instead, in the intervals ( $d$ - $f$ ) of figures 3.15A,B and figure 3.9A,C, the growth is limited by the precipitation kinetics (fast growth interval), and these data are useful in the evaluation of the growth mechanism. In the code, several diffusion-limited growth models are implemented, and the local surface equilibrium condition is assumed. The best results are obtained when assuming that the growth is limited by  $Ca^{2+}$  ion diffusion. In spite of that, the diffusion coefficient obtained is lower than that estimated for  $Ca^{2+}$  ions at these experimental conditions of temperature and viscosity. This calculation might be interpreted in various ways:

- A low diffusion coefficient can be associated with species of a size substantially larger than ions, such as clusters. Applying the Stoke-Einstein equation to the aforementioned diffusion coefficient, the estimated hydrodynamic diameter resulted in being about 2.2 nm, which might be in agreement with Posner's cluster with a diameter of about 1 nm. Moreover, our thermodynamic calculations are consistent with the presence of Posner's clusters in solution. Nevertheless, their concentration ranges between about  $2 \times 10^{-5} \text{ mol kg}^{-1}$  close to the nucleation zone (figure 3.9A,  $d$ ) and as little as to  $10^{-7} \text{ mol kg}^{-1}$  to  $10^{-8} \text{ mol kg}^{-1}$  in ( $f$ ). In the same regions, the concentration of  $Ca^{2+}$  ions or  $CaHPO_4$  ion pair is about 1 and 3 order of magnitudes higher, respectively, than that of Posner's clusters. Thus, it seems plausible that the nature of growth unit changes during the precipitation and the involvement of Posner's clusters in the initial fast growth rate stage cannot be excluded. However, such events are taken into account in the presented model and considered as secondary nucleation events and not as growth events. The calculated critical size for primary and secondary

### 3. CaCs & CaPs studies

---

nucleation (figure 3.10B) is close to the estimated hydrodynamic diameter of Posner's clusters and nucleation occurs in the zone where they are at maximum concentration. Thus, the involvement of Posner's clusters in the primary and secondary nucleation stages by dehydration and incorporation of  $\text{PO}_4^{3-}$  ions seems plausible.

- The diffusion of  $\text{PO}_4^{3-}$  ions from solution might play a role in the growth mechanism, resulting in a reduced effective diffusion coefficient. In the model, the surface concentration of  $\text{PO}_4^{3-}$  ions is considered equivalent to the value in solution, *e.g.*, far from the growing surface. This approximation might be justified because in the experiments the concentration of phosphate buffer is three orders of magnitude higher than that of  $\text{Ca}^{2+}$  ions.
- The particles are strongly anisotropic (figures 3.12, 3.13): the incorporation of building units is possible only along a particular direction thus not all the solid surface is available for growth, resulting in a reduced growth rate, which is reflected in a reduced effective diffusion coefficient. In other words, an additional contribution due to the surface diffusion of  $\text{Ca}^{2+}$  ions needs to be considered. The influence of the particle shape on the growth mechanism has recently been studied for the calcium silicate system [155] where platy-shaped particles are produced: a similar approach is currently a future objective for our study for both the OCP and HA systems.

Very often, the involvement of clusters in the growth mechanism is claimed because they are experimentally detected both in solution and on the surface of growing crystals and because the calculated saturation level is too high to justify a slow growth rate. Nevertheless, since the precipitation pathway described here is controlled by a driving force that changes over time, the “true” supersaturation, *i.e.* that it needs to be considered to evaluate the driving force for solid formation, is always relatively low. For instance, in the H-IS series, at the beginning of the precipitation (a)-(e) the supersaturation is calculated with respect to DCPD ( $S < 2.6$ ), but as soon as the point (e) is crossed, the supersaturation – which is now the driving force of the growth process in the range (f)-(g) – is calculated with respect to OCP ( $\approx 10 < S < 1.05$ ). These changes induce a sort of physical discontinuity close to (e), which needs to be corrected in an even more sophisticated model, where the continuum of the driving force needs to be correlated to a continuum solid-solid DCPD-OCP transformation via dehydration. To be able to investigate such kinetic details, *in-situ* experimental



### 3.2. Formation and Transformation of Calcium Phosphate Phases under Biologically Relevant Conditions: Experiments and Modelling

data on the solid phase with a time resolution of the order of few seconds need to be collected; considering that the concentration of the solid phase in (e) is in the range of  $10 \text{ mg l}^{-1}$  to  $100 \text{ mg l}^{-1}$ , such an experimental investigation is rather ambitious. So far, our most recent results, using synchrotron-based small and wide angle X-ray scattering techniques, were just able to identify the presence of solid particles, but not their nature.

#### 3.2.6 Conclusions

A quantitative mathematic model for the kinetic and thermodynamic description of the OCP and HA formation, first postulated by Francis and Webb in 1970, has been developed. The calculated solubility values for OCP and HA are close to each other; they are higher than those commonly assumed but consistent with the literature for solids prepared under similar conditions. In the thermodynamic package of the model, the only parameter regressed is the stability constant of Posner's clusters, and their stoichiometry. The former allows the estimation of the Posner's clusters concentration during the entire solid formation process whereas the latter is in agreement with the literature and seems to be influenced by the ionic strength. It is plausible that Posner's clusters play a role in the nucleation stage where they may incorporate  $\text{PO}_4^{3-}$  ions generating primary and secondary nuclei of DCPD. The estimated surface energy from the nucleation rate refers to the formation of DCPD, therefore cannot be associated with OCP or HA. After the nucleation stage, DCPD becomes rapidly undersaturated with respect to OCP and - in isotonic conditions - the latter crystallizes and grows limited by diffusion of  $\text{Ca}^{2+}$  ions. At lower IS, HA is formed instead. The growth rate is consistent with a  $\text{Ca}^{2+}$  diffusion-limited model even if the diffusion rate is lower than that expected for ions. This discrepancy can be justified by the platy-shaped particles and an additional surface diffusion contribution, determining a lower apparent diffusion coefficient. It turns out that all experimental data are consistent with a classical precipitation pathway, where primary and secondary nucleation events are considered, in which a transient phase is involved, and where the growth is mainly diffusion limited. Moreover, considering that pH, temperature, and phosphate buffer concentration are kept constant, and the same level of  $\text{Ca}^{2+}$  ion activity is attained at the end of the solid formation for all experiments irrespective of the IS level, it is argued that the selection of solid phase obtained is driven by the activity coefficient of  $\text{PO}_4^{3-}$  ions, which change by a factor of 3 to 5 among the experimental datasets: the higher the ionic strength, the lower the activity coefficient of  $\text{PO}_4^{3-}$  ions

### 3. CaCs & CaPs studies

---

(*i.e.*, the lower the activity of  $\text{PO}_4^{3-}$  ions at constant concentration), and the higher the stabilization of OCP with respect to HA. Moreover, the thermodynamic-kinetic model for solid calcium phosphates formation is a useful tool to predict the appropriate experimental condition in order to promote the formation of calcium phosphate phases *in vitro* and can contribute toward the comprehension of the apatitic phases formation mechanism *in vivo*.

### **3.3 In-situ liquid WAXS and SAXS studies on the early stage of amorphous calcium carbonate (ACC) formation**

Author's contribution to this publication:

- i. extrapolation of experimental conditions by modelling;
- ii. preparation of chemicals;
- iii. experimental data collection;
- iv. critical data analysis.

---

This chapter is adapted from Ahmed S. A. Mohammed\*, A. Carino\* et al., In-situ liquid WAXS and SAXS studies on the early stage of amorphous calcium carbonate (ACC) formation, under finalization. Preliminary results are reported, the data analysis is still ongoing. Therefore, the scientific outcomes that will be published might be different. \*Both authors contributed equally to this work.

---

### 3. CaCs & CaPs studies

---

#### 3.3.1 Abstract

Calcium carbonate is a well-known model system for the investigation of the solid formation by precipitation from solutions, and it is often considered in the debated classical (CNT) and non-classical (NCNT) theories of precipitation. Despite the great scientific relevance of calcium carbonate in different areas of science, little is known about the early stage of its formation. We, therefore, designed contactless devices capable of providing informative investigations on the early stages of the precipitation pathway of calcium carbonate in undersaturated and supersaturated solutions using classical scattering methods such as Wide-Angle X-ray Scattering (WAXS) technique and Small-Angle X-ray Scattering (SAXS) technique. SAXS, in particular, was mainly exploited for investigating the size of entities formed in solutions, before the critical conditions for precipitation. The saturation level was controlled by mixing four diluted solutions (*i.e.*, NaOH, CaCl<sub>2</sub>, NaHCO<sub>3</sub>, H<sub>2</sub>O) at constant T and pH and the scattering data were collected on a liquid jet generated about 75 s after the mixing point. The data were modelled using parametric statistical models providing insight about the size and shape distribution of denser matter in the liquid jet.

#### 3.3.2 Introduction

Understanding the early stage in the precipitation pathway is of fundamental relevance to achieving an appropriate control at the macroscopic level on the solid formation, for instance in terms of morphology, physicochemical properties, and a crystalline phase [4]. The precipitation pathway includes the nucleation and growth of a solid phase from supersaturated solutions. At the early stage, *i.e.* before the nucleation events, the physical nature of entities in solution is a matter of debate: CaCO<sub>3</sub> is a model system, the archetype of several sparsely soluble inorganic materials. The precipitation is a complex process. Homogeneous primary nucleation is the first elementary process in solid formation [1]. There are two descriptions developed for such phenomenon occurring in solutions and, in particular, how the critical conditions for nucleation are attained in the system: the classical and the non-classical nucleation theory (CNT and NCNT). In both cases, the formation of new entities starts with a reacting solution of dissolved aqueous species: a change in the saturation of the system triggers the formation of initial entities which increase of size until the nucleation occurs. Afterwards, the reaction follows many pathways over a period until a final product is obtained. In the formulation of the CNT, a series of approximation

### 3.3. In-situ liquid WAXS and SAXS studies on the early stage of amorphous calcium carbonate (ACC) formation

and simplifications are assumed with the aim to obtain a simplified mathematical framework. One of the most relevant assumptions is the so-called approximation that leads to the definition of a landscape of the Gibbs free energy *vs.* embryo size characterised by only one maximum which coordinates identify the activation energy and the critical size for nucleation. Any alternative landscapes identify an NCNT where, for instance, an arbitrary mathematical equation is assumed for the surface energy as a function of embryo size. In this case, the Gibbs free energy landscape can admit more than one point where the derivative is zero, *e.g.* a minimum before the critical size. The existence of a minimum in the Gibbs free energy identifies a preferential size for clusters of subcritical dimension. In fact, according to the NCNT, in a supersaturated solution, stable and well-defined clusters (called pre-nucleation clusters) exist, and they may aggregate into larger entities particles [6]. In the specific case of calcium carbonate, these larger entities have an amorphous nature as well as the first solid formed (amorphous calcium carbonate, ACC). Some authors claim that such intermediate amorphous entities have a kind of order, which depends on the *pH* value and which can define the crystal phase that may be formed by their evolution [6], naming these intermediates as proto-calcite or proto-vaterite. According to our recent finding, the *pH* influences the calcium-to-carbonate ratio in ACC as well as in the pre-nucleation entities, in dynamic equilibrium with the solution: this ratio might be the reason of the preferential phase obtained upon crystallisation [97].

Indeed, the existence of sub-critical embryo is expected even following the CNT reasoning with a statistical size distribution of embryos, which is influenced by the saturation level. Therefore, other authors claim that there is no preferential size and thus the nucleation is classical [97, 133]. The common point of the two view is the fact that subcritical embryos or cluster exist. Using advanced analytical equipment, such as cryoTEM [156] and by AUC, small entities were also identified [6]. Nevertheless, sample manipulation was necessary and considering that such entities are in equilibrium with the liquid in which they are formed, any small physicochemical modification can strongly influence their stabilisation/destabilisation. As a consequence, the investigations of these labile entities needs to be done *in-situ*, without modifying the equilibrium conditions that lead to their formation. The needed information is not merely the existence of sub-critical entities since this is considered a matter of fact, but their size distribution, which can reflect the existence of a preferential size or a statistical distribution of size or even a different scenario. The identification of the cluster size distribution as a function of the saturation level is the goal of this experimental and modelling work. Synchrotron-based scattering techniques play an

### 3. CaCs & CaPs studies

---

important role in extracting information from entities suspended in the liquid phase. They are very powerful techniques thanks to the high brightness and flux and modern photon counting detectors. X-ray scattering is sensitive to the sample's electron density spatial variations. In particular, SAXS is sensitive to density variations on the scale of nanometres to micrometres. In fact, systems with nanometer-scale spatial variations of the electron density provide very strong, meaningful, and informative scattering information at small angle [157], yielding information on particles size and their size distribution. At higher angles (WAXS) the scattering yields information on a subnanometric scale, such as the atomic structure and more detailed information on crystallinity, defects, and size and shape distribution. Nevertheless, the WAXS diffraction signal is typically weaker by several orders of magnitude with respect to SAXS, which therefore remains the only method that can be used when a combination of weak contrast and small concentrations characterises the sample, as is the case for near-saturation  $\text{CaCO}_3$  solutions. Moreover, the scattering process follows the reciprocity law [158], which means to have scattering information from larger features one has to reach lower angles and *vice versa*. The application of scattering techniques might be not sufficient in the specific case of our scientific question. In fact, three additional features might be required in order to be able to collect experimental data: *i*) the background signal should be minimized; *ii*) the presence of solid surfaces in contact with the liquid under analysis might be avoided in order to do not induce heterogeneous nucleation; *iii*) a time-invariant setup, not influenced by the X-ray beam, need to be conceived in order to accumulate experimental data for a relatively long time (high signal-to-noise ratio). A pulsation-free micrometric-size reactive horizontal liquid jet setup was built to solve this issue. The liquid jet is not confined by a solid, thus it is a contactless setup not susceptible to wall effects [156, 159–161], the liquid interrogated by the beam is continuously renovated, and beam damage is intrinsically avoided, and the dynamic mixing conditions allows a time-independent setting of  $T$ ,  $pH$  and saturation ( $S$ ) level. The saturation level is computed thanks to the developed thermodynamic model for ACC precipitation [97].

In this dissertation, we present both the results on cluster size distribution as a function of the saturated level with respect to ACC and the appropriate setup to carry out such measurements even on other systems.

### 3.3. In-situ liquid WAXS and SAXS studies on the early stage of amorphous calcium carbonate (ACC) formation

#### 3.3.3 Material and methods

Calcium chloride, sodium hydroxide, and sodium bicarbonate were purchased from Sigma Aldrich (analytical grade, ReagentPlus). Aqueous solutions  $\text{CaCl}_2$  ( $2 \text{ mmol L}^{-1}$ ),  $\text{NaOH}$  ( $5 \text{ mmol L}^{-1}$ ),  $\text{NaHCO}_3$  ( $20 \text{ mmol L}^{-1}$ ) and pure  $\text{H}_2\text{O}$  were prepared using  $\text{CO}_2$ -free milliQ water. A pulsation-free micrometric-size horizontal reactive liquid jet setup was specifically built for the measurements. The system (figure 1.5) as a whole was composed of four HPLC pumps – each of them equipped with a pulsation damper system and a high precision Coriolis liquid mass flowmeters –, a mixing system, a delay loop, and a catcher. A micromixer manifold, equipped with 5 inputs and one exit, was used to mix the solutions. The fifth input was connected with an additional HPLC pump delivering a 10 wt.% acetic acid solution, which serves to clean the system. The manifold exit holds the delay loop which consists of a Teflon tube of a certain length and internal diameter of 1 mm. This tube defines the delay time between the mixing point and the irradiated liquid jet. Delivering tubes before the mixer and the delay loop were thermostated using a double-walled water-jacketed tubing system. The delay loop outflow was connected with a capillary. The overall flow rate of the four chemicals depends on the internal capillary diameter. Different material and size can be used for the capillary; in this study, stainless steel capillaries with  $250 \mu\text{m}$  of internal diameter and an overall flow rate of  $8 \text{ mL min}^{-1}$  were used. Saturation (calculated as in eq. (2.9), section 2.1.1) and  $\text{pH}$  values were kept constant during each acquisition. In order to achieve the specific  $\text{pH}$  and  $S$  values, the concentration and relative flow rates of the four chemicals were calculated by means of a speciation model previously developed [97]. The pumping system was remotely controlled and monitored. A catcher, collecting the ejected liquid after X-ray exposure, was equipped with a micro stirrer, a  $\text{pH}$  electrode, and a PT1000 temperature sensor. The measured  $\text{pH}$  value was used to validate the prediction of the speciation model, which also computes the existence of clusters in solution. Experiments were conducted at different flow rates for each chemical; to each flow rates combination, a defined  $S$  level corresponds. Each  $S$  level can be achieved with an infinite combination of  $\text{Ca}/\text{C}$  ratio. Nevertheless, in these experiments,  $\text{pH}$  and overall carbonate concentration were kept at the value of our previous studies [97], *i.e.*, at  $\text{pH} = 9$  and an overall carbonate content equal to  $9.71 \text{ mmol}$ . Therefore, the  $\text{Ca}/\text{C}$  ratio is univocally defined at each  $S$  level. We carried out liquid jets measurements selecting four  $S$  levels ( $S = 0, 0.74, 1.46$  and  $2.83$  with the corresponding  $\text{Ca}/\text{C}$  molar ratio of  $0, 1.09 \times 10^{-2}, 2.22 \times 10^{-2}$  and  $4.56 \times 10^{-2}$ ), hereafter named as  $C_0, C_2, C_4$ , and  $C_8$ , respectively. The time delay was fixed to  $75 \text{ s}$ .

### 3. CaCs & CaPs studies

---

Synchrotron Small-Angle Scattering (SAXS) measurements were carried out at the Material Science beamline (X04SA-MS) of the Swiss Light Source (SLS) at PSI [162]. This synchrotron station is built for the WAXS powder diffraction measurements, but it also has some SAXS capabilities. Modern photon-counting detectors (Mythen II and PILATUS 6M) are installed. The liquid jet, horizontal and orthogonal to the X-ray beam, was mounted on a double micrometric translation stage and optically centred with respect to the diffractometer circle (figure 1.5) by a high-resolution camera. The X-ray beam was set at 9.5 keV ( $\lambda=1.305 \text{ \AA}$ ) where the X-ray flux is maximized. Data were collected with the Mythen II detector system [163], that with its  $0.0036^\circ$  step, has a sufficient resolution for SAXS on this system with a minimum accessible  $2\theta$  scattering angle of  $\approx 0.18^\circ$  to  $0.20^\circ$ , corresponding to a minimum accessible momentum transfer of  $Q = 4\pi \frac{\sin(\theta)}{\lambda} = 0.016 \text{ \AA}^{-1}$  where  $\lambda$  is the wave length of incident X-ray.

#### 3.3.4 Preliminary data analysis

Before their analysis, the experimental data need a careful conversion, from raw data (photon counting) into diffraction data (intensity-angle (fig. 3.16); intensity-momentum transfer  $Q$  on regular step). Scattering patterns were collected with reasonable acquisition times from ACC solutions at the selected saturation levels, as well as from pure water, and from the air. The system was washed with acetic acid, followed by water, before each acquisition. Ancillary data (S, time-delay, T, pH, and jet size) were also recorded. To express the data in absolute unit, the signal generates by a standard suspension of NPs were collected as well. In following sections, the applied calibration and fitting approaches are described.

##### 3.3.4.1 Evaluation of the scale factor

As most often the scattering data were collected in arbitrary unit. A suitable standard must be measured to obtain the appropriate scale factor and convert the data to absolute units. We exploited a homemade [164] spherical gold nanoparticle (AuNP's) suspension of known concentration ( $200 \text{ mgL}^{-1}$  as Au) and narrow size distribution (18 nm, evaluated by TEM), measured using the same liquid jet setup.

The resulting signal can be modelled assuming a monodisperse distribution of non-interacting spherical particles with radius  $R$ . Hence, the observed scattering intensity



### 3.3. In-situ liquid WAXS and SAXS studies on the early stage of amorphous calcium carbonate (ACC) formation

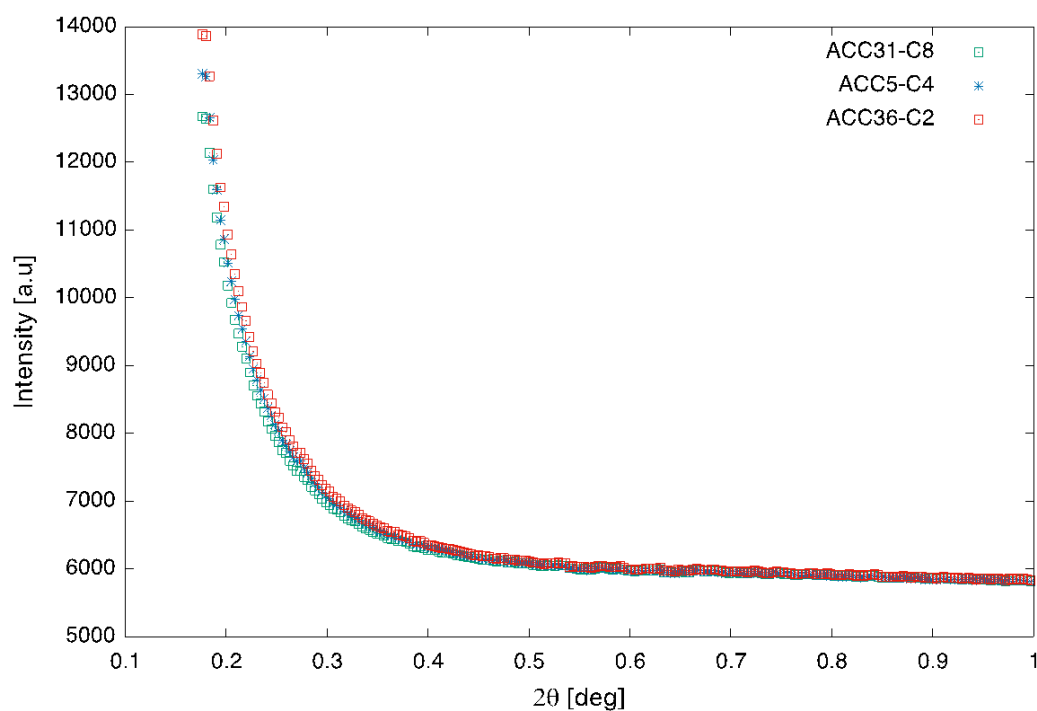


**Figure 3.16** – The SAXS data in the angular range from three representative supersaturated levels ( $C_2$ ,  $C_4$ , and  $C_8$ ). The data were collected at the material science beam-line (X04SA-MS) of the Swiss Light Sources (SLS) at PSI.

### 3. CACs & CAPs studies

(after subtracting from the background) for a given sample volume reads

$$I(Q) = k N (\Delta\rho)^2 V_p^2 \left( 3 \frac{\sin(QR) - QR \cos(QR)}{(QR)^3} \right)^2 \quad (3.1)$$

where  $N$  is the number of particles,  $\Delta\rho$  is particles scattering contrast,  $V_p$  is the particle volume,  $Q = 4\pi \frac{\sin(\theta)}{\lambda}$  is the amplitude of the scattering vector at the scattering angle  $\theta$ , and  $k$  is a constant pertaining to the experimental setup. The scattering contrast (in electron units) corresponds to the difference in the volume electron density between the particle and the solvent; dimensionally it corresponds to an inverse volume. Using the density of the bulk gold and approximating the average electron density of the solvent with that of pure water, we therefore obtain a scattering contrast  $\Delta\rho = 4.33 \times 10^{24} \text{ cm}^{-3}$ . At  $Q = 0$ , the term in brackets in eq. (3.1) is equal to unity, so we have the scale factor determined to be  $4.59 \times 10^{-19}$  using the relation

$$k = \frac{I(Q=0)}{n V_s (\Delta\rho)^2 (V_p)^2} \quad (3.2)$$

where  $I(Q=0) = 6.69 \times 10^4$  counts / sec is the extrapolated forward intensity at  $Q = 0$ ,  $n = 2.71 \times 10^{12} \text{ cm}^{-3}$  is the particle number density,  $V_s = 1.96 \text{ cm}^{-3}$  is the volume of the illuminated sample,  $V_p = 3.83 \times 10^{-18} \text{ cm}^{-3}$  is the volume of the particle.

#### 3.3.4.2 Fitting approaches

ACC colloidal suspensions were assumed to consist of polydisperse particles with a spherical shape [158]. A parametric distribution model was used for modelling and analysing the collected data [165, 166]. Two approaches were attempted based on the type of the distribution function. Firstly, a more classical approach was evaluated. We assumed a log-normal size distribution of spherical clusters with an unknown density. The scattering intensity of this polydisperse system is also represented by eq. (3.3) (where the  $P_m$  is derived from a two-parameter log-normal function). The observed data (after background subtraction) for the supersaturation levels ( $C_2$ ,  $C_4$ ) were fitted very nicely with the model intensity plus a rescaled background parameter, but the results presented several weak points (too broad distributions, little correlation between samples, not all fits were successful). This approach was rejected in favour of a slightly more conceptually complex one (bimodal approach), albeit without increasing the number of parameters.

### 3.3. In-situ liquid WAXS and SAXS studies on the early stage of amorphous calcium carbonate (ACC) formation

#### 3.3.4.3 Bimodal approach

In this approach, we assumed that the whole system is composed of two populations of particles: one population includes SDC, with diameter of about 2 nm to 3 nm; a second population includes a polydisperse population of aggregate (i.e., superclusters) with higher volume, formed by several SDC loosely packed and without coalescence. We assume a packing fraction of 50% (vol.) of SDC in the superclusters, and a minimum diameter of  $\approx 5$  nm (i.e., a supercluster contains at least 8 SDC). The contributions of these two populations lead to two terms for the intensity (one from the population of the SDC and one from the population of the superclusters), plus the separately measured background (chC0).

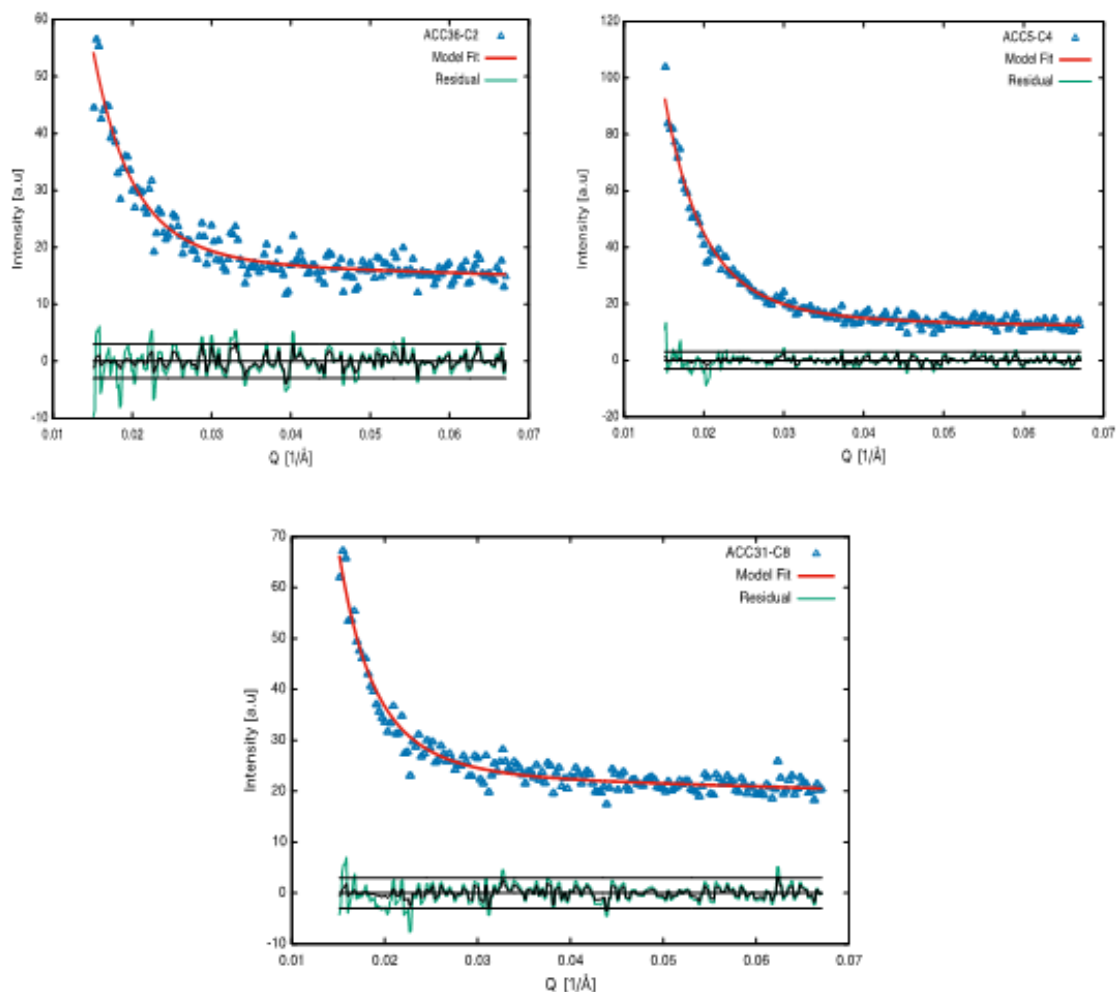
The term due to the SDC, as they result to be rather small is a relatively flat and featureless trace in the experimental  $Q$  range ( $0.015 \text{ \AA}^{-1}$  to  $0.07 \text{ \AA}^{-1}$ ), and it is weak and highly correlated with the background, therefore *i*) the scale of this trace cannot be precisely determined, *ii*) the SDC diameter – approximated as monodisperse spheres – can be determined within a 20 to 30% error, which may also be intrinsic in the SDC nature. Nevertheless, the fact that this signal is refined to consistent values (diameter of 2 nm to 3 nm) in all of our best experimental patterns (8 series of data) at all conditions adds credibility to their existence, at least qualitatively.

Figure 3.17 reports the best fitting for  $C_2$ ,  $C_4$ ,  $C_8$ . For the polydisperse superclusters, the size distribution function has been refined both as a log-normal and an exponential  $P_m = C \exp\left(\frac{-D_m}{D_0}\right)$ , where  $C$  is a normalization constant (such that  $P_m$ , the number fractions, sum to 1),  $D_0$  is the distribution parameter,  $D_m = m\delta$  is the diameter of the  $m^{th}$  cluster (variable between 5 nm to 100 nm) and  $\delta$  is the diameter of a sphere containing 1 SDC and an equal volume of water. The latter distribution was then selected as giving the most credible results. The scattering intensities must be summed over all the particle sizes and weighted by their size distribution function  $P_m$ . Hence, the calculated scattering intensity of this polydisperse system is given by

$$I(Q) = k N \sum_m P_m (\Delta\rho_m)^2 V_m^2 \left( 3 \frac{\sin(QR_m) - QR \cos(QR_m)}{(QR_m)^3} \right)^2 \quad (3.3)$$

where  $m$  is indexing over the possible different spherical clusters (see below),  $N$  is the total number of objects in the beam,  $R_m = \frac{D_m}{2}$  is the sphere radius,  $Q$  is the transferred momentum,  $V_m$  is the volume of the clusters,  $\Delta\rho_m$  is the clusters electron density contrast. A simple grid search algorithm dealt with finding optimal values of the distribution parameter, while scale factors were separately optimized at each step as a

### 3. CaCs & CaPs studies



**Figure 3.17** – Best fits for condition C<sub>2</sub>, C<sub>4</sub>, C<sub>8</sub> (goodness of fit 1.15, 0.97, and 0.99, respectively) using the bivariate model (SDC + superclusters with an exponential size distribution).

### 3.3. In-situ liquid WAXS and SAXS studies on the early stage of amorphous calcium carbonate (ACC) formation

linear minimisation problem. As for the gold experiment, at  $Q = 0$ , we could have the scattering forward intensity given as

$$I(Q = 0) = kN \sum_m P_m (\Delta\rho_m)^2 V_m^2 \quad (3.4)$$

As indicated in eq.(3.4), the scattering intensity is proportional to the square of the scattering contrast which represents the excess electron density of the suspended particles with respect to the medium surrounding them. The superclusters consist of poly-hydrated ACC suspended in water; the composition is generally  $\text{CaCO}_3 \cdot n\text{H}_2\text{O}$  with an atomic weight of  $100.1 + 18.02n$  and  $50 + 10n$  electrons per unit formula. Assuming partial densities for ACC and water, a molar volume of  $62.55 + 18.02n \text{ cm}^{-3}$  is the case. We reasonably assume a variable number of a water molecule ( $n$ ) for  $\text{CaCO}_3$  unit, so the excess electron density and the mass density change with  $n$ . When considering the packing fraction for the aggregates, in addition to the SDC, we should have two contrasts for the whole system: one is for the dense clusters and the other one for the polydisperse superclusters, should be multiplied by the packing fraction (*e.g.*, if we have the packing fraction of 0.5 we should have superclusters with a contrast half that of the dense clusters). The observed data (with subtracted background  $C_0$ ) were fitted with the model intensity as described above. Even with the small contrast of this system, the SAXS signal was clearly visible. Due to the low solubility of  $\text{CaCO}_3$  (an overall concentration of  $\text{CaCO}_3$  ion pair is estimated to be  $<10 \text{ mgL}^{-1}$  in the considered experimental conditions [97]), the superclusters concentrations were very low and hence the interparticle interferences could be neglected. The subtracted background pattern was also freely scaled, to compensate for small differences in the experimental conditions (mainly jet diameter); its scale factor always resulted close to 1 (within  $10^{-3}$ ). The goodness of fit and the other relevant factors were also evaluated. Figure 3.18 shows the results obtained for the data of the selected condition levels ( $C_2$ ,  $C_4$ ,  $C_8$ ).

#### 3.3.5 Preliminary results and discussion

The analysis of the experimental data, in particular, the identification of the value of  $n$  as a function of the saturation level, is in progress. At the moment, it seems reasonable to interpret the data according to a model of sequential de-hydration of the entities in the pre-nucleation zone, *i.e.* the amount of water in the SDC as well as in the superclusters decreases approaching the critical conditions (figure 3.19). According to

### 3. CaCs & CaPs studies

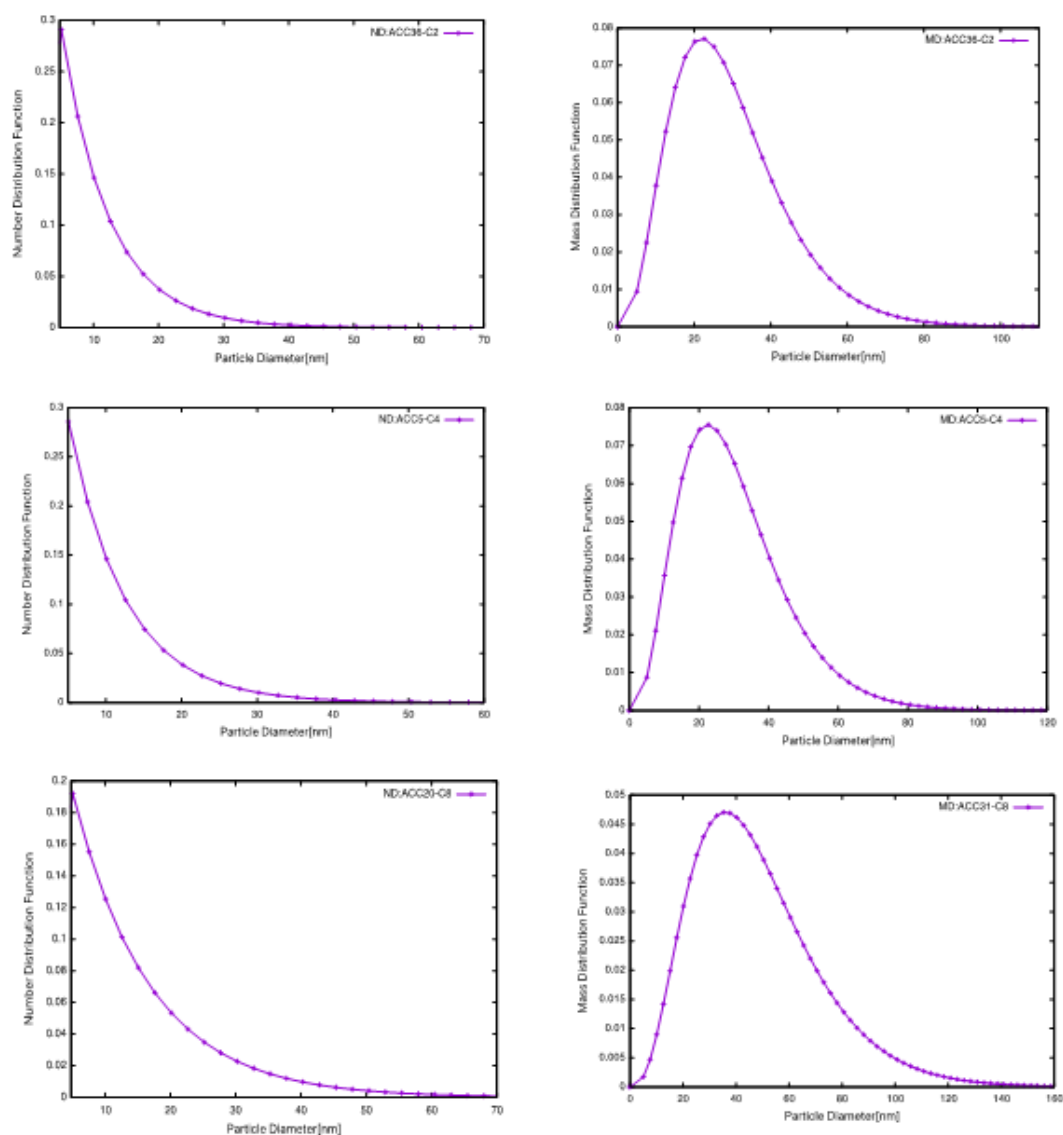


**Figure 3.18** – Left column: the obtained number distribution of the objects (C<sub>2</sub>, C<sub>4</sub>, C<sub>8</sub>). Right column: the corresponding mass distribution. These distribution functions were obtained based on the bimodal approach.

### 3.3. In-situ liquid WAXS and SAXS studies on the early stage of amorphous calcium carbonate (ACC) formation

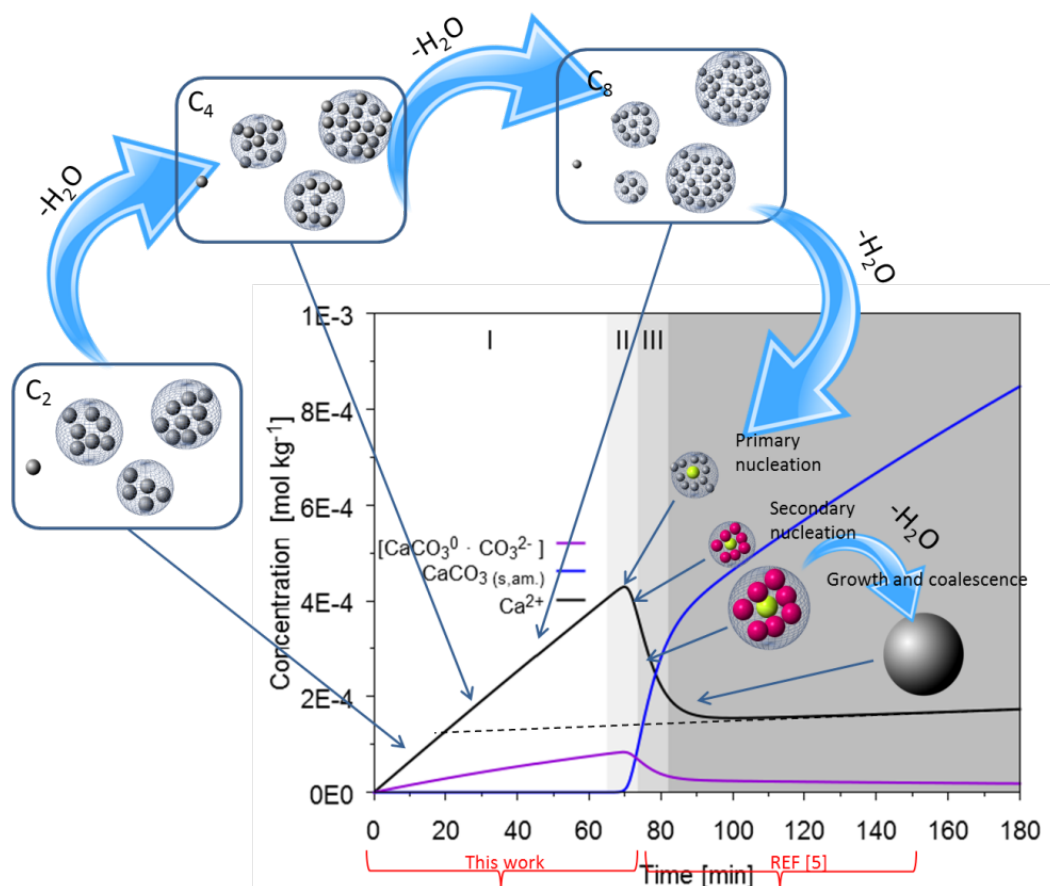


**Figure 3.19** – Preliminary interpretation of the experimental data.

this interpretation, there is no a preferential size neither for SDC nor for superclusters but a continuous de-hydration-driven process which leads to a critical water content in the superclusters. At the critical point, primary nucleation occurs, followed by secondary nucleation and growth events, according to the findings described in the section 3.1).





## 4 | Investigation methods

This chapter describes the experimental techniques applied in my doctoral work. Before each technique description, a short section summarises the context in which that technique was used and some instrumental and analysis details.

### 4.1 Infra-Red and Raman spectroscopy

*Infra-Red (IR) analyses were done on dried calcium phosphate powders collected after the precipitation experiments. The infra-red spectra were collected in the attenuated total reflection mode ATR-IR using a Vertex 80V spectrometer (Bruker), equipped with a Platinum ATR unit. The instrument accumulates 100 interferograms with a resolution of  $4\text{ cm}^{-1}$ . The powder was placed onto the small crystal area, applying a gentle pressure to push the sample onto the diamond surface and then analysed.*

*The Raman spectra were acquired on CaP dried powder samples using a Kaiser Raman-RXN1 Analyzer supplied with Invictus™ 785-nm VIS laser (Kaiser Optical Systems). The instrument is equipped with a CCD camera (1024x256 EEC MPP Type, Kaiser Optical Systems) with collimated incident radiation and a probe size of 2 mm. Spectra were collected at ambient conditions by averaging 300 scans with 2 s time exposure at  $2\text{ cm}^{-1}$  spectral resolution and an average power of 300 mW.*

Infra-red spectroscopy is an analytical technique based on the absorption of the light. The latter has its characteristic frequency in the infrared wavelength region, which can interact with the molecule of the sample. The vibrating molecule absorbs the IR radiation; the characteristic frequencies absorbed are related to the structure of the molecule, which generates a transition in its vibrational energy levels.

Raman spectroscopy is based on very weak inelastic scattering (Raman) of light, where the light source is a laser. The Raman spectroscopy gives information about the chem-

## 4. Investigation methods

---

ical structure and the physical state of the samples; in particular, the investigated system can be identified by the vibrational, rotational, and other low-frequency modes resulting from the interaction between the molecules and the electromagnetic radiation in a characteristic shift in the energy of the photons. The scattered light is collected through the same lenses and pass through various gratings and notch filters. The latter cut any other more intense radiations, leaving only the weak Raman scattering signals.

Raman and IR spectroscopy are complementary. For instance, some modes can be Raman active and IR silent (or *vice versa*).

## 4.2 Imaging techniques

### 4.2.1 Optical Microscopy

*In this thesis, the light microscopy analyses were performed using a Leica microscope equipped with a CCD camera in the framework of the HA ceramics activities. The investigation was done on the cross-section of pellets to identify differences in the macroporosity of the samples and the deformation induced by the thermal treatments. The specimens preparation were done by incorporation of the samples in a resin, and then they were ground and polished according to a standard metallographic protocol.*

The optical microscope, also called light microscope, uses the visible light and magnifies the image of a sample through a system of lenses. Nowadays, the microscopes are equipped with CCD cameras, and the micrographs are digital, directly shown on a computer screen, without using the eyepieces.

### 4.2.2 Scanning Electron Microscopy with Focus Ion Beam system

*Scanning Electron Microscopy (SEM) analyses were done on calcium phosphate samples collected after precipitation experiments and on titanium samples coated with calcium phosphates. The collected powders after the precipitation were dispersed in isopropanol and deposited on the standard copper grid for transmission electron microscopy. The material grown on the titanium surfaces was investigated directly without carbon sputtering, introducing the discs (or screws) directly into the SEM chamber. The FIB technique, coupled with SEM, was applied to obtain a cross-section of the titanium*

discs, both uncoated and coated with calcium phosphate layer. When necessary, a thin carbon layer was deposited near the milled area to protect the sample from melting induced by the beam. The morphology analyses were done by a ZEISS NVision40 FIB/SEM. The cross-beam focused ion beam system (Schottky field emission gun for the electron column) is equipped with ESB, SE2, inlens, QBSE, STEM and EDX (Oxford) detectors, a micromanipulator (Keindiek) as well as with a cryo shuttle (VCT100, Leica) and cryo stage (LEICA) for treatment of frozen samples in the FIB and for their transfer to other instruments. An example of a cross-section prepared using the FIB is reported in figure C.2.4.

Scanning electron microscopy technique allows imaging the sample with a resolution down to 1 nm using an electrons beam as a radiation source, which presents a smaller wavelength than the visible light, used in the optical microscopes. In fact, under a microscope, the shorter resolved distance is proportional to the source wavelength, as shown by the *Abbe* relation reported in equation (4.1).

$$\delta = \frac{0.61 \cdot \lambda}{n \cdot \sin \alpha} \quad (4.1)$$

The cathode, for instance, a tungsten mono-crystal or a field emission gun (FEG), generates the electrons beam. It is accelerated through the microscope column, and focused by the use of condenser lenses down to a size of 0.4 nm to 5 nm, and kept under vacuum to avoid any possible interaction with the surrounding environment. The surface of the sample is scanned line by the line forming a raster. By synchronised scanning of the electron bundle across the sample with the image on the screen, an image is constructed, and a linear magnification is realised. By changing the size of the raster on the sample, the magnification can be altered, and a value of up to 500000 x can be reached.

The electrons lose their energy hitting the surface of the sample within a drop-shaped interaction volume (figure 4.1); that extends from less than 100 nm to around 5 µm, depending on the sample characteristics. These interactions generate different signals that are associated with the electrons mean free path,  $\lambda$  and the cross-section,  $Q$ . The former represents the medium path length of a particle, *e.g.* an electron, before its interaction with the sample, or better between successive collisions. The mean free path is related to the penetration deep of the electrons as expressed in equation (4.2),

$$\lambda = \frac{A}{N_0 \cdot \rho \cdot Q} \quad (4.2)$$

## 4. Investigation methods

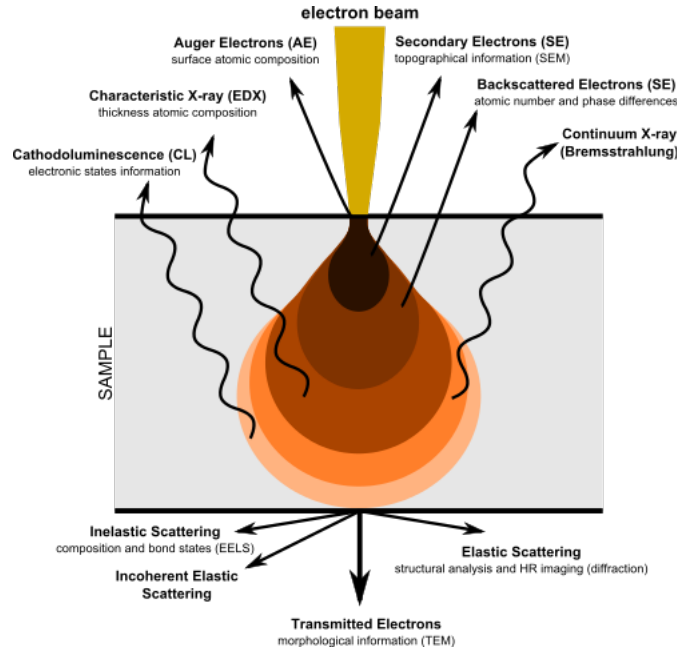


**Figure 4.1** – A schematic illustration of the interactions between a beam of high energy electrons and a sample.

where  $A$  is the atomic weight,  $N_0$  is the Avogadro number ( $6.022 \times 10^{23} \text{ atoms mol}^{-1}$ ),  $\rho$  is the density.  $Q$  quantifies the probability of interaction between beam and specimen; this probability is expressed in terms of area.

The cross-section is defined as

$$Q = \frac{N}{n_t \cdot n_i} \quad (4.3)$$

where  $N$  is the number of events per unit volume,  $n_t$  unit of target particles per unit of volume,  $n_i$  number of incident particles per unit of area. The most important interaction in the electron microscopy is given by the inelastic scattering of the secondary electrons (SE), with an energy  $< 50 \text{ eV}$ . Because of the low energy of the signal, SE can be produced within a deep of  $5\lambda$ . The secondary electrons emitted by the sample are detected and amplified to be finally represented on a screen as a grey dot where the intensity corresponds to the measured intensity. Depending on the topography of the sample more or fewer electrons will reach the detector, and the spot will appear more or less bright giving a three-dimensional appearance, but since they do not depend on the atomic number ( $Z$ ), the compositional contrast is almost zero. The samples for SEM analysis have to be stable under vacuum and conductive to avoid charging of the surface.

High energy backscattered electrons (BSE) are electrons beam emitted by the sample after different inelastic collisions with the samples electrons; they have energy close to the incident beam. The amount of BSE produced is proportional to the mean atomic number of the emission point, which allows the sample observation through a compositional contrast. The sample areas composed of atoms with higher atomic number give a higher signal that generates lighter areas in the elaborated image on a computer screen. The contrast difference is proportional to the difference in the atomic number of the compared areas.

The energy dispersive X-ray spectroscopy allows measuring the elemental composition and orientation of the specimen. The high energy electrons beam promote the ionisation of the core electrons of the sample. The transition of the electrons from an excited energy state to the ground state generates characteristic X-ray emissions. These signals are collected by an energy dispersive solid detector (ESD), and after several elaborations, the emission spectrum is obtained.

The Focused ion beam (FIB) technique is used in many different fields and, recently, it becomes a powerful tool for material and life science. FIB systems use a focused beam of ions (*i.e.*, gallium). In the biological field, FIB is mostly applied for site-specific analysis, deposition, and ablation of materials. In fact, compared to electrons, ions have a higher mass and higher momentum. Thus, when interacting with a sample, ions modify it by implantation, sputtering, or milling. Moreover, a gas precursor can react under the ion beam that induces a vapour deposition onto the sample surface, as a protective layer. The most applied is the tungsten, but platinum, cobalt, carbon, and gold are often used. When the FIB is coupled with an SEM, a dual beam station is generated. Using this configuration, the FIB is used for TEM lamella preparation, cross-section, and tomography. To prepare both lamellas and cross-section areas, the sample is first covered by a protecting material, *i.e.* carbon. The lamellas are prepared and lift-out *in-situ* using a micromanipulator; the obtained lamellas is then glued on support. To prepare the sample for the cross-section, a hole is milled before the area of interest creating a flat surface perpendicular to the sample surface. Moreover, when a flat surface is obtained, it is possible to cut slices through the region of interest generating 3D images (tomography).

## 4. Investigation methods

---

### 4.2.3 Transmission Electron Microscopy

*To investigate the precipitated powders, the samples were collected and dispersed in isopropanol. One suspension drop was deposited onto carbon coated copper grids. A JEOL JEM 2010 transmission electron microscope was used; it is equipped with a LaB<sub>6</sub> cathode, a high-resolution pole piece, an EDX-detector (Oxford) and an EELS spectrometer (Gatan, Enfina). Moreover, a Talos Transmission Electron Microscopy (TEM) ThermoFisher is equipped with CETA camera (16 Mpixel CMOS), HAADF STEM, Super-X EDS system, characterised by high voltage (80 kV, 200 kV), and an X-FEG emitter, was used. TEM has been largely used and examples are given in section 3.2. The early stage of calcium carbonate precipitation was investigated using the JEOL JEM 2200FS microscope. This cryo-transmission electron microscope is equipped with a Schottky field emission gun, a tomography stage, an in-column filter for EELS/EFTEM, and a CMOS camera (TVIPS). Moreover, it has a cryo-shield and a high-tilt pole piece, which are optimised for the imaging of biological samples. The solution samples, collected before the critical supersaturation value for the different calcium carbonate experiments, were deposited onto a standard carbon grid and immediately vitrified in liquid ethane. Neither clusters nor dense aggregate has been observed for the different conditions.*

The transmission electron microscopy technique allows the analysis of samples down to the sub-nanometric range thanks to the low wavelength of the electrons. The electron beam is generated and accelerated by the gun; the beam is focused by a series of condenser lenses until it interacts with the specimen. The diameter and the intensity of the beam can be controlled by these lenses. Below the samples, there is the objective lens, and selected area electron diffraction (SAED) aperture can be inserted. The beam after the interaction with the samples hits the objective lenses; here the images are created and can be further magnified by the projector lenses. It is possible to create magnified images and diffraction patterns controlling the projector lenses.

TEM images can be generated in two different operation modes. In the bright field imaging mode, the image is generated by the electrons in the direct beam, while in the dark field imaging, the scattered electrons generate it. The incoherent electrons, the elastically-scattered electrons, the atomic number, and even the thickness of the sample influence the image contrast. Since the beam has to be transmitted through the sample, it should not exceed 100 nm in thickness.

Especially in the case of a crystalline sample, the electron beam undergoes Bragg scat-

tering, and diffraction occurs as a consequence the orientation and the structure of the crystalline sample. The apertures are placed above the sample allow the selection of a sample specific area (SAED). The specimen can be moved to investigate different diffraction conditions by tilting the sample holder. The electron diffraction measurements generate 2D diffraction patterns. A crystalline sample generates spots, while a polycrystalline nanostructured sample generates rings. The amorphous samples give halos.

In Scanning Transmission Electron Microscopy (STEM) mode, a fine spot is investigated by a highly focused electrons beam. The sample is scanned, using scanning coils, placed over the specimen in a raster. The STEM is equipped with more scanning coils and detectors than a conventional TEM microscope. Because the objective aperture is located over the samples, this instrument allows analysing samples with a greater thickness than in the conventional TEM mode. Moreover, it permits microanalysis with a much higher resolution.

Cryo-TEM is a special type of TEM technique where the sample under observation is rapidly frozen and embedded in a thin film of vitrified amorphous ice for preservation purposes. The thin specimen, after deposition on the support, is rapidly plunged into a liquid ethane bath. The rapid freezing prevents the crystallisation of the water contained in the specimen itself so that the signal contribution related to the crystalline - ice is reduced. In fact, when the crystalline ice is formed, it readily absorbs the electrons beam, and the sample is obscured. Liquid nitrogen or ethane is applied in the freezing procedure. The ethane has higher heat capacity and is also liquid at temperatures slightly above that of liquid nitrogen; the ethane is sufficiently cold to freeze water rapidly and appropriately without boiling off.

The advantages of this technique are associated with the beam damage reduction on the sample, which is usually a classical issue in the standard TEM, especially for biological samples. The specimen can be studied in its native environment or suspended medium, preserving its mutual temporal and spatial arrangements without having to deal with drying-out effects under vacuum, which is usually the case with standard TEM observation.

## 4.3 Dynamic light scattering

*For this thesis, dynamic light scattering (DLS) measurements were conducted using a Zetasizer Nano ZS (Malvern instruments). On-line and ex-situ analyses were per-*

## 4. Investigation methods

---

*formed. In the case of CaC and CaP experiments, it was impossible to get reproducible measurements, because the concentration of such species was too low to be detected by the instrument. Therefore, the measurements are not reported in this thesis. Instead, the technique was used to characterised the synthesised gold nanoparticles (section C.3).*

Dynamic light scattering is used to determine the size distribution of particles or polymers dispersed in a solution. The temporal intensity fluctuations due to the Brownian motion of the particles [167] depends on their size. The information about the velocity of the motion, and therefore the particles size is obtained using an autocorrelation function. The laser, light source of the instrument, illuminate the sample, disposed of in a cuvette. The light that hits the particles is scattered in all possible directions. The detector measures the intensity of the scattered light in a specific direction with respect to the incident beam.

### 4.4 Titration

*In this work, the conductometric and acid-base titrations are used to measure the concentration of the NaOH solutions and its carbonate content.*

The volumetric analyses (titrations,) represent one of the quantitative analytical techniques. It is used to determine the unknown concentration of an *analyte* contained in a solution, called *titrand*, via the addition of a reagent solution, called *titrant*, with a known concentration. The final titration point is called equivalence point, which represents the volume of *titrant* needed to neutralise the analyte. The equivalence point allows calculating the concentration of the *titrand* solution. There are different types of titrations, depending on the measured quantity to determine the equivalent point, that is directly related to the chemical reaction involved in the titration, such as acid-base, conductometric, potentiometric, red-ox, complexometric titrations.

#### 4.4.1 Potentiometric measurements

*In the framework of this doctoral activity, potentiometric measurements were used mainly to study the formation of the solid from solution. In chapter 2, section 1.2.2.1 reports the analytical tools used for such measurement and the methodology applied to collect appropriate kinetic data. Moreover, the experimental results are reported in chapter 4 for both calcium carbonate and calcium phosphate systems.*



Potentiometry measures the chemical potential of a specific ion in solution using an electrochemical cell. The cell is composed by two semi-cells (electrodes), one is sensitive to the variation of the activity of the *analyte*, and the other one is a reference cell (e.g. Ag/AgCl). The two semi-cell can be combined in one electrode (combined electrodes). The electrode has to be immersed in a solution containing the *analyte* to measure a potential difference between the two semi-cells. The reference electrode has a highly stable potential due to the stable concentration of the electrode-electrolyte solution in which it is immersed. The electrode is electrically connected to the solution via a junction, the diaphragm; the latter allows an out-flux of the electrolyte solution. This flux, which has a defined rate depending on the diaphragm material, prevents the diffusion of the *analyte* solution inside the electrode. The depletion of ions from the high electrical conductive solution generates the potential. The ion-sensitive electrodes (ISEs) possess a high degree of selectivity for a specific *analyte*. The selectivity is determined by the membrane of the ISE. Ideally, the membrane allows the uptake of only one specific ion into it. It can be hydrophilic or hydrophobic, depending on the selectivity of the electrodes.

In the case of a pH electrode, the membrane is made of glass. The hydrogen ions contained in the analyte solution move toward the glass membrane and an ion-exchange equilibrium is established at the solution membrane-interface. The different degree of hydrogen-ion activity on the two surfaces of the glass generates a charge difference. In the case of ISEs used, the membrane is polymeric and contains an *ionophore*, a neutral “carrier” molecule (chelating agents). It cannot diffuse out of the membrane but can “trap” (selective binding) the *analyte* ion at the interface between the solution and membrane. This ion transport process occurring at the interface develops the potential. Again, the final signal is generated by the potential difference between the reference system and the measuring system.

Within the electrode housing, a temperature sensor can also be allocated, typically a Pt100 or a Pt1000. The potential measured by the electrode is proportional to the logarithm of the *analyte* ion activity in solution. This relation is given by the Nernst equation (4.4).

$$E = E_0 - \frac{RT}{nF} \cdot \ln(a_i) \quad (4.4)$$

where  $E$  is the electrode potential,  $E_0$  is the standard potential of the electrode,  $R$  represents the universal gas constant ( $8.314 \text{ J mol}^{-1} \text{ K}^{-1}$ ),  $F$  is the Faraday constant ( $96485 \text{ As mol}^{-1}$ ),  $T$  is the temperature in K,  $n$  represents the charge of the ion or number of

## 4. Investigation methods

electrons participating in the reaction,  $a_i$  is the activity of the ion  $i$ . The exact values for  $E_0$  as well as the pre-logarithmic factor are determined using a calibration method and an appropriate model for the calculation of the activity coefficients.

Calibration experiments for ISEs can be performed using standard solutions in the same condition of the measurement operations. The activity coefficient of an ion depends on its charge, hydrodynamic size, the ionic strength (IS), and the temperature of the solution (eq. (2.12), in section 2.1.1). To minimise the error of the measurement, the experiment should be run in conditions where the calibration curve shows a linear behaviour.

### 4.5 Investigation using X-rays

#### 4.5.1 X-ray scattering and diffraction

*For screening and standard analyses, XRD patterns were collected with a Bruker D8 Advance diffractometer (Cu  $K_{\alpha}$  radiation) in the angular range between  $2^\circ$  to  $100^\circ$   $2\theta$ , with a scan rate of  $1^\circ \text{ min}^{-1}$ . This analysis was applied to characterised calcium phosphate powder, of the samples related to CerInk project (calcium phosphate), and for the Ti discs coated with phosphates. The dried powder was disposed of directly in the standard holder, while the discs were attached to the holder, preserving the alignment with the holder surface. During my work at PSI, I was responsible for such equipment, and I was in charge also to define the in-situ X-ray diffraction (XRD) experiments under reactive atmosphere and high temperature for my lab.*

X-ray diffraction (XRD) is a non-destructive X-ray elastic scattering technique used to analyse solid structures. This analysis provides averaged structural information on the bulk. In fact, the X-ray can deeply penetrate the material. The wavelength of X-rays photons is in the range between 0.01 and 10 nm (100 eV to 100 keV), *i.e.* in the same order of magnitude of the interatomic distances. The interference behaviour between X-ray waves, being scattered from different crystal planes, gives rise to constructive and destructive interference. Bragg's law gives the condition of constructive interferences:

$$n\lambda = 2d \sin\theta \quad (4.5)$$

with  $\lambda$  the wavelength of the electron beam,  $d$  the spacing between the lattice planes

and  $\theta$  the angle of the diffracted wave. Depending on the crystal structure and the related  $d$ -spacings, constructive interferences occur at different angles giving rise to a characteristic XRD pattern being a fingerprint of the crystalline ordering of the material. If the scattered beam has the same energy of the incident one, meaning that the X-rays photons did not lose any energy because of the interaction with the matter and that only momentum has been transferred, the process is elastic, and it is called Thompson scattering. When some of the energy of the incident photons is transferred to the sample, the scattering is inelastic, and it is called Compton scattering. In this case, the scattered X-rays will have a different wavelength compared to the incident beam.

The elastic scattering of the diffracted X-rays provides the crystalline information about the structure of the material under investigation, that is derived from the density and distribution of electrons in materials. Moreover, it allows to detect the presence of polymorphs and quantify them. Considering the wave-like properties of the X-ray, the diffraction of such waves by matter is due to the combination of two phenomena:

- the scattering of X-rays by the different electrons in the individual atoms;
- the interference between the scattered outgoing waves from these atoms.

The scattering vector,  $\vec{q}$ , is the difference between the diffracted ( $\vec{K}_d$ ) and incoming ( $\vec{K}_i$ ) wave vectors,

$$\vec{q} = \vec{K}_d - \vec{K}_i \quad (4.6)$$

$$q = |\vec{q}| = \frac{4\pi}{\lambda} \sin \theta \quad (4.7)$$

being  $2\theta$  the scattering angle,  $k = \frac{4\pi}{\lambda}$  the wave number (which is conserved because of the elastic scattering), and  $\lambda$  the wavelength. By recording the intensities of the scattered beam as a function of the angle  $2\theta$ , the pattern with the peaks characteristic of the sample is obtained. X-rays scattering and Bragg diffraction can access the morphological and structural information of the investigated materials. In fact, the atomic crystal structure can be solved, and the crystalline phases contained in a mixture can be quantified. Depending on the information needed, it is possible to realise a different experiment and to use a specific scattering technique among the available ones. However, scattering occurs on every atom, creating secondary waves.

## 4. Investigation methods

---

The interference among the secondary waves, diffracted by each atom in the cell, which explains the Bragg diffraction pattern. The higher the lattice coherence, the larger the number of ordered cells, the stronger the interference, i.e., the sharper the Bragg diffraction peaks.

Wide Angle X-ray Diffraction (WAXD) is crucial to investigate a crystalline material at the atomic scale; from WAXD patterns, it is possible to obtain reliable quantitative results on shape, size distributions, and defects using the whole pattern approach, such as using the Rietveld refinement (see section 4.5.2). It is possible to collect diffraction pattern down to an angular range as low as  $2\text{--}5^\circ$  (depending on the equipment used). Below  $2\theta = 1^\circ$  small angle X-ray scattering (SAXS) can be spanned. This technique provides information at the nanometric scale, such as morphological features of particles (size, shape, and density).

The standard WAXD analyses were done using Bruker D8 Advance diffractometer. It presents a  $\theta - \theta$  Bragg-Brentano geometry using a conventional  $\text{Cu } K_\alpha$  X-ray tube. In this geometry, both the X-ray source and the detector rotate towards each other maintaining the same angle with respect to the flat sample surface. Thus, the diffraction vector, bisecting the incident and scattered beam, always coincides with the normal vector of the sample surface. The XRD patterns provided by standard lab instruments carry substantial and unequivocal information on particles that are sufficiently large ( $>2\text{ nm}$ ), but the technique is silent to particles below that size and amorphous matter. This instrument is usually used for conventional *ex-situ* room-temperature characterisation of as-prepared and thermally treated or spent samples. It is also possible to carry out experiments under non-ambient conditions, using typical chambers. The samples can be a study from  $25^\circ\text{C}$  up to  $900^\circ\text{C}$  and use reactive atmospheres.

### 4.5.2 Rietveld analysis

*In this work, GSASII was used for the Rietveld analyses of the diffraction pattern [168]. Using this analysis, the discrimination and quantification of the different phases present in the powders of calcium phosphates after precipitation under biorelevant conditions were assessed (see section 3.2).*

The Rietveld method is known as a whole or full pattern analysis technique which can analyse the height, width, and positions of the XRD peaks to extract and quantify structural information [169]. A theoretical (calculated) diffraction pattern is generated from

the crystal structure, together with instrumental and microstructural information. Thus, this pattern is compared to the observed data, and the least squares method is used to minimise the difference between them. By adjusting the model parameters, the theoretical pattern is refined until the best possible match is obtained. It is, therefore, possible to create a virtual separation of overlapping peaks and accurately determine the structure, which would be prevented otherwise because the results of the factors giving rise to the observed peak shape are convoluted. Some programs that can be used in structure determination are GSASII, TOPAS, FullProf, and a few others.

### 4.5.3 Synchrotron radiation

*Synchrotron radiation was largely used in the framework of this thesis and collaborative activities. WAXS and SAXS were done at the Material Science beamline (SLS-Villigen PSI), WAXS at ID11 (ESRF- Grenoble ), and X-ray absorption spectroscopy XAS (XANES/EXAFS) at the LISA (ESRF- Grenoble), and during the Hercules European school different beamlines at ESRF and DESY (Hamburg). Ex-/in-situ synchrotron diffraction measurements were collected at the Material Science beamline (MS-X04SA) at the Swiss Light Source at PSI. Experimental details are given in section 3. The experiments were done on powders collected after precipitation studies in the lab (WAXS analyses).*

The synchrotron light is produced when charged particles are accelerated to relativistic speed. These particles are produced in the electron gun at an energy of 90 keV. Once produced, the electrons are accelerated within a linear particle accelerator (linac) to 100 MeV, and then, they are further accelerated to a maxim speed into the booster, a circular accelerator. Then the high energy electrons are kept accelerated with an (almost) circular trajectory in the storage ring under vacuum using bending magnets and quadrupoles. Moreover, the beam is maintained collimated in both directions perpendicular to the direction of the observation, thanks to undulators and wigglers allocated in the ring. Because of the acceleration and the electromagnetic field in which they are immersed, their speed is almost the speed of light that corresponds to high energy of different GeV. The electrons lose energy every time that their direction is deviated by the magnets. The speed of the particle is inversely proportional to the wavelength of the emitted radiation; the critical wavelength usually corresponds to 0.5 Å which is in the range of wavelengths needed for the X-ray studies. The emitted radiation is canalised in linear sections, tangents to the ring, called beamlines. In this sectors, using optics and monochromators, the beam is optimised depending on

## 4. Investigation methods

the characteristic analysis required for the sample investigation. In the experimental hutch, the experiments take place after that the desired wavelength has been set. The synchrotron light is used in many different applications such as XAS (X-ray absorption spectroscopy), and high energy diffraction and scattering. The synchrotron X-ray is characterised by high brilliance due to its high collimation, which is related to the photon flux impinging the sample and it leads to a very low signal-to-noise ratio. The high coherence of the beam produced by synchrotron facilities permits to investigate diffracted angles as low as  $\approx 0.05^\circ$ . Moreover, it allows the collection of time-resolved data with acquisition times as low as 1 ms.

### 4.5.4 Small Angle X-Ray Scattering at the Material Science beam-line X04SA (SLS-Villigen PSI)

*In the framework of this research activity, SAXS analyses were applied to study the early stage of precipitation at the Swiss Light Source (SLS) at the beamline of Material Science X04SA. Two different detectors were applied, such as the Mythem (Microstrip sYstem for Time-rEsolved experimeNTs) detector, and a 2D direct-detection photon counting detector systems such as the PIxel apparATUs (PILATUS, DECTRIS). In these experiments, the data were collected from a liquid-jet of supersaturated carbonate or phosphate solution. The characteristics of setup and experimental conditions are reported in section 1.6.*

In the SAXS measurements, the angular range investigated is between  $0.05^\circ$  to  $1^\circ$ . The detector is placed at a longer distance in comparison with WAXS analyses in order to collect data at low angles with high resolution. SAXS patterns are usually plotted as intensity profiles over the scattering vector,  $q$  ( $\text{\AA}^{-1}$ ):

$$q = \frac{4\pi}{\lambda} \sin\theta = \frac{2\pi}{d} \quad (4.8)$$

It is possible to define two the region of interest, the Guinier regime, which mainly gives information about the radius of the scattering objects, and the Porod regime, which provides additional information about the liquid-solid interface in suspended particles. In the data analysis, the signal intensity is plotted *vs*  $q$ , as depicted in figure 4.2. In the Guinier regime, the relationship between the measured intensity and the  $q$

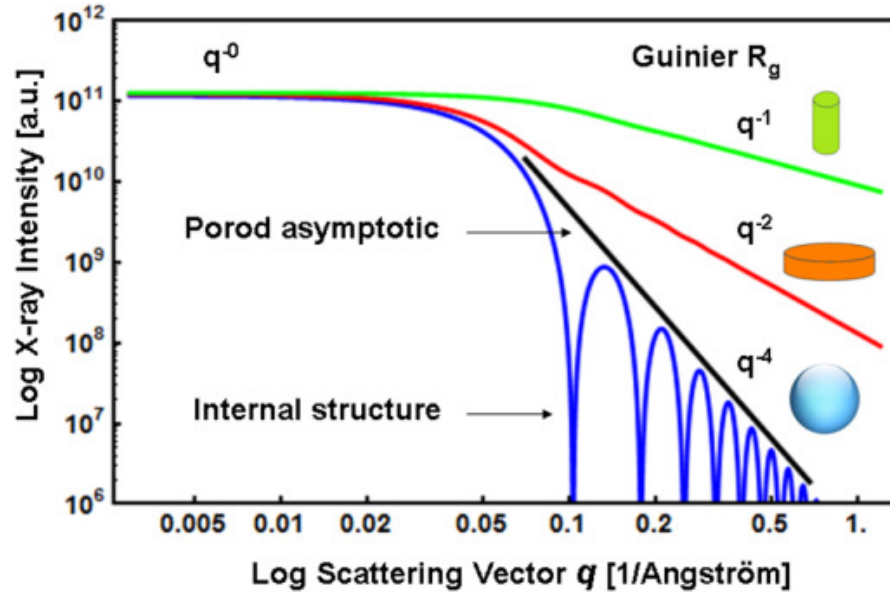


Figure 4.2 – Guinier and Porod regime in SAXS analyses.

value can be described as

$$I(q) = I_0 \exp\left(-\frac{q^2 R_g^2}{3}\right) \quad (4.9)$$

with  $I_0$  representing the extrapolated intensity of the signal at  $q = 0$ , and  $R_g$  being the radius of gyration.  $R_g$  is the weighted average radius of all cross-sections through a particle and can be obtained from plotting  $\ln(I(q))$  vs  $q^2$  of the Guinier region and determining the slope of the graph [170]. This data analysis allows the evaluation of the size of the heterogeneities. If the particles are spherical and monodisperse, the derivation is simplified. Otherwise, more complex models need to be applied.

## 4.6 Thermal analyses

Thermo-gravimetric Analysis, differential thermal analysis, and thermo-mechanical analyses.

*In the framework of the CerINK project, the prepared pellets of calcium phosphate were analysed using a Mettler Toledo TGA/SDTA 851e equipped with autosampler working up to 1100 °C under controlled atmosphere. In the framework of this doctoral work, a Setaram SETSYS Evolution system equipped with TMA module was used to study the sintering properties of the porous HA ceramics. A load of 2 g was applied, and the*

## 4. Investigation methods

---

*sintering profile measured in flowing air up to 1500 °C. For these investigations, 5 mm diameter, 5 mm height green pellets were produced by uniaxial pressing (2 Tons). The samples were treated first in the TGA, up to 800 °C, where the weight loss, DTA, and evolved gas were measured and then sintered in the TMA. These activities are briefly described in section C.1.*

During thermal analysis, the physical and chemical properties of the samples are measured as a function of the temperature and time. In a thermogravimetric analysis (TGA), usually, a programmed thermal profile is defined, and the weight change of the sample against temperature is analysed. The mass gain or loss provides information about physical (and chemical) phenomena, such as a change in composition, degradation mechanisms, burnout of organics, volatilisation of inorganics, *etc.* Using the differential scanning calorimetry (DSC), or the differential thermal analysis (DTA), is possible to investigate processes that are associated to exothermic or endothermic transformation by measuring a differential signal between the sample and the inner reference. The DSC measurements evaluate the heat flow at a constant temperature during the transformation, whereas in the DTA analyses the temperature difference between the sample and the reference is measured. TGA and DTA (or DSC) are combined in a single instrument having TGA-DTA signals simultaneously. The instrument is composed of a precision balance connected to a sample holder stage, both housed in a furnace, which provides the controlled heating and cooling of the sample. The balance can host the sample, placed in a ceramic or metallic crucible, and the reference crucible. Both balance and furnace are purged with gasses to maintain a controlled environment. The gas is inert in the balance, while the furnace can be purged with reactive gases. The instrument may be connected with a mass spectrometer MS, and then is possible to analyse the effluent gasses (the evolved gas analysis, EGA) induced by the thermal treatment. The hyphenated system is then a TGA/DTA/MS-EGA equipment.

The mechanical properties of a sample against temperatures, such as expansion coefficient, tensile modules, and sintering behaviour, are measured by the thermomechanical analysis (TMA). As for the techniques described above, in this case also, the nomenclature for the analysis can vary, depending on the load applied to the sample; in the TMA, a particular load is applied on it, while in the “Dilatometry”, no load is applied. In both techniques, the sample deformation is measured as a function of temperature. The influence of the load on the measurement is sample dependent. For a specific sample, when the applied load is low enough, the difference between the



two techniques vanished.

4. INVESTIGATION  
METHODS

## 5 | Concluding remarks

In this section, the significant findings of this doctoral thesis on *the precipitation pathway of biorelevant* minerals are summarised. The precipitation of calcium carbonate (CaC) and calcium phosphate (CaP) systems were defined as scientific thesis objectives.

Beside the basic-science objectives, other two activities were pursued: an *applicative* study, as a direct consequence of the fundamental scientific outcomes, and a *pragmatic* study. Additionally, more *explorative* activities were carried out.

### Conclusions on the precipitation modelling

This section reports the conclusions related to the basic-science activities, namely the calcium carbonate and the calcium phosphate precipitation studies. The scientific problems were approached using a multidisciplinary approach, where an accurate *in-situ* time-resolved non-invasive analytical method was combined with standard and cutting-edge characterisation techniques, and with a computational tool.

The application of such an approach allowed the deconvolution of a complex problem, such as the solid formation pathway, into its elementary processes (*deconvolution approach*). This approach was applied for both calcium carbonate and calcium phosphate systems.

The accurate analysis has allowed the design of a new “strategy”, the understanding of the overall processes, and – combined with other system-specific findings as summarised in the following sections – it represents the primary scientific contribution of my doctoral work. The novelty of this strategy consists of focusing the analysis on the experimental data where the precipitation process is under kinetic control and into the meaning of the quantities expressed in the formulation of the involved elementary

## 5. Concluding remarks

---

processes. In particular, the diffusion coefficient of the growth unit was correlated, through the Einstein equation, to the size of the building unit and indeed unravelling the details of the solid formation pathway of both systems.

Furthermore, in the mathematical formulation of the classical nucleation theory, approximations are included, *e.g.*, the independence of surface energy to the embryos-nuclei size. Nevertheless, if the supersaturation during the nucleation stage is almost constant – as demonstrated to be the case for the studied systems – the surface energy can be considered constant as well. It turned out that the classical nucleation theory can be applied since the discussed approximation has no theoretical implication on its validity.

Moreover, the calculated surface energy values, extracted from the nucleation rate, have to be properly addressed to the specific nucleating matter, considering its size and physicochemical properties and neither to the macroscopic solid nor the final product of the precipitation process.

Nucleation is very sensitive to small variations in conditions, which may be reflected in a significant variation in the nucleation-derived surface energy values. Thus, different experimental conditions could lead to different nucleating matter, which is associated with different surface energy values. With this understanding, it becomes comprehensible why the surface energy values published in the literature for each material are widely variable.

### Calcium carbonate system:

#### amorphous calcium carbonate formation pathway

Several datasets on amorphous calcium carbonate precipitation were collected and the same rigorous model, based on the classical nucleation theory and the classical precipitation pathway, was applied. The agreement between the calculated and experimental data shows that the precipitation pathway is in agreement with a combination of primary nucleation, “true” secondary nucleation, and diffusion controlled growth.

The thermodynamic quantities for amorphous calcium carbonate, as well as for two chemical species formed as a consequence of the interaction between carbonate ions with ACC and with  $\text{CaCO}_3^0$ , were regressed. The surface and the cohesion energies for about 2 nm amorphous calcium carbonate entities were estimated to be  $30 \pm 5$

$\text{mJ mol}^{-1}$  and  $38 \pm 5 \text{ mJ mol}^{-1}$ , respectively. Moreover, the solubility of amorphous calcium carbonate as a function of  $T$  and  $pH$  was defined. These thermodynamic quantities were not available in the literature. Consistent with a classical crystallisation mechanism, the growth mechanism is limited by the diffusion of  $\text{Ca}^{2+}$  and  $\text{CO}_3^{2-}$  ions on the solid particles. Thus, clusters do not take part in the growth process and if present act as spectator species.

It was possible to assess the concentration of ion pairs during the entire precipitation, but it was not possible to disclose their nature (monomeric or polymeric species). These findings were published in the journal *Crystal Growth and Design* (first author).

Different techniques were applied to study the early stage of the amorphous calcium carbonate precipitation and, considering the latest literature results, cryo-TEM and SAXS were selected in this doctoral work.

Cryo-TEM analyses – done with the support of experts in the field - were applied to investigate if the clusters are present in the pre-nucleation zone, and were not able to assess their existence. To our experience, this can be due to the low concentration of such species in the solution or as a consequence of the operations carried out during the TEM sampling.

Nevertheless, our latest studies carried out using liquid jet SAXS measurements seem to confirm the existence of clusters in solution before the critical saturation for nucleation and even in undersaturated solution. The most plausible interpretation of the experimental results indicates the presence of small clusters of about 2 nm to 3 nm and a broad population of superclusters. Their density increases approaching the critical size. According to this interpretation, there is no preferential size but a continuous de-hydration (and the consequent increase of density) processes of the clusters from undersaturated solution until the critical conditions. The overall concentration of  $\text{CaCO}_3$  units in the form of clusters is in the order of  $10 \text{ mg L}^{-1}$ . These findings will be reported in a scientific publication under preparation (section 3.3).

### **Calcium phosphate system: formation and transformation of calcium phosphates**

Following a similar approach as for the calcium carbonate system, a quantitative thermodynamic-kinetic model for octacalcium phosphate (OCP) and hydroxyapatite

## 5. Concluding remarks

---

(HA) formation was developed. The mechanism involves the formation of an intermediate phase, namely dicalcium phosphate dihydrate (DCPD), which then disappears by recrystallisation. Afterwards, the formation of OCP or HA takes over. The value of the ionic strength seems to influence the selection of the formed solid phase, probably because of its influence on the activity coefficient on phosphate ions. The estimated surface energy and cohesion energy from nucleation rate for DCPD and corresponds to  $38 \pm 5 \text{ mJ mol}^{-1}$  and  $69 \pm 1 \%$  of the maximum theoretical value ( $2\Gamma$ ), respectively. The stability constant for Posner's clusters and their stoichiometry was also evaluated. According to the experimental data and modelling results, it is plausible that Posner's clusters play a role in the nucleation stage where they may incorporate  $\text{PO}_4^{3-}$  ions, generating primary and secondary nuclei of DCPD. The growth rate is consistent with a  $\text{Ca}^{2+}$  diffusion-limited model, but the influence of a surface contribution due to the particle shape justifies a lower *apparent* diffusion coefficient.

Despite the complex mechanism, all experimental data are consistent with a classical precipitation pathway, where primary and secondary nucleation events are considered, in which a transient phase is involved, and where the growth is mainly diffusion limited. These findings were published in *Acta Biomaterialia* (first author).

As for CaC, SAXS data were collected as well. In this case, the preliminary data analysis confirms the presence of pre-critical species but with a non-equiaxed shape. Because of the shape, the data treatment is more complicated, and the data analysis is still in progress.

### Application-oriented studies on calcium phosphate system

1. The *applicative* study was focused on the controlled deposition of CaP, specifically OCP, on Ti implants for biomedical applications, in particular for dental implants. As the details of the CaP formation mechanism are known, a controlled deposition can be achieved. The appropriate physicochemical conditions to promote the heterogeneous nucleation and growth of the wanted crystalline phase can be defined using the obtained thermodynamic-kinetic model from the fundamental study on calcium phosphate system, used in predictive mode. Specifically, tailored thickness and crystalline phase can be obtained in the shortest time (section C.2, EU patent application). This activity was driven by my interest in the field and has led to attractive perspectives and opportunities for a following project (see Outlook in section 5).

2. The *pragmatic* study was focused on the definition of a ceramic processing protocol, which includes 3D printing, finalized to the preparation of materials mimicking the density and mechanical properties of natural bones. Also, this target was achieved (section C.1), but a more extended optimisation study is needed to investigate the applicative potentialities.
3. More *explorative* activities were performed and finalized, as the continuous synthesis of gold nanoparticles using the segmented flow tubular reactor (section C.3). Here the aim was to produce nanoparticles for biocompatibility screening purpose, as a calibration standard for the liquid jet SAXS measurements, as well as to produce seeds for CaP heterogeneous nucleation. The latter topic was only partially explored and therefore not discussed in this dissertation, but it represents an exciting follow-up activity toward the preparation of gold NP-labelled synthetic biocements.

## General conclusions

In this chapter, I attempted to address the scientific questions posed at the beginning of the doctoral project, which are quoted in the introduction (Introduction, p.3).

- *If clusters are present before the nucleation stage, are they involved in the calcium carbonate and calcium phosphate crystallisation pathways?*
- *In which elementary process do they take part and, consequently, how does the Gibbs free energy landscape of the solid formation look like?*
- *Is it still possible to describe the experimental data in the presence of clusters using the classical approach?*

All the experimental data collected, via indirect and direct methods, on pre-critical species (clusters) are in agreement with their existence, and their concentration in the sub-critical saturation value is in the order of ppm. In the experimental conditions explored, the clusters seem not to be involved in the growth of the solid, *i.e.*, the crystallisation mechanism is in agreement with a classical pathway, that is, dominated by the incorporation on the solid surface of ionic species, such as  $\text{Ca}^{2+}$ .

Nevertheless, plausibly, clusters are involved in the nucleation stage, in particular in the “true” secondary nucleation. Therefore, in a more extended view, the solid

## 5. Concluding remarks

---

is indeed formed by “particle incorporation”, but these events should be properly addressed as “secondary nucleation events” and not “growth events”. Since these two elementary processes are characterised by a specific dependence on the saturation level and a specific activation energy barrier, their involvement in the solid formation pathway were evaluated using a complete thermodynamic-kinetic model.

Finally, a way to identify the specific Gibbs free energy landscape before the critical point could be the *in-situ* investigation of the clusters average size as a function of the supersaturation level. The access to these analytical data is complicated by the fact that the concentration of these species is very low. Some signals might be recognized above the background using cutting-edge investigation techniques, such as those discussed in this thesis. In the specific case of CaC and CaP investigated using SAXS the signal is very labile not only because of the low clusters concentration but also because of the limited difference in electron density between clusters and solvent. According to the experimental data analysed so far, the density of the cluster changes with their size, therefore both bulk and surface terms of the Gibbs free energy are affected. Thus, the picture seems even more complex than expected, paving the way towards further and exiting advanced investigations and interpretations!

## Outlook

The obtained results on the early-stage of the precipitation, combining model and experimental data, can be further explored and extended. The liquid jet setup is a powerful tool for the non-invasive study of such time-depended system, and the SAXS results represent a relevant step in the direction of *in-situ* controlled composition investigations. For instance, the liquid jet can be frozen in liquid nitrogen or liquid ethane and used for cryo-TEM investigations. Thus, the SAXS measurements can be compared with the cryo-TEM investigations, where both analyses refer to the same sample.

The difficulties associated to the detection of the pre-nucleation clusters associated to their low concentration in solution could be overcome using techniques offering an even higher signal-to-noise ratio, such as an X-ray Free Electron Laser (*e.g.*, the Swiss-FEL). Thanks to its outstanding brilliance, it is expected a substantial improvement of the data quality. The results obtained so far at the synchrotron identify reasons to invest toward such an effort.



---

On the application viewpoint, the controlled deposition of calcium phosphate on Ti implants, which immediately aroused the interest of industrial partners, has defined an exciting perspective toward the application of the scientific results. The coating procedure was explicitly applied for dental implants, but other metal implants can be coated, such as spine or hip implants, or the coating performed on other metals, alloys, or polymers. In a more general view, several materials can be coated with a precipitating ceramic phase, to improve their functionality or to prevent their degradation, provided that the details of the precipitation pathway of the ceramic phase are studied.

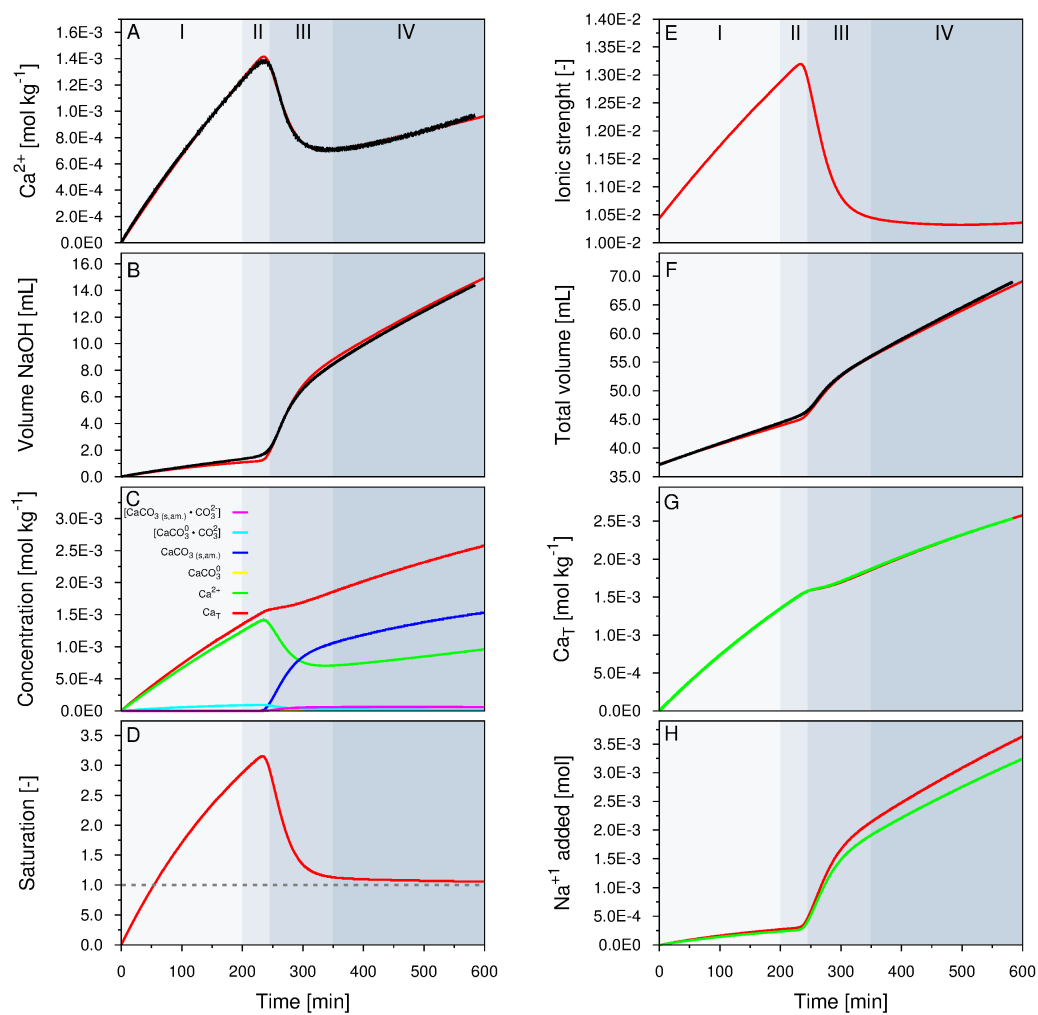
5. CONCLUDING  
REMARKS

## A | Calcium carbonates

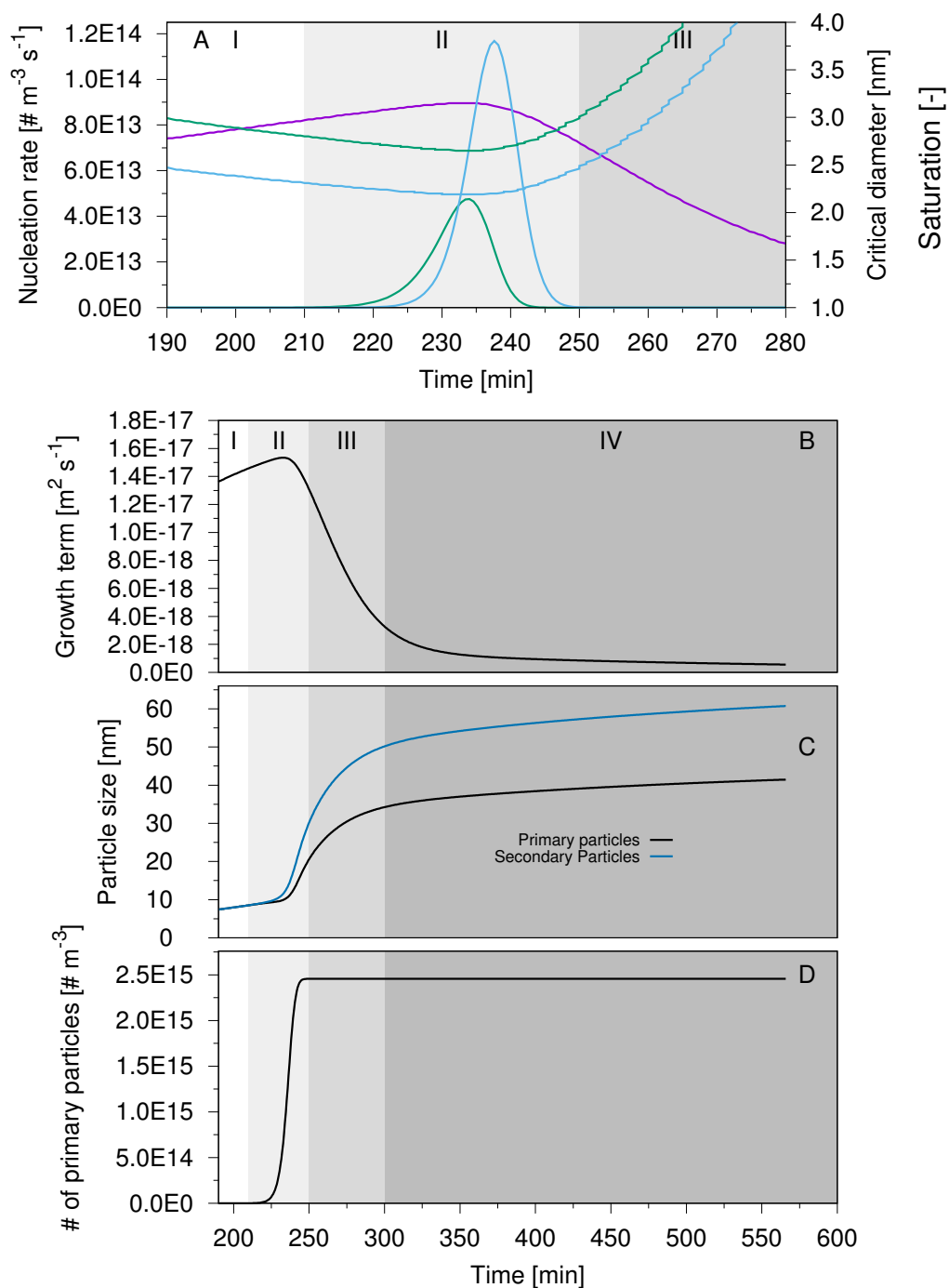
### A.1 TD and K results for all datasets

Label applied for all Figure A.*odd numbers* at the indicated experimental conditions. Experimental (black) and calculated (colored) data for the experiment at  $T=278.35\text{ K} \pm 0.2\text{ K}$  and  $pH=9.00 \pm 0.02$  against time. (A)  $\text{Ca}^{2+}$  molality in solution, derived from the ISEs electrodes; (B) volume of NaOH added into the system to achieve iso-pH conditions; (C) relevant chemical species; (D) calculated saturation. The horizontal dotted line in highlights the condition  $S=1$ ; (E) ionic strength; (F) experimental total volume (black) and calculated (red); (G) total Ca into the system experimentally added (green) and an calculated form the mass balance Eq. 11 (red); (H) sodium amount calculated from Eq. 10 (red) and from Eq. 3 (green). The discrepancy is due to cabonation of NaOH solution, experimentally measured. The Roman numerals refer to the zones associated to the precipitation evolution and identified by shaded greys.

Label for all Figure A.*even numbers* (second page) at the indicated experimental conditions – Calculated kinetic data on particle evolution. (A) Primary (green) and secondary (blue) nucleation rates, supersaturation (red), and critical nucleation size for primary homogeneous (dashed green) and true secondary nucleation (dashed blue) against time; (B) linear growth rate; (C) averaged primary (orange) and secondary (yellow) particles size, calculated as described in the text; (D) number of primary particles.

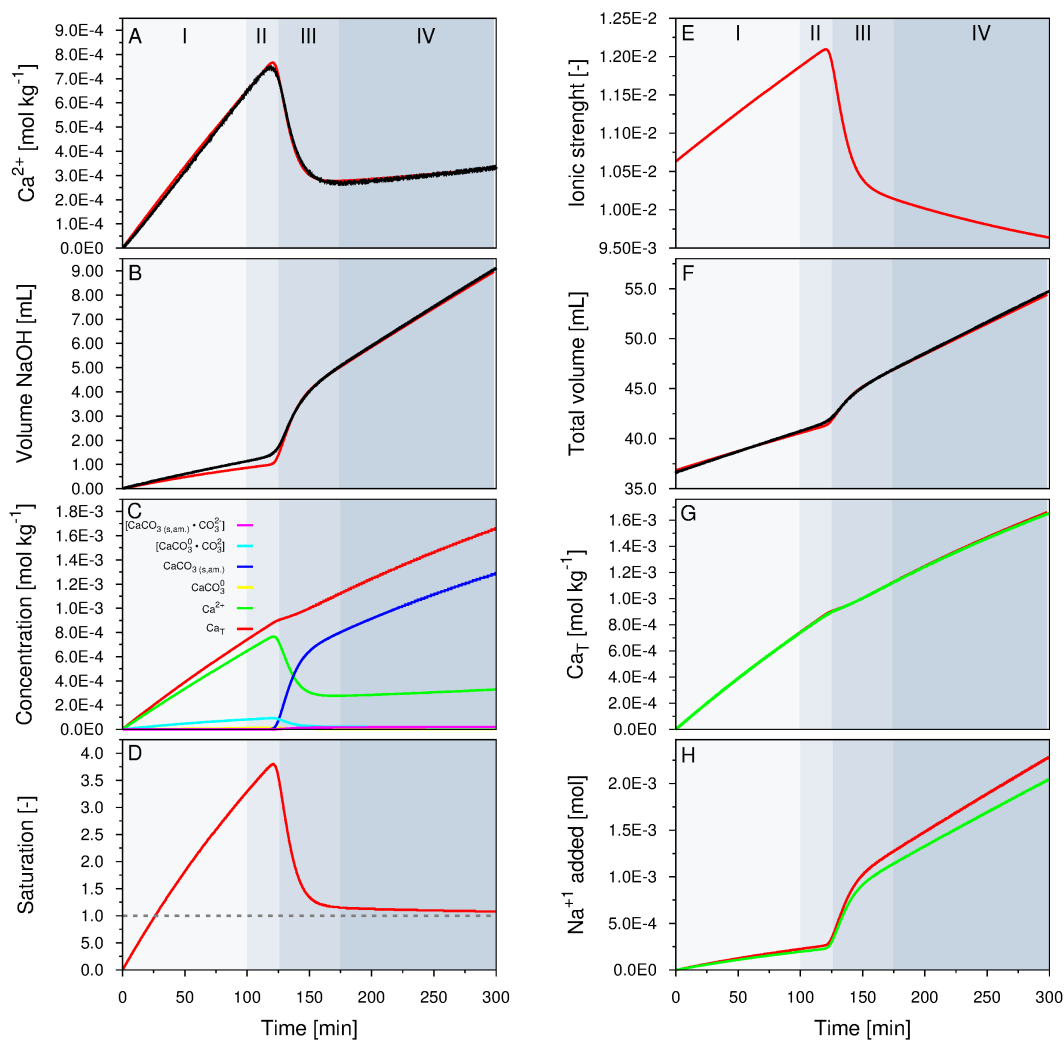


**Figure A.1** – Experiments at  $T = 278.35 \text{ K}$  and  $pH = 9.00$ .

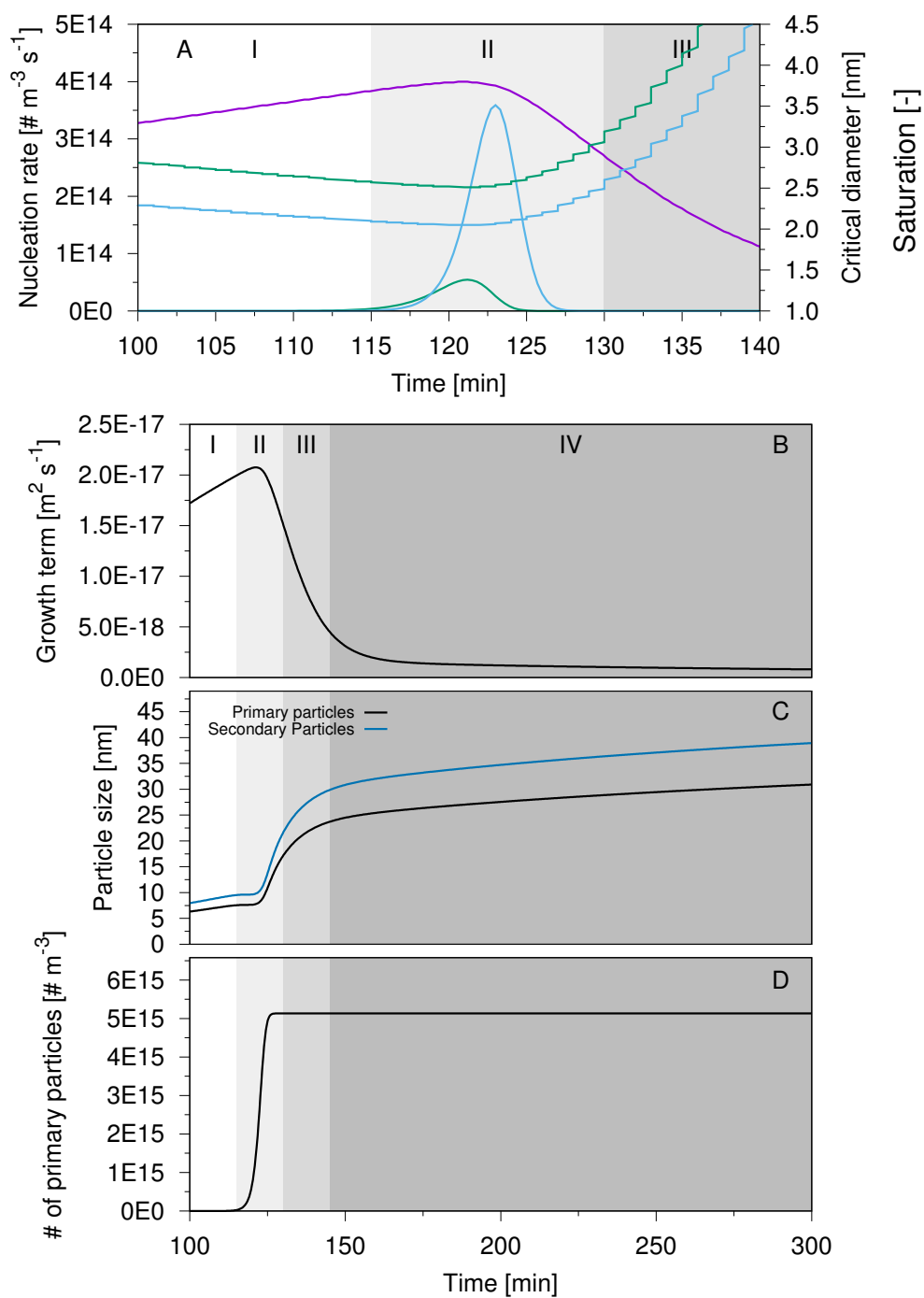


**Figure A.2** – Experiments at  $T = 278.35 \text{ K}$  and  $pH = 9.00$ .

## A. Appendix A

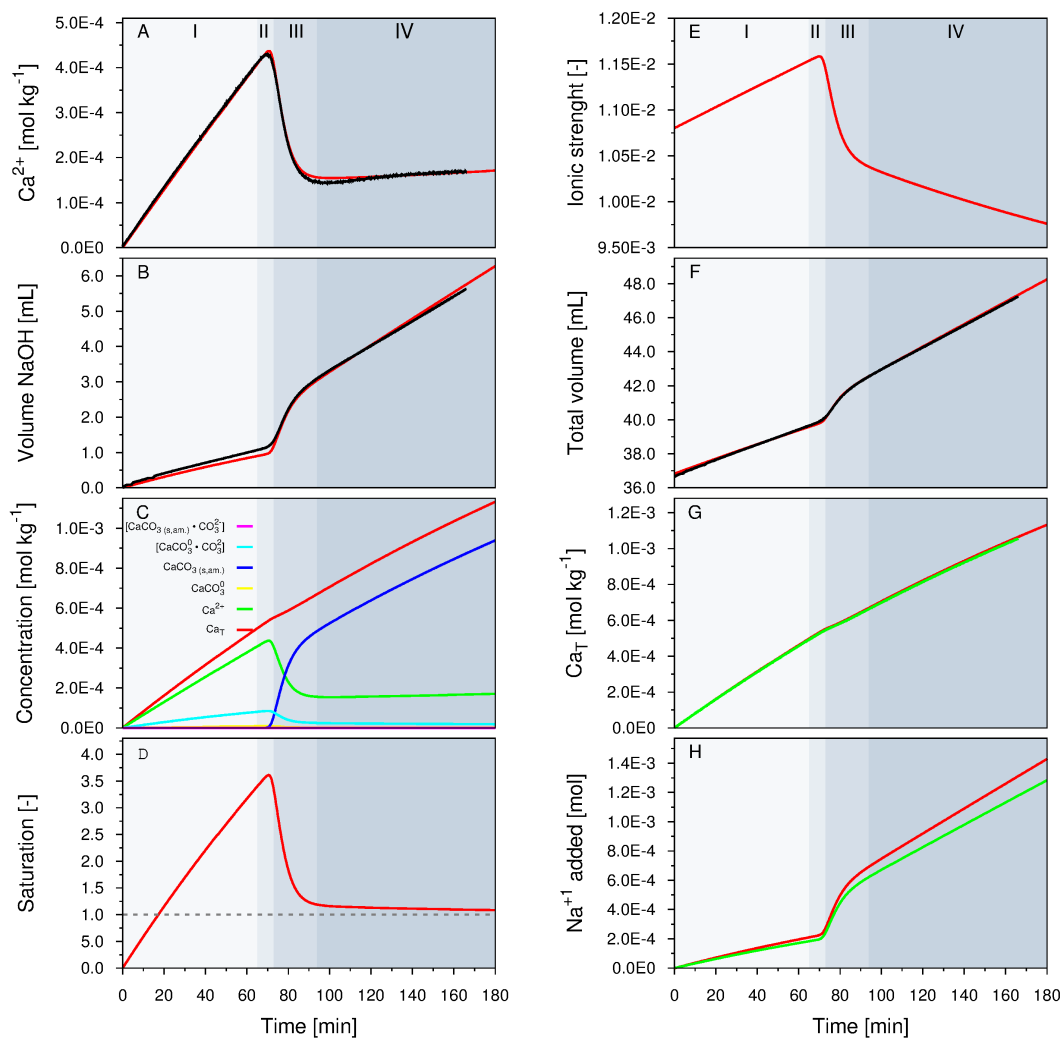


**Figure A.3** – Experiments at  $T=288.15\text{ K}$  and  $pH=9.00$ .



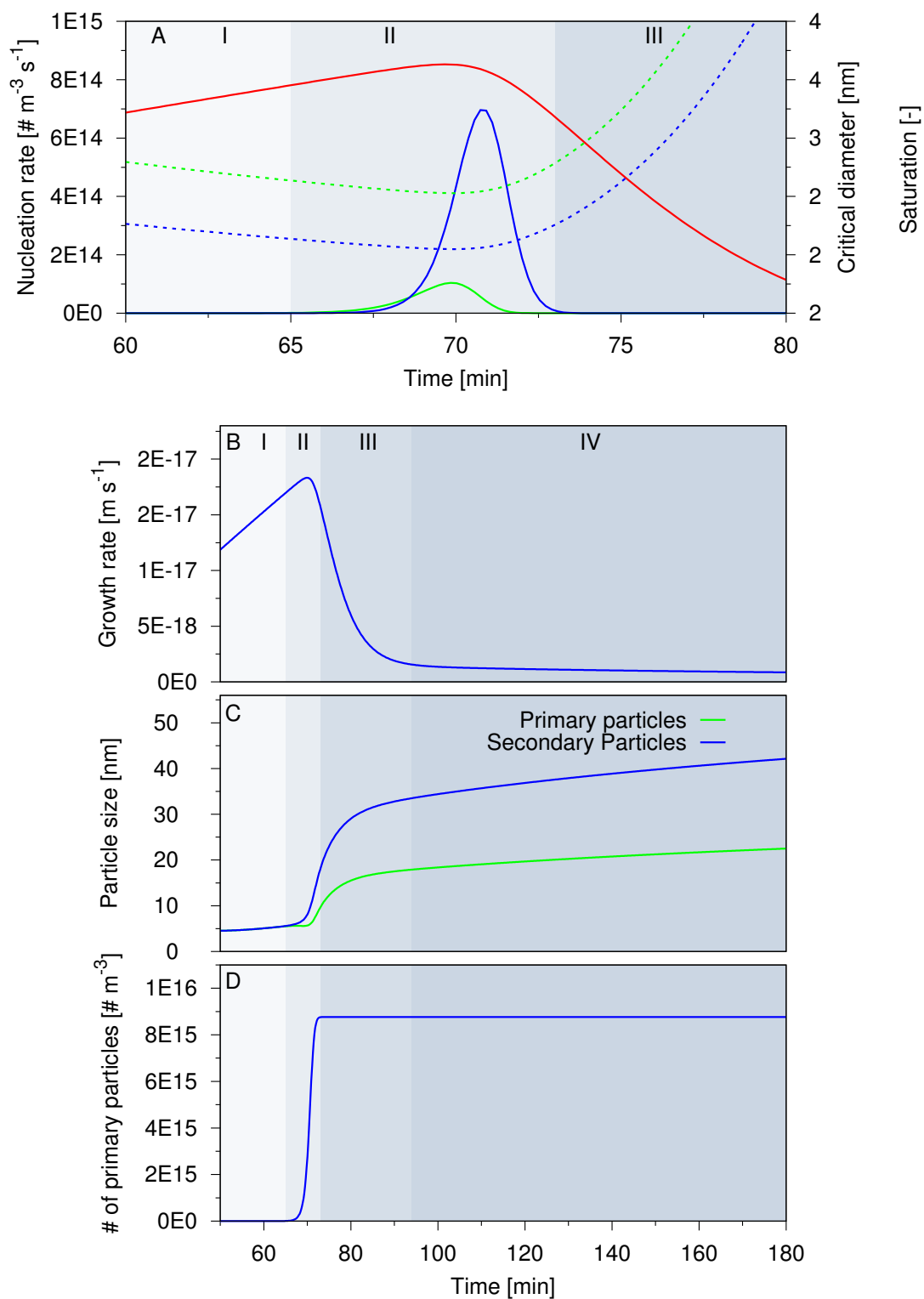
**Figure A.4** – Experiments at  $T = 288.15 \text{ K}$  and  $pH = 9.00$

## A. Appendix A



**Figure A.5** – Experiments at  $T=298.15\text{ K}$  and  $pH=9.00$ .



Figure A.6 – Experiments at  $T = 298.15$  K and  $pH = 9.00$ .

## A. Appendix A

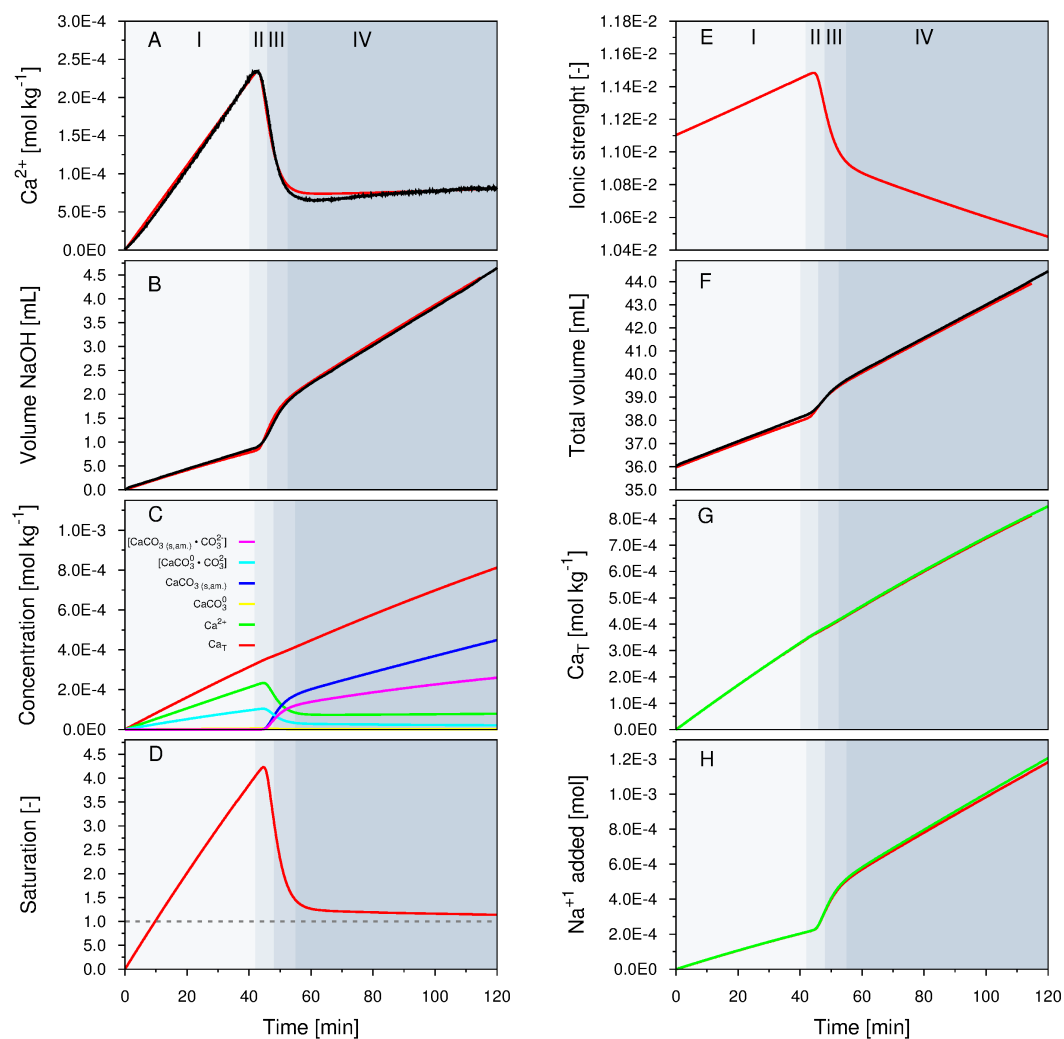


**Figure A.7** – Experiments at  $T = 308.15 \text{ K}$  and  $pH = 9.00$ .

## A.1. TD and K results for all datasets

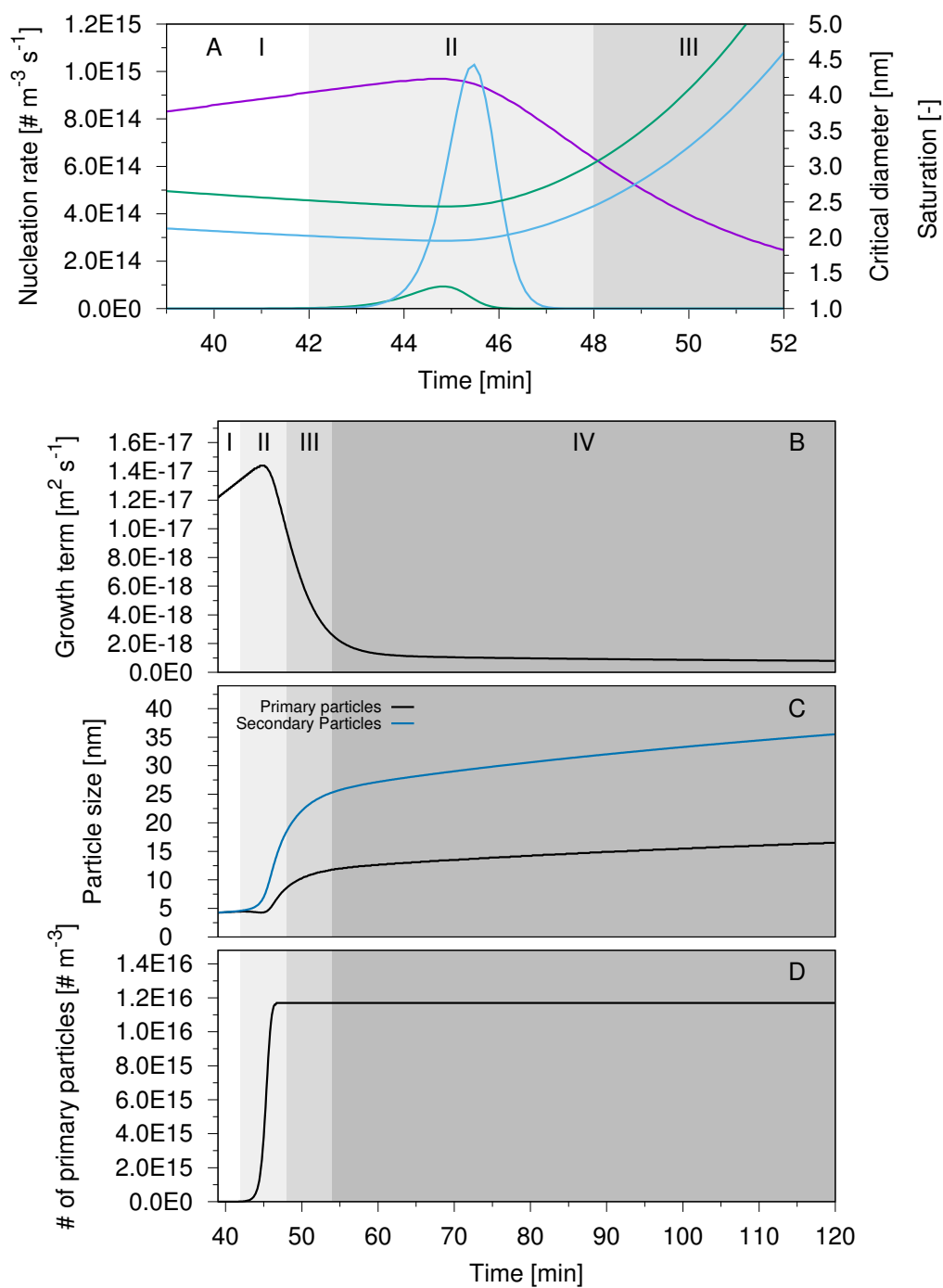


**Figure A.8** – Experiments at  $T = 308.15$  K and  $pH = 9.00$ .

## A. Appendix A

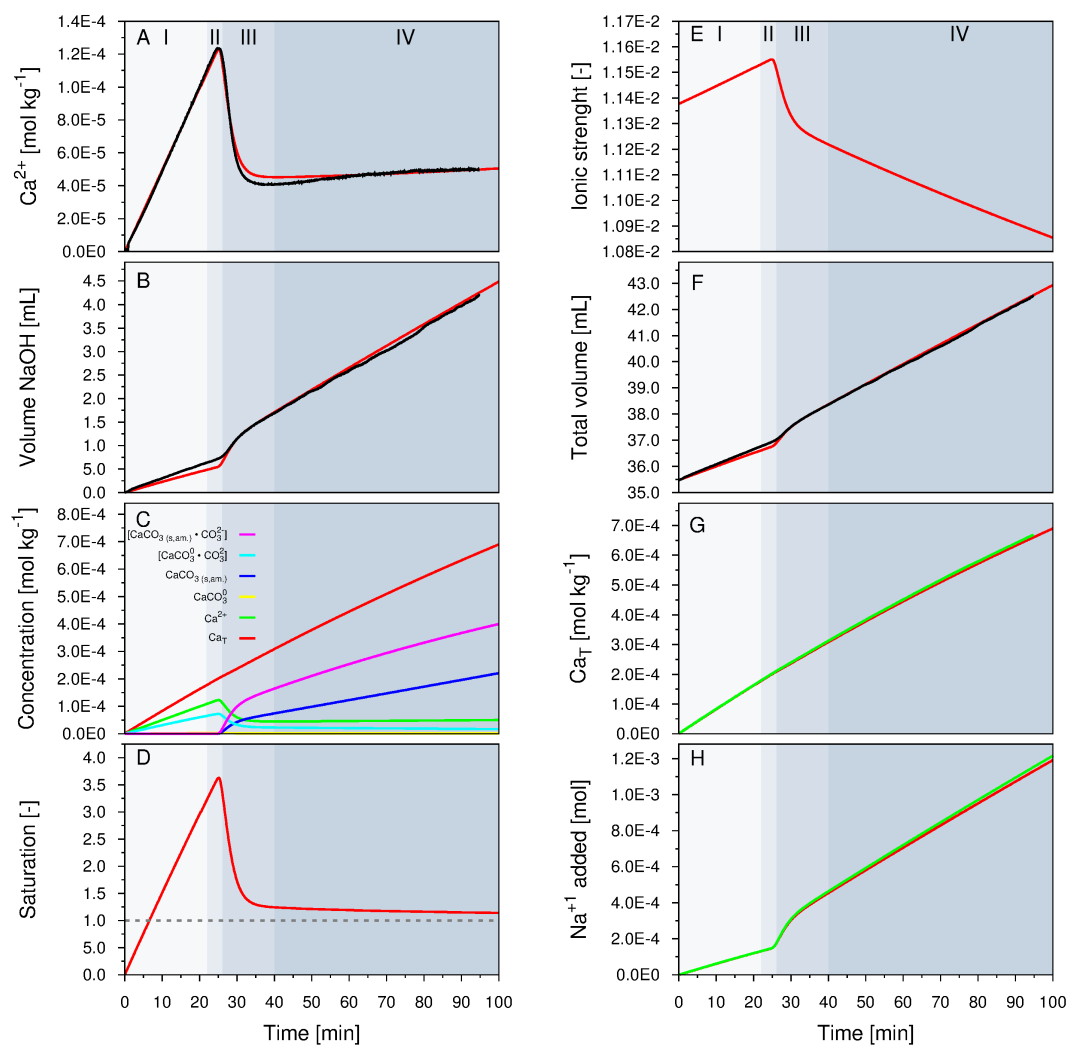


**Figure A.9** – Experiments at  $T = 318.15 \text{ K}$  and  $pH = 9.00$ .

## A.1. TD and K results for all datasets

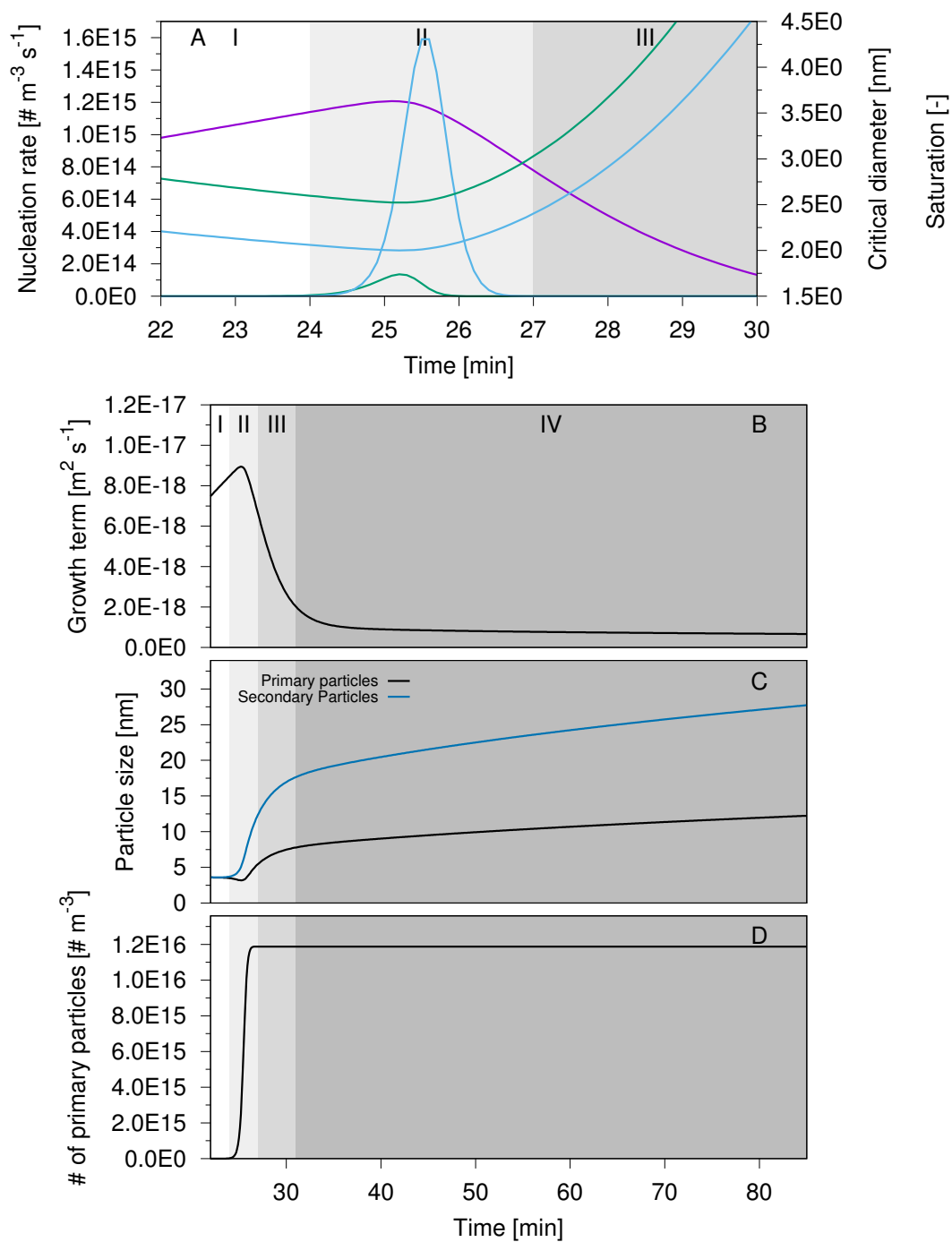


**Figure A.10** – Experiments at  $T = 318.15 \text{ K}$  and  $pH = 9.00$ .

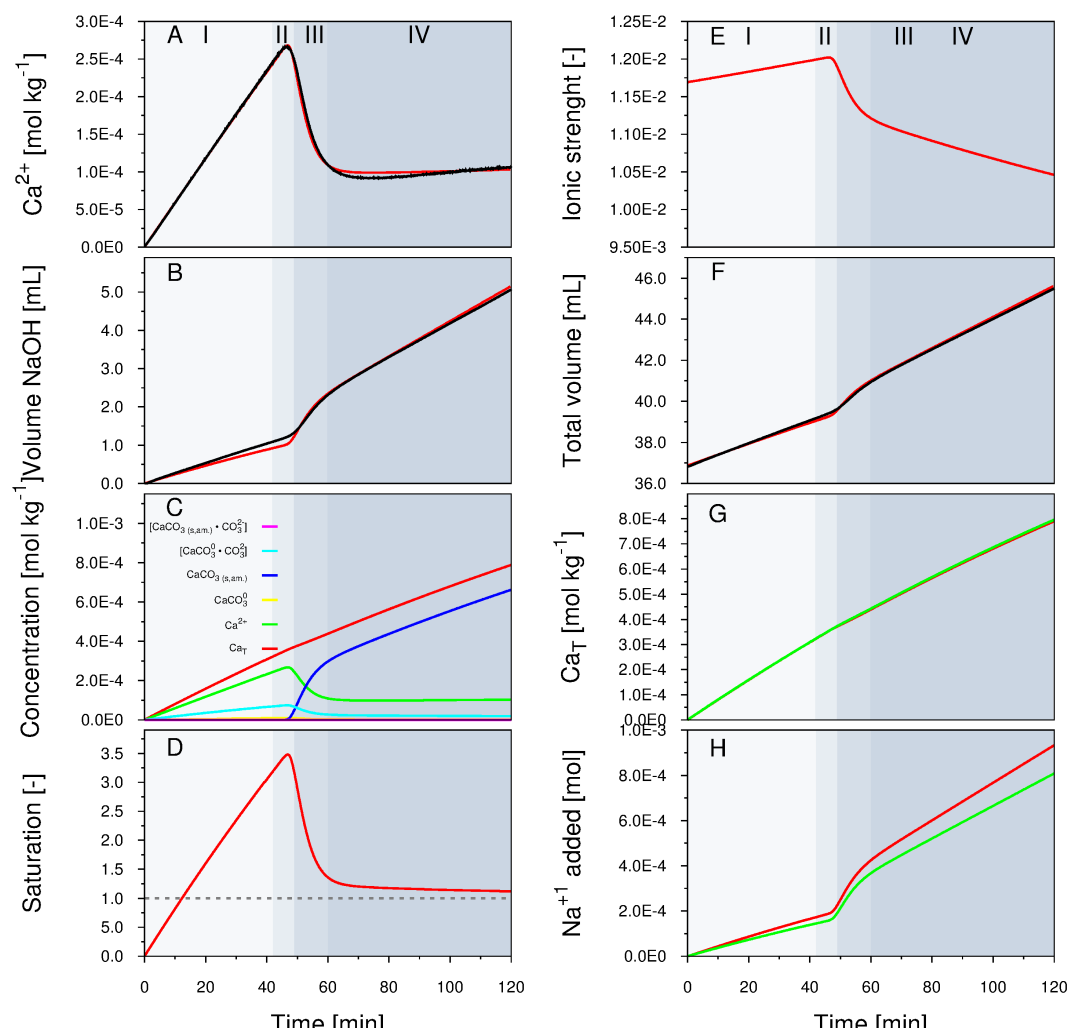
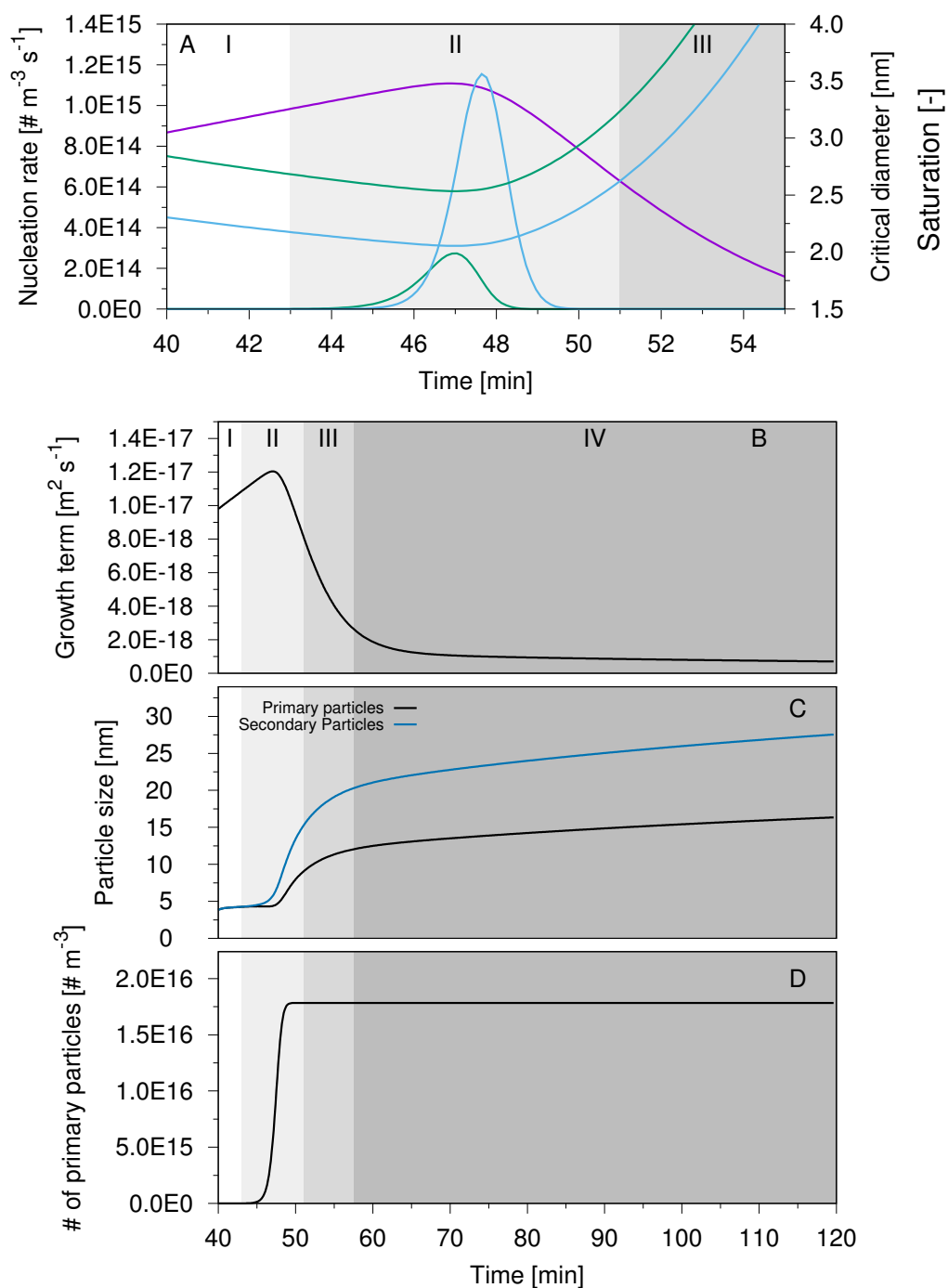


Figure A.11 – Experiments at  $T = 298.15 \text{ K}$  and  $pH = 9.25$ .



**Figure A.12** – Experiments at  $T=298.15 \text{ K}$  and  $pH=9.25$ .

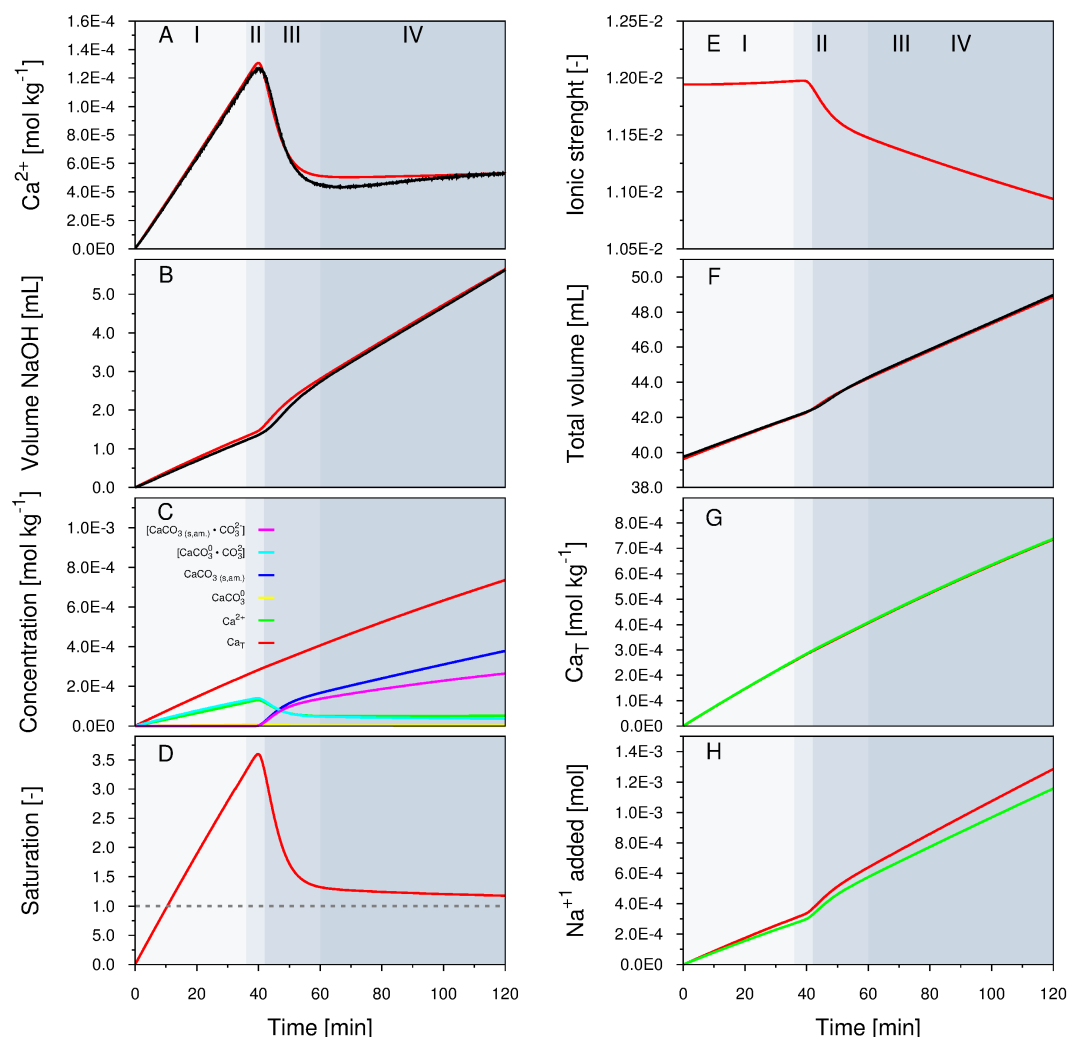
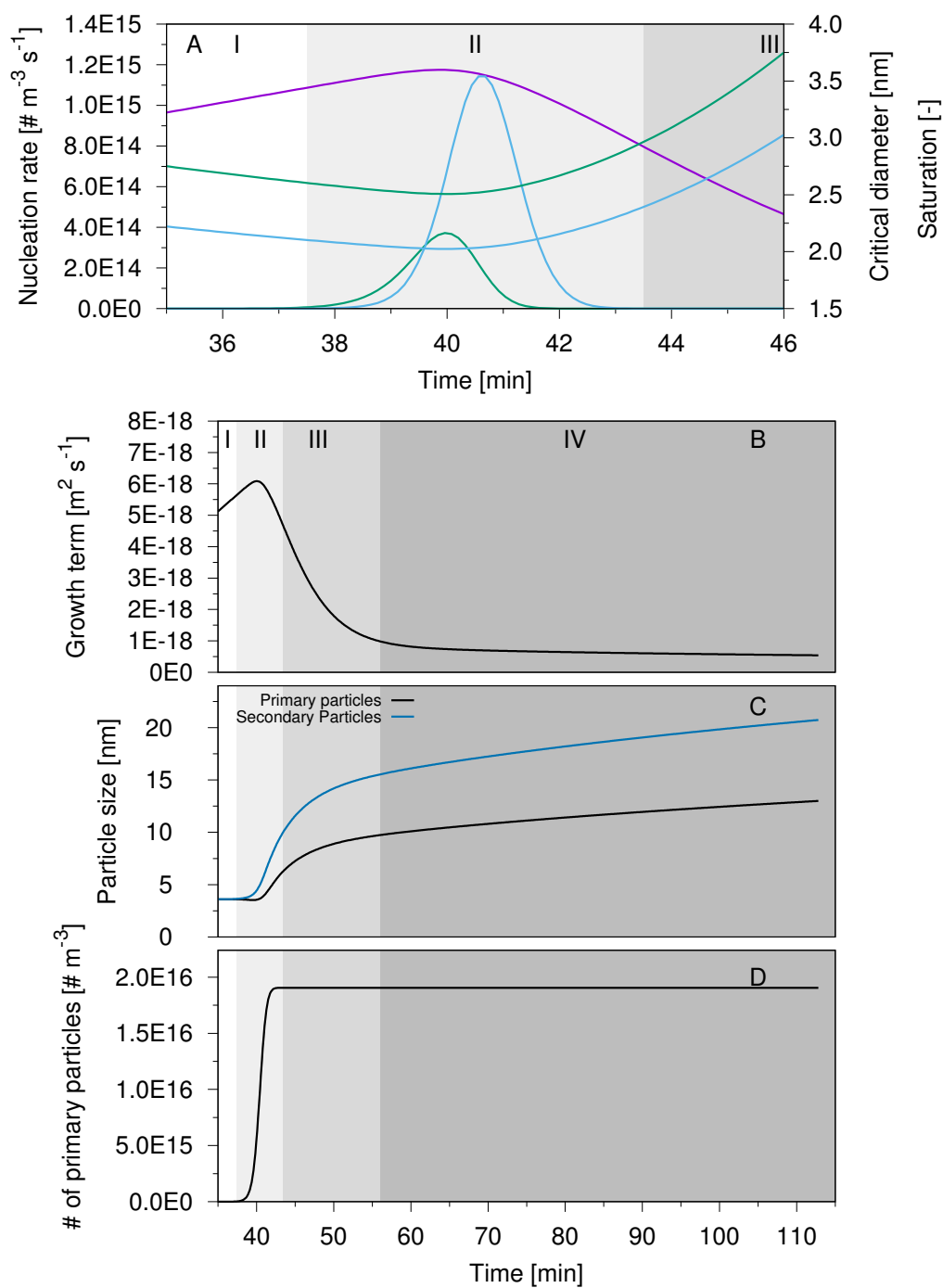


Figure A.13 – Experiments at  $T = 298.15 \text{ K}$  and  $pH = 9.50$ .





**Figure A.14** – Experiments at  $T = 298.15$  K and  $pH = 9.50$ .

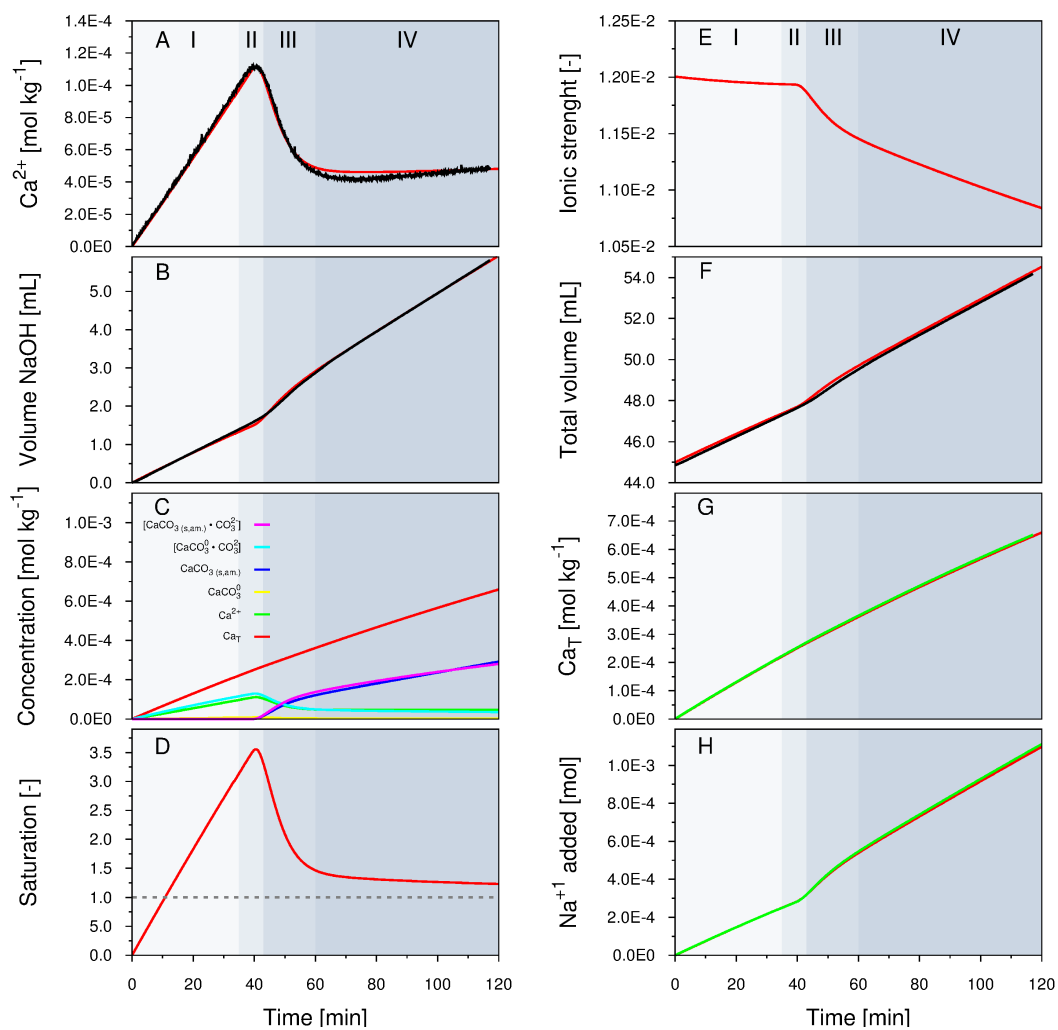
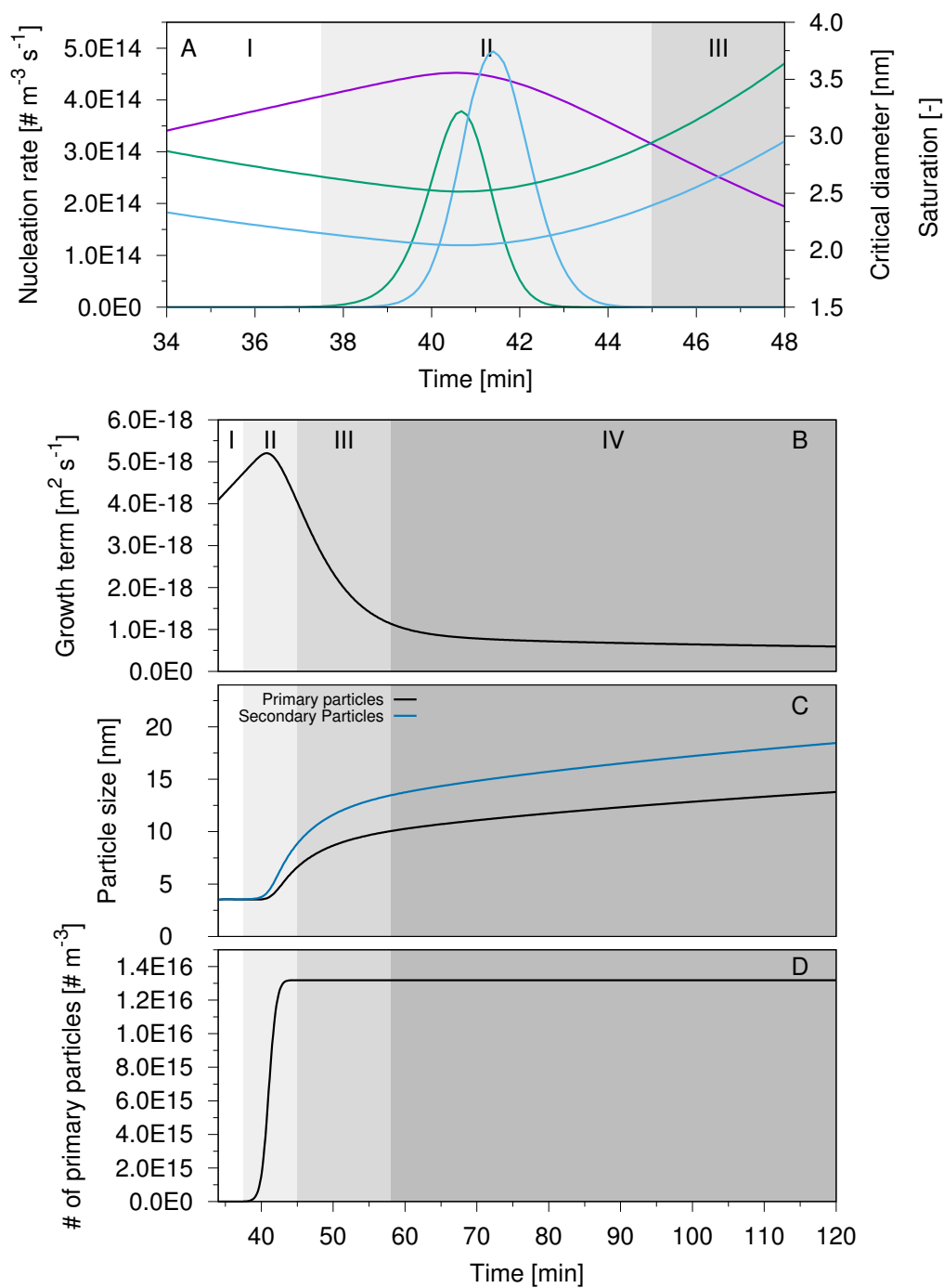
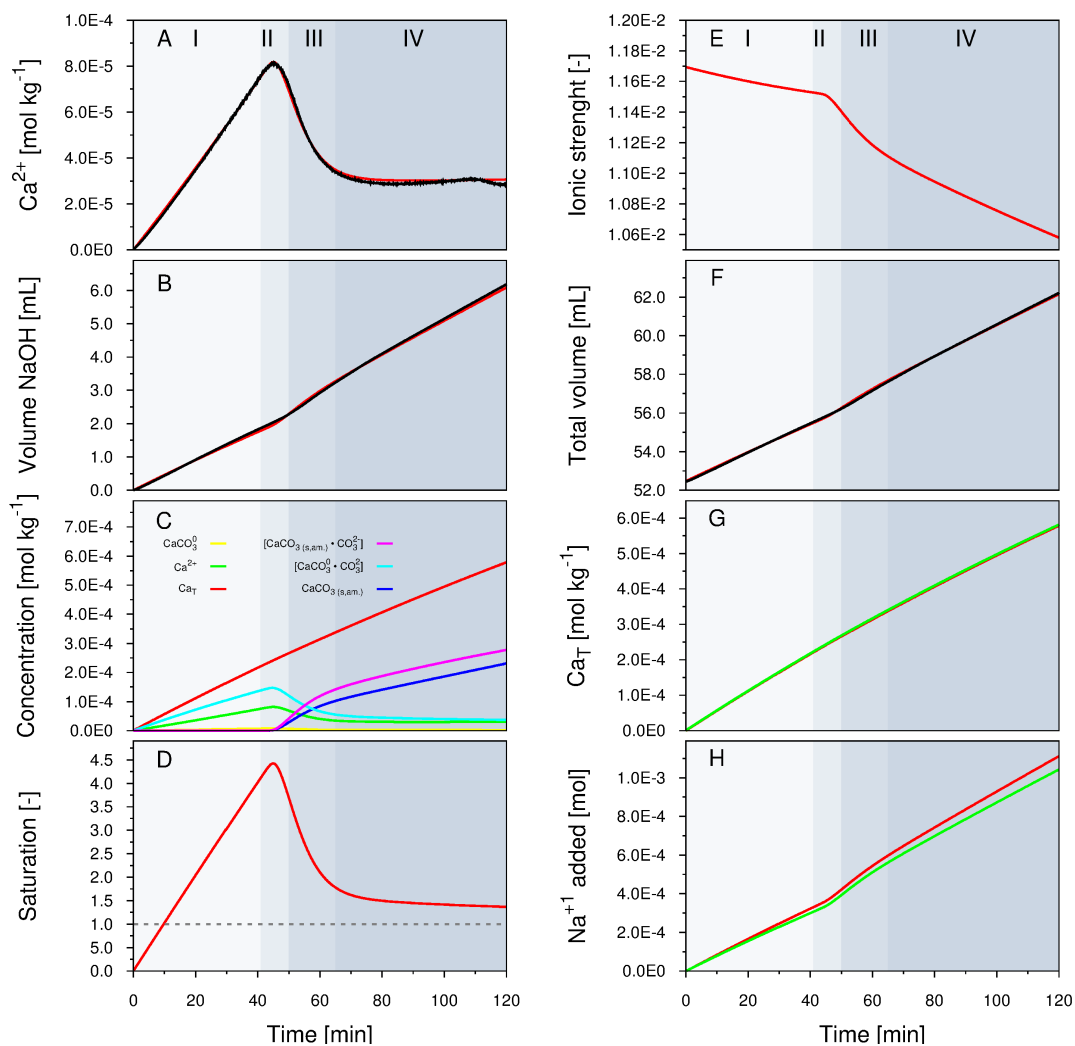


Figure A.15 – Experiments at  $T = 298.15 \text{ K}$  and  $pH = 9.75$ .



**Figure A.16** – Experiments at  $T=298.15$  K and  $pH=9.75$ .

## A. Appendix A



**Figure A.17** – Experiments at  $T = 298.15 \text{ K}$  and  $pH = 10.00$ .

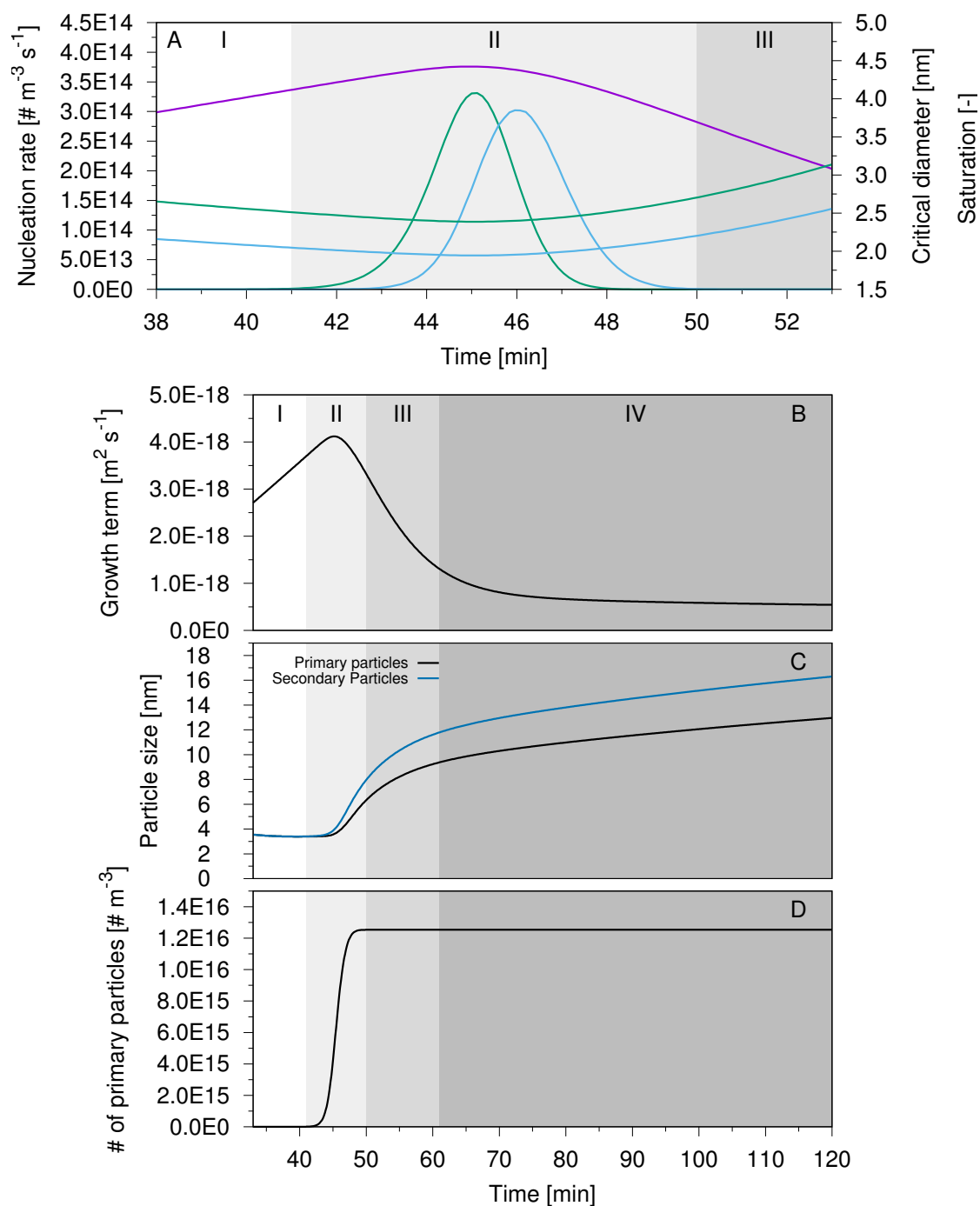


**Figure A.18** – Experiments at  $T = 298.15$  K and  $pH = 10.00$ .

## A. Appendix A

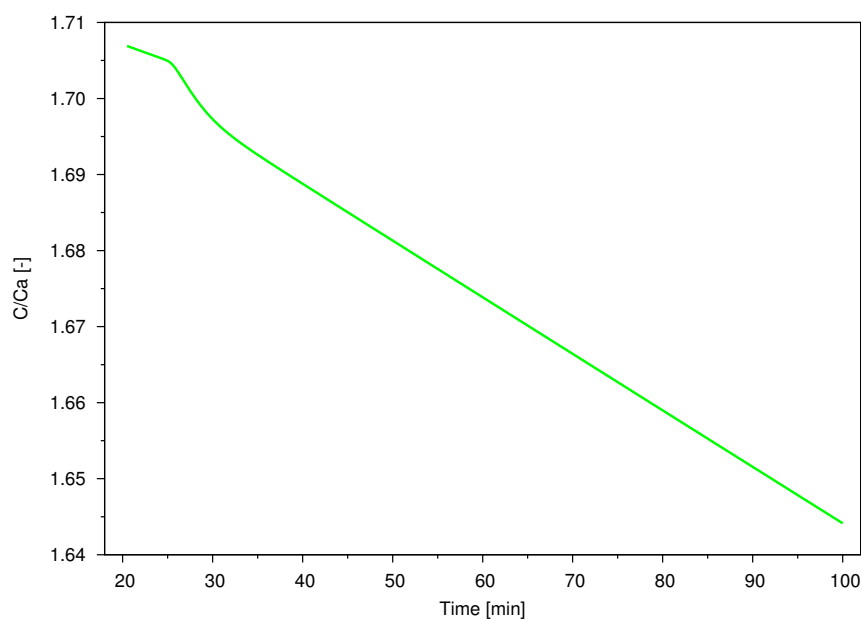


**Figure A.19** – Example of carbonate-to-calcium ratio against time in the solid phase for the experiment at  $T=318.15$  K and  $pH=9.00$ .

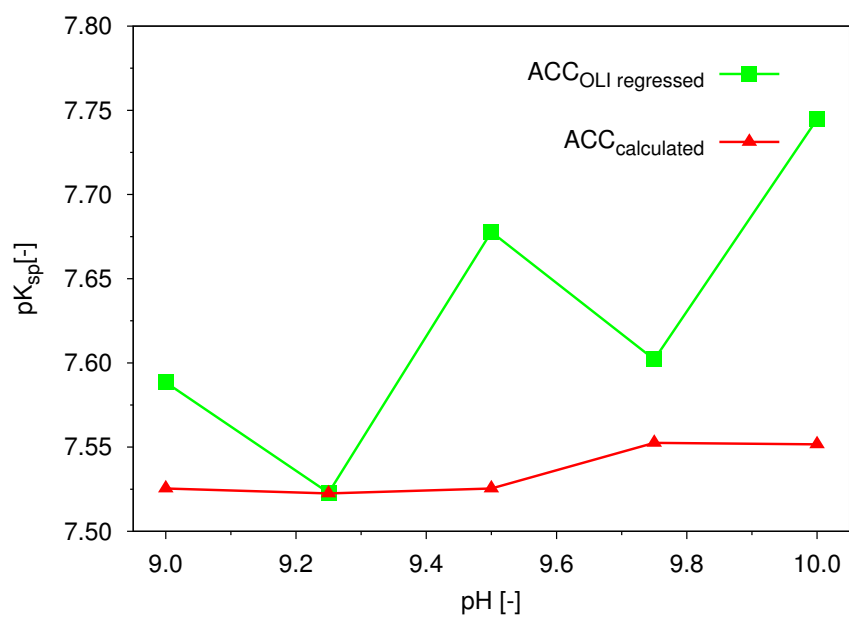


**Figure A.20** – Values of  $pK_{sp}$  of ACC calculated from both OLI and the model developed for the experiments at  $T=298.15$  K and  $pH$  in the range between 9.00 to 10.00.

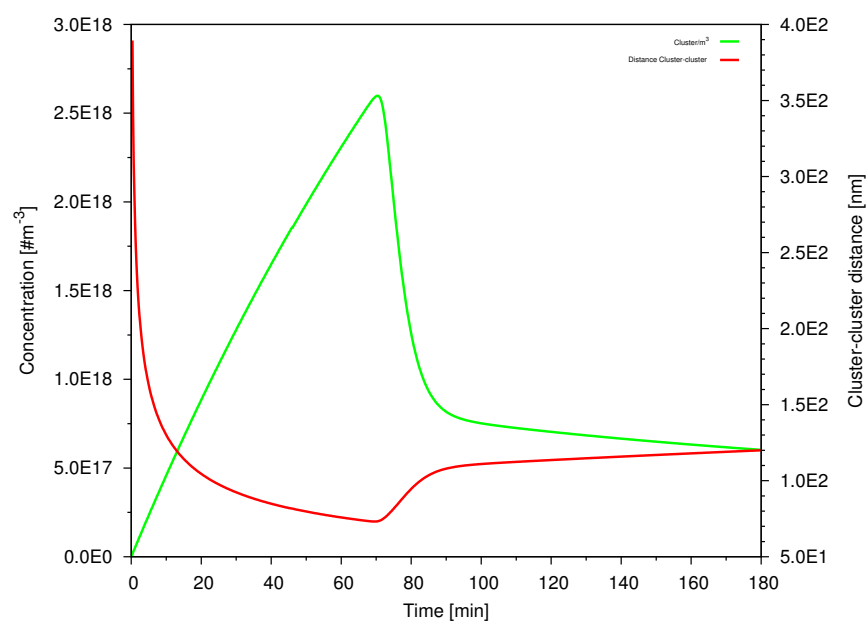


**Figure A.21** – Cluster concentration and average cluster-cluster distance for the experiment done at  $T = 298.15$  K and  $pH = 9.00$ .

## A.2 Additional figures

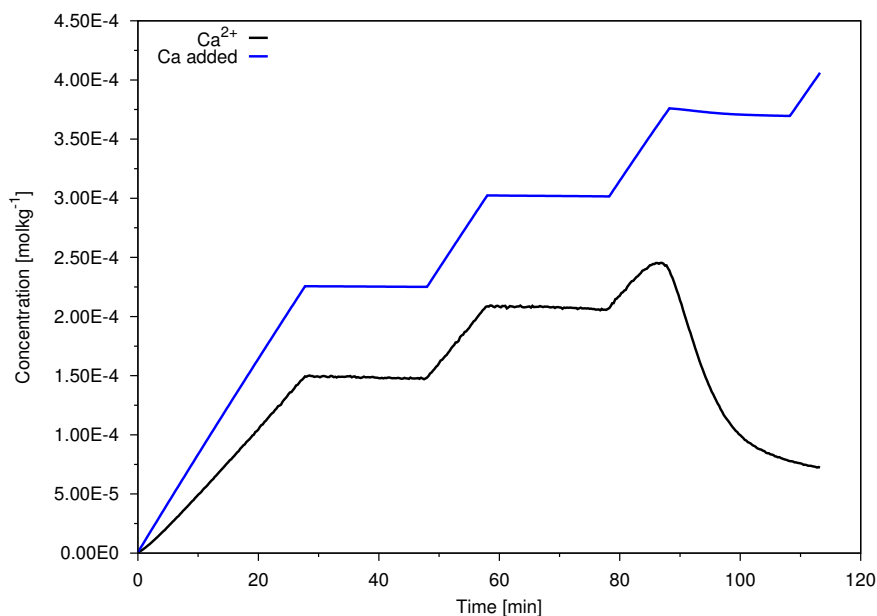


**Figure A.22** – Experiment carried out stopping the  $\text{CaCl}_2$  added into the system at defined time (horizontal plateaus) in order to maintain the supersaturation ( $S$ ) at a constant value. The precipitation does not occur until a critical supersaturation value is reached. The blue line represents  $\text{CaCl}_2$  added in to the reactor, while the black line represents the  $\text{Ca}^{2+}$  in solutions ( $T=298.15\text{ K}$  and  $\text{pH}=9.00$ ).



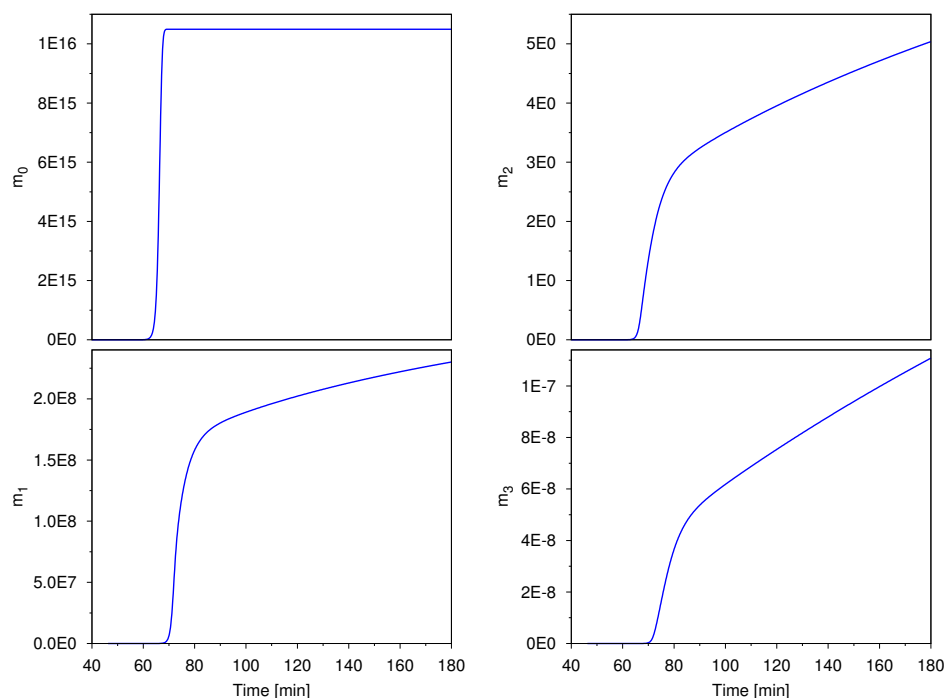


**Figure A.23** – Moments of the primary particle size distribution which correspond to the overall particle number ( $m_0$ ) and the overall particle length ( $m_1$ ). The ratio  $m_1 / m_0$  represents the average primary particle size;  $m_2$  and  $m_3$  are proportional to the overall surface and the overall volume of the particle population, respectively. (Experiments at  $T=298.15$  K and  $pH=9.00$ ).

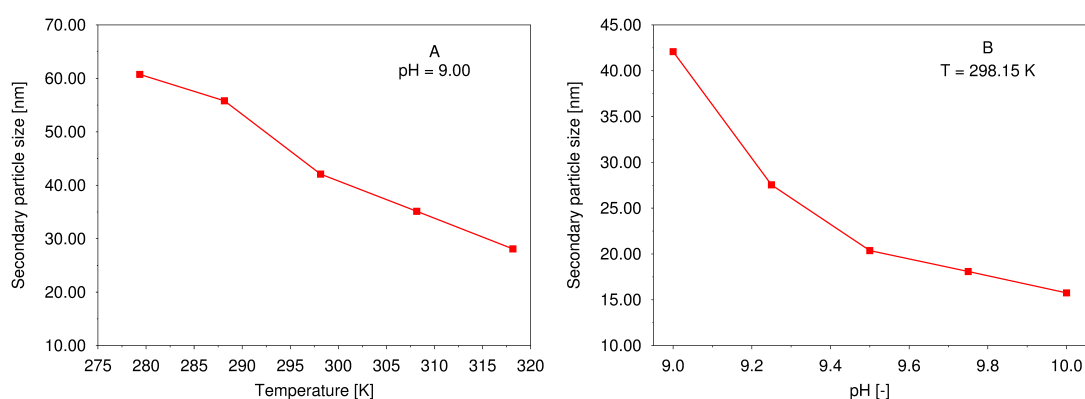


**Figure A.24** – Averaged secondary particle size at the end of the computational time versus (A) temperature at  $pH=9.00$  and versus (B)  $T=298.15$  K.

### A.3 Additional tables

**Table A.1** – Thermodynamic quantities for ACC and  $\text{CaCO}_3^0$  ion pair obtained by regression of experimental data using OLI EPS (v.9.2). The reference values for calcite and  $\text{CaCO}_3^{0*}$  reported in the MSE PUB mix-solvent database in OLI [9] for standard conditions.

	$\Delta G_f^0$ $\text{kJ mol}^{-1}$	$\Delta H_f^0$ $\text{kJ mol}^{-1}$	$S_f^0$ $\text{kJ mol}^{-1} \text{K}^{-1}$
Calcite*	-1128.9	-1207.8	89.9
ACC <sub>regressed</sub>	-1123.9	-1044.4	160
$\text{CaCO}_3^{0*}$	-1099.6	-1193.1	41.2
$\text{CaCO}_3^0$ <sub>regressed</sub>	-1092.4	-1006.1	183

**Table A.2** – Calculated ( $\text{CO}_3^{2-}/\text{Ca}^{2+}$ ) in ACC at the end of the computational time.

pH (T=298.15 K)	9.00	9.25	9.50	9.75	10.00
$\text{CO}_3^{2-}/\text{Ca}^{2+}$	1.08	1.00	1.41	1.30	1.55
Temperature [K] (pH=9.00)	279.35	288.15	298.15	308.15	318.15
$\text{CO}_3^{2-}/\text{Ca}^{2+}$	1.04	1.02	1.08	1.37	1.64

### A.4 Additional notes

1. For pH= 9.00 and T=298.15 K ( $K_{H2(298.15\text{ K})} = 4.68 \times 10^{-11}$ )

$$J = \frac{2D}{L} (C_{bulk} - C_s) \quad (\text{A.1})$$

and from equation 1.11

$$\{\text{CO}_3\}_{bound} = 1.0468 \{\text{OH}\}_{to\ add} \approx \{\text{OH}\}_{to\ add}$$

Thus, the error induced by the assumption that all NaOH added into the system is due to the formation of bound carbonate is affected by an error of 4.68 percent. The error increases dramatically with pH; at pH=10.00 the error corresponds to 46.8% (!).

2.  $\xi$  represents the activity of  $\text{H}^+$  ions to be “removed” from the system by dosing  $\text{OH}^-$  ions. For a precise calculation it is necessary to recall the equation (2.13). In fact, the ionic size of  $\text{OH}^-$  and  $\text{H}^+$  are different and the appropriate correction of the activity coefficient might slightly improve the quality of the calculated data.

## A.5 Evaluation of the term $\left[Ca_{surf}^{2+}\right]$

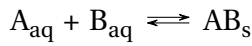
Considering the linear growth rate term

$$\begin{aligned} G &= \frac{dr}{dt} \\ &= J \cdot v_m \end{aligned} \quad (A.2)$$

where  $r$  is the particle radius,  $t$  is time,  $J$  is flux molar flux and  $v_m$  is the molar volume, the flux  $J$  can be written as

$$J = \frac{2D}{L} (C_{bulk} - C_s) \quad (A.3)$$

where  $D$  is the diffusion coefficient,  $L$  is the particle diameter, and  $C_{bulk}$  and  $C_s$  are the concentrations of the building unit in the liquid bulk (far from the particles) and on the surface, respectively. If the solid phase is formed as a consequence of the generic reaction:



where  $A_{aq}$  and  $B_{aq}$  are the chemical species that form the solid phase  $AB_s$ , the fluxes for the species can be written as

$$J_A = \frac{2 \cdot D_A}{L} \cdot (a_A \cdot A_{bulk} - a_A \cdot A_s) \quad (A.4)$$

$$J_B = \frac{2 \cdot D_B}{L} \cdot (a_B \cdot B_{bulk} - a_B \cdot B_s) \quad (A.5)$$

The lower flux is rate determining and the condition

$$J_B = J_A \quad (A.6)$$

is attained. Considering the equilibrium

$$K_{SP} = a_A \cdot A_s \cdot a_B \cdot B_s \quad (A.7)$$

where  $a_A$  and  $a_B$  are the activity coefficient for the species A and B, respectively, and

## A. Appendix A

---

the activity product

$$Q = a_A \cdot A_{bulk} \cdot a_B \cdot B_{bulk} \quad (A.8)$$

the saturation is defined as

$$S = \frac{Q}{K_{SP}} \quad (A.9)$$

Defining the ratio between the diffusion coefficients of A and B as

$$h = \frac{D_A}{D_B} \quad (A.10)$$

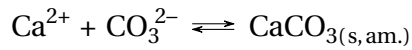
Equation A.6 can be rewritten including equations A.4-A.10 as

$$a_A^2 \cdot H \cdot A_{bulk} \cdot A_S^2 - h \cdot A_{bulk}^2 \cdot A_S^2 \cdot a_A^2 + K_{SP} \cdot A_{bulk} = 0 \quad (A.11)$$

That can be analytically solve for  $A_S$

$$A_S = \frac{(a_A^2 \cdot h \cdot A_{bulk}^2 - K_{SP} \cdot S)}{2 \cdot a_A^2 \cdot h \cdot A_{bulk}} + \frac{\sqrt{(h^2 \cdot A_{bulk}^4 \cdot a_A^4 - 2 \cdot K_{SP} \cdot S \cdot h \cdot A_{bulk}^2 \cdot a_A^2 + 4 \cdot K_{SP} \cdot h \cdot A_{bulk}^2 \cdot a_A^2 + K_{SP}^2 \cdot S^2)}}{2 \cdot a_A^2 \cdot h \cdot A_{bulk}} \quad (A.12)$$

Thus, for the reaction



the quantities  $A_S$  and  $A_{bulk}$

corresponds to  $\text{Ca}_{\text{surf}}^{2+}$  and  $\text{Ca}_{\text{bulk}}^{2+}$  of equation 1.56.

## A.6 Equations for $\Delta G_h^*$ and $\Delta G_S^*$ and critical size

$$\Delta G_h^* = \frac{4}{27} \frac{\varepsilon_A^3}{\varepsilon_V^2} \frac{v^2 \cdot \gamma^3}{k_B^2 \cdot T^2 \cdot \ln^2(S)} \quad (\text{A.13})$$

$$\Delta G_S^* = \frac{4}{27} \frac{\varepsilon_A^3}{\varepsilon_V^2} \frac{v^2 \cdot \gamma_{eq}^3}{k_B^2 \cdot T^2 \cdot \ln^2(S)} \quad (\text{A.14})$$

$$L_h^* = \frac{2}{3} \frac{\varepsilon_A}{\varepsilon_V} \frac{v \cdot \gamma}{k_B \cdot T \cdot \ln(S)} \quad (\text{A.15})$$

$$L_S^* = \frac{2}{3} \frac{\varepsilon_A}{\varepsilon_V} \frac{v \cdot \gamma_{eq}}{k_B \cdot T \cdot \ln(S)} \quad (\text{A.16})$$

where  $\varepsilon_A$  is the surface geometrical factor;  $\varepsilon_V$  is the volumetric geometrical factor; and  $v$  represents molecular volume.



## B | Calcium phosphates

### B.1 Additional Characterization analyses

#### B.1.1 IR and Raman spectroscopy

Raman and IR analyses results show similar spectra among the different experimental conditions, as reported in figure B.1. Figure B.1, A, reports the results of IR analyses for L-IS and H-IS experiments. The absence of peaks at 1410 and 875  $\text{cm}^{-1}$  allows excluding the presence of carbonated calcium phosphate phases, reflecting the efficiency of the precautions taken during the syntheses. The  $\nu_1(\text{PO}_4)$  band at 962  $\text{cm}^{-1}$  is a weak peak in IR spectroscopy but is particularly strong in Raman spectroscopy. This signal is typical of both HA and OCP phases. The spectra present broad bands, which could be related to nanocrystalline (biomimetic) apatite structures. Indeed, the characteristic bands of hydroxyl group in the apatitic environment at 632 and 3572  $\text{cm}^{-1}$ , typical of bulk crystalline HA, are not detected. The nanocrystalline nature of the samples could be confirmed by the absence of the peaks at 632  $\text{cm}^{-1}$ , that is related to the stretching mode of the hydroxyl group ( $\nu_L(\text{OH})$ ), and the doublet related to the stretching mode of P-O bonds ( $\nu_3(\text{PO}_4)$ ) at 1048 and 1090  $\text{cm}^{-1}$ . Moreover, the weak band at 870  $\text{cm}^{-1}$  of  $\text{HPO}_4^-$  bearing apatite [139] due to the P-O stretching of P-OH groups is present, and it can be associated to both nanocrystalline HA and OCP structures. The signals at 602 and 561  $\text{cm}^{-1}$  correspond to the bending mode of OPO groups ( $\nu_4(\text{PO}_4)$ ). Both nanocrystalline and OCP are usually associated with water molecules, giving a strong absorption at 3000-3700  $\text{cm}^{-1}$  in the infra-red region. Here, only a weak band was detected for both samples. Moreover, the OCP presence in the C-IS and H-IS samples is confirmed by the very weak peak at 912  $\text{cm}^{-1}$  and the shoulder at 1122  $\text{cm}^{-1}$  attributed to the P-(OH) stretching of  $\text{HPO}_4$ . The shoulder at 530  $\text{cm}^{-1}$  and the weak band at 1195  $\text{cm}^{-1}$  are assigned to non-apatitic  $\text{HPO}_4^{2-}$  ions. In the  $\nu_3(\text{PO}_4)$  region, the 912  $\text{cm}^{-1}$  and the 1195  $\text{cm}^{-1}$  bands can be assigned to the OCP

## B. Appendix B

lattice configuration, and thus confirms the presence of OCP phase, together with apatitic phase. The Raman spectra (B.1, B) present a very strong signal at  $962\text{ cm}^{-1}$ , that corresponds to the symmetric stretching mode ( $\nu_1$ ) of the tetrahedral  $\text{PO}_4^{3-}$  groups (P-O bond) [171–173]. The absence of signals at  $1103\text{ cm}^{-1}$  and  $1070\text{ cm}^{-1}$  indicates no incorporation of carbonate ions in the samples.

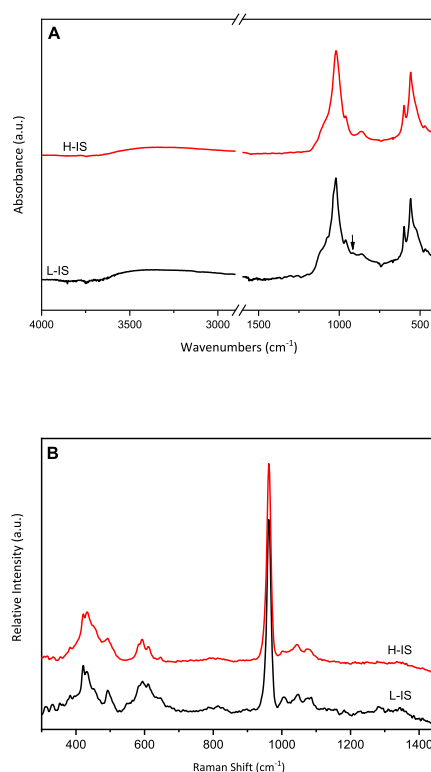


**Figure B.1** – The spectra for H-IS (red) and L-IS (black) are reported in panel A. The Raman shift for H-IS (red), and L-IS (black) are reported in panel B.

### B.1.2 SEM and EDX analyses

The SEM analyses show the presence of particles composed of needle and platelet substructures. The EDX analyses confirm the presence of P, Ca, and O. Moreover, the presence of Na and Cl is not detected, that can confirm an appropriate washing procedure of the samples. Specifically, figure B.2 reports a SEM micrograph of a particle from H-IS experiment together with the spectrum acquired by energy-dispersive X-ray spectroscopy (EDX). Copper and aluminum signals derive from the TEM grid onto which the sample was deposited and from the holder onto which this grid was



mounted for the SEM investigation, respectively.

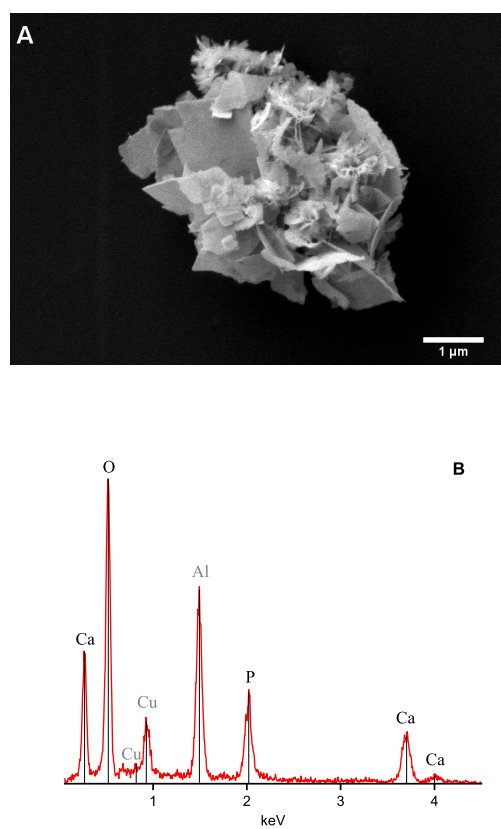


**Figure B.2** – Particles of H-IS experiment (A) reported with its corresponding EDX spectrum (B).

## B.2 Additional table and figure

Table B.1 – Surface energy values vs the ionic strength.

	IS	$\gamma_{primary}$ $\text{J m}^{-2}$	$\gamma_{secondary}$ $\text{J m}^{-2}$	$\beta$ $\text{J m}^{-2}$
L-IS	$2.19 \times 10^{-2}$	$4.25 \times 10^{-2}$	$3.25 \times 10^{-2}$	$6.00 \times 10^{-2}$
H-IS	$1.25 \times 10^{-1}$	$3.55 \times 10^{-2}$	$2.73 \times 10^{-2}$	$4.92 \times 10^{-2}$
C-IS	$1.54 \times 10^{-1}$	$3.28 \times 10^{-2}$	$2.53 \times 10^{-2}$	$4.50 \times 10^{-2}$

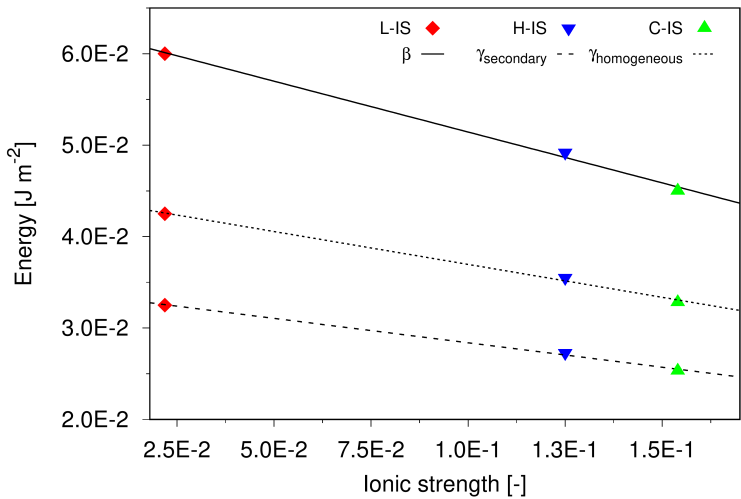
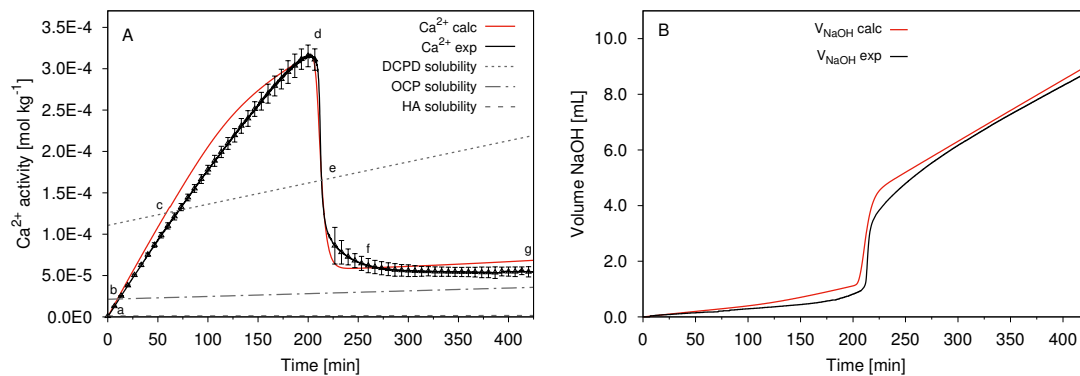
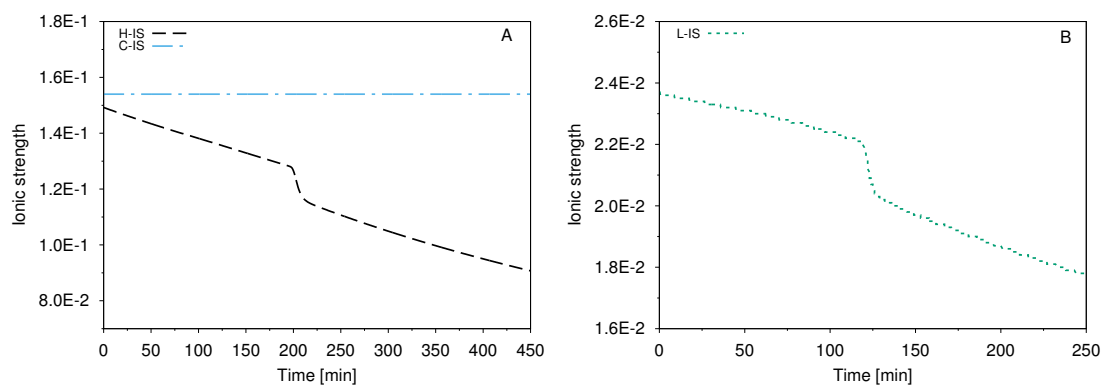


Figure B.3 – Surface energy for L, H, C-IS experiments reported as a function of ionic strength (IS).

## B.3 Complete datasets



**Figure B.4** – Constant Ionic Strength (C-IS) experimental (black) and calculated (red) data. (A) calcium ion activity and (B) NaOH volume added into the system for iso-pH condition.



**Figure B.5** – Ionic Strength of H-IS, C-IS experiments (A), and of L-IS (B).

## B. Appendix B

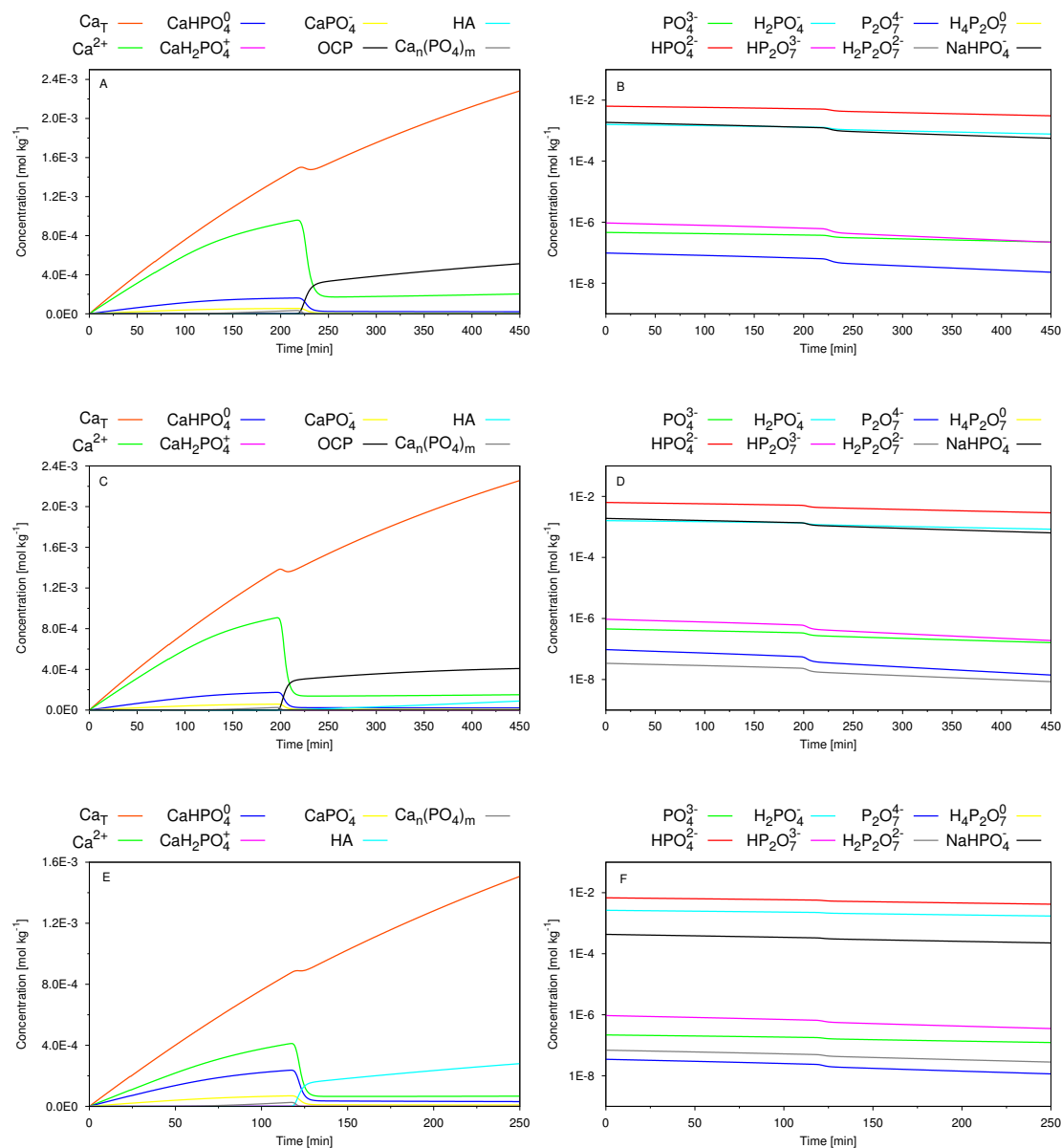


**Figure B.6** – Chemical speciation of calcium (A, C, E), and of phosphorous (B, D, F) for C-IS, H-IS, and L-IS, respectively.

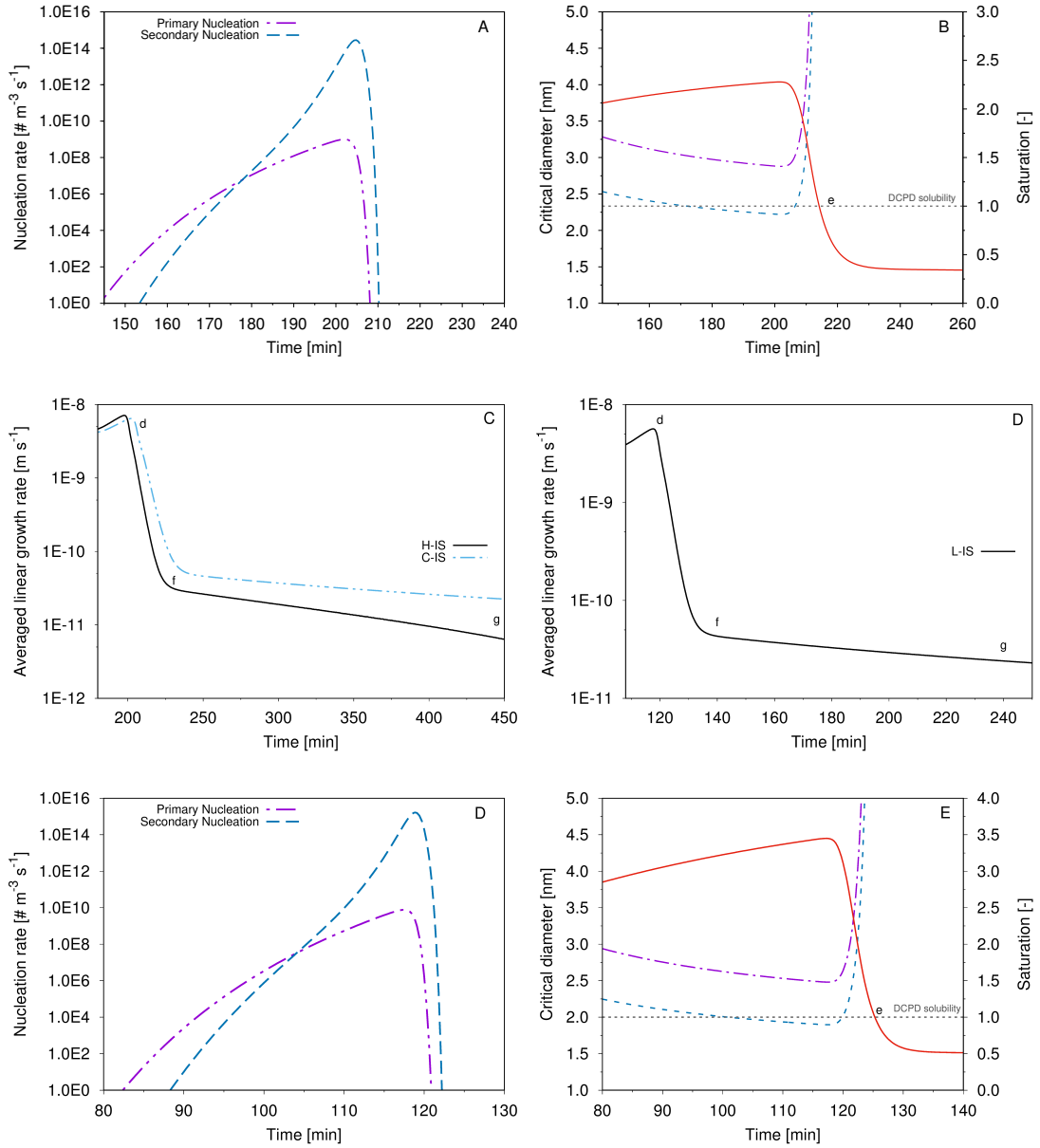


**Figure B.7** – Kinetic data reported for every experiment. Calculated kinetic data on particle evolution for C-IS experiment. (A) Primary (purple,  $\cdots -$ ) and secondary (blue,  $-$ ) nucleation rate, (B) critical nucleation size for primary homogeneous (purple,  $\cdots -$ ) and "true" secondary nucleation (blue,  $-$ ) both in the interval of maximum supersaturation (red). Averaged linear growth rate for the experiment H-IS, C-IS (C), and L-IS (D). The meaning of the letters are discussed in the text of the main paper. Calculated kinetic data on particle evolution for L-IS experiment. (D) Primary (purple,  $\cdots -$ ) and secondary (blue,  $-$ ) nucleation rate, (E) critical nucleation size for primary homogeneous (purple,  $\cdots -$ ) and "true" secondary nucleation (blue,  $-$ ) both in the interval of maximum supersaturation (red).

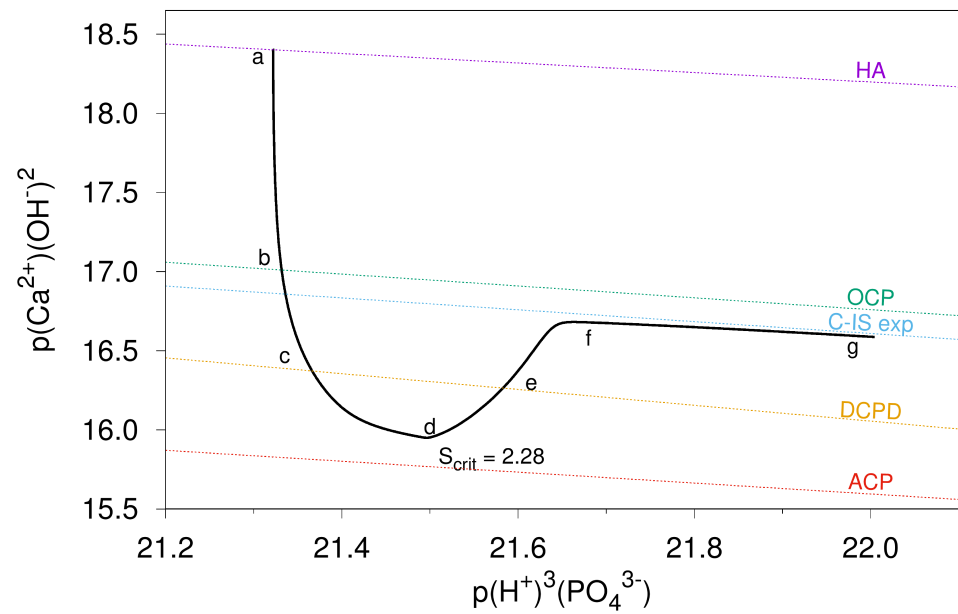


Figure B.8 – Chemical potential plot for C-IS series.

## **C | Application oriented studies**





## C.1 CerInk project

### Biomimetic ceramic scaffolds with density gradient and improved mechanical stability fabricated by Binder-into-Bed 3D-printing and ceramic NanoInk

#### C.1.1 Introduction

The 3-dimensional printing (3DP) technology has become a convenient tool in different fields. It is defined as flexible solid freeform fabrication technology, with the advantage of versatility with respect to the materials used, such as ceramic, metals and polymers. In the medical field, metal 3D-printed scaffolds are a well-established technology and nowadays used routinely in orthopaedic surgery. Instead, the production of 3D-printed ceramic scaffolds remains a challenge albeit, in the recent years, relevant improvements have been done. Ceramic scaffolds can be made of hydroxyapatite (HA), the most abundant inorganic compounds of natural bone. Although the excellent biocompatibility, additional properties need to be reproduced in a synthetic bone such as an optimal trade-off between mechanical properties and porosity. The aim of the two-year CerInk project was ambitious: manufacturing ceramic scaffolds by 3DP mimicking the natural bones in term of biocompatibility, mechanical properties and porosity. In particular, a natural bone is composed of cortical and cancellous/trabecular zones, being the former more porous and the latter characterized by a higher compressive strength. In order to be able to mimic such a complex 3D structure, an *ad-hoc* 3DP technology was needed. Since 2008, the Life Science FHNW in Basel established a considerable know-how on the Binder-into-Bed (BiB) 3DP of calcium phosphate bioceramics. In order to improve the mechanical characteristics of the 3D-printed scaffolds, biopolymeric infiltration and nano-HA powder have been used to modify the sintering properties of the bulk material and promote densification. Figure C.1 of [175] represented the state-of-the-art, before the CerInk project: it was clear that the ceramic-ceramic junction needed to be improved. Thus, a modified BiB 3DP system was conceived. The new technology allows the use of two inks, each of them with a specific composition, in order to promote, upon

---

This chapter is adapted from **A. Carino** *et al.*, Project A11.01 CerInk: Biomimetic ceramic scaffolds with density gradient fabricated by Binder-into-Bed 3D-printing and ceramic NanoInk. From Annual Report Swiss Nanoscience Institute, **2018**, [174].

---

## C. Appendix C

---

sintering, a controlled densification only where required, leaving other zones with higher porosity. Consequently, the complexity of the natural bone can be reproduced. At PSI the appropriate ceramic NanoInk compositions were developed, and several green bodies with controlled porosity were produced by conventional techniques. The sintering properties of the ceramic bodies were systematically studied by thermomechanical analysis and the composition optimized to promote a good ceramic-ceramic junction between parts, while the different mechanical properties and porosity were preserved.

### C.1.2 Results

During the first year, several NanoInks were prepared. The NanoInks were water- and water/ organic based and containing micro- and nano-HA and biocompatible sintering aids. The NanoInks were designed based on specific rheological constraints in order to be compatible with low-cost commercial HP print heads. In particular, viscosity and surface tension were kept in the range of 8 mPas to 100 mPas and  $46 \text{ mNm}^{-1}$  to  $57 \text{ mNm}^{-1}$ , respectively. Nano-HA was included in the formulation up to 40 wt.% in order to improve densification upon sintering. However, formulations with >20 wt.% solid load results to be non-printable or with a too short shelf time even if polymeric additives, such as polyacrylic acid (PAA), and surfactants were used. Some NanoInks containing >20 wt.% of nano- HA powders were produced with a shelf life of 48 hours and different green bodies were 3D-printed [176]. It was concluded that solid load limit was a major issue and the maximum allowed nano-HA was not enough to promote the aimed controlled densification. A more efficient strategy was required: a formulation containing an optimal combination of sintering aids and nano-HA. In the second year of the project, we applied a fast prototyping strategy in order to define the appropriate ceramic NanoInk compositions to achieve the density gradient upon sintering. Several green bodies with a porosity equivalent to that obtained by BiB were prepared using potatoes starch as pore former and binder. In particular, micro-HA powders (50%wt) and the pore former (50wt%) were wet milled in a planetary milling machine for one hour and then dried in the oven at 50 °C. Afterwards, defined amounts of nano-HA, bioglass (Schott Vitryxx, MD01), and colloidal silica were added and mixed to the previous formulation to get all compositions reported in Figure C.2. Nano-HA, bioglass, and colloidal silica act as a sintering aid and bioactivity improver. It has been reported that the addition of such sintering aids promotes the osteoblast differentiation and proliferation compared to pure hy-

droxyapatite samples. Finally, the dry powders were uniaxially pressed in a 5 mm die with a pressure of 2 t. A first thermal treatment (TT) was then applied to burn out the pore former and achieve the equivalent BiB sample's density ( $\approx 1 \text{ g cm}^{-3}$ ). The porous green bodies undergo sintering treatment (ST). The maximum temperature (hold for 1 h) was set to 1450 °C, 1400 °C and 1350 °C for ST1, ST2 and ST3, respectively. In such a way, 42 different compositions were prepared and sintered according to three different thermal profiles, generating 142 sintered bodies. Density, compressive strength and sintering properties of each sample were measured. The temperature selected for TT and ST were optimized after thermogravimetry, dilatometry, and XRD diffraction analyses. In fact, if the pore former is not burned out properly, the green bodies collapse or massive cracks occur. Similarly, if the sintering temperature too low, densification does not occur; if it is too high, the sample might partially melt and vitreous samples are obtained. The so-called diffusion couple technique was applied in order to evaluate the co-firing behaviour at the interface between different formulations. Bi-component samples were prepared by pressing two layers of powders, each of them prepared according to the aforementioned protocol and following the TT and the selected ST profile. Since 42 formulations and three sintering profile was investigated, 5166 couples of the formulation can be prepared. Thus, only the most promising couple of formulations, with appropriate density, mechanical properties, and sintering behaviour, were studied. For the morphological investigation, the axial cross-section of the co-fired samples was prepared and polished using conventional metallographic techniques and analysed by optical and scanning electronic microscopy (SEM). Figure C.1 shows an example where an appropriate ceramic-ceramic junction was obtained upon co-firing. After sintering the two ceramic layers show different densifications and porosities and, at the interface, no delamination occurs. The ceramic on the left-hand-side has a density of  $1.5 \text{ g cm}^{-3}$  and a compressive strength of 9 MPa, which corresponds to the properties of cancellous/trabecular bone (2 MPa to 12 MPa) whereas the layer on the right-hand-side shows a density of  $1.8 \text{ g cm}^{-3}$  and a compressive strength of about 70 MPa, which is approaching the properties of cortical bone ( $> 100 \text{ MPa}$ ). Thus, ceramic scaffolds can be produced using two ceramic NanoInks: the first ink – for the porous ceramic – is composed by 4wt% of colloidal silica, 10% of nano-HA and 2 wt% of bioglass; the second ink - for the densified ceramic - is composed by 4wt% of colloidal silica, 10% of nano-HA and 8 wt% of bioglass. These NanoInks contain an overall solid load compatible with low-cost print heads.

### C.1.3 Conclusion

In the CerInk project, we prepared and tested different NanoInks for ceramic 3DP. The inks were evaluated with respect to the rheological parameters reported in the literature. The solid content of the ink, up to a maximum value of  $\approx 20\text{wt}\%$ , was identified as a limit for commercial low-cost print heads. In order to achieve the aimed controlled densification gradient, a different approach was followed. We explored several formulations in order to identify couples of materials that can be co-fired without delamination and mimicking porosity and mechanical properties of a natural bone. An extended experimental trial based on 42 different formulations and three sintering profiles was systematically studied. Based on the material characterization, the appropriate compositions for the ceramic NanoInks were identified. It has been demonstrated that

- the porosity and the mechanical properties of the co-fired ceramics are appropriate to mimic a natural bone;
- the obtained ceramic-ceramic junction does not present delamination and the aimed density gradient is achieved;
- NanoInk formulations, within the solid load limitation, for controlled densification is possible;
- 3DP using a double-NanoInk BiB technology for ceramic scaffold is feasible.

The CerInk project results were considered of high impact in the biomedical field. They were disseminated as a "successful stories" of SNI projects, section C.1.4.

### C.1.4 SNI successful story 2017

## Individually adapted and stable

The goal of the Nano Argovia project CerInk is to develop custom-made bone replacement materials that closely resemble natural bone

Humans have over 200 different bones with varying shapes, each of which performs a specific, important function in the body. In the event of bone defects due to accidents, inflammation, or tumors, it is possible to replace the damaged bone – or parts of it – with artificial bone. Given the considerable variations between individual patients and bone types, 3D printing seems the obvious method for producing customized replacement bones. However, optimum bone replacement materials must meet a series of demanding requirements. They must be long-lasting and well tolerated by patients. In addition, they should be lightweight and yet mechanically stable – in other words, they should resemble natural bone as closely as possible. As part of the Nano Argovia project CerInk, scientists from the FHNW School of Life Sciences, the Paul Scherrer Institute (PSI), and the Aargau-based company Medicoat AG worked together closely to develop future bone replacement materials of this kind.

### Layers with different properties

Human bones are not homogeneous. Rather, they are characterized by a solid outer surface with a dense, mechanically stable (cortical) bone structure, in combination with an internal, sponge-like (trabecular) structure that acts as a sort of shock absorber. The size of these different layers varies depending on the type of bone. This type of multi-layered structure is also desirable in artificial bones that are implanted into patients following accidents or injuries. Scientists from the FHNW School of Life Sciences, the PSI, and the Aargau-based company Medicoat AG have already gained valuable

experience in the field of innovative bone replacement materials and have previously combined bioceramic materials with polymers to imitate natural bones using 3D printing. Now, as part of the Nano Argovia project CerInk, they have investigated how the printing process can be used to produce compacted layers with improved mechanical stability. To do so, the scientists added ceramic nanoparticles (nano ink) to the base material. In a subsequent sintering process (which consolidates the artificial bone at high temperature), the nanoparticles bring about a change in density.

### Twenty percent is not enough

The team, initially led by Ralf Schumacher (formerly of the FHNW) and later by Dr. Andrea Testino (PSI), used calcium phosphate – the major inorganic component of natural bones – as a scaffolding material for the synthetic bones. They first tested various nano inks with different concentrations of calcium phosphate nanoparticles and biocompatible sintering aids. After some time, it became clear from the experiments that standard print heads can only be used in the 3D printing process if the nano ink contains no more than 20% calcium phosphate nanoparticles. However, this would not allow them to increase the density of the base material to the desired level.

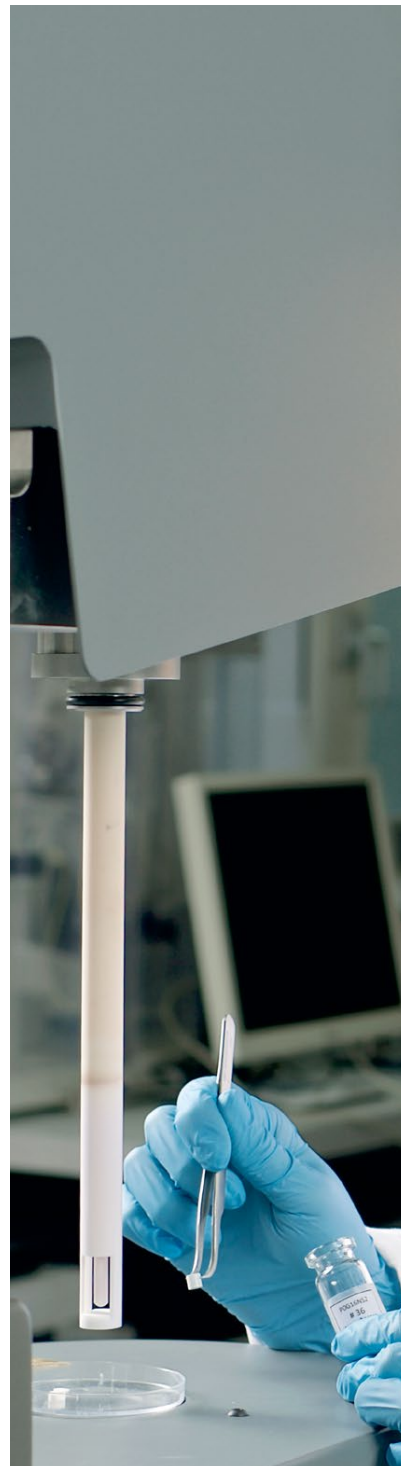
### Potato starch to form pores

In the second year of the project, the scientists therefore adopted a different strategy. To find out which nano ink was the most suitable additive, they produced sample pieces from various combinations of materials – without a printing process. This involved combining a calcium phosphate matrix with potato starch, whose purpose was to form pores and to act as a binder. The base materials were ground, dried, and mixed with differing quantities of calcium phosphate nanoparticles, bioglass, and colloidal silica. These sintering aids support the differentiation and multiplication of osteoblasts in the finished bone implant. Finally, the scientists pressed these mixtures into a casting mold. In the first heat-treatment step, they burned the potato starch to create a porous material with the desired initial density. In the subsequent sintering process, the researchers tested three different temperatures between 1,350°C and 1,450°C. In total, they were left with almost 150 different samples, whose mechanical properties and density they analyzed.

### A successful approach

The scientists then combined two layers of materials with different composition, carefully selected among more than 5,000 possibilities, to find out how stable the boundary was between the two materials after sintering. As a result, the most suitable combinations, in terms of sintering behavior, density, and mechanical stability for modern bone replacement materials, were identified. Based on morphological analyses using both optical and electron scanning microscopes, the team of researchers established that the chosen approach is promising and could be used to bond two layers together firmly even if they have different densities and mechanical properties.

“In the Nano Argovia project CerInk, we showed that we can produce bone replacement materials that closely resemble natural bone,” says Andrea Testino, the project leader. “In our tests, we were able to produce synthetic bone whose properties correspond to the spongy trabecular structure of bone on one hand and the more-stable cortical structure of bone on the other.” Philipp Gruner, CEO of the industrial partner, Medicoat, also considers the completed Nano Argovia project a success: “Thanks to our project partners’ expertise in this outstanding collaboration, we are in a position to break new ground and develop truly innovative products and technologies for the benefit of patients.”





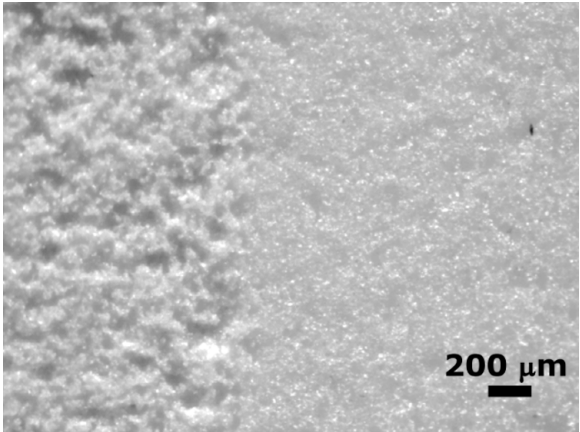


**Figure C.1** – Example of the interface between porous and densified co-fired ceramic (optical micrograph) sintered according to ST2. On the left-hand side, the ceramic has a density of  $1.53 \text{ g cm}^{-3}$  and a compressive strength of 9 MPa, whereas on the right-hand side the ceramic shows a density of  $1.76 \text{ g cm}^{-3}$  and a compressive strength of about 70 MPa.

		Bioglass wt. %											
		0.5		1		2		4		8		16	
		CS MPa	d g cm <sup>-3</sup>	CS MPa	d g cm <sup>-3</sup>	CS MPa	d g cm <sup>-3</sup>	CS MPa	d g cm <sup>-3</sup>	CS MPa	d g cm <sup>-3</sup>	CS MPa	d g cm <sup>-3</sup>
Colloidal Silica wt. %	0.0	9	1.4	15	1.5	15	1.6	23	1.7	14	1.6	--	1.3
	0.5	41	1.7	33	1.7	31	1.7	23	1.6	12	1.5	4	1.5
	1.0	33	1.7	29	1.6	37	1.7	37	1.7	4	1.4	--	1.5
	2.0	42	1.8	37	1.7	32	1.7	21	1.6	10	1.5	--	1.6
	4.0	38	1.6	39	1.9	9	1.5	48	1.8	70	1.8	--	2.1
	8.0	88	2.4	91	2.5	93	2.5	78	2.5	33	2.3	6	2.2
	16	78	2.4	77	2.5	89	2.6	75	2.3	39	2.1	24	2.2

**Figure C.2** – Compression strength (CS) and density of the samples sintered according to ST2. The blue values correspond to the bi-component samples reported in Figure C.1.



## **C.2 Patent application**

### **Method for biomimetic growth of calcium phosphates ceramics on metal implants, 2017P22445EP01**

PTC-European patent

Applicant: Paul Scherrer Institut

Priority date: 20<sup>th</sup> October, 2017

#### **C.2.1 Abstract**

The objective of the present invention to provide a method for growth of calcium phosphates ceramics (CPs) on metal implants, particularly on Ti and Ti-alloy implants, that generates thin and durable coatings of metal implants without the limitation of other techniques known in the art. This objective is achieved according to the present invention by a biomimetic method for which comprises the following steps:

- a) a combination of mechanical, chemical, and thermal treatments in order to generate an appropriate grafting layer on the metal implant; and
- b) a coating procedure of the treated metal implant by controlled CaPc precipitation.

The results demonstrated that metal implants can be efficiently coated with CaPc in a short time using a wet method, offering unprecedented opportunities. This wet route is carried out at almost room temperature, at low cost, with an environmental-friendly method with low energy consumption, and in a short time. According to the invention, an innovative and extremely competitive method for coating of metal implants with CaPc is claimed.

---

This chapter is adapted from **A. Carino** and A. Testino, Method for biomimetic growth of calcium phosphates ceramics on metal implants. From Patent 2017P22445EP, **2017**, [177].

---

### C.2.2 Introduction

The present invention relates to a method for biomimetic growth of calcium phosphates ceramics on metal implants, particularly on Ti and Ti-alloy implants.

Parallel to the development of economy and technology, the number of aged people demanding compromised tissue replacement is rapidly increasing. Moreover, there is an expanding requirement for hard tissue replacement as a consequence of sports related and degenerative injuries. It is estimated that >70% of biomedical implants are made of metallic materials. Among them, Ti and its alloys are widely used in dental, craniomaxillofacial, spinal and orthopaedic surgery because of their excellent mechanical properties that are required for load bearing applications.

Titanium implants can be osseointegrated, that is the structural and functional connection between bone tissue and the surface of an artificial implant. This phenomenon was discovered in 1952 by the Swedish professor Per-Ingvar Brånemark – considered the father of the modern dental implantology – who found that titanium attaches itself to the bone when it is implanted in it. The osseointegration is possible thanks to the native thin layer of  $\text{TiO}_2$  on the Ti surface.

The topography and chemistry of the metal surface is usually modified to improve its biocompatibility and bioactivity: as the interaction between the cells and tissues with biomaterials is a surface phenomenon occurring at the tissue-implant interface, implant surface properties play a major role in determining both the biological response to implants and the material response to the physiological conditions. Several studies were carried out in order to improve osseointegration and it was concluded that an optimal surface roughness of the metal implants, which is in the range of few micrometers, offers clinical advantages. This roughness is generally obtained by blasting or electrochemical methods. Additional surface treatments may be applied, such as acidic etching, in order to further promote the natural bone growth *in vivo*. A further improvement is achievable if the implant is coated with bone-like ceramic materials, such as calcium phosphate ceramics (CaPc), which are promoting a much faster osseointegration.

Several CaPc exist. The most commonly used is hydroxyapatite (HA), but alternative materials, such as octacalcium phosphate (OCP), dicalcium phosphate dihydrate (DCPD), tri-calcium phosphate (TCP), and dicalcium phosphate anhydrous (DCPA) might be applied. HA is mainly deposited by plasma-spraying technique directly onto Ti substrate. Plasma-spray, although clinically established, has specific drawbacks such as the extremely high processing temperatures and, as for other spray techniques,

difficulties to coat complex- shaped parts due to the line of sight issues. Alternatively, CaPc can be deposited by electrochemical deposition (ECD) methods: typically DCPD or HA is deposited in solution with this technique. ECD offers advantages because no high temperature is applied and some line of sight difficulties are solved. Nevertheless, the non-homogeneous electric field in solution produces areas where the coating is rather thick and other zones where no deposition occurs due to shielding effects. Moreover, thin coating capability remains a major limitation.

Recently the discrete particle deposition (DPD) method has been reported. Here, the implant is immersed in a suspension of CaPc particles, typically HA nanoparticles, and some of those particles remain on the implant surface. This method, known in several others fields as “dip coating”, allows the fast and easy materials deposition on the substrate but the interaction between the particles and the substrate is rather labile. Moreover, the surface can be only partially coated. Nevertheless, even this simple surface deposition was reported to be beneficial for faster osseointegration. To overcome some limitations of the aforementioned deposition techniques, wet or biomimetic methods were studied.

Most of the reported wet method approaches consist of soaking the implant in a simulated body fluid (SBF) solution for several days and let the CaPc grows on the implant surface. The main disadvantage of this method is the long time required for coating which makes the process not commercially valuable. One of the main concerns about ceramic coatings, in particular for dental implants, is related to delamination that is the disconnection between the metal implants and the ceramic coating. In case of delamination, inflammation occurs, and the implant fails. Delamination can be avoided by an appropriate metal-ceramic joining and by controlling the CaPc thickness. Furthermore, the disadvantage of a thick coating is that the micro-topography of the implant surface and the consequent beneficial topographical effect of the surface morphology might be lost.

In particular, in the field of dental implants, the stability of the implants is a key feature. Just after the implantation, a primary stability (or mechanical stability) is attained; this mainly depends on the design of the screw, the surgical technique, and the bone conditions. After a longer time, *e.g.*, three-six months, osseointegration occurs and the so-called secondary stability (or biological stability) is attained. The overall implant stability is the sum of primary and secondary stabilities, which shows a minimum 2-4 weeks after the implantation. During this timeframe, the probability of implant failure is maximized. Rapid osseointegration (*e.g.*, a short healing time) shifts the overall implant stability towards a shallower minimum, thereby decreasing the implant

## C. Appendix C

---

failure probability and reducing the unpleasant patient period between surgery and a normal chewing performance. CaPc coating on dental implants can play a relevant beneficial role by shortening the healing time provided that the aforementioned issues associated to the deposition method are solved.

It is therefore objective of the present invention a method for CaPc coating of metal implants, particularly of Ti and Ti alloy implants, that provide a thin CaPc coating which is strongly bonded to the metal implants and deposited in a short time, thus without the limitations and drawbacks of the techniques currently known in the art.

### C.2.3 Objectives

This objective is achieved according to the present invention by a biomimetic method for CaPc coating of metal implants, particularly on Ti and Ti alloy implants, comprising the following steps:

Step-1: a combination of treatments in order to generate an appropriate grafting layer on the metal implant; such Step-1 is preferably composed of one or more of the following Sub-process:

Sub-proc-1: a mechanical or electrochemical treatment on the machined surface in order to generate a primary roughness in the range of few micrometers; and/or

Sub-proc-2: a chemical treatment with an alkaline solution, in order to generate an appropriate chemical phase on the surface of the metal implant; and/or

Sub-proc-3: a thermal treatment in order to promote an appropriate metal- ceramic joining of the grafting layer; and/or

Sub-proc-4: a final chemical treatment with an alkaline solution in order to improve the reactivity of the grafting layer; and

Step-2: the implant treated according to Step-1 is coated with CaPc by controlled precipitation.

The results demonstrated that metals, in particular, Ti and Ti alloy, can be efficiently coated with CaPc in a short time using a wet method, offering unprecedented opportunities. This wet route is carried out at almost room temperature, at low cost, with an environmental-friendly method with low energy consumption, and in a short

time. According to the invention, an innovative and extremely accurate method for metal implant coating with CaPc has been developed. Moreover, the present results carried out in controlled precipitation conditions are showing efficient control over the CaPc phase deposited. In particular, OCP can be deposited. *In vivo* experiments have shown that OCP is rapidly converted to HA within 7-10 days after implantation and the rate of new bone formation on HA converted from OCP was much greater than that of both calcium-deficient HA and stoichiometric HA implanted directly. The effect of calcium phosphates on the osteoblastic activity and bone regeneration, with particular emphasis on OCP activity, has been recently reviewed concluding that, *in vivo*, OCP seems more bioactive than other calcium phosphate phases. Using the present invention method, DCPD, OCP, HA and combination thereof can be deposited by controlled precipitation on metal implants.

### C.2.4 Preferred embodiments

Preferred embodiments of the present invention are alone or in combination mentioned in the following:

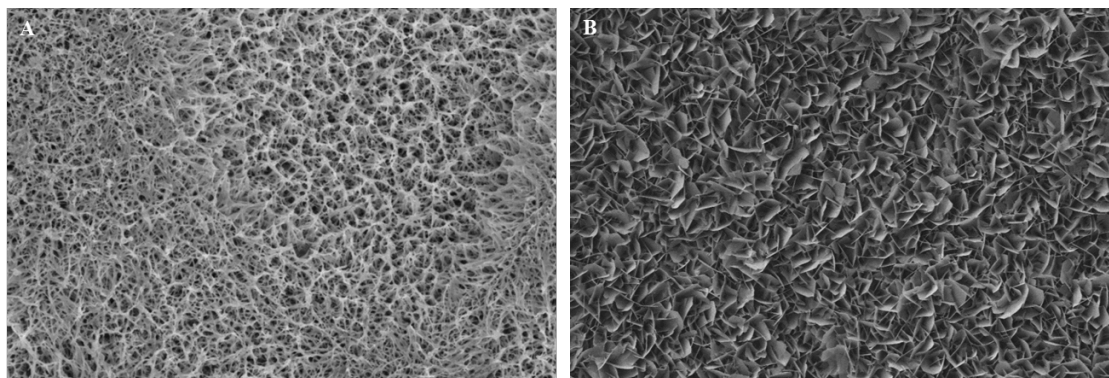
- a) the Sub-process-2, 3 and 4 of Step-1 are performed, Sub-process-1 is dismissed;
- b) the Sub-process-2 of Step-1 is performed under hydrothermal conditions;
- c) the Sub-process-1, 2 and 3 of Step-1 are performed, Sub-process-4 is dismissed;
- d) the Sub-process-2 of Step-1 is carried out using a solution comprising NaOH or KOH or H<sub>2</sub>O<sub>2</sub> or combination thereof;
- e) the Sub-process-3 of Step-1 is carried out under controlled atmosphere comprising inert gas or reducing gas;
- f) the Ca<sup>2+</sup> activity during Step-2 is actively controlled according to a defined profile; and
- g) the implant is a non-Ti or non-Ti-alloy and the chemical Sub-process-2 and Sub-process-3 make use of acidic solutions.

Preferred embodiments of the present invention are hereinafter described in more detail with respect to the attached drawings which depict:

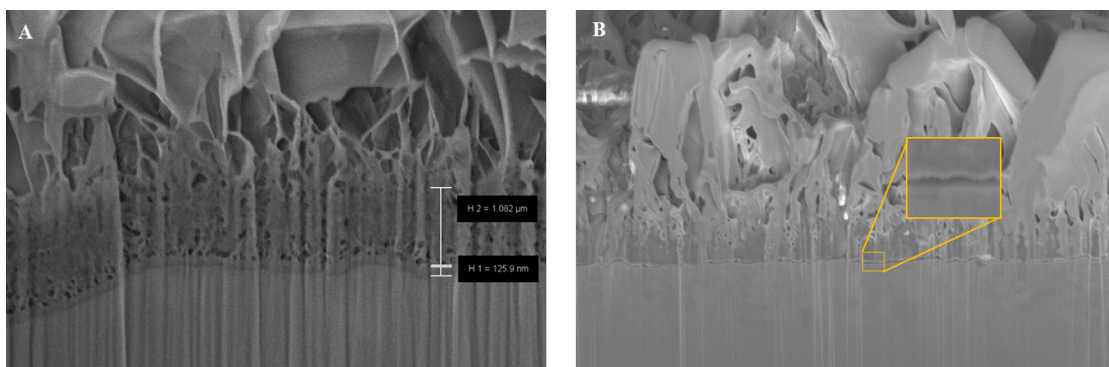
## C. Appendix C

---

In figure C.2.4.1, SEM micrographs: (A) grafting layer obtained on machined Ti surface and after Step-1. (B) The same sample after coating with OCP (Step-2) with its typical nano-lamellar morphology.

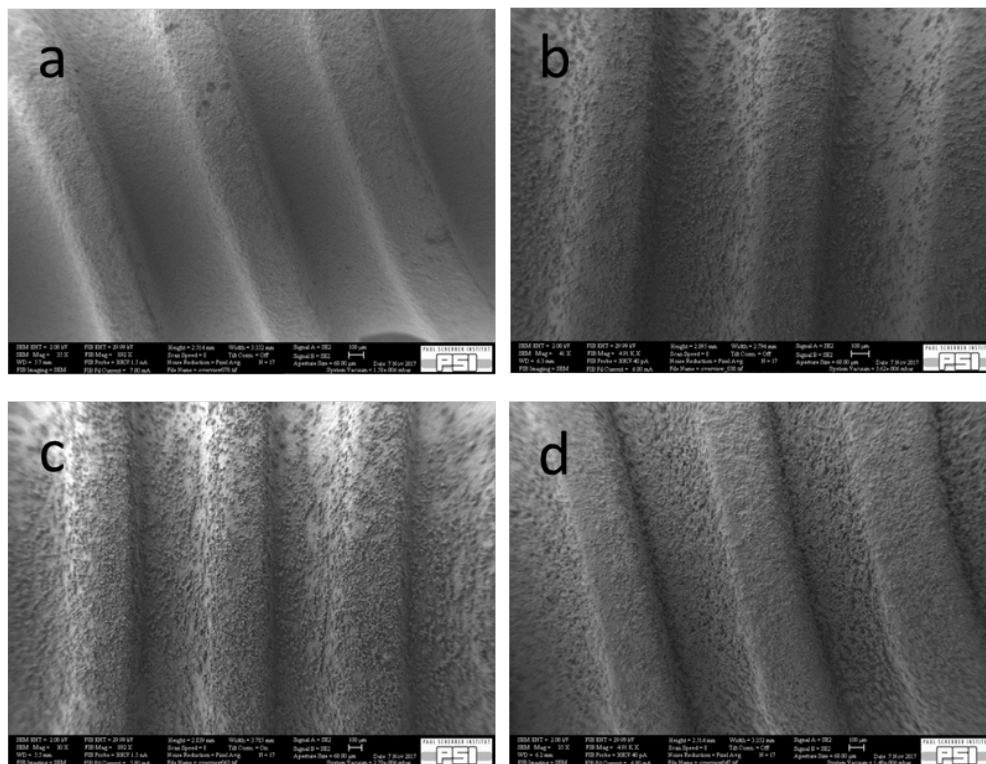


In figure C.2.4.2, SEM micrographs after FIB milling: (A) Machined Ti surface after step 1 & 2; (B) Sample after HA deposition (Step-2) without grafting layer (Step-1).



The method provides an efficient protocol for biomimetic coatings of metal (*e.g.*, Ti and Ti-alloy) implants with CaPc. The obtained control over the precipitation process has been achieved because of several years of research focused on the theoretical study of solid phases' formation from solution with the aim to disclose the details of the precipitation mechanism. Such studies were developed on amorphous calcium carbonate (ACC), which is a model system, on calcium silicate hydrate (CSH), which is the main constituent of cements, and on CaPc phases. Thanks to these theoretical and experimental studies on the nucleation and growth mechanism of such materials and the development of the thermodynamic-kinetic models for their formation from solution, the method was fine-tuned to predict the exact experimental conditions at every time step of the CaPc formation (*e.g.*, temperature, *pH*, ionic strength, concentration of all chemicals, and speed of adding such chemicals into a defined reactor) to promote heterogeneous nucleation and, then, growth of a layer of the target ceramic material on the metallic surface. To evaluate the *in vitro* performance of the coated materials, the method can be applied to a polished Ti Grade 4 disks.

213



step (Step-1) comprises a sequence of sub-processes: the metal surface to be treated may undergo several mechanical, electrochemical, chemical, and thermal processes to obtain a rough and highly porous surface with appropriate grafting features (see Figure 1A, grafting layer). A preferential first sub-process comprises a mechanical (such as blasting) or electrochemical treatment on the machined surface to generate a primary roughness in the range of few micrometers. A preferential second sub-process comprise a chemical treatment with an alkaline solution (which include but it is not limited to NaOH, KOH, H<sub>2</sub>O<sub>2</sub>, and combination thereof) at temperature between 25 °C to 400 °C, pressure between 1 bar to 300 bar, and time between 10 minutes and 1 week, in order to generate an appropriate chemical phase on the surface of the metal implant. A preferential third sub-process comprises a thermal treatment in the oven under controlled atmosphere in the temperature range between 100 °C to 1000 °C and for the time between 0.1 h to 48 h to promote the phase transformation of the chemical phase formed during the second sub-process and an appropriate metal-ceramic joining of the grafting layer. A preferential fourth treatment comprises a chemical treatment with an alkaline solution in order to improve the reactivity the thermally treated grafting layer.

Thus, Step-1 includes fourth sub-processes, and it is substantially different with respect to the procedure described by Kokubo *et al.* [178]. The grafting layer can be obtained according to the described procedure on Ti and Ti-alloy, but the same functional properties of such grafting layer can be achieved on other metals and metals alloy using a modified protocol which can comprise the use of acidic solution in the second and fourth Sub-processes. In the second step (Step-2), the sample is immersed into a coating reactor for controlled CaPc precipitation. The coating is done under controlled conditions in order to obtain the desired calcium phosphate phase(s), comprising hydroxyapatite (HA), octacalcium phosphate (OCP), tricalcium phosphate (TCP), amorphous calcium phosphate (ACP), dicalcium phosphate dihydrate (DCPD), dicalcium phosphate anhydrous (DCPA), and combination thereof, with controlled porosity, morphology, thickness, and deposition rate.

In the given example of Figure C.2.4B, the experimental conditions were selected to promote the formation of OCP. The ceramic phase was confirmed by X-ray diffraction and Raman spectroscopy. In the applied experimental conditions, OCP has a delicate nanomorphology, which consists of lamellas with a thickness of few nm and an equivalent diameter of few μm. The coating method is able to provide a CaPc layer in aqueous media by controlling the nucleation and growth process of the targeted



ceramic phase(s). The layer grows into and onto the grafting layer which is strongly joined to the metallic implant.

The solid phase formation is promoted by controlling the saturation ratio of the system. The saturation ratio can be controlled in a different way comprising the addition of calcium ion solution into a phosphate ions solution where the parts to be coated are immersed. The saturation ratio can be kept either constant during the coating procedure or increased or decreased according to the desired coating protocol in order to obtain the appropriate gradient ceramic properties comprising morphology, phase, thickness, adhesion, and the optimal deposition rate. The concentration of the calcium and phosphate ion solutions can be in the range  $1 \text{ mmol L}^{-1}$  to  $500 \text{ mmol L}^{-1}$ , more specifically in the range  $5 \text{ mmol L}^{-1}$  to  $50 \text{ mmol L}^{-1}$ , and the  $pH$  in the range 6-10 more specifically in the range 7-9, more specifically close to the physiological  $pH$  ( $7.4 \pm 0.5$ ). The  $\text{Ca}^{2+}$  solution may contain other cations comprising, for instance,  $\text{Mg}^{2+}$  or  $\text{Sr}^{2+}$ . The phosphate solution may contain other anions comprising for instance carbonate and/or fluorine ions and/or organic carboxylic acid. The temperature is kept in the range  $5^\circ\text{C}$  to  $95^\circ\text{C}$ , more specifically in the range  $25^\circ\text{C}$  to  $80^\circ\text{C}$ , more specifically in the range close to the physiological temperature ( $37^\circ\text{C} \pm 5^\circ\text{C}$ ). The ionic strength can be in the range  $0.002 \text{ mol L}^{-1}$  to  $0.5 \text{ mol L}^{-1}$ , more specifically in the range  $0.01 \text{ mol L}^{-1}$  to  $0.2 \text{ mol L}^{-1}$ , more specifically close to the human isotonic condition ( $0.154 \text{ mol L}^{-1} \pm 0.05 \text{ mol L}^{-1}$ ). The calcium ion solution is added into the phosphate solution according to a defined flow rate in a range which depends on the reactor volume. The ratio between the flow rate (in  $\text{L h}^{-1}$ ) and the reactor volume (in L) can be in the range  $0.005 \text{ h}^{-1}$  to  $0.5 \text{ h}^{-1}$ , more specifically in the range  $0.05 \text{ h} \pm 0.005 \text{ h}$ . The gas atmosphere in the reactor can be controlled in term of temperature, humidity, and composition. Typically, air or  $\text{N}_2$  stream,  $\text{CO}_2$ -free, water-saturated, and at the same temperature set in the Step-2, is used.

Temperature,  $pH$ , ionic strength, calcium ion solution flow rate, and calcium ion activity can be kept either constant during the entire coating process or varied according to a predefined protocol or actively controlled during the coating process. The coating time, which depends on the specific experimental conditions, the calcium phosphate phase targeted, and the wanted thickness, can be in the range 0.1 h to 24 h, more specifically 1 h to 5 h, more specifically 1 h to 2 h. The saturation level during the coating process with respect to the solubility of the formed ceramic phase is controlled by the deposition conditions and can be in the range 1 to 50, more specifically in the range 1 to 10. The saturation level is evaluated by a complex kinetic-

## C. Appendix C

thermodynamic model, which is calculating the activities of all known chemical species in solutions comprising:  $\text{OH}^-$ ,  $\text{Ca}^{2+}$ ,  $\text{PO}_4^{3-}$ ,  $\text{H}_2\text{PO}_4^-$ ,  $\text{H}_3\text{PO}_4$ ,  $\text{CaHPO}_4$ ,  $\text{CaPO}_4^-$ ,  $\text{H}^+$ ,  $\text{CaH}_2\text{PO}_4^+$ ,  $\text{P}_2\text{O}_7^{4-}$ ,  $\text{HP}_2\text{O}_7^{3-}$ ,  $\text{H}_2\text{P}_2\text{O}_7^{2-}$ ,  $\text{H}_3\text{P}_2\text{O}_7^-$ ,  $\text{H}_4\text{P}_2\text{O}_7$ ,  $\text{HPO}_4^{2-}$ ,  $\text{M}^+$ ,  $\text{X}^-$ , clusters such as  $\text{Ca}_x(\text{PO}_4)_y(\text{OH})_z(\text{H})_k(\text{M})_m(\text{X})_n^h$ ,  $\text{MHPO}_4$  where M is a cation including – but it is not limited to –  $\text{Na}^+$ ,  $\text{K}^+$ ,  $\text{NH}_4^+$  and X an anion including – but it is not limited to –  $\text{Cl}^-$ ,  $\text{NO}_3^-$ ,  $\text{F}^-$  and the solid phase(s) formed including HA, OCP, TCP, ACP, DCPD, and DCPA. In a typical Step-1 procedure, a blasted metal implant is immersed in NaOH or NaOH/ $\text{H}_2\text{O}_2$  solution and soaked for 12 h to 24 h at 40 °C to 90 °C, while the part is kept under constant rotation in the static or mixed alkaline solution. Alternatively, a blasted metal implant is treated with KOH or KOH/ $\text{H}_2\text{O}_2$  solution in an autoclave for 0.5 h to 6 h at 100 °C to 250 °C. The chemically treated implant is washed and treated in a static oven in air for 0.5 h to 6 h at 400 °C to 900 °C.

Alternatively, the chemically treated and washed implant is treated in an oven with controlled flowing atmosphere (inert or reducing atmosphere) for 0.5 h to 6 h at 200 °C to 700 °C. The thermally treated implant is soaked in a solution containing a phosphate buffer. Alternatively, the thermally treated implant is immersed in an alkaline solution for 0.5 h to 6 h at 25 °C to 90 °C. In a typical Step-2 procedure, the implant treated according to Step-1 is soaked in a reactor containing a phosphate solution, which is kept under stirring. Preferentially, the implant is kept under constant rotation during the entire Step-2 procedure. The position of the implant into the reactor can be optimized base on fluid dynamic modelling in order to achieve an optimal coating homogeneity. The coating may be triggered by addition of  $\text{Ca}^{2+}$  solution into the reactor. The coating process is monitored by online data collection, that is performed using a commercial analytical setup composed by titrator devices equipped with dosing burettes and anti-diffusion tips, pH electrodes equipped with Pt1000, ion-sensitive electrodes, and in-situ Raman spectroscopy. The ionic strength evolution is controlled online by a conductivity module.

The saturation level is evaluated by means of the signals generated by the ion-sensitive electrodes and computed by means of the thermodynamic-kinetic model for the precipitation process. The saturation level is related to the driving force of the deposition and needs to be kept in a range where nucleation and growth occur only on the surface to be coated. Thus, during the entire Step-2 the activity of  $\text{Ca}^{2+}$  ion into the reactor is monitored and actively controlled. The activity of  $\text{Ca}^{2+}$  can be kept constant, increased or decreased during the entire Step-2 in order to optimize the coating in term of CaPs phase, thickness, porosity, morphology, and deposition rate. An optimal coating pro-

tocol is defined by a specific  $\text{Ca}^{2+}$  activity profile during the entire Step-2 procedure. The coating method can be easily scaled up to coat simultaneously several Ti implants immersed in a large reactor. In a simplified lab-scale procedure, a  $10 \text{ mmol L}^{-1}$   $\text{CaCl}_2$  solution is added at a constant rate ( $30 \mu\text{L min}^{-1}$ ) in a 0.035 L of a  $10 \text{ mmol L}^{-1}$   $\text{NaH}_2\text{PO}_4/\text{Na}_2\text{HPO}_4$  buffer, kept under constant stirring and temperature ( $37^\circ\text{C}$ ) in a double-jacket pyrex-glass vessel connected with an external thermostatic bath. The pH is kept constant at 7.4 via counter titration of alkaline ( $\text{NaOH}$ , 10 mM) and acidic ( $\text{HCl}$ ,  $10 \text{ mmol L}^{-1}$ ) solutions. The ionic strength is kept constant at  $0.154 \text{ mol L}^{-1}$  by  $\text{NaCl}$  addition. The solid calcium phase formation is followed by the ion-sensitive electrodes and the coating time is of 2 h. The coated parts are removed from the reactor and rinsed with milliQ water. In such experimental conditions, a layer of  $3 \mu\text{m}$  to  $5 \mu\text{m}$  of OCP phase is deposited on the metallic support. The layer is composed by lamellar calcium phosphate. Each lamella has a thickness of about 2 nm to 5 nm and an average equivalent diameter of  $2 \mu\text{m}$  to  $5 \mu\text{m}$ . The ceramic phase grew in the porosity of the grafting layer and on top of it. The ceramic layer is highly porous and strongly joined with the metallic support. Figure C.2.4A shows a scanning electron microscopy (SEM) cross section, obtained by focused ion beam (FIB) milling, of the sample. The coating time of such sample was about 12 h; as a result, it was over-coated with OCP. In those specific experimental conditions, 1 h to 2 h treatment is sufficient to reach an appropriate coating thickness. As a comparison, Figure 2B shows the result of OCP deposition on a polished Ti metal surface (Step-2 without Step-1): OCP is anyway deposited, but the ceramic layer is clearly delaminated at the metal-ceramic interface because an appropriate grafting layer is missing. Thus, the not-properly deposited CaPc layer can easily delaminate once implanted. Figure C.2.4 shows SEM micrographs: (A) grafting layer obtained on machined Ti surface and after Step-1; (B) reports on the same sample after OCP coating (Step-2) with its typical nano-lamellar morphology. Figure C.2.4 shows SEM micrographs after FIB milling. Figure C.2.4(A) refers to a machined Ti surface after step 1 & 2. On the Ti substrate, first a dense layer (about 120 nm) of Ti-based material and then a porous layer (about  $1 \mu\text{m}$ ) of Ti-based material are formed by chemical and thermal treatments. After Step-2, most of the porosity of the grafting layer was filled with OCP. On top, a thick but open-porous layer of several microns of OCP was grown. Figure 2(B) shows the same sample after OCP deposition (Step-2) without grafting layer (Step-1). Thus, OCP was grown directly on a machined Ti surface. The absence of a grafting layer induces delamination of the CaPc layer from metal. In the inset, the consequent extended fracture at the metal-ceramic interface is shown. The chemical composition of each layer was identified by EDX

analysis. Figure C.2.4 shows SEM micrographs of dental implants treated according Step-1 and different Step-2 treatment in order to achieve different coatings. In Figure C.2.4a, only a very small amount of CaPc is deposited inside the porous structure of the grafting layer. In Figure C.2.4a-d, a progressively higher amount of OCP is deposited (0.5 h, 2 h, 4 h and 8 h, respectively).

### C.2.5 Patent claims

1. A method for biomimetic growth of CaPc on a metal implant, particularly on a Ti and Ti-alloy implant, comprising the following steps:
  - $\alpha$ . Step-1: a combination of treatments in order to generate an appropriate grafting layer on the metal implant; such Step-1 is preferably composed of one or more of the following Sub-process:
    - i. Sub-process-1: a mechanical or electrochemical treatment on the machined surface in order to generate a primary roughness in the range of few micrometers; and/or
    - ii. Sub-process-2: a chemical treatment with an alkaline solution, in order to generate an appropriate chemical phase on the surface of the metal implant; and/ or
    - iii. Sub-process-3: a thermal treatment in order to promote an appropriate metal-ceramic joining of the grafting layer; and/or
    - iv Sub-process-4: a final chemical treatment with an alkaline solution in order to improve the reactivity grafting layer; and
  - $\beta$ . Step-2: coating of the implant treated according to Step-1 by controlled CaPc precipitation.
2. The method according to claim 1 wherein the Sub-process-2, 3 and 4 of Step-1 are performed.
3. The method according to claim 1 or 2 wherein the Sub-process-2 of Step-1 is performed under hydrothermal conditions.
4. The method according to claim 1 wherein the Sub-process-1, 2, and 3 of Step-1 are performed.
5. The method according to any of the preceding claims, where the Sub-process-2

of Step-1 is carried out using a solution comprising NaOH or KOH or H<sub>2</sub>O<sub>2</sub> or combination thereof;

6. The method according to any of the preceding claims, where the Sub-process-3 of Step-1 is carried out under controlled atmosphere comprising inert gas or reducing gas.
7. The method according to any of the preceding claims, where the Ca<sup>2+</sup> activity during Step-2 is actively controlled according to a defined profile.
8. The method according to any of the preceding claims where the implant is not Ti or Ti-alloy and the chemical Sub-process-2 and Sub-process-3 an acidic solutions might be used.



### C.3 Continuous synthesis of gold nanoparticles using the segmented flow tubular reactor (SFTR)

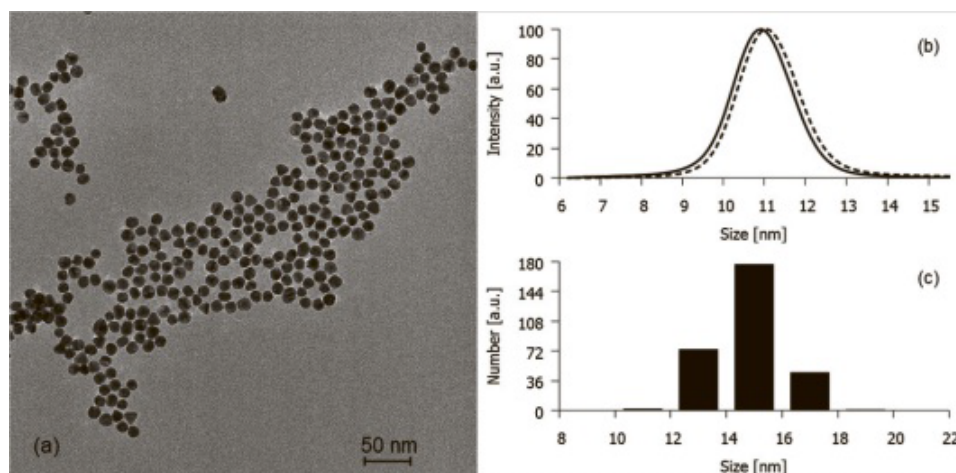


**Figure C.3** – (a) Low magnification TEM micrograph of *Au* NPs; (b) particle size distribution in number (–) and volume (–) by differential sedimentation methods, CPS Instruments, Inc. and (c) in number from TEM micrographs.

Author's contribution to this publication:

- i. samples synthesis using SFTR;
- ii. DLS measurements.

Nanomaterials are nowadays produced in many laboratories worldwide at the mg scale via bottom-up approaches. The upscaling from mg to g quantities by increasing the reactor volume, maintaining a well-defined particle size distribution (PSD), morphology, stoichiometry and polymorphic phase, is generally problematic because of the lack of fine control over mass and heat transport in large batches. In fact, the relative contribution of elementary processes which control the solid formation from solution, such as nucleation, growth and agglomeration, are extremely sensitive to the local environment of each particle.

In the last 20 years, a reliable concept for high quality nanoparticles (NPs) produc-

This chapter is adapted from **A. Carino** *et al.*, Continuous Synthesis of Gold Nanoparticles Using the Segmented Flow Tubular Reactor (SFTR). From *CHIMIA International Journal for Chemistry*, **2016**, 70 (6), [164].

tion in relatively large quantities was developed: the Segmented Flow Tubular Reactor (SFTR) [179–185]. The SFTR concept is as elegant as it is simple: instead of increasing the batch size, the number of small reactors, in form of droplets, is multiplied. The physicochemical transformation occurs in droplets confined in a tubular reactor and segmented by a secondary immiscible fluid. The solid formation could occur in water [180–182] or in an organic solvent [183, 184] expanding the portfolio of the possible chemical reactions. This methodology was applied for the preparation of metals, simple and complex metal oxides, and salts. Here we present an additional SFTR product, gold NPs for biomedical application. The synthesis is realized by the citrate route, *i.e.* by reducing the gold precursors ( $\text{HAuCl}_4$ ) with sodium citrate in water. Using the SFTR, the concentration of the chemicals, their ratio, the ageing temperature and time can be accurately controlled and reset to different values within minutes, allowing a rapid screening of several experimental conditions. Fig. C.3 shows an example of Au NPs prepared at 95 °C, with an aging time of 5 min, at the flow rate  $1 \text{ L h}^{-1}$  and at the concentration of about  $0.2 \text{ g L}^{-1}$ . As demonstrated by several systems, the material properties, such as the PSD, are maintained over time thanks to the prevention of fouling action of the segmenting fluid. The daily throughput of such gold NPs can easily reach 5 g per reaction tube. The NP suspension can be concentrated by ultrafiltration and purified by dialysis.

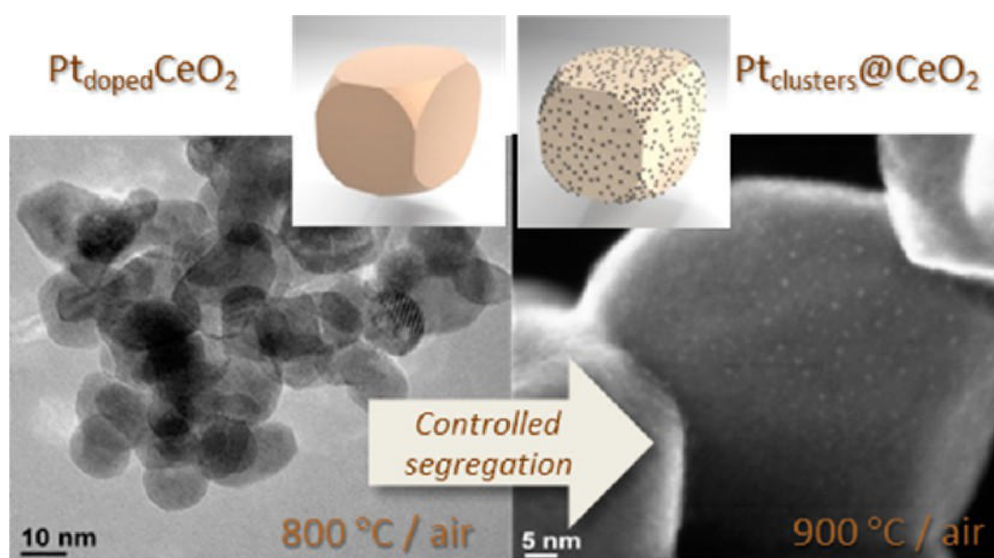
The SFTR technology is able to provide NPs with a narrow PSD, in a reproducible manner, at a limited cost, and in relatively high amount. The colloidal suspensions were produced to assess the interaction between NPs and biological systems by *in vitro* testing; they will be applied as long-term reference materials for toxicology, traceability, reliability, and measurement uncertainty testing by interlaboratory comparison that involves different Swiss research institutes and industrial partners with a direct link to regulatory European and American medical institutions [186].



## D | Co-authorship



## D.1 Size Control of Pt Clusters on CeO<sub>2</sub> Nanoparticles via an Incorporation-Segregation Mechanism and Study of Segregation Kinetics



Author's contribution to this publication:

- i. samples preparation for Synchrotron experiments;
- ii. synchrotron experiments.

# Size Control of Pt Clusters on CeO<sub>2</sub> Nanoparticles via an Incorporation–Segregation Mechanism and Study of Segregation Kinetics

Frank Pilger,<sup>†,‡</sup> Andrea Testino,<sup>\*,†</sup> Agnese Carino,<sup>†,‡</sup> Christian Proff,<sup>†,§</sup> Anastasios Kambolis,<sup>†,||</sup> Antonio Cervellino,<sup>§</sup> and Christian Ludwig<sup>†,‡</sup>

<sup>†</sup>Paul Scherrer Institut, Energy and Environment Research Division, Villigen PSI CH-5232, Switzerland

<sup>‡</sup>École Polytechnique Fédérale de Lausanne (EPFL), ENAC-IIE, CH-1015 Lausanne, Switzerland

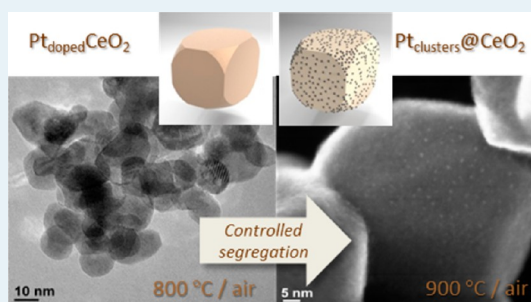
<sup>§</sup>Paul Scherrer Institut, Synchrotron Radiation and Nanotechnology Research Department, Villigen PSI CH-5232, Switzerland

<sup>||</sup>École Polytechnique Fédérale de Lausanne (EPFL), Institut des Sciences et Ingénierie Chimiques, CH-1015 Lausanne, Switzerland

## Supporting Information

**ABSTRACT:** Recent literature on Pt/CeO<sub>2</sub> catalysts reveals that ionic Pt species could be incorporated into the CeO<sub>2</sub> lattice. Here we present a detailed study of Pt segregation in air and under a reducing atmosphere conducted on thermally treated samples by high-resolution X-ray diffraction (XRD) and X-ray absorption spectroscopy. We further perform a kinetic study by *in situ* XRD measurements with the aim of estimating the activation energy for Pt cluster segregation and coalescence in air, which was found to be ~3.88 eV. This high activation energy indicates that Pt clusters are strongly anchored on the CeO<sub>2</sub> surface and that their mobility is activated only at >900 °C. We clearly show the correlation between the nature of the segregated Pt particles and the applied thermal treatment for Pt/CeO<sub>2</sub> nanomaterials prepared by the wet chemical route. On the basis of thorough characterization, we present a possible segregation pathway under oxidizing conditions as opposed to a mere surface reduction during a reducing treatment, leading to the coalescence of less anchored Pt. The catalytic performances confirm the remarkable activity and thermal stability of entities obtained via an incorporation–segregation mechanism.

**KEYWORDS:** Pt/CeO<sub>2</sub>, segregation kinetics, ionic dispersion, polyol synthesis, *in situ* XRD



## 1. INTRODUCTION

Because rare earth elements (REEs), mainly in the form of oxides, are a worldwide issue because of their limited availability and, under the present economic situation, only a few countries control the market, their demand and, consequently their costs have risen dramatically over the past decade.

Among REEs, cerium dioxide-based materials have attracted considerable attention in recent years because of their superior performance in several technological fields.<sup>2–11</sup> The high cost of the raw materials is justified by the performance and stability of the derived product materials. In catalysis, CeO<sub>2</sub> is used as a support for noble metals, such as Pt or Pd, which act as a catalytic center for a series of reactions, such as CO oxidation.<sup>12</sup> Today, it is largely accepted that CeO<sub>2</sub> is not merely a support for the noble metals but is actively involved in the catalytic process itself. Its action is associated with remarkable redox properties.<sup>13,14</sup> CeO<sub>2</sub> is able to accommodate a large number of oxygen vacancies, compensated by Ce<sup>3+</sup> species, resulting in a material with significant oxygen mobility and oxygen storage capacity (OSC).<sup>15,16</sup> As a consequence, the catalytic activity is

localized to areas where the noble metal, CeO<sub>2</sub>, and the gaseous reactants are simultaneously present (three phase points). To increase the number of these catalytic centers, the noble metal should be dispersed on the metal oxide surface in entities that are as small as possible. Moreover, such entities should not diffuse on the metal oxide surface *in operando*; otherwise, they rapidly coalesce into larger particles with a rapid activity loss. The diffusion of the noble metal entities can be prevented if they are strongly bonded on the CeO<sub>2</sub> surface. Pt and Pd present both a rather stable oxidation state IV and an ionic size compatible with the CeO<sub>2</sub> host lattice, meaning that Pt ions can be accommodated at the Ce positions (Pt<sub>Ce</sub>) without the need for compensation defects. Thus, Ce–O–Pt (or Pd) chemical bonds are possible both on the metal oxide surface and in the form of dispersed ions in the fluorite-like CeO<sub>2</sub> lattice. The presence of such surface chemical interactions as well as the

Received: March 31, 2016

Revised: April 26, 2016

Published: April 29, 2016

## D.1. Size Control of Pt Clusters on CeO<sub>2</sub> Nanoparticles via an Incorporation-Segregation Mechanism and Study of Segregation Kinetics

ionic dispersion of Pt and Pd into the metal oxide lattice has been theoretically predicted<sup>17,18</sup> and experimentally proven.<sup>19–24</sup> In parallel, several authors have reported interesting correlations between the type of interaction and catalytic activity.<sup>25–47</sup>

The applied procedure for preparing catalysts and their processing is highly relevant. Traditionally, catalysts are prepared by impregnation or deposition–precipitation methods followed by an appropriate thermal treatment to reduce the deposited metal salts to metal particles. As a result, the active metal particles are poorly anchored to the support and control over the size of the metal particle is questionable.

An innovative alternative approach is to follow a segregative preparation method: the biphasic solid nanophase is obtained by promoting phase exsolution from a parent compound. Neagu et al.<sup>48</sup> presented a study on nonstoichiometric perovskites in which, upon thermal treatment, the metal oxide particles became decorated by a segregated secondary phase in the form of nanoparticles.

A similar approach can be applied to produce Pt/CeO<sub>2</sub> catalysts provided that the parent phase contains Pt ions dispersed into the CeO<sub>2</sub> lattice. Bera et al.<sup>26</sup> prepared doped CeO<sub>2</sub> materials by combustion synthesis, demonstrating that Pt is ionically dispersed into the CeO<sub>2</sub> host lattice. The catalytic activities were tested for several reactions, and the most appropriate conclusion was that the catalytic centers were the noble metal ions incorporated into the CeO<sub>2</sub> lattice. It was also reported that, upon extended thermal treatment at 800 °C in air, Pt segregates out of the host lattice forming metal particles. Nevertheless, during combustion synthesis, the local sample temperature and the local oxygen partial pressure are unknown and the segregation of metal Pt clusters during the synthesis itself is plausible as their presence is difficult to identify, in particular on partially sintered samples. Thus, the correlation between catalytic activity and the chemical nature of the noble metal is affected by a fair degree of uncertainty.

Recently, we presented a new wet synthesis method that overcomes the disadvantages of combustion synthesis, including the high cost, poor control over the process, scalability issues, and the partial sintering of the obtained material. The method allowed for the preparation of Pt-doped CeO<sub>2</sub> nanoparticles (NPs), with an average size of <5 nm, using a single-pot procedure.<sup>19</sup> Like Bera et al.,<sup>26</sup> we were able to produce doped materials containing ionically dispersed Pt, but using instead a scalable and controllable wet chemistry route. In agreement with the cited literature, Pt particles segregate out of the CeO<sub>2</sub> lattice upon thermal treatment. Thus, by starting from a unique parent phase and tuning properly the thermal treatment, we were able to produce several scenarios: from ionically dispersed noble metal incorporated into the host lattice to partially segregated subnanometric Pt clusters to completely segregated Pt nano- or microparticles.

The objectives of this study are (a) to find a rational pathway to promote the incorporation of Pt into CeO<sub>2</sub>, (b) to measure the Pt metal segregation kinetics upon heating by means of X-ray absorption spectroscopy and *in situ* X-ray diffraction (XRD), (c) to estimate the activation energy for segregation, (d) to investigate the nature of the segregated clusters or nanoparticles out of the cerium dioxide lattice, and (e) to study the influence of the atmosphere on segregation behavior.

The obtained information would contribute to the understanding of the nature of the active species for a specific reaction, to optimizing the material functionalities, and to

minimizing the amount of noble metal required. This study will also provide relevant insights into the structure–performance relationships, thus allowing the preparation of materials with superior performance.

### 2. EXPERIMENTAL DETAILS

**2.1. Materials.** Chemical reagents, including cerium(III) nitrate hexahydrate [Ce(NO<sub>3</sub>)<sub>3</sub>·6H<sub>2</sub>O, >99.0%], ethylene glycol (EG, puriss. p.a., >99.5%), and sodium hydroxide (NaOH, >98%), were obtained from Sigma-Aldrich and used as received without further purification. An aqueous solution of hydrogen hexachloroplatinate(IV) (H<sub>2</sub>PtCl<sub>6</sub>, 8% in H<sub>2</sub>O) was prepared from metal Pt (99.99% pure) as a precursor for the preparation of the doped materials. Reagent grade ethanol and acetone were used for powder washing purposes and obtained from VWR.

**2.2. Preparation of Pt-Doped CeO<sub>2</sub> Nanopowders by Polyol-Mediated Synthesis.** The materials were prepared as described in a previous work.<sup>19</sup> In a typical synthesis, a fixed amount of the cerium salt (10 mmol) was heated and dissolved in 100 mL of EG at 80 °C. A second solution containing 30 mmol of NaOH was heated and dissolved in 100 mL of EG and 10 mL of Milli-Q water at 80 °C. After being cooled to room temperature (RT), the two solutions were mixed. The mixture was heated to 160 °C and held at that temperature for 30 min under magnetic stirring. During this treatment, the color of the liquid changed from white to gray-purple. The suspension was then cooled and sonicated (Sonics-VibraCell, VCX130, 130 W, 20 kHz) at 100% power for 1 min. A defined amount of Pt precursor solution was then added to the CeO<sub>2</sub> nanoparticle suspension to achieve a desired loading of noble metal. The mixture was again heated to 180 °C and held at that temperature for 30 min, which yielded a black suspension. The suspension was cooled to RT and the final product collected by centrifugation. The solid was then washed twice in ethanol and once in acetone by redispersing the solids via sonication (100% power, 1 min). Finally, the catalyst was dried at RT overnight. The total noble metal content of the catalyst was determined by chemical analysis (ICP-MS). Two series of samples were prepared with different Pt loadings, namely, 7 wt % (high load, series H) and 0.7 wt % (low load, series L). The H series served for the high-resolution transmission electron microscopy (HR-TEM) study of the segregated Pt particles that result from thermal treatments in air. The L series, produced with a composition commonly used in catalysis, were pretreated in air (series L<sub>ox</sub>) or under a reducing atmosphere (2% H<sub>2</sub>, balance Ar, series L<sub>red</sub>) in a tubular oven.

The samples with 0.7 wt % Pt were also used for the *in situ* XRD studies of the segregation kinetics. In this case, the powders were pretreated in air for 3 h at 500 °C in a chamber oven (heating rate of 3 K min<sup>−1</sup>) to remove the organic residuals. The samples were named the K series.

**2.3. Characterizations.** The thermally treated samples (H, L<sub>ox</sub>, and L<sub>red</sub> series) and the *in situ* measurements (K series) were performed at the X04SA-Materials Science beamline, Swiss Light Source (SLS), Paul Scherrer Institut (PSI). The powders were confined in 0.3 mm quartz capillaries, and the X-ray beam energy was set to 22 keV. For the *in situ* measurements (K series), the capillary was positioned in an oven (STOE furnace), equipped with graphite heating elements, a capillary spinning tool, and 90° Kapton X-ray transparent windows. The temperature of the sample was measured in the proximity of the capillary by a thermocouple.

The temperature offset between the sample temperature and the thermocouple signal was determined by precalibration, collecting the diffraction patterns of reference substances across their melting temperatures. For the kinetic study, the XRD patterns were collected every 4.5 min at 930, 940, 950, and 960 °C. Cell parameters and phase quantifications were calculated by Rietveld refinement using General Structure Analysis System (GSAS II)<sup>49</sup> and the Inorganic Crystallographic Structure Database (ICSD).<sup>50</sup> For screening purposes, X-ray powder diffraction patterns were collected with a Bruker D8 Advance diffractometer (Cu K $\alpha$  radiation) in the  $2\theta$  range of 15–90° ( $\Delta 2\theta = 0.019$ ) equipped with an Anton Paar hot chamber (XRK 900).

High-resolution transmission electron microscopy and scanning transmission electron microscopy (STEM) images were recorded with a FEI Tecnai F20ST TEM/STEM microscope operated at 200 kV, permitting high-angle annular dark field (HAADF) imaging. Energy-dispersive X-ray (EDX) spectroscopy and morphological characterization with the secondary electron (SE) detector have been performed on the dedicated Cs-corrected STEM microscope (Hitachi HD-2700CS) operated at 200 kV. The samples for TEM characterization were dispersed in 2-propanol, and a drop of the suspension was deposited onto either carbon-coated or holey carbon-coated copper grids, allowing the solvent to evaporate in air. In addition, for the acquisition of STEM data, some samples were gently cleaned with an Ar (75%)/O<sub>2</sub> (25%) plasma for a few seconds to remove hydrocarbon contamination.

Morphological observations and compositional analysis for bulk and individual particles were performed with a Zeiss Ultra-55 field emission scanning electron microscope operated at 10 keV and equipped with an energy-dispersive X-ray (EDX) detector. The samples were Cr-sputtered.

X-ray absorption spectroscopy was conducted on selected samples of the L<sub>ox</sub> and L<sub>red</sub> series. The treated powders were diluted with cellulose and pressed into pellets for the measurements. The XAS fluorescence spectra were recorded at 80 K at the Pt L<sub>3</sub>-edge and at the Ce L<sub>3</sub>-edge. The experiments were conducted at the BM08 beamline at the European Synchrotron Radiation Facility (ESRF, Grenoble, France). As reference materials, Pt(IV) oxide (PtO<sub>2</sub>), metallic Pt foil [Pt(0);  $d = 50 \mu\text{m}$ ], and Ce(III) and Ce(IV) salts were measured in transmission mode.

Chemical analysis was performed with an Agilent 7700x ICP-MS instrument after digestion of the samples and dilution in Milli-Q water, using external standard calibration. For the Pt/CeO<sub>2</sub> samples, 20 mg of powders was dissolved in 1 mL of HNO<sub>3</sub> (65%). To perform a complete dissolution of the samples, a high-pressure microwave digestion unit was used. The digested samples were diluted with a two-step process in a water solution (Milli-Q water, 3% HCl, and 1% HNO<sub>3</sub>) with a total dilution factor of  $\sim 2.5 \times 10^6$ . Calibration and blank solutions were prepared by diluting (single-element) standard solutions down to a range of concentrations between 0 and 20 ppb (milligrams per liter). The same acidic matrix containing 3% HCl and 1% HNO<sub>3</sub> was used for the preparation of the calibration and sample solutions.

Catalytic activity data for CO oxidation were obtained in a quartz tube plug flow reactor ( $d_i = 6 \text{ mm}$ ) that was loaded with 50 mg of the catalyst mixed with cordierite, firmly fixed between two quartz wool plugs. A thermocouple was inserted at the middle of the catalyst bed, and the catalytic tests were

conducted in the temperature range of 30–300 °C (heating rate of 5 °C min<sup>−1</sup>). A gas flow of 3% O<sub>2</sub> with 1000 ppm of CO (100 mL min<sup>−1</sup>, balance N<sub>2</sub>) was introduced into the quartz tube (GHSV = 120000 mL g<sup>−1</sup> min<sup>−1</sup>). The outflowing gases were monitored using a Thermo Scientific Antaris IR spectrometer. Conversion data are reported as  $X_i = 100(C_{\text{CO}}^{\text{in}} - C_{\text{CO}}^{\text{out}})/C_{\text{CO}}^{\text{in}}$ .

### 3. RESULTS

**3.1. Preliminary Study of the H Series.** In this study, the samples were thermally treated in a chamber oven in air at different dwell temperatures and for different durations. Table 1

Table 1. Samples from the H Series

sample	dwell temperature (°C)	dwell time (h)
H1	as prepared	—
H2	500	3
H3	700	3
H4	800	3
H5	900	3
H6	900	0.5
H7	900	6
H8	900	12

summarizes the prepared samples. As our previous studies have shown, in the as-prepared samples (H1), Pt is found mainly on the ceria particle surface in oxidation states +2 and +4. Upon thermal treatment at 500 °C in air (H2), Pt is incorporated into the CeO<sub>2</sub> lattice.<sup>19</sup>

Samples treated at <900 °C showed no evidence of Pt segregation. After the samples had been heated at 900 °C for 0.5 h, the Pt peaks were not detected from the XRD pattern (sample H6). After a longer time (3, 6, and 12 h for samples H5, H7, and H8, respectively), Pt peaks were clearly detected by XRD. Figure 1 shows the XRD pattern for sample H8 with

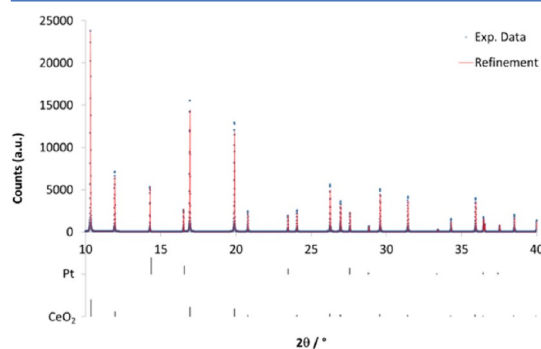


Figure 1. Diffraction pattern of sample H8 (collected at 22 keV). The crosses are the experimental points, and the red line represents the result of the Rietveld refinement. The  $2\theta$  positions and relative intensities of the Pt and CeO<sub>2</sub> peaks are also marked.

the Rietveld refinement. The calculated amount of Pt is in agreement with the chemical analysis, confirming that after this treatment, within the experimental error, all Pt is segregated in metal form.

The XRD patterns were also measured against time and temperature by *in situ* XRD using standard lab equipment. The CeO<sub>2</sub> and Pt peak evolution is summarized in Figure S1



## D.1. Size Control of Pt Clusters on CeO<sub>2</sub> Nanoparticles via an Incorporation-Segregation Mechanism and Study of Segregation Kinetics

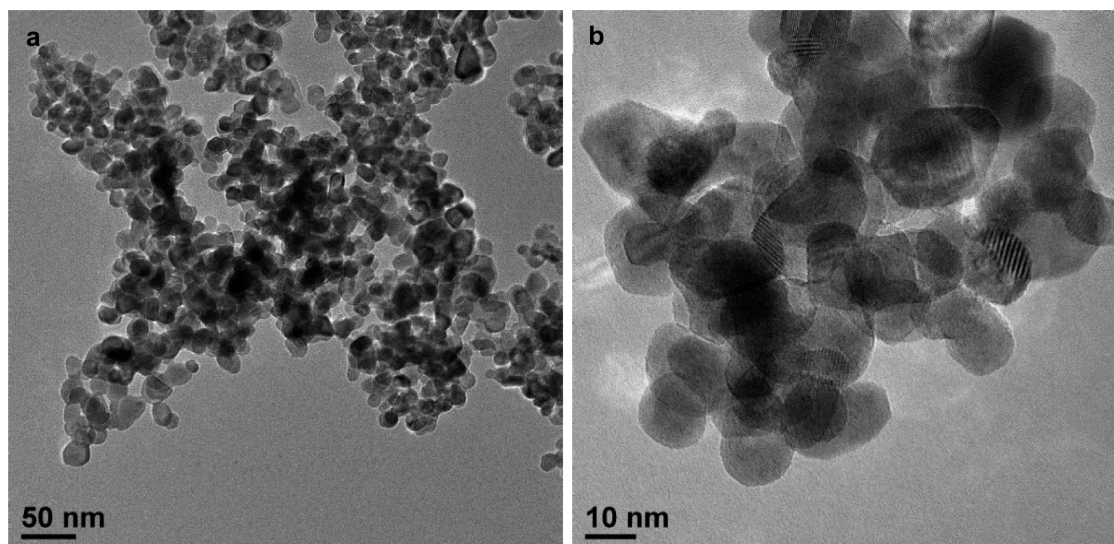


**Figure 2.** TEM micrographs of Pt-doped CeO<sub>2</sub> treated at 800 °C for 3 h (H4). (a) Even after thermal treatment at elevated temperatures, the particles are loosely packed and show a relatively narrow size distribution. (b) At a higher magnification, the lattice fringes of the crystalline material become clearly visible; metal Pt particles, however, cannot be detected.

(Supporting Information), where it is confirmed that the Pt peaks are XRD visible only after 1 h at 900 °C.

The samples were investigated by TEM and HAADF-STEM. Below the segregation threshold temperature (900 °C), traces of metal Pt could not be detected in the EM images, in agreement with the XRD results. The powders are loosely packed and show a rather narrow size distribution even at elevated temperatures (such as 800 °C for 3 h, sample H4); only minor particle–particle necking was identified (Figure 2).

HR-TEM micrographs for sample H6 are shown in Figure S2 (Supporting Information). Because of the thermal treatment, the CeO<sub>2</sub> particles grow up to approximately 10–15 nm, maintaining their equiaxed shape. Several particles were analyzed, but no evidence of Pt segregation could be detected, in agreement with the XRD analysis. The EDX chemical mapping did not show any zone with a distinctly higher Pt content (Figure S3). After longer thermal treatments (6 h), Pt segregation was detected by TEM, as well.

The HAADF-STEM micrograph of sample H7 is shown in Figure 3. Bright spots in the HAADF-STEM images became visible and correspond to Pt particles of approximately 1–2 nm. This preliminary XRD study clearly defines the experimental conditions in terms of temperature and duration to be set for the detailed *in situ* kinetic study.

**3.2. L Series: *Ex Situ* Pt Segregation Assessed by XRD, STEM, and XAS.** Table 2 summarizes the samples prepared for the L series. The samples were treated in a tubular oven and then analyzed by XRD, EM imaging, and XAS. Because of the small amount of Pt, reliable XRD data can be collected only by using a synchrotron radiation facility.

Figure 4 shows the evolution of the XRD patterns versus time and temperature of the L<sub>ox</sub> and L<sub>red</sub> series. In both series, the evolution toward larger CeO<sub>2</sub> crystallites against temperature can be easily deduced from the peak broadening (Figure 4a).

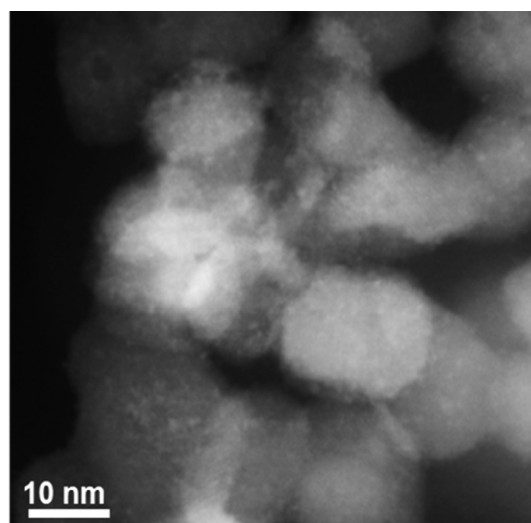


**Figure 3.** HAADF-STEM micrograph of sample H7 (900 °C for 6 h). The lighter spots correspond to approximately 1–2 nm Pt particles segregated out of the CeO<sub>2</sub> lattice.

Under an oxidizing atmosphere, the Pt peaks are detectable after thermal treatment at 900 °C for only 3 h (L<sub>ox</sub>7) whereas they are not present if the treatment is conducted at 850 °C (Figure 4b, L<sub>ox</sub>5). The anomalies on the shape and intensity of the Pt peak in Figure 4b are discussed in section 4.

Under reducing conditions, Pt peaks were already detectable at 550 °C. A clear evolution against temperature toward larger particles (from the peak broadening) and an increasing amount of Pt (from the normalized peak intensity) can be deduced in the temperature window of 500–650 °C. At higher temper-

**Table 2. Samples from the L\_ox Series (top) and L\_red Series (bottom)**

sample	dwel temperature (°C)	dwel time (h)
L_ox1	500	3
L_ox2	700	3
L_ox3	750	3
L_ox4	800	3
L_ox5	850	3
L_ox6	875	3
L_ox7	900	3
L_ox8	850	0.5
L_ox9	850	6
L_red1	500	3
L_red2	550	3
L_red3	600	3
L_red4	650	3
L_red5	700	3
L_red6	800	3
L_red7	900	3

atures (650–900 °C), the peaks' shape and normalized intensity do not change anymore. Because of the small amount of the metallic phase, the calculation of phase composition and Pt crystallite size is affected by a significant error and could be not more than speculation.

The secondary electron (SE) STEM micrographs on the L\_ox7 sample revealed bright spots on the CeO<sub>2</sub> surface

corresponding to ~0.5 nm Pt nanoclusters (Figure 5a). Such spots were not detected on other samples within the L\_ox series. The chemical nature of the bright spots was confirmed by EDX spectroscopy (Figure 5b). Because of the Cs corrector, the dedicated STEM microscope has a beam diameter of 0.1 nm, which results in atomic resolution in SE imaging and conclusive EDX spectra even for subnanometric particles.<sup>51–53</sup> On the other hand, HR-TEM revealed few intragranular particles with a higher contrast with a size of a few nanometers. According to the nominal composition of the samples, the XRD patterns, and the XAS spectra (as described below), it is plausible to consider these internal particles as Pt (Figure 5c,d). On the CeO<sub>2</sub> surface, such particles were not detected after STEM observation for several hours and in several repetitions of sample L\_ox7. Larger sample areas (350 μm × 300 μm) at lower magnifications were observed by field emission scanning electron microscopy (FE-SEM). In the overall EDX mapping, some spots (1 over ~5000 μm<sup>2</sup> of scanned surface) with a higher Pt concentration (Figure S4) are visible. These spots correspond to micrometer-sized Pt particles deposited on the CeO<sub>2</sub> agglomerates (Figure 6).

According to the XRD analyses, the evolution and growth of Pt peaks in the L\_red series already occur at much lower temperatures. This was confirmed by the HAADF-STEM micrographs and EDX elemental mapping, where Pt particles on the CeO<sub>2</sub> surface were clearly identified (Figure 7). Because of the thermal treatment under a reducing atmosphere, the growth of CeO<sub>2</sub> particles was developed with partial sintering

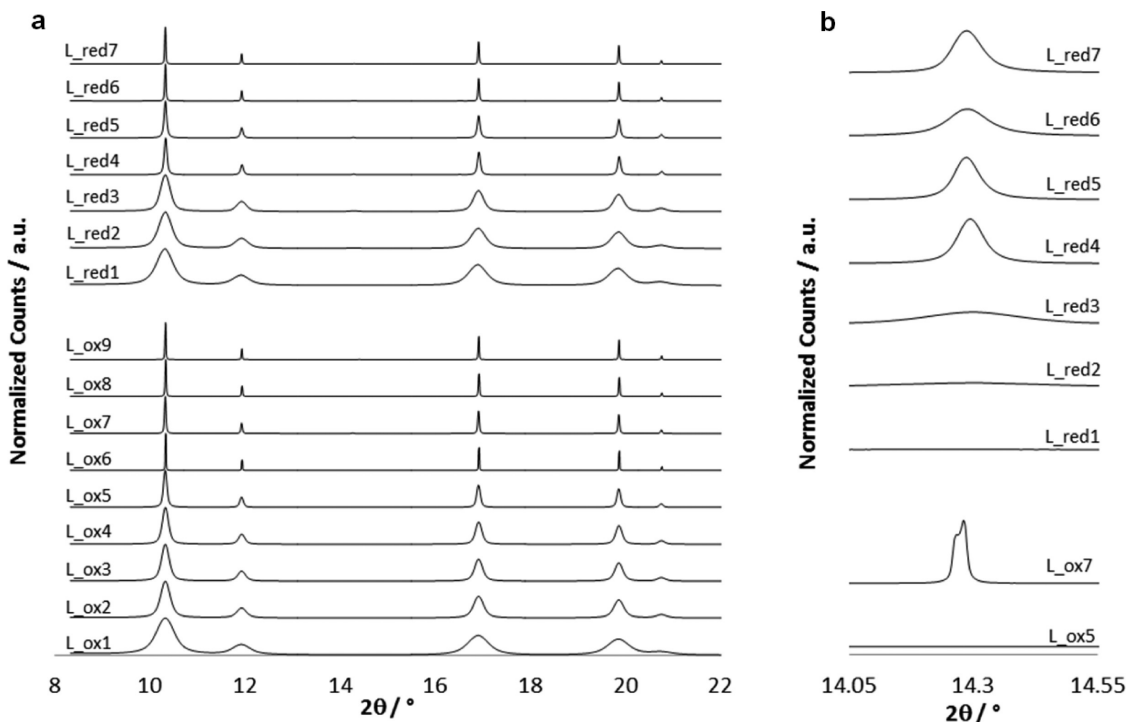


**Figure 4.** High-resolution XRD patterns of the L\_ox and L\_red samples collected at an energy of 22 keV for the samples listed in Table 2. (a) Patterns normalized by the maximal intensity of the CeO<sub>2</sub> (111) peak. (b) Close-up of the Pt (111) peak region for patterns of selected samples normalized by the integrated intensity of the CeO<sub>2</sub> (111) peak.



## D.1. Size Control of Pt Clusters on CeO<sub>2</sub> Nanoparticles via an Incorporation-Segregation Mechanism and Study of Segregation Kinetics

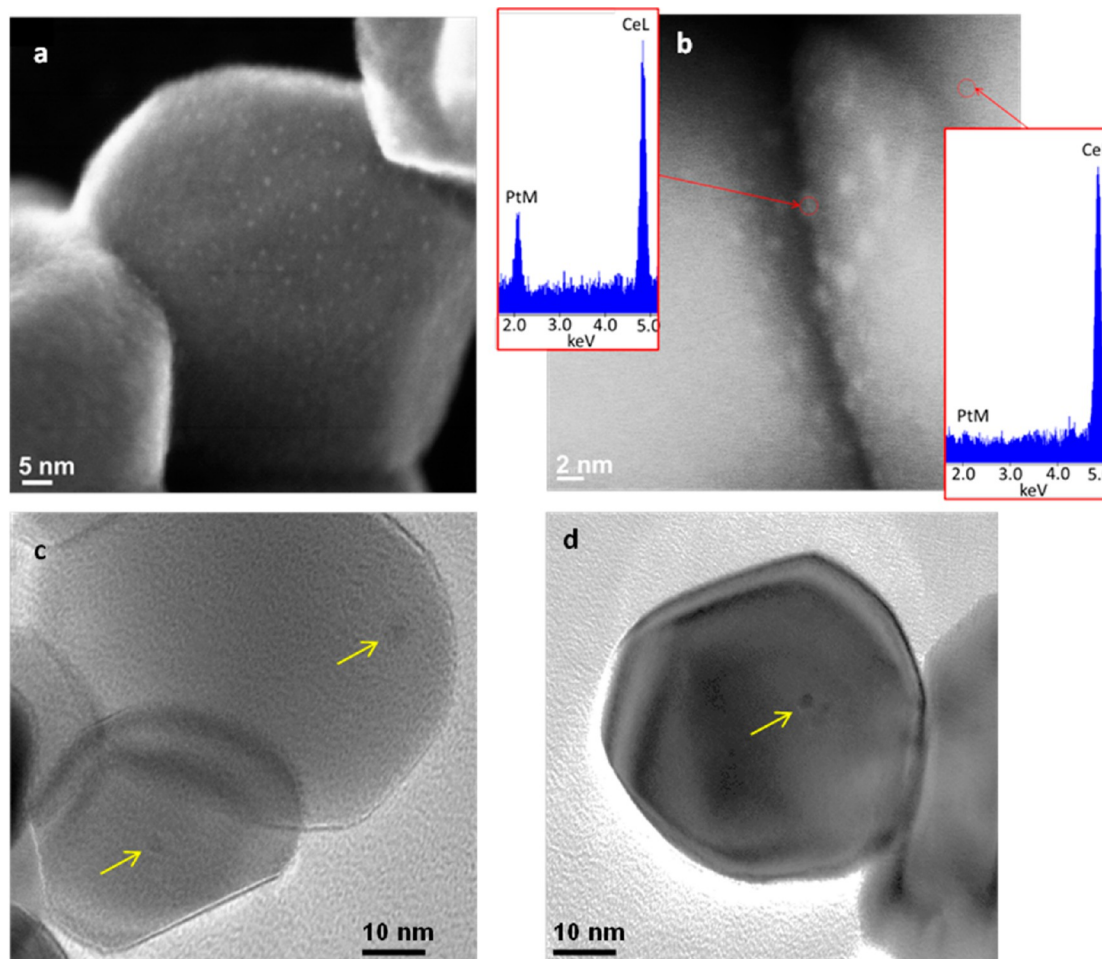


**Figure 5.** EM micrograph of a Pt/CeO<sub>2</sub> sample treated at 900 °C for 3 h under an oxidizing atmosphere (L<sub>ox7</sub>). (a) SE-STEM micrograph in which the lighter spots on the CeO<sub>2</sub> crystal correspond to surface subnanometric Pt clusters as confirmed by EDX spectroscopy (shown in panel b). Because of the Cs corrector, the dedicated STEM microscope has a beam diameter of 0.1 nm, resulting in atomic resolution even in SE imaging. (c and d) HR-TEM micrographs in which the arrows are indicating intragranular Pt particles a few nanometers in size.

and pronounced faceting. CeO<sub>2</sub> lattice parameters and the crystallite size of the samples listed in Table 2 are reported in Figure S5.

Selected samples were analyzed by X-ray absorption near edge structure (XANES) spectroscopy. The measurements at the Pt L<sub>3</sub> edge allowed clear insight into the average Pt oxidation states. The amplitude reduction and shift of the white line clearly show the increase in the intensity of the Pt(0) signal upon thermal treatment.

According to the previous HR-XRD results, the evolution of Pt peaks is expected to occur between 875 and 900 °C under oxidizing conditions (Figure 8a), whereas the reducing atmosphere promotes the occurrence of XRD-detectable metal Pt already after a thermal treatment at 550 °C (Figure 8b). Correspondingly, changes in the EXAFS signals were also detected (not shown; the details of the EXAFS spectra were outside the scope of this study).

In the L<sub>ox</sub> series, the contribution of Pt<sup>0</sup> increases rapidly at the threshold temperature of 900 °C, whereas under reducing conditions, for the L<sub>red</sub> series, Pt is in metallic form already at 500 °C, even if it is not yet XRD-detectable. Specifically, under oxidizing conditions at <900 °C, a relevant fraction of Pt is still in ionic form.

A similar XAS study was conducted on the Ce L<sub>3</sub> edge. Measured spectra indicated the presence of Ce(IV) only, while Ce(III) was not detected in any of the samples (not shown), regardless of thermal treatment or atmosphere. This suggests that the material easily undergoes reoxidation, most probably upon cooling, emphasizing the relevance of XAS *in situ* measurements for a more detailed investigation.

**3.3. K Series: *In Situ* Pt Segregation Kinetics Determined by XRD.** The kinetic data were measured at four temperatures, namely, 930, 940, 950, and 960 °C. Each diffraction pattern was measured with an accumulation time of 4.5 min, and the samples were analyzed for several hours. The

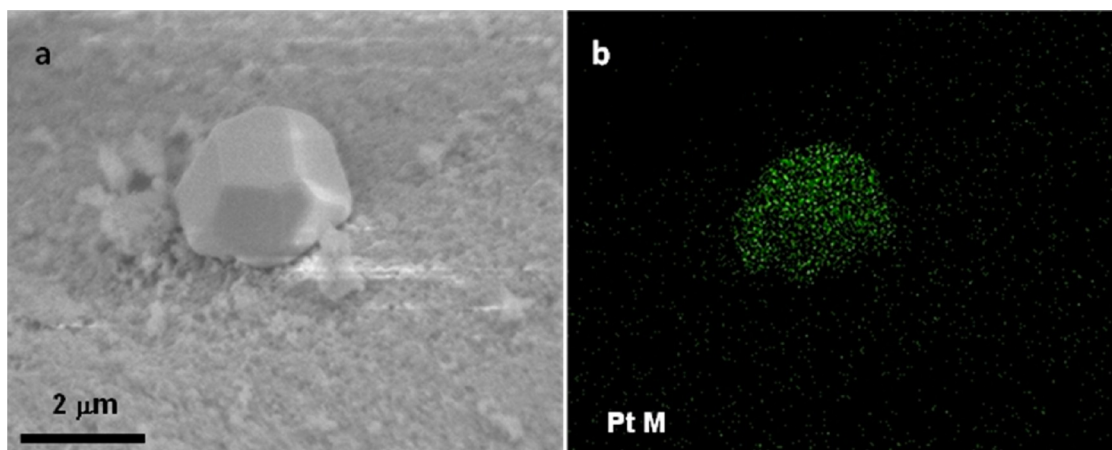


**Figure 6.** (a) FE-SEM micrograph and (b) EDX Pt mapping of sample L<sub>ox7</sub>. A few large (2–3 μm) well-faceted Pt particles deposited on the CeO<sub>2</sub> agglomerates can be detected.

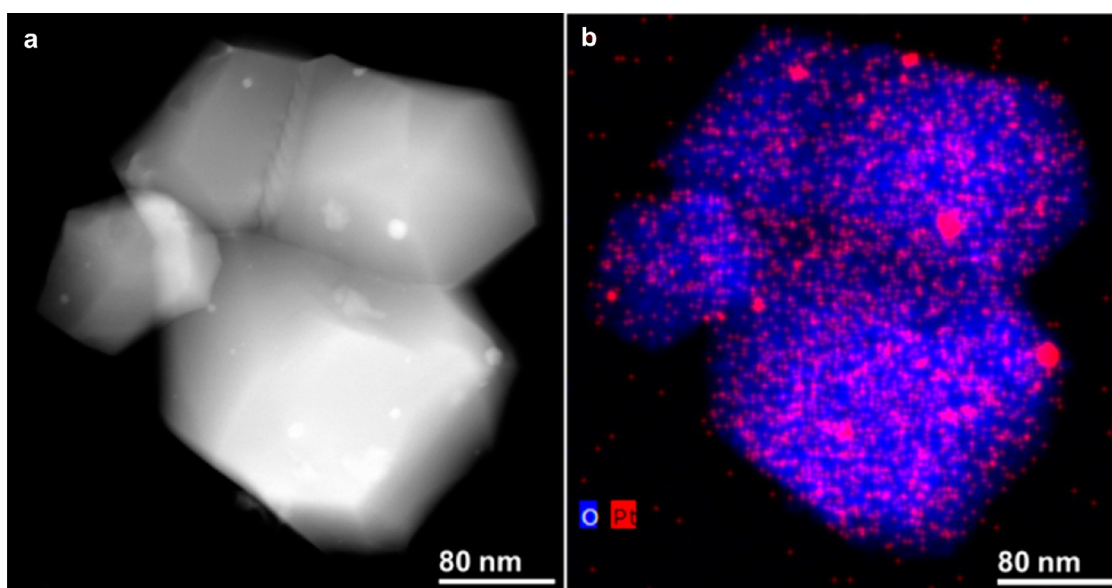
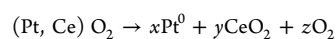


**Figure 7.** Pt/CeO<sub>2</sub> sample treated at 900 °C for 3 h under a reducing atmosphere (L<sub>red7</sub>): (a) HAADF-STEM micrograph and (b) EDX elemental mapping. The bright spots in the HAADF image can be identified as Pt particles (red) in the EDX mapping.

collected patterns were background-corrected, and the integrated intensities for the Pt (111) peak [ $I_{\text{Pt}(111)}$ ] and for the CeO<sub>2</sub> (111) peak [ $I_{\text{CeO}_2(111)}$ ] were calculated. Because of sintering at the measuring temperature, the material in the capillary shrinks. Thus, the normalized Pt peak intensities,  $\frac{I_{\text{Pt}(111)}}{I_{\text{Pt}(111)}}$ , were calculated as

$$\frac{I_{\text{Pt}(111)}}{I_{\text{Pt}(111)}} = \frac{I_{\text{Pt}(111)}}{I_{\text{CeO}_2(111)}} \quad (1)$$

The Pt segregation could be represented by a simplified model, such as the chemical equation



where (Pt, Ce) O<sub>2</sub> and Pt<sup>0</sup> represent a generic Pt ion dissolved in the CeO<sub>2</sub> lattice and the segregated metallic Pt, respectively. More complex reactions, involving Ce<sup>3+</sup> and Pt<sup>2+</sup> ions and oxygen vacancies, could be suggested without adding significant insight about the segregation path.

The evolution of the Pt (111) peak over time for the four experimental data sets is shown in Figure 9a, whereas the value of  $\frac{I_{\text{Pt}(111)}}{I_{\text{Pt}(111)}}$  versus time is shown in Figure 9b. From the experimental data, we could see an extended linear behavior that could be associated with an apparent zero-order kinetic reaction, such as

## D.1. Size Control of Pt Clusters on CeO<sub>2</sub> Nanoparticles via an Incorporation-Segregation Mechanism and Study of Segregation Kinetics

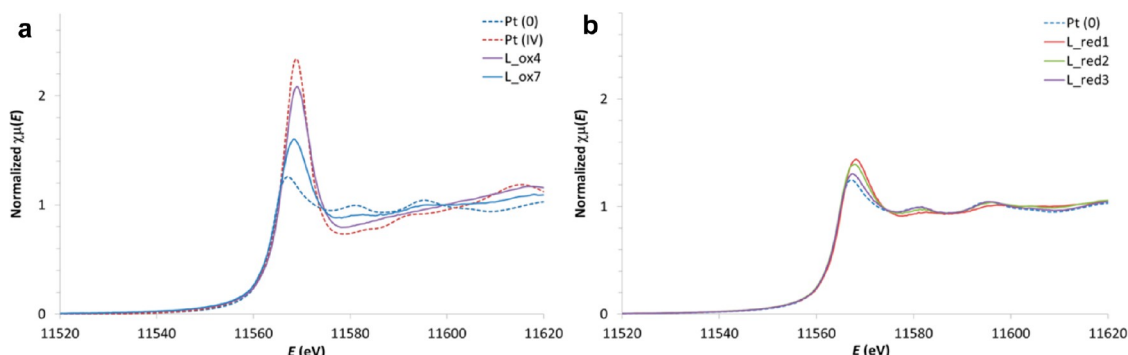


**Figure 8.** Pt L<sub>3</sub> edge XANES spectra of selected samples and references Pt(0) and Pt(IV) oxide compounds (dotted blue and red, respectively). (a) Samples L<sub>ox4</sub> (violet) and L<sub>ox7</sub> (blue). (b) Samples L<sub>red1</sub> (red), L<sub>red2</sub> (green), and L<sub>red3</sub> (violet).

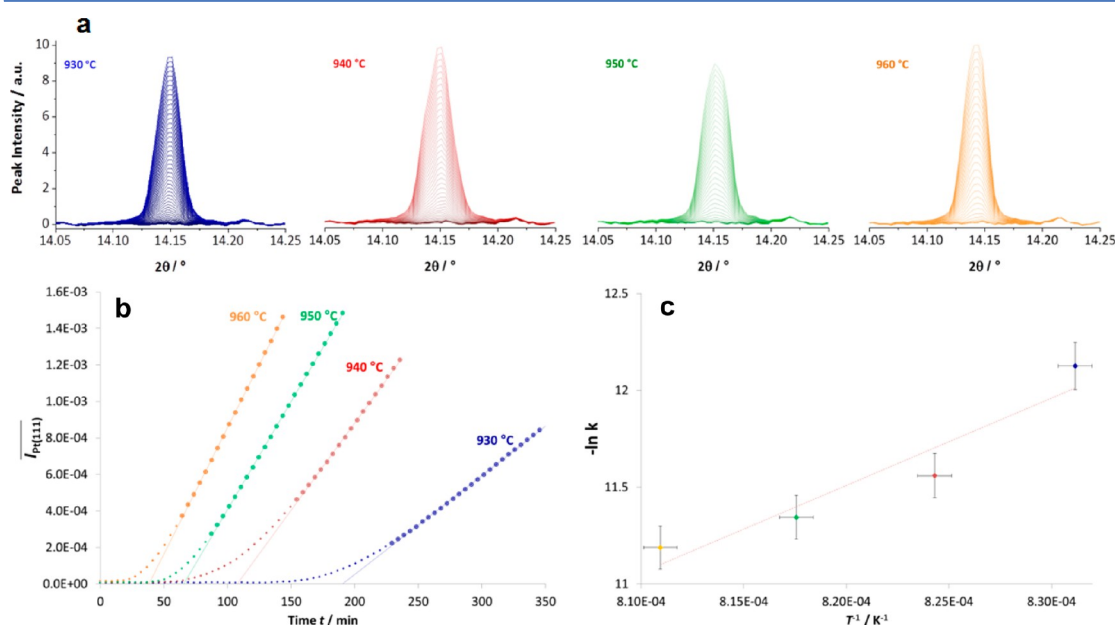


**Figure 9.** (a) Evolution of the Pt (111) peak intensity over time collected *in situ* at 930, 940, 950, and 960 °C (K1–K4, respectively). Each line belongs to a pattern that accumulated for 4.5 min. (b) Normalized integrated intensities of the Pt (111) peak [ $I_{\text{Pt}(111)}/I_{\text{Pt}(111)}^0$ ] over time at 930, 940, 950, and 960 °C. The crosses depict the measured values, and the circles are the values chosen for the linear fits. The calculated slopes are used to determine kinetic constant  $k$  at the respective temperature. (c) Arrhenius plot derived from the slopes of the normalized Pt (111) peak intensities. The errors are estimated to be 0.1 and 1% on the horizontal and vertical axes, respectively.

$$\frac{d(\text{mass of segregated Pt}^0)}{dt} = k(T) \quad (2)$$

The Arrhenius plot of the peak growth rate is given in Figure 9c. The calculated activation energy for the Pt segregation from the CeO<sub>2</sub> lattice in air corresponds to 3.88 eV (374 kJ mol<sup>−1</sup>). The extracted numerical values for the Arrhenius plot are reported in Table S1.

Figure 10 shows the preliminary results of the catalytic tests for CO oxidation collected on selected samples.

The L<sub>red1</sub> sample shows a relevant activity already at a low temperature, as the  $T_{50}$  is at ~50 °C. After a thermal treatment at a higher temperature (L<sub>red6</sub>, 800 °C), the activity is rather

poor and  $T_{50}$  corresponds to ~260 °C, while the  $T_{50}$  is shifted to a slightly lower temperature (225 °C) when the sample is treated at an even higher temperature (L<sub>red7</sub>, 900 °C). The catalytic behavior of the samples treated in air is radically different. The sample treated at 500 °C (L<sub>ox1</sub>) is not particularly active, showing its 50% CO conversion at ~180 °C. When the Pt segregation is promoted by the thermal treatment in air at 800 °C (L<sub>ox4</sub>), increased activity is observed as 50% of CO conversion can be achieved at relatively low temperatures (100 °C). A thermal treatment at an even higher temperature (L<sub>ox7</sub>, 900 °C) promotes a pronounced activity loss, setting the 50% conversion at 215 °C. Both samples treated at 800 °C show some anomalies in the expected

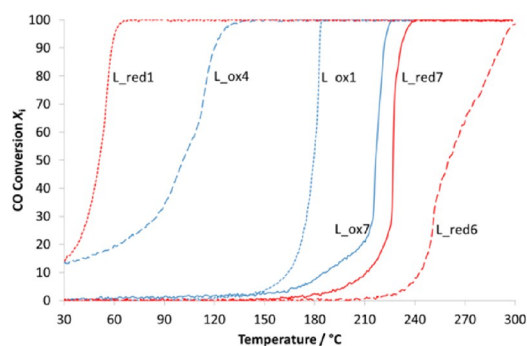


**Figure 10.** CO conversion ( $X_i$ ) vs temperature for selected samples treated in air (L\_ox1, L\_ox4, and L\_ox7) and in a reducing atmosphere (L\_red1, L\_ox6, and L\_red7). The dotted, dashed, and solid lines correspond to treatment temperatures of 500, 800, and 900 °C, respectively.

sigmoidal shape curve, which can be ascribed to a population of different catalytic sites with different activity toward CO oxidation.

#### 4. DISCUSSION: INCORPORATION AND SEGREGATION PATHWAYS

The reported experimental evidence, combined with our previous findings,<sup>19</sup> is summarized in Figure 11. The as-prepared material is composed of ~5 nm CeO<sub>2</sub> NPs where Pt is in the Pt<sup>2+</sup> form and Pt<sup>4+</sup> ions are on the CeO<sub>2</sub> surface. Upon calcination, two different pathways can be discerned, under an oxidizing (air) or a reducing (2% H<sub>2</sub>, balance Ar) atmosphere. In Figure 11, the oxidizing pathway is indicated by blue arrows whereas the reducing pathway is described by the red arrow.

Under the oxidizing atmosphere and in the temperature range of 500–900 °C, Pt ions diffuse into the CeO<sub>2</sub> lattice. This fact is validated by a sensible CeO<sub>2</sub> lattice contraction in highly doped samples<sup>19</sup> and by the spectroscopic evidence presented in Figure 8a. Accordingly, evidence of crystalline Pt particles is found neither with XRD (Figure 4b) nor with EM (Figure 2). XANES spectra show that after thermal treatment at 800 °C for 3 h Pt is mainly present in its ionic form (Figure 8a). The ionically dispersed Pt acts as a sintering and crystal growth

inhibitor.<sup>19</sup> At ≥900 °C, Pt subnanometric clusters are segregated on the CeO<sub>2</sub> particle surface (Figure 5a,b). The metallic nature of Pt at 900 °C is spectroscopically proven (Figure 8a). Few Pt nanometric particles (<5 nm) are detected within the CeO<sub>2</sub> crystals (Figure 5c,d), and few micrometric particles (2–3 μm) are deposited on the CeO<sub>2</sub> agglomerates (Figure 6). These few large particles give rise to the Pt peaks in the diffraction patterns (Figure 4b).

The Pt peak in Figure 4b, sample L\_ox7, shows anomalies (detectable only using high-resolution synchrotron X-ray diffraction) that are poorly reproducible and, if they occur, affect all Pt peaks in the respective XRD pattern. Moreover, the angular gap between the maximum and the shoulder is 2θ-independent, which excludes the possibility of two populations of particles with slightly different lattice parameters and other crystallographic features (such as strain effects). The peak's irregular profile (a visible shoulder, Figure 4b, bottom) is attributed to the poor particle statistics.<sup>54</sup> In fact, considering the sample volume probed by the beam, the overall concentration of Pt (0.7 wt %), and the size of the Pt particles (~3 μm), the number of such Pt particles can be estimated to be fewer than 4000. Moreover, it is worth mentioning that only a small fraction of these particles [0.3% (Supporting Information)] are in average under scattering conditions for each peak. Thus, the number of contributing grains to each Bragg peak is estimated to be 10–20, which is not enough to give a statistically consistent profile.

Consistently, the peaks of L\_red series are rather broad with a regular profile: in these cases, no micrometric Pt particles can be detected and the Pt grains responsible of the diffraction are those highlighted by Figure 7, which are present in a statistically appropriate number.

The evolution of Pt peaks is studied *in situ* in the temperature range of 930–960 °C by high-resolution XRD (Figure 9a). Also in this case, and in particular for the experiment conducted at 940 °C, the peak shape is affected by the aforementioned anomalies, even against time. Because the acquisition is conducted at high temperatures, the resolution is not as high as that reported in Figure 4b (collected at RT) and the shoulder is only partially resolved. Consistently, the peak position at high temperatures is shifted toward smaller angles because of the thermal lattice expansion. The initial velocity for segregation and coagulation of Pt clusters into larger crystalline particles is experimentally evaluated, and the activation energy

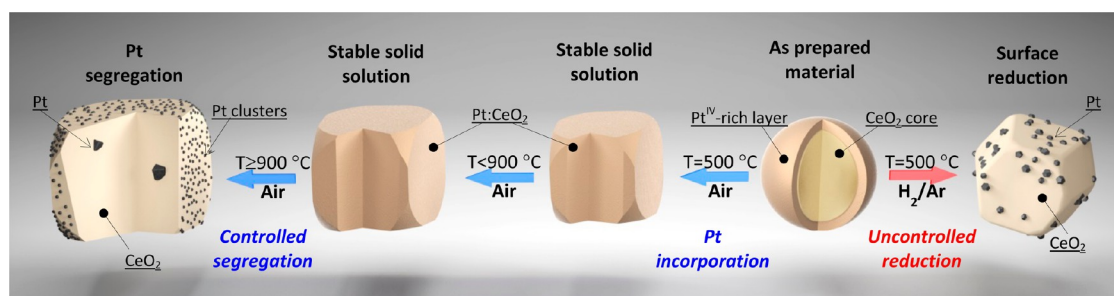


**Figure 11.** Incorporation–segregation pathways for Pt-doped CeO<sub>2</sub> nanopowders. The thermal treatment under oxidizing conditions (blue arrows) promotes the ionic dispersion of Pt into the CeO<sub>2</sub> lattice, whereas treatments above a threshold temperature of ≥900 °C lead to Pt segregation and the formulation of subnanometric Pt metal clusters on the CeO<sub>2</sub> and few intragranular Pt particles. At ≥900 °C and long dwell times, Pt particles segregate in micrometer-size particles (not shown in this figure). On the other hand, thermal treatment under reducing conditions (red arrow) promotes the direct formation of relatively large Pt particles (3–10 nm) on CeO<sub>2</sub>.



## D.1. Size Control of Pt Clusters on CeO<sub>2</sub> Nanoparticles via an Incorporation-Segregation Mechanism and Study of Segregation Kinetics

is estimated to be  $\sim 3.88$  eV (Figure 9b,c). Because it is clear that Pt occurs in its metallic form (Figure 8a) and the particles responsible for the diffraction peaks are the large particles, the evolution of the Pt peak corresponds to the depletion of the Pt clusters on the CeO<sub>2</sub> surface. Thus, the measured high activation energy indicates that the Pt clusters are strongly stabilized (anchored) on the CeO<sub>2</sub> particle surface.

Under a reducing atmosphere, sintering and ripening of CeO<sub>2</sub> particles are promoted at lower temperatures and are more pronounced than under oxidizing conditions. For instance, sample L<sub>ox5</sub> (treated at 850 °C for 3 h) shows a peak broadening similar to that of sample L<sub>red4</sub> (treated at 650 °C for 3 h) and the faceting of the particles of sample L<sub>red7</sub> is more marked than that of sample L<sub>ox7</sub>. This behavior is well-known and caused by the high solid state ionic mobility in the presence of oxygen vacancies, which are promoted when the material is treated under reducing conditions. The experimental results show that the Pt(IV)-rich layer of the as-prepared material is directly reduced to Pt metal particles. These particles rapidly grow up to 3–10 nm and are easily detected by X-ray diffraction (Figure 4b), XAS (Figure 8b), and EM (Figure 7).

The peculiarities of the samples' morphology are reflected by the preliminary catalytic tests of Figure 10, which suggest a clear structure–function correlation. The results clearly indicate that to prepare a nanometric CeO<sub>2</sub> material decorated with Pt clusters with high catalytic activity and thermal stability, a defined pathway has to be followed. Specifically, (a) a synthesis method that can produce CeO<sub>2</sub> nanoparticles surface-doped with Pt has to be considered, (b) a mild thermal treatment under oxidizing conditions to incorporate Pt ions into the CeO<sub>2</sub> lattice is required, and (c) a controlled thermal treatment under oxidizing conditions is crucial to being able to tailor the segregation of subnanometric Pt metal clusters on the CeO<sub>2</sub> surface, preserving the loosely packed nanostructure. The material so obtained is thermally stable; Pt clusters become mobile only at  $>900$  °C, and thus, they are strongly anchored at a lower working temperature, i.e., up to 800 °C. The preserved nanostructure is reflected by the relevant catalytic activity of sample L<sub>ox4</sub> (Figure 10). If the material is treated at a high temperature (such as 900 °C) for several hours, the Pt cluster disappears, larger Pt particles are formed, and the material loses the catalytic properties of L<sub>ox7</sub> (Figure 10). If a thermal treatment under a reducing atmosphere is performed on the as-prepared material, Pt ions are not incorporated into the particle but directly reduced on the CeO<sub>2</sub> surface. The obtained material is equivalent to that produced by standard impregnation techniques; it might indeed show good performance [sample L<sub>red1</sub> (Figure 10)], but the Pt nanoparticles are poorly anchored on the support material. As a consequence, even if small Pt particles can be produced on the catalyst surface (Figure 4b), they rapidly grow into larger particles at a relatively low temperature and the material is easily deactivated *in operando* [sample L<sub>red6</sub> (Figure 10)].

Starting from the same as-prepared material with tunable Pt loading and applying the incorporation–segregation pathways of Figure 11, we can tune the nature of Pt according to the specific material requirements. A variety of scenarios can be realized: from a material composed of Pt ions dispersed in the CeO<sub>2</sub> lattice to CeO<sub>2</sub> nanoparticles decorated by strongly anchored subnanometric Pt clusters. On the other hand, a material with relatively large Pt particles supported on CeO<sub>2</sub>

can be produced by a thermal treatment under a reducing condition.

This flexibility allows the study of the structure–property relationships with the aim of understanding the nature of catalytically active centers. This allows one to minimize the amount of precious metal required and to increase the lifetime of catalytically active materials. Moreover, the applied synthesis and processing methods for the preparation of the advanced material are fully scalable. For instance, the material can be produced using the segmented flow tubular reactor (SFTR) technology.<sup>55</sup>

### 5. CONCLUSIONS

The rational incorporation–segregation pathways for the Pt/CeO<sub>2</sub> system are clearly outlined. In addition to the previous result, that the preparation of nanometric CeO<sub>2</sub> surface-doped with Pt ions can be achieved using a scalable and cost-effective process,<sup>19,55</sup> the major outcomes and findings of this study are summarized as follows. (a) The condition for promoting the incorporation of Pt ions into the CeO<sub>2</sub> lattice is defined. The result is that a mild thermal treatment in air is mandatory. (b) The condition for segregating subnanometric Pt clusters on the CeO<sub>2</sub> nanoparticles is described, and it occurs at  $\sim 900$  °C. (c) The metallic nature of the segregated clusters is confirmed by X-ray absorption near edge structure (XANES) spectroscopy and EDX analyses. (d) The size of Pt clusters is proven by secondary electron (SE) STEM. (e) The segregation kinetics are followed by *in situ* high-resolution X-ray diffraction conducted at the Swiss Light Source at  $>900$  °C. The result is that the activation energy for Pt cluster segregation and coagulation is  $\sim 3.88$  eV, which strongly suggests that the clusters are strongly anchored on the CeO<sub>2</sub> surface. (f) The well-dispersed and strongly anchored Pt entities obtained via segregation by an oxidative treatment outperform those obtained by surface reduction in the catalytic testing, which are prone to coalesce.

With this study, we show the correlation between the nature of the segregated Pt particles and the applied thermal treatment for Pt/CeO<sub>2</sub> nanomaterials prepared by a wet chemical synthesis method. The strategy can be applied to other materials with the aim of deeply investigating the structure–property relationships and the nature of catalytically active centers. The combination of scalable processes and reliable control over the material nanostructure paved the way toward the development of advanced materials of industrial application.

### ■ ASSOCIATED CONTENT

#### Supporting Information

The Supporting Information is available free of charge on the ACS Publications website at DOI: 10.1021/acscatal.6b00934.

*In situ* XRD patterns for screening the CeO<sub>2</sub> and Pt peak evolution of sample H2 up to 900 °C (Figure S1); HR-TEM micrographs of sample H6 with a high Pt load above the segregation temperature but below the segregation duration, including the corresponding fast Fourier transformed image (Figure S2); EDX chemical mapping of sample H6 (Figure S3); EDX chemical mapping of sample L<sub>ox7</sub> (Figure S4); CeO<sub>2</sub> lattice parameters and crystallite sizes for the samples of Table 2 (Figure S5); values for the determined kinetic constant (*k*) for the respective samples of the K series (Table S1); and a comment on particle statistics (PDF)

## ■ AUTHOR INFORMATION

## Corresponding Author

\*Paul Scherrer Institut, Energy and Environment Research Division, Villigen PSI CH-5232, Switzerland. Phone: +41 56 310 5449. E-mail: [andrea.testino@psi.ch](mailto:andrea.testino@psi.ch).

## Notes

The authors declare no competing financial interest.

## ■ ACKNOWLEDGMENTS

We thank A. Trapananti for her contribution to the XAS characterization. The XRD and XAS data were collected at the X04SA-MS beamline of the Swiss Light Source (SLS-PSI) and the LISA beamline of the European Synchrotron Radiation Facility (ESRF), respectively. The HRTEM data were collected with the help of A. Falqui at the Italian Institute of Technology in Genoa and N. J. Zaluzec at Argonne National Laboratory. Use of the Center for Nanoscale Materials, including resources in the Electron Microscopy Center, was supported by the U.S. Department of Energy, Office of Science, Office of Basic Energy Sciences, under Contract DE-AC02-06CH11357. We thank E. Müller Gubler and F. Krumeich for STEM imaging, using the facilities at PSI and at ScopeM ETH Zurich. We thank M. Tarik for the chemical analysis of our samples. We gratefully acknowledge E. De Boni for SEM-EDX analyses. We thank M. Džambegović for the realization of the three-dimensional figures. Financial support was provided by PSI and Swiss National Foundation (SNF) Project 200021\_144302.

## ■ REFERENCES

- (1) <http://geology.com/articles/rare-earth-elements/> (accessed November 10, 2015).
- (2) Yu, T.; Zeng, J.; Lim, B.; Xia, Y. N. *Adv. Mater.* **2010**, *22*, 5188–5192.
- (3) Zhou, H. P.; Wu, H. S.; Shen, J.; Yin, A. X.; Sun, L. D.; Yan, C. H. *J. Am. Chem. Soc.* **2010**, *132*, 4998–4999.
- (4) Yoon, K.; Yang, K.; Lu, P.; Wan, D.; Peng, H.; Stamm Masias, K.; Fanson, P.; Campbell, C.; Xia, Y. *Angew. Chem., Int. Ed.* **2012**, *51*, 9543–9546.
- (5) Chu, Y. Y.; Wang, Z. B.; Jiang, Z. Z.; Gu, D. M.; Yin, G. P. *Adv. Mater.* **2011**, *23*, 3100–3104.
- (6) Schweitzer, N. M.; Schaidle, J. A.; Ezekoye, O. K.; Pan, X. Q.; Linic, S.; Thompson, L. T. *J. Am. Chem. Soc.* **2011**, *133*, 2378–2381.
- (7) Anumol, E. A.; Kundu, P.; Deshpande, P. A.; Madras, G.; Ravishanker, N. *ACS Nano* **2011**, *5*, 8049–8061.
- (8) Perkas, N.; Rotter, H.; Vradman, L.; Landau, M. V.; Gedanken, A. *Langmuir* **2006**, *22*, 7072–7077.
- (9) Yu, X.; Kuai, L.; Geng, B. Y. *Nanoscale* **2012**, *4*, 5738–5743.
- (10) Trogadas, P.; Parrondo, J.; Ramani, V. *Chem. Commun.* **2011**, *47*, 11549–11551.
- (11) Melchionna, M.; Fornasiero, P. *Mater. Today* **2014**, *17*, 349–357.
- (12) Kopelent, R.; van Bokhoven, J. A.; Szlachetko, J.; Edebeli, J.; Paun, C.; Nachttegaal, M.; Safonova, O. V. *Angew. Chem., Int. Ed.* **2015**, *54*, 8728–8731.
- (13) Fu, Q.; Deng, W.; Saltsburg, H.; Flytzani-Stephanopoulos, M. *Appl. Catal., B* **2005**, *56*, 57–68.
- (14) Cai, W. J.; Wang, F. G.; van Veen, A. C.; Provendier, H.; Mirodatos, C.; Shen, W. J. *Catal. Today* **2008**, *138*, 152–156.
- (15) Trovarelli, A. *Catalysis by Ceria and Related Materials*; Catalysis Science Series; Imperial College Press: London, 2013; pp 139–222.
- (16) Campbell, C. T.; Peden, C. H. F. *Science* **2005**, *309*, 713–714.
- (17) Bruix, A.; Lykhach, Y.; Matolínová, I.; Neitzel, A.; Skála, T.; Tsud, N.; Vorokhta, M.; Stetsovykh, V.; Ševčíková, K.; Mysliveček, J.; Fiala, R.; Václavík, M.; Prince, K. C.; Bruyère, S.; Potin, V.; Illas, F.; Matolín, V.; Libuda, J.; Neyman, K. M. *Angew. Chem., Int. Ed.* **2014**, *53*, 10525–10530.
- (18) Sayle, T. X. T.; Parker, S. C.; Catlow, C. R. A. *J. Phys. Chem.* **1994**, *98*, 13625–13630.
- (19) Pilger, F.; Testino, A.; Lucchini, M. A.; Kambolis, A.; Tarik, M.; El Kazzi, M.; Arroyo, Y.; Rossell, M. D.; Ludwig, C. *J. Nanosci. Nanotechnol.* **2015**, *15*, 3530–3539.
- (20) Baidya, T.; Priolkar, K. R.; Sarode, P. R.; Hegde, M. S.; Asakura, K.; Tatenno, G.; Koike, Y. *J. Chem. Phys.* **2008**, *128*, 124711.
- (21) Hiley, C. I.; Fisher, J. M.; Thompson, D.; Kashtiban, R. J.; Sloan, J.; Walton, R. I. *J. Mater. Chem. A* **2015**, *3*, 13072–13079.
- (22) Lykhach, Y.; Figueroba, A.; Camellone, M. F.; Neitzel, A.; Skala, T.; Negreiros, F. R.; Vorokhta, M.; Tsud, N.; Prince, K. C.; Fabris, S.; Neyman, K. M.; Matolín, V.; Libuda, J. *Phys. Chem. Chem. Phys.* **2016**, *18*, 7672–9.
- (23) Figueroba, A.; Kovács, G.; Bruix, A.; Neyman, K. M. *Catal. Sci. Technol.* **2016**, DOI: [10.1039/C6CY00294C](https://doi.org/10.1039/C6CY00294C).
- (24) Bruix, A.; Neyman, K. M.; Illas, F. *J. Phys. Chem. C* **2010**, *114*, 14202–14207.
- (25) Bera, P.; Hegde, M. S. *RSC Adv.* **2015**, *5*, 94949–94979.
- (26) Bera, P.; Patil, K. C.; Jayaram, V.; Subbanna, G. N.; Hegde, M. S. *J. Catal.* **2000**, *196*, 293–301.
- (27) Summers, J. C.; Ausen, S. A. *J. Catal.* **1979**, *58*, 131–143.
- (28) Jin, T.; Okuhara, T.; Mains, G. J.; White, J. M. *J. Phys. Chem.* **1987**, *91*, 3310–3315.
- (29) Jin, T.; Zhou, Y.; Mains, G. J.; White, J. M. *J. Phys. Chem.* **1987**, *91*, 5931–5937.
- (30) Harrison, B.; Diwell, A. F.; Hallett, C. *Platinum Metals Rev.* **1988**, *32*, 73–83.
- (31) Löff, P.; Kasemo, B.; Andersson, S.; Frestad, A. *J. Catal.* **1991**, *130*, 181–191.
- (32) Nunan, J. G.; Robota, H. J.; Cohn, M. J.; Bradley, S. A. *J. Catal.* **1992**, *133*, 309–324.
- (33) Serre, C.; Garin, F.; Belot, G.; Maire, G. *J. Catal.* **1993**, *141*, 1–8.
- (34) Serre, C.; Garin, F.; Belot, G.; Maire, G. *J. Catal.* **1993**, *141*, 9–20.
- (35) Martínez-Arias, A.; Coronado, J. M.; Cataluña, R.; Conesa, J. C.; Soria, J. *J. Phys. Chem. B* **1998**, *102*, 4357–4365.
- (36) Baidya, T.; Gayen, A.; Hegde, M. S.; Ravishanker, N.; Dupont, L. *J. Phys. Chem. B* **2006**, *110*, 5262–5272.
- (37) Baidya, T.; Dutta, G.; Hegde, M. S.; Waghmare, U. V. *Dalton Trans.* **2009**, *3*, 455–464.
- (38) Bera, P.; Gayen, A.; Hegde, M. S.; Lalla, N. P.; Spadaro, L.; Frusteri, F.; Arena, F. *J. Phys. Chem. B* **2003**, *107*, 6122–6130.
- (39) Bera, P.; Hegde, M. S. *Catal. Lett.* **2002**, *79*, 75–81.
- (40) Bera, P.; Hegde, M. S. *Catal. Surv. Asia* **2011**, *15*, 181–199.
- (41) Bera, P.; Malwadkar, S.; Gayen, A.; Satyanarayana, C. V. V.; Rao, B. S.; Hegde, M. S. *Catal. Lett.* **2004**, *96*, 213–219.
- (42) Bera, P.; Priolkar, K. R.; Gayen, A.; Sarode, P. R.; Hegde, M. S.; Emura, S.; Kumashiro, R.; Jayaram, V.; Subbanna, G. N. *Chem. Mater.* **2003**, *15*, 2049–2060.
- (43) Fu, Q.; Saltsburg, H.; Flytzani-Stephanopoulos, M. *Science* **2003**, *301*, 935–938.
- (44) Gayen, A.; Priolkar, K. R.; Sarode, P. R.; Jayaram, V.; Hegde, M. S.; Subbanna, G. N.; Emura, S. *Chem. Mater.* **2004**, *16*, 2317–2328.
- (45) Hegde, M. S.; Madras, G.; Patil, K. C. *Acc. Chem. Res.* **2009**, *42*, 704–712.
- (46) Priolkar, K. R.; Bera, P.; Sarode, P. R.; Hegde, M. S.; Emura, S.; Kumashiro, R.; Lalla, N. P. *Chem. Mater.* **2002**, *14*, 2120–2128.
- (47) Sharma, S.; Hegde, M. S. *J. Chem. Phys.* **2009**, *130*, 114706.
- (48) Neagu, D.; Tsekouras, G.; Miller, D. N.; Ménard, H.; Irvine, J. T. S. *Nat. Chem.* **2013**, *5*, 916–923.
- (49) Toby, B. H.; Von Dreele, R. B. *J. Appl. Crystallogr.* **2013**, *46*, 544–549.
- (50) <https://icsd.fiz-karlsruhe.de/> (accessed November 10, 2015).
- (51) Zhu, Y.; Inada, H.; Nakamura, K.; Wall, J. *Nat. Mater.* **2009**, *8*, 808–812.

## D.1. Size Control of Pt Clusters on CeO<sub>2</sub> Nanoparticles via an Incorporation-Segregation Mechanism and Study of Segregation Kinetics

(52) Inada, H.; Su, D.; Egerton, R. F.; Konno, M.; Wu, L.; Ciston, J.; Wall, J.; Zhu, Y. *Ultramicroscopy* **2011**, *111*, 865–876.

(53) Krumeich, F.; Müller, E.; Wepf, R. A.; Nesper, R. *High-Resolution Electron Microscope. J. Phys. Chem. C* **2011**, *115*, 1080–1083.

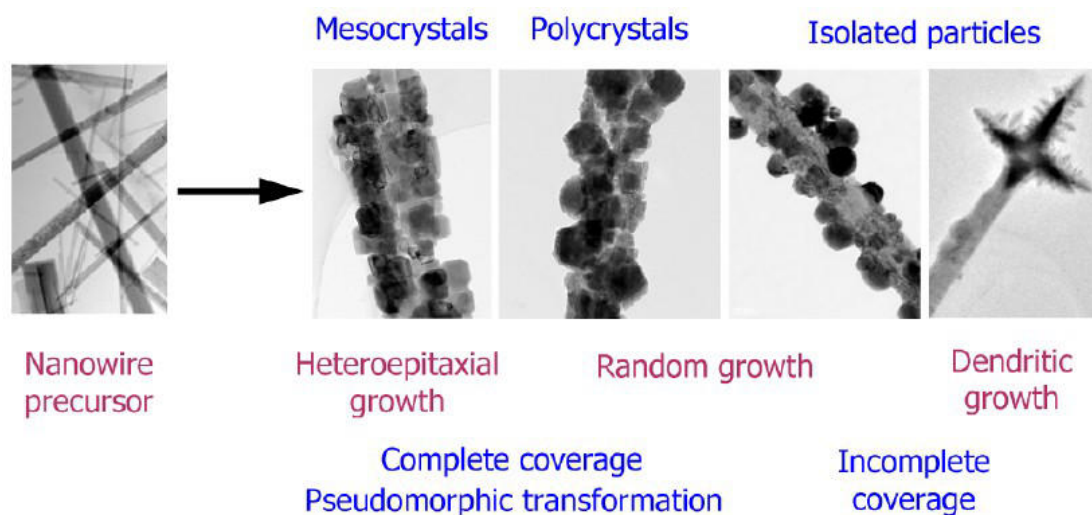
(54) Ida, T. *J. Appl. Crystallogr.* **2011**, *44*, 911–920.

(55) Testino, A.; Pilger, F.; Lucchini, M. A.; Quinsaat, J. E. Q.; Stähli, C.; Bowen, P. *Molecules* **2015**, *20*, 10566–10581.





## D.2 Hydrothermal Synthesis of SrTiO<sub>3</sub>: Role of Interfaces



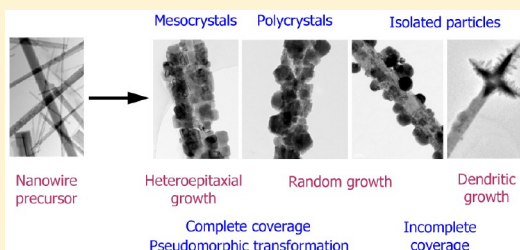
Author's contribution to this publication:

- i. preparation of mixed-organic-aqueous thermodynamic database using OLI software.

Hydrothermal Synthesis of SrTiO<sub>3</sub>: Role of InterfacesVishwanath Kalyani,<sup>†,‡,⊥</sup> Bogdan S. Vasile,<sup>#</sup> Adelina Ianculescu,<sup>#</sup> Andrea Testino,<sup>§</sup> Agnese Carino,<sup>§,||</sup> Maria Teresa Buscaglia,<sup>‡</sup> Vincenzo Buscaglia,<sup>\*,‡</sup> and Paolo Nanni<sup>†</sup><sup>†</sup>Department of Process and Chemical Engineering, University of Genoa, Fiera del Mare, P.le Kennedy, I-16129 Genoa, Italy<sup>‡</sup>Institute for Energetics and Interphases, National Research Council, Via De Marini 6, I-16149 Genoa, Italy<sup>#</sup>Department of Science and Engineering of Oxide Materials, Polytechnics University of Bucharest, 1–7 Gh. Polizu, P.O. Box 12-134, 011061 Bucharest, Romania<sup>§</sup>General Energy Research Department, Paul Scherrer Institute, CH-5232 Villigen PSI, Switzerland<sup>||</sup>École Polytechnique Fédérale de Lausanne (EPFL), ENAC – IIE, CH-1015 Lausanne, Switzerland

## Supporting Information

**ABSTRACT:** The hydrothermal synthesis of SrTiO<sub>3</sub> in a Sr(OH)<sub>2</sub>/NaOH solution by reaction of four different single crystalline titanium precursors (anatase, rutile, sodium titanate, and hydrogen titanate) having the same nanowire morphology was investigated under stagnant fluid conditions. Owing to the low solubility and dissolution rate of the parent phases, the reaction mainly occurs in a thin interfacial fluid layer. The new phase only grows on the substrate surface, and the morphology evolution is largely controlled by the interface through the coupling of substrate dissolution and SrTiO<sub>3</sub> crystallization. The pseudomorphic replacement of the precursor by the product occurs if complete surface coverage is attained. Depending on the crystallographic matching, the parent crystal can either transform in a mesocrystal as happens with anatase via a topochemical transformation or in a polycrystalline product as observed with sodium titanate. In contrast, if the product grows in the form of isolated particles or with dendritic morphology, as in the case of hydrogen titanate and, to a lesser extent rutile, the new compound will not inherit the precursor morphology. When well-defined interfaces are missing, as happens when amorphous titanium hydroxide gel suspensions are used as precursors, the crystallization of SrTiO<sub>3</sub> occurs by a completely different pathway, i.e., oriented self-assembly of nanocrystals in mesocrystals.



## 1. INTRODUCTION

Alkaline earth titanates with perovskite structure, such as CaTiO<sub>3</sub>, SrTiO<sub>3</sub>, and BaTiO<sub>3</sub> as well as their solid solutions, are functional materials which have attracted a strong scientific interest in the last 50 years due to their dielectric, ferroelectric, piezoelectric, and optical properties. BaTiO<sub>3</sub> is the oxide ceramic material most widely used in the electronic industry, mainly as a dielectric in multilayer ceramic capacitors.<sup>1,2</sup> Strontium titanate, SrTiO<sub>3</sub>, is one of the most interesting multifunctional oxides because its properties can be easily modified and tailored by changing the oxygen stoichiometry, doping with foreign elements and applying elastic stresses in the case of films. Thus, the material can be made as ferroelectric, electronic conductor, or mixed ionic-electronic conductor.<sup>3–9</sup> More recently it has been shown that semiconducting SrTiO<sub>3</sub> is also a promising thermoelectric material in both ceramic and thin film form.<sup>10,11</sup> Fine doped strontium titanate powders also exhibit good catalytic and photocatalytic properties.<sup>12–17</sup> The preparation of alkaline-earth titanates by the hydrothermal method has a considerable industrial interest for the production of high-quality fine powders for the electronic industry.

Strontium titanate nanoparticles can be easily prepared by hydrothermal synthesis and related methods in a broad temperature range (40–250 °C) using a variety of precursors, including soluble strontium compounds such as hydroxide, nitrate, chloride, and acetate, and several titanium compounds, such as rutile TiO<sub>2</sub>, anatase TiO<sub>2</sub>, amorphous titanium hydroxide, TiCl<sub>4</sub>, TiOCl<sub>2</sub>, and alkoxides.<sup>18–29</sup> As discussed by Lencka and Riman,<sup>30,31</sup> the hydrothermal synthesis of SrTiO<sub>3</sub> and alkaline earth titanates requires a strong alkaline environment for thermodynamic reasons. For instance, quantitative formation of the perovskite at 160 °C requires a pH above 10 when the Sr concentration exceeds 0.01 mol/L. Less concentrated solutions require a progressively higher pH. Therefore, the addition of a strong base such as NaOH or KOH is often required. When soluble Ti compounds such as TiOCl<sub>2</sub> and butoxide are used as precursors, the high alkalinity of the reaction environment determines a very rapid hydrolysis of the precursor with formation of an amorphous titanium hydroxide

Received: June 4, 2015

Revised: October 19, 2015

Published: October 26, 2015

gel which is the effective precursor of the hydrothermal reaction.

The mechanism of hydrothermal crystallization of BaTiO<sub>3</sub>, which is isostructural to SrTiO<sub>3</sub> above 125 °C, has been investigated in some detail.<sup>32–42</sup> Two different crystallization pathways for BaTiO<sub>3</sub>, in situ transformation and dissolution–precipitation, were proposed by Eckert Jr. et al.<sup>42</sup> and recently revised by Modeshia and Walton.<sup>32</sup> According to in situ transformation, crystallization starts on the surface of TiO<sub>2</sub> particles and continues by inward diffusion of barium ions. Owing to the very slow ionic diffusion in the perovskite lattice at the typical temperatures (<300 °C) adopted in hydrothermal synthesis, this mechanism is operative only when porous titania particles are used as precursors.<sup>43–46</sup>

In the dissolution–precipitation process, titanium aqueous species originated from the dissolution of titania or titania-like precursors in highly alkaline conditions determine the crystallization of BaTiO<sub>3</sub> by nucleation (homogeneous nucleation in the liquid phase or heterogeneous nucleation at the surface of a solid substrate) and ion-mediated growth.<sup>10,12</sup> Although dissolution–precipitation is often invoked to explain the solution mediated formation of many perovskites including SrTiO<sub>3</sub>, this term is extremely vague and does not provide further insight into the real mechanism. The existing literature on the hydrothermal synthesis of barium and strontium titanate<sup>18–42</sup> indicates that the composition, the crystal structure, as well as the particle size and morphology of the solid precursor can strongly modify the crystallization pathway, but the main factors which control the final morphology of the perovskite are not yet well understood.

In this study the morphogenesis of hydrothermal SrTiO<sub>3</sub> has been investigated using six different titanium precursors. Four different crystalline precursors (Na<sub>2</sub>Ti<sub>3</sub>O<sub>7</sub>, H<sub>2</sub>Ti<sub>3</sub>O<sub>7</sub>, anatase, rutile) with the same nanowire (NW) geometry were obtained by successive topochemical transformations. As the initial morphology is highly preserved during topochemical reactions, the morphogenesis of SrTiO<sub>3</sub> could be investigated minimizing side effects related to the use of precursors with different sizes and shapes. Therefore, variations in the product morphology can be directly related to the nature of the crystalline substrate. Thermodynamic modeling provided an estimation of some fundamental parameters such as precursor solubility, supersaturation, and formation of secondary phases. Considering the rather low solubility of the parent phases, the interfaces and the solid–liquid interactions are expected to play a significant role in the hydrothermal synthesis of strontium titanate and other perovskites. In order to further clarify the importance of interfaces and structural order, the formation of SrTiO<sub>3</sub> was also investigated using two amorphous titanium hydroxide (ATH) gel suspensions prepared *in situ* just before the hydrothermal treatment.

## 2. MATERIALS AND METHODS

**Preparation of the Solid Precursors and Hydrothermal Synthesis.** Six different precursors were used in the hydrothermal crystallization experiments: sodium titanate NWs, hydrogen titanate NWs, anatase NWs, rutile NWs, and two different kinds of ATH gels. In addition a few experiments were performed using rutile micro-particles (Aldrich, 99.9%).

Sodium titanate NWs were prepared by hydrothermal synthesis. First, 2 g of anatase powder (grade P90; Evonik Degussa, Germany) together with 20 mL of 10 M NaOH solution were put in a PTFE lined acid digestion bomb (model PA4748, Parr Instrument Company). The vessel was heated in an oven at about 1 °C/min up

to 200 °C and kept at this temperature for 7 h. The resulting solid product is composed of single crystal NWs, mainly Na<sub>2</sub>Ti<sub>3</sub>O<sub>7</sub> with a minor amount of Na<sub>2</sub>Ti<sub>6</sub>O<sub>13</sub>. (Figure S1). The other types of single crystal precursors were obtained from the sodium titanate NWs by topochemical transformations. Their morphology, crystallographic orientation, and phase composition are shown in Figures S2 and S3. The preparation of hydrogen titanate (H<sub>2</sub>Ti<sub>3</sub>O<sub>7</sub>) and anatase NWs is described in detail elsewhere.<sup>47</sup> The rutile NWs were obtained using the same procedure adopted for the anatase NWs with two differences: (i) HCl was used instead of HNO<sub>3</sub> for the acidic washing treatments, and (ii) calcination was performed at 900 °C instead of 700 °C. Despite the high calcination temperature the wire morphology is well preserved; only some coarsening due to the crystallographic fusion of adjacent parallel NWs is observed (Figure S3).

The hydrothermal crystallization experiments were carried out in two different solvents, water and a water/ethanol mixed solvent with a volume ratio of 5.82. A small amount (~0.13 wt %) of polyethylene glycol (PEG) was added to the mixed solvent as a potential growth modifier.

In a typical synthesis with the mixed solvent, 1 g (0.0125 mol) of anatase or rutile was suspended in 10 mL of ethanol by stirring. This suspension was added over 30 s to a solution obtained by dissolving 3.30 g (0.0125 mol) of Sr(OH)<sub>2</sub>·8H<sub>2</sub>O (Aldrich) in 20 mL of water while stirring. Then 10 mL of NaOH 5 M solution, 10 mL of PEG solution (MW 400, 0.8 wt % in water, Aldrich), and 10 mL of water were subsequently added. The final suspension was poured in a PTFE-lined stainless steel acid digestion bomb (model PA4748, volume 120 mL, Parr Instrument Company). The Sr/Ti molar ratio of the suspension was 1, and the strontium concentration was about 0.2 mol/L. The vessel was heated at 200 °C at about 1 °C/min and then kept at 200 °C for times ranging from 15 min to 48 h.

The experiments in water were performed following the same procedure, but the crystalline precursor was suspended in water rather than in ethanol and the PEG solution was replaced by water. After cooling, the bomb was opened and the reaction product was washed several times with water. The final powder suspension was then freeze-dried. Crystallization of SrTiO<sub>3</sub> from the other crystalline precursors was carried out with the same experimental procedure described above.

Two ATH gels were prepared using Ti tetrabutoxide (Aldrich) and TiCl<sub>4</sub> (Acros) as precursors. In a typical synthesis with the mixed solvent, 1.28 g of Ti(OC<sub>4</sub>H<sub>9</sub>)<sub>4</sub> or 0.94 g of a solution containing 2.8 mol/kg of TiCl<sub>4</sub> in water was dissolved in 10 mL of ethanol. The solution was added dropwise over 5 min while stirring to a second solution obtained by dissolving 1.0 g (0.00376 mol) of Sr(OH)<sub>2</sub>·8H<sub>2</sub>O in 20 mL of water. Then 10 mL of 5 M NaOH aqueous solution, 10 mL of PEG (400 MW) solution (0.8 wt %), and 10 mL of water were added in sequence while stirring. The strontium concentration in the final suspension was ~0.06 mol/L. Ethanol and PEG solution were replaced by water in a second series of experiments. The hydrothermal crystallization process and the subsequent powder treatments were carried out as described above.

**Characterization.** The phase composition of the reaction products was determined by X-ray diffraction (XRD, Panalytical CubicX, Cu K $\alpha$  radiation). The morphology of the particles was observed by scanning electron microscopy (SEM, LEO 1450 VP), high-resolution scanning electron microscopy with field emission gun (SEM-FEG, Quanta InspectF, FEI Co., The Netherlands), and high-resolution transmission electron microscopy (HRTEM, Tecnai G2 F30 S-TWIN, FEI Co., The Netherlands). For this purpose, a small amount of powder was suspended in ethanol by 15 min ultrasonication. For SEM analysis, a drop of the suspension was put on a carbon tape stuck on a stub and dried under a IR lamp for 5 min. Finally the sample was sputtered with a gold film. For TEM observation, a drop of suspension was put onto a 400 mesh, holey carbon coated film Cu grid and dried.

**Thermodynamic Modeling.** Hydrothermal reactions involve the interaction between neutral and ionic species in aqueous solution and one or more solid phases. The equilibrium concentration of aqueous species and solid phases is obtained solving a system of linear and nonlinear equations including chemical equilibrium reactions, mass

balance equations, and electroneutrality equations provided that reference thermodynamic data are available for all species. Thus, the evolution of the equilibrium composition as a function of fundamental physicochemical variables such as temperature, pressure, pH, and reactant concentration can be estimated. A thermodynamic model of the  $\text{TiO}_2\text{-Sr}(\text{OH})_2\text{-NaOH-H}_2\text{O}$  system was built considering a solid titanium precursor (rutile, anatase, and  $\text{Ti}(\text{OH})_4$ ),  $\text{Sr}(\text{OH})_2$ ,  $\text{SrCO}_3$  and  $\text{SrTiO}_3$  as solid phases and the aqueous species  $\text{H}^+$ ,  $\text{OH}^-$ ,  $\text{Na}^+$ ,  $\text{NaOH}$ ,  $\text{Sr}^{2+}$ ,  $\text{SrOH}^+$ ,  $\text{Sr}(\text{OH})_2$ ,  $\text{CO}_2$ ,  $\text{CO}_3^{2-}$ ,  $\text{HCO}_3^-$ ,  $\text{NaHCO}_3$ ,  $\text{NaCO}_3^-$ ,  $\text{Ti}(\text{OH})_n^{(4-n)+}$  ( $n = 0-3$ ),  $\text{Ti}(\text{OH})_n^{(n-4)-}$  ( $n = 4-6$ ),  $\text{Ti}(\text{CO}_3)_2^{2-}$  and  $\text{Ti}(\text{HCO}_3)_3^{3-}$ . The initial state of the system corresponds to a mixture of  $\text{Sr}(\text{OH})_2$ , the solid Ti precursor, water, and NaOH. The amount of the different compounds was selected to reproduce the experimental conditions. Reliable thermodynamic reference data for sodium titanate and hydrogen titanate were not found, and, consequently, these species are not considered in calculations. The calculations were then repeated replacing water with the mixed solvent. Because of the relatively high solute concentration (of the order of 0.1 mol/L) used in the experiments and the multitude of competing chemical reactions which make the concentration of the various species strongly dependent on the activity coefficients, calculations were performed using a realistic activity coefficient model<sup>48</sup> and its extension to mixed-solvent electrolyte systems.<sup>49-51</sup> This model has been developed for the calculation of speciation, phase equilibria, pH, thermodynamic quantities and properties in complex systems and is implemented in the OLI Systems software.<sup>52</sup>

In this study thermodynamic modeling was mainly applied for the calculation of (i) the solubility of the different precursors, (ii) the reference driving force (supersaturation) for formation of  $\text{SrTiO}_3$ , and (iii) the possible precipitation of side products  $\text{SrCO}_3$  and  $\text{Sr}(\text{OH})_2$ .

As a major difference in comparison to the former calculations of Riman and co-workers,<sup>42,48</sup> we took into account two additional Ti hydroxocomplexes,  $\text{Ti}(\text{OH})_5^-$  and  $\text{Ti}(\text{OH})_6^{2-}$ . This latter is by far the predominant titanium aqueous species in the highly alkaline conditions used in this study, and its inclusion has resulted in the correct prediction of rutile solubility, as will be discussed in the next section. Moreover, we have included the ionic couple NaOH which is important at high pH and determines a decrease of hydroxide ion concentration and ionic strength.

### 3. RESULTS

**Thermodynamic Modeling.** The precursor solubility was calculated by considering the starting titanium compound in the reaction environment and equilibrating the system while inhibiting the formation of any other solid phases. The aqueous species  $\text{Ti}(\text{OH})_n^{(n-4)-}$  ( $n = 4-6$ ) predominate at  $\text{pH} \geq 7$ , and  $\text{Ti}(\text{OH})_6^{2-}$  is the major one in the strong alkaline conditions used in this study. The calculated solubility of rutile, anatase, and  $\text{Ti}(\text{OH})_4$  in the water solution at 20–320 °C is reported in Figure 1 (solid lines). The solubility of rutile is rather low and ranges between  $2 \times 10^{-6}$  at 20 °C and  $2 \times 10^{-4}$  mol/kg at 320 °C. The calculated values are in good agreement with the experimental data in 1 M NaOH of Knauss et al.<sup>53</sup> in the whole temperature range. The solubility of anatase is 3–10 times higher than that of rutile. Schmidt and Vogelsberger<sup>54</sup> have investigated the solubility of anatase nanopowders at room temperature (RT) in a wide pH range up to 13. Extrapolation of their data to the present experimental conditions gives the estimate reported in Figure 1, which confirms the higher solubility of anatase in comparison to rutile. We are not aware of anatase solubility data at higher temperatures. Given their low solubility, the crystalline precursors will not dissolve appreciably, and a high number of solid/liquid interfaces will exist in the reaction environment. The equilibrium concentration of Ti aqueous species at 200 °C is 3–4 orders of

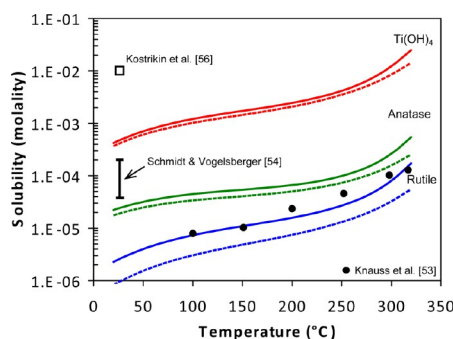
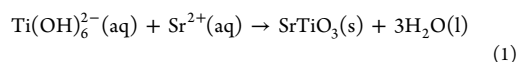


**Figure 1.** Calculated solubility of rutile (blue lines), anatase (green lines), and  $\text{Ti}(\text{OH})_4$  (red lines) in water solution (solid lines) and mixed solvent solution (dotted lines) containing 0.2 mol/L  $\text{Sr}(\text{OH})_2$  and 0.833 mol/L NaOH. Literature data from refs 53 (rutile, full circles) 54 (anatase), and 56 ( $\text{Ti}(\text{OH})_4$ ) are reported for comparison.

magnitude lower than the overall Sr concentration ( $\sim 0.1$  mol/L).

The solubility of  $\text{Ti}(\text{OH})_4$  in the aqueous solution is more than 2 orders of magnitude higher than that of rutile and attains  $2.5 \times 10^{-3}$  mol/kg at 200 °C. The RT solubility of freshly prepared amorphous  $\text{Ti}(\text{OH})_4$ <sup>55</sup> was reported to be  $3 \times 10^{-6}$  mol/L at pH 5–12, i.e., about 300 times higher than that of rutile at 100 °C at pH 3–10.<sup>53</sup> Kostiuk et al.<sup>56</sup> measured the solubility of  $\text{Ti}(\text{OH})_4$  in concentrated NaOH solutions. A moderate solubility of  $\sim 0.01$  mol/L at RT is reported when  $[\text{NaOH}] = 1$  mol/L. Overall, the available albeit limited experimental data support the reliability of the thermodynamic calculations considering that the main goal of the model is to provide some general indications rather than an accurate estimate. The addition of EtOH determines only a small ( $\text{Ti}(\text{OH})_4$ ) to moderate (rutile) lowering of the solubility of the three precursors (dotted lines in Figure 1). At 200 °C the solubility is reduced of a factor  $\sim 2$  for rutile.

Assuming a dissolution and precipitation mechanism, the formation of  $\text{SrTiO}_3$  can be represented by the reaction



and the supersaturation  $S$  can be written as

$$S = \frac{a(\text{Ti}(\text{OH})_6^{2-})a(\text{Sr}^{2+})}{K_s} \quad (2)$$

where  $K_s$  is the solubility product; i.e., the reciprocal of the equilibrium constant of reaction 1 and the numerator corresponds to the product of the activity of the aqueous species immediately before the perovskite formation. The calculation of this latter quantity was performed following the same approach used in the solubility calculations: the titanium precursor is introduced in the reaction environment and the system is equilibrated while inhibiting the formation of any other solid phases. The calculation results are shown in Figure 2. The supersaturation is very high and increases with increasing precursor solubility, from  $10^7$  to  $10^8$  for rutile to  $10^{10}$  for  $\text{Ti}(\text{OH})_4$ . The addition of EtOH has a minor influence. It is worth noting that the model gives an upper bound to the real supersaturation existing in the system as it is implicitly assumed that the equilibrium concentration of the soluble



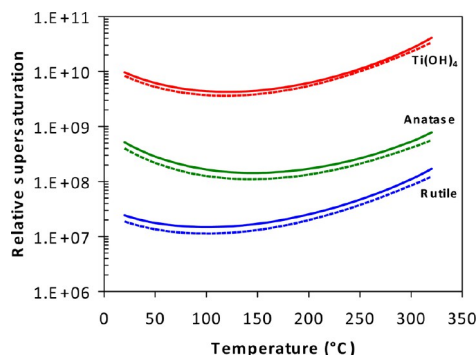


**Figure 2.** SrTiO<sub>3</sub> supersaturation calculated for rutile (blue lines), anatase (green lines), and Ti(OH)<sub>4</sub> (red lines) in water solution (solid lines) and mixed solvent solution (dotted lines) containing 0.2 mol/L Sr(OH)<sub>2</sub> and 0.833 mol/L NaOH.

titanium resulting from precursor dissolution is instantaneously established. However, the dissolution of the parent phase can be very slow, and thermodynamic equilibrium may not be achieved during the reaction leading to a significant decrease of the available driving force. As will be discussed later, the morphology evolution observed for some precursors clearly indicates that the effective driving force is much lower than the thermodynamic value and crystallization is under kinetic control.

The thermodynamic calculations confirm that SrTiO<sub>3</sub> is the predominant reaction product in the wide range of explored conditions ( $T = 25\text{--}300\text{ }^{\circ}\text{C}$ ,  $[\text{NaOH}] = 0.01\text{--}2\text{ mol/kg}$ ) when  $[\text{Sr}^{2+}] = 0.05\text{--}0.2\text{ mol/L}$ . However, as already pointed out by Lencka and Riman,<sup>30,31</sup> the presence of carbon dioxide or carbonate ions in the reaction vessel can often result in the formation of SrCO<sub>3</sub> as a side-product. Calculations were performed assuming a maximum amount of SrCO<sub>3</sub> corresponding to 2 mol % of the overall strontium concentration. The results obtained for a total Sr concentration of 0.2 mol/L show (Figure 3a,d) that precipitation of SrCO<sub>3</sub> is complete over a wide range of experimental conditions. When the Sr concentration is lowered to 0.06 mol/L (Figure 3b,e), the precipitation of strontium carbonate is promoted at low NaOH concentration. The addition of ethanol has a minor effect on the amount of SrCO<sub>3</sub>. The amount of precipitated SrCO<sub>3</sub> increases during cooling to room temperature. Consequently the absorption of CO<sub>2</sub> by the solid reactants or during the preparation of the corresponding solutions always determines the contamination of the main reaction product by strontium carbonate. In contrast, precipitation of Sr(OH)<sub>2</sub> that could be induced by the high hydroxide ion concentration is predicted to begin only at high temperature ( $\sim 300\text{ }^{\circ}\text{C}$ ) and NaOH concentration  $>1.5\text{ mol/kg}$  (Figure 3c,f). Thus, formation of SrCO<sub>3</sub> by reaction of precipitated Sr(OH)<sub>2</sub> with atmospheric CO<sub>2</sub> can be discarded.

**Product Morphology.** Morphology evolution with reaction time was investigated by SEM and TEM. In the case of crystalline precursors, the morphology is largely independent of the solvent (mixed solvent or water) meaning that PEG does not act as a growth modifier in the present experimental conditions. Significant morphological differences related to the solvent were only observed in the case of ATH gel precursors. Formation of a small amount of SrCO<sub>3</sub>, probably related to

absorption of CO<sub>2</sub> or/and carbonate contamination of Sr(OH)<sub>2</sub> and NaOH, was detected by XRD in all samples.

**Synthesis from Anatase NWs.** As detailed in a previous paper,<sup>47</sup> the hydrothermal reaction of anatase NWs results in the formation of strontium titanate mesocrystals composed of SrTiO<sub>3</sub> nanocubes with a lateral size on the order of 50–100 nm, which are aligned along the [100] crystallographic direction (Figure 4). Crystallization is quite rapid and SrTiO<sub>3</sub> is the main phase after 15 min (Figure S4). The mesocrystals retain the elongated morphology of the anatase precursor. The simplest example of mesocrystal corresponds to two rows of aligned perovskite nanocubes, as shown in Figure 4a. The mesocrystals result from the heteroepitaxial growth of the perovskite on the (001) surfaces of the anatase NWs.<sup>47</sup> Thus, two rows of perovskite crystal form on the opposite (001) faces of the anatase NWs and grow by attachment of ionic species ( $\text{Sr}^{2+}$ ,  $\text{Ti}(\text{OH})_n^{4-n}$  ( $n = 4\text{--}6$ )). More abundant are wires composed of several rows of aligned nanocubes (Figure 4b) resulting from the transformation of NW bundles. The morphology is rather stable and significant recrystallization/coarsening was not observed even for the longest time adopted in this investigation (48 h). The anatase NWs have a 2-fold role, as substrates for the epitaxial growth of the perovskite and as source of aqueous titanium species. The gap between the two rows of SrTiO<sub>3</sub> nanocubes observed in Figure 4a is likely to be a consequence of the complete dissolution of the anatase NW. The elastic stresses arising from lattice mismatch (3.2%) between anatase and SrTiO<sub>3</sub> are relieved by the formation of dislocations in the growing perovskite. This fact, together with the possible presence of defects and irregularities on the anatase surface, will result in a nonperfect matching of the lattices of adjacent SrTiO<sub>3</sub> nanocubes with formation of a mesocrystal rather than single crystal. The primary nanocubes are clearly visible in the TEM images (Figure 4) because of their different height and the contrast variations existing in the interface region between adjacent nanocubes due to the presence of extended defects such as dislocations and elastic strains. A substantial amount of anatase is revealed by XRD even after 24–48 h reaction. Since unreacted anatase NWs were not observed, the existence of an unreacted anatase core in the SrTiO<sub>3</sub> mesocrystals is likely.

**Synthesis from Sodium Titanate NWs.** As indicated by the diffraction pattern (see Figure S5) a significant fraction of sodium titanate is still present after 15 min hydrothermal treatment in W/EtOH, whereas the reaction is almost complete after 24 h. The product largely retains a wire-like morphology and shows a duplex microstructure corresponding to the formation of SrTiO<sub>3</sub> particles with two distinct morphologies, as illustrated in Figure 5. Regular patterns of well aligned nanocubes (indicated by arrows in Figure 5a) have developed on the sodium titanate surface, suggesting a heteroepitaxial growth mechanism. Isolated bigger particles with more irregular morphology and rough surface have grown on this first layer, as also evident from Figure 5b. Coarsening of these particles occurs at longer times leading to polycrystalline wires with irregular surface (Figure 5c,d). Some of these particles show enhanced growth in the corner region similar to the first stage of dendritic growth. The morphology as well as the ED pattern indicate a predominant random orientation of the crystallites.

**Synthesis from Hydrogen Titanate NWs.** The formation of heterostructures corresponding to the growth of isolated cuboidal SrTiO<sub>3</sub> nanocrystals on the surface of the hydrogen titanate wires occurs for short reaction times, 15 min to 3 h

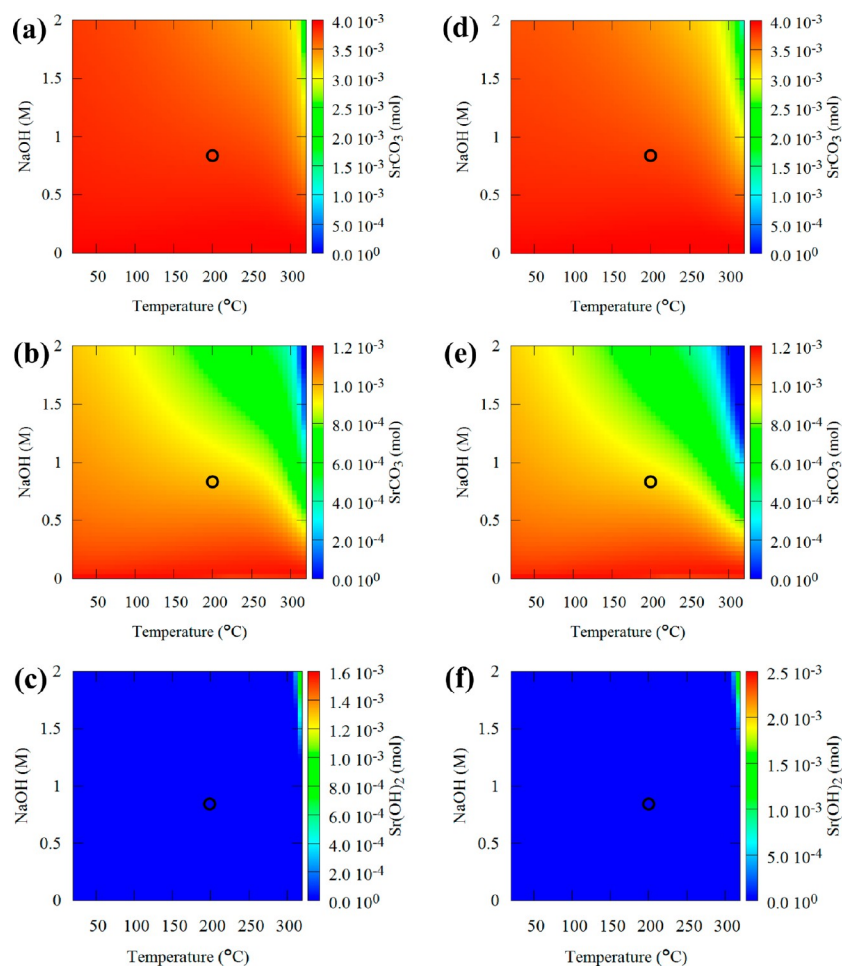


**Figure 3.** Amount of secondary phases ( $\text{SrCO}_3$  and  $\text{Sr(OH)}_2$ ) precipitated as a function of temperature and NaOH concentration in (a–c) water solution and in (d–f) mixed solvent. (a, d)  $\text{SrCO}_3$ , total strontium concentration 0.2 mol/L. (b, e)  $\text{SrCO}_3$ , total strontium concentration 0.06 mol/L. The calculations were performed assuming that up to 2 mol % total strontium can precipitate as carbonate. (c, f)  $\text{Sr(OH)}_2$ , total strontium concentration 0.2 mol/L. The black circle indicates the present experimental conditions.

(Figures 6 and S6). SEM and TEM observations reveal that only part of the hydrogen titanate wire surface is coated with the perovskite particles. The ED patterns of the  $\text{SrTiO}_3$  heterostructures show circles rather than spots, meaning that the perovskite nanoparticles which have grown on a single hydrogen titanate wire have no preferential crystallographic orientation. The growth of spatially isolated particles indicates that heterogeneous nucleation of the perovskite is difficult. The absence of epitaxial growth of  $\text{SrTiO}_3$  on the surface of the hydrogen titanate wires suggests an increase of the free energy barrier for nucleation, and this contributes to decrease the density of surface nuclei. As the reaction time increases, an increasing number of  $\text{SrTiO}_3$  loose particles detached from the wires is observed. However, partly uncoated  $\text{H}_2\text{Ti}_3\text{O}_7$  NWs can still be observed after 24 h reaction, a clear indication of low effective supersaturation which hinders nucleation. After 48 h, the reaction product is mainly composed of cuboidal loose particles and irregular aggregates (Figure 6b). This morphology

evolution clearly indicates that the  $\text{SrTiO}_3$  particles do not grow in close contact and are initially held together only by the hydrogen titanate wire core. When the reaction approaches completion, the hydrogen titanate cores disappear, and the memory of the original wire-like morphology is nearly lost. In contrast, the initial wire morphology of the anatase and sodium titanate parent phases is largely retained in the final product.

**Synthesis from Rutile NWs.** The transformation kinetics of the rutile NWs is slower in comparison to the other titania/titanate precursors (Figure 7a). Strontium titanate dendrites with four to eight branches, often with irregular morphology and different growth levels can be observed in Figure 7b,c. The star-like crystals in Figure 7b are most likely dendrites in their early development stage. A very similar dendritic growth is also observed when rutile microparticles are used as precursors (Figure 7d). As indicated by the parallel lattice fringes (Figure 7f) and the ED pattern, the dendrites correspond to  $\text{SrTiO}_3$  single crystals. The rutile NWs are partially coated by the

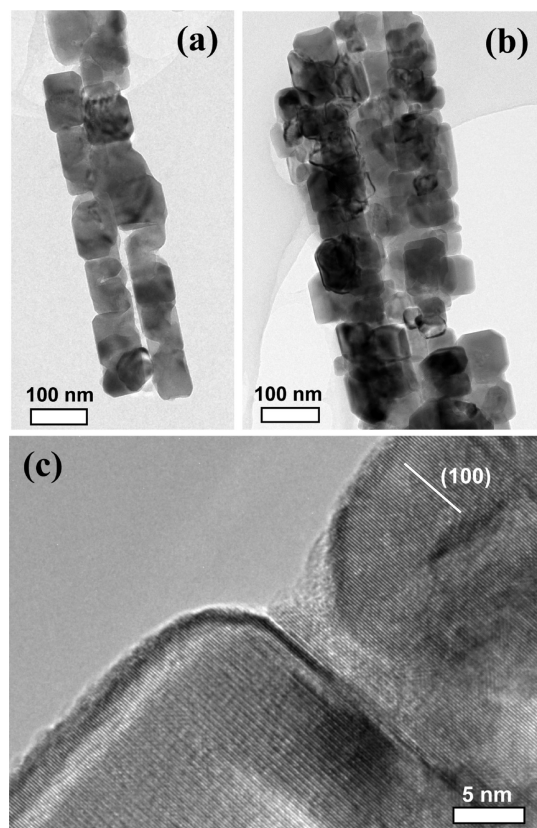


**Figure 4.** Morphology of SrTiO<sub>3</sub> mesocrystals obtained after 24 h hydrothermal reaction of anatase NWs at 200 °C in mixed solvent. (a, b) Typical examples of observed morphologies, TEM. (c) HRTEM image of the lattice of two primary SrTiO<sub>3</sub> nanocubes.

growing SrTiO<sub>3</sub> dendrites after 15 min reaction, as shown in Figure 7b. At longer times (24 and 48 h) the dendritic growth produces chaotic agglomerates, and the original elongated morphology of the rutile NWs is no longer evident. The completely different morphological evolution of the anatase and rutile NWs during the reaction provides clear evidence of the importance of the titania polymorph on the hydrothermal crystallization mechanism of SrTiO<sub>3</sub>.

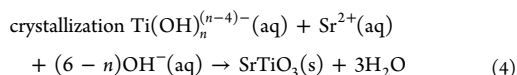
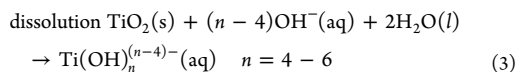
**Synthesis from TiOCl<sub>2</sub> Gel.** SEM and TEM images (Figure 8) as well as XRD patterns (Figure S7) show that the gel is completely transformed in SrTiO<sub>3</sub> after 13 h hydrothermal treatment irrespective of the solvent. As shown in Figure 8a, the product obtained with the mixed solvent is composed of spheroidal strontium titanate particles with a diameter of 200–500 nm characterized by the presence of evident surface pores. In agreement, TEM inspection (Figure 8b,c) has revealed highly porous or partially hollow particles with rounded morphology. Some of these latter particles show the development of facets (Figure 8c). In addition to this predominant morphology some irregular aggregates (denoted with arrows in Figure 8b) composed of primary particles with size of 30–70 nm are also observed. Overall, TEM investigation indicates an almost continuous evolution from shapeless aggregates of nanocrystals to largely recrystallized porous particles.

Hydrothermal reaction of the TiOCl<sub>2</sub> gel in water leads to spherical aggregates (50–150 nm) composed of primary nanocrystals with size on the order of 5 nm (Figure 8d). Contrast variations inside the aggregates indicate the existence of nanopores and other imperfections in the interfacial regions. As shown by the HRTEM image of Figure 8e, the primary nanocrystals are highly aligned along the same crystallographic direction forming a mesocrystal. The existence of nanopores, small misalignments of the lattice planes, and dislocations indicate that the mesocrystals are probably produced via an oriented attachment mechanism. Some of the mesocrystals appear partially recrystallized, with formation of faceted hollow particles (Figure 8f).

**Synthesis from Ti Butoxide Gel.** Residual gel phase enveloping the SrTiO<sub>3</sub> particles (not shown) is observed after 3 h reaction, whereas formation of the perovskite is completed after 13 h (Figure S8 and Figure 9). Observation at low magnification of the reaction product obtained in the mixed solvent (Figure 9a) shows single or grouped SrTiO<sub>3</sub> cubic particles of 150–500 nm. At higher magnification the majority of particles clearly reveal a substructure corresponding to the ordered aggregation of nanocrystals with size on the order of 5 nm (Figure 9b,c) in mesocrystals. The existence of terraces and steps on the mesocrystal surfaces indicates that growth proceeds layer-by-layer through the oriented attachment of the nano building units at kink and step sites. This process mimics the classical crystal growth mechanism reported in textbooks—except that ions and molecules are replaced by nanocrystals.<sup>57,58</sup> The attachment of the primary nanoparticles at the surface of a mesocrystal along the [100] direction is evident in the HRTEM images (Figure 9d,e). Systematic observation has revealed, in addition to mesocrystals, a fraction of particles with smooth surface (see, for example, the leftmost particle in Figure 9b). This indicates the possible evolution of the mesocrystals (which are metastable moieties) in single crystals. The reaction product obtained after reaction in water corresponds to cubic particles with irregular surface clearly originated by the fusion of several smaller cubic units with the same crystallographic orientation (Figure 9f).

#### 4. DISCUSSION

Considering that the direct growth of SrTiO<sub>3</sub> on the crystalline precursor surface by solid-state diffusion is unlikely because of the very low mobility of the constituting ions in the perovskite lattice at the typical temperatures used in hydrothermal synthesis, a two-step mechanism including the dissolution of the parent phase and the crystallization of the perovskite better describes the crystallization process. In the case of titania precursors the two reactions can be written as



Similar reactions can be formulated for H<sub>2</sub>Ti<sub>3</sub>O<sub>7</sub> and Na<sub>2</sub>Ti<sub>3</sub>O<sub>7</sub>. In the case of ATH gels, because of their extremely high surface area and amorphous nature, in situ transformation may play a role during the early reaction stages.

The results obtained for the crystalline precursors clearly indicate that formation of SrTiO<sub>3</sub> occurs on the surface of the



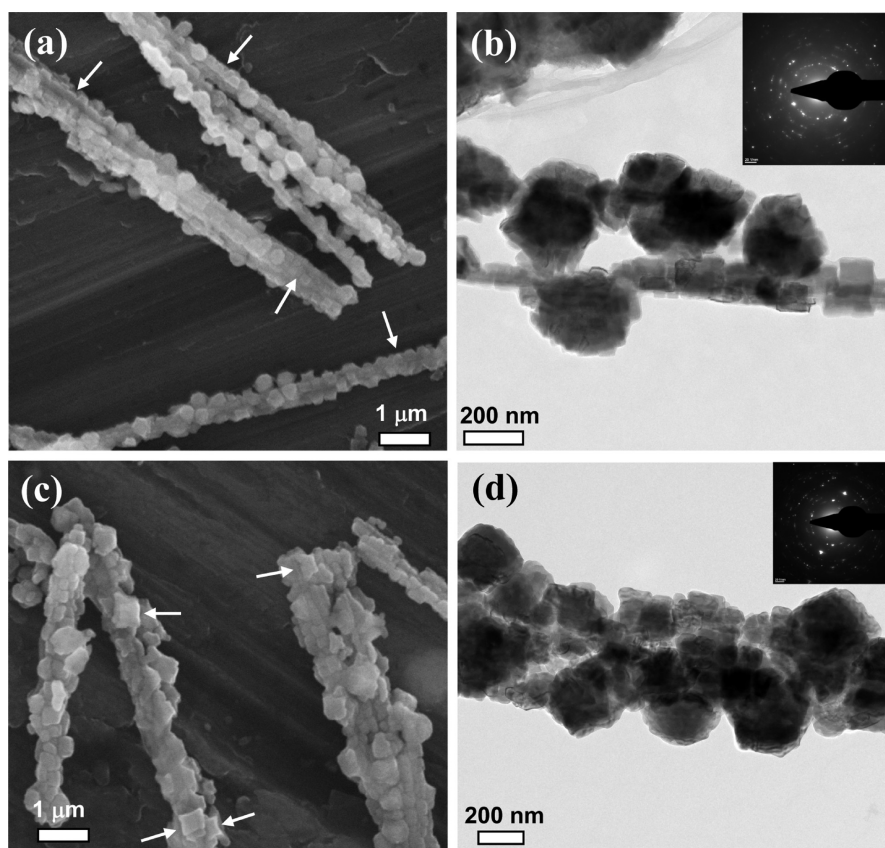


**Figure 5.** Morphology of  $\text{SrTiO}_3$  wires obtained by hydrothermal reaction of sodium titanate NWs at  $200^\circ\text{C}$  in mixed solvent. (a) After 15 min, SEM. The arrows denote regions of the rods consisting of well aligned nanocubes. (b) After 15 min, TEM. A duplex morphology is evident. (c) after 24 h, SEM. The arrows indicate crystals with preferred growth in the edge region. (d) After 24 h, TEM. The insets of parts (b) and (d) show typical ED patterns.

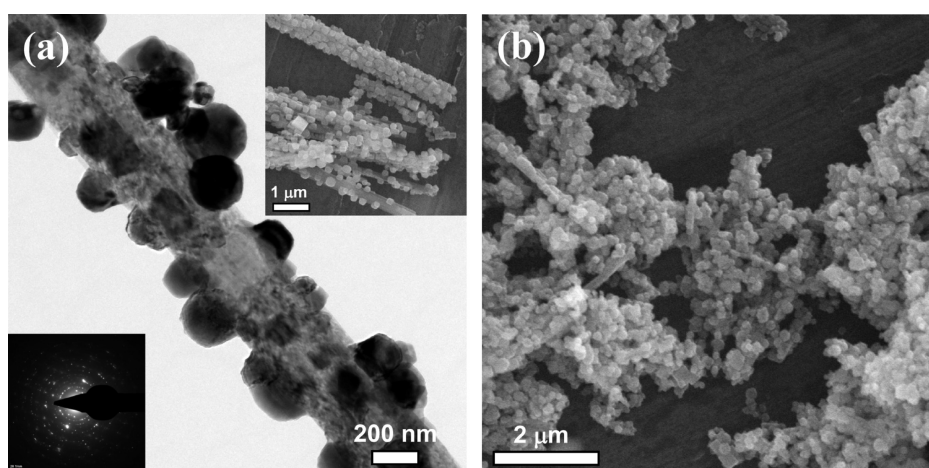


**Figure 6.** Morphology of  $\text{SrTiO}_3$  particles obtained by hydrothermal reaction of hydrogen titanate NWs at  $200^\circ\text{C}$  in mixed solvent. (a) after 15 min, TEM. Insets: typical ED pattern and lower magnification SEM image of a sample reacted 24 h. (b) after 48 h, SEM.



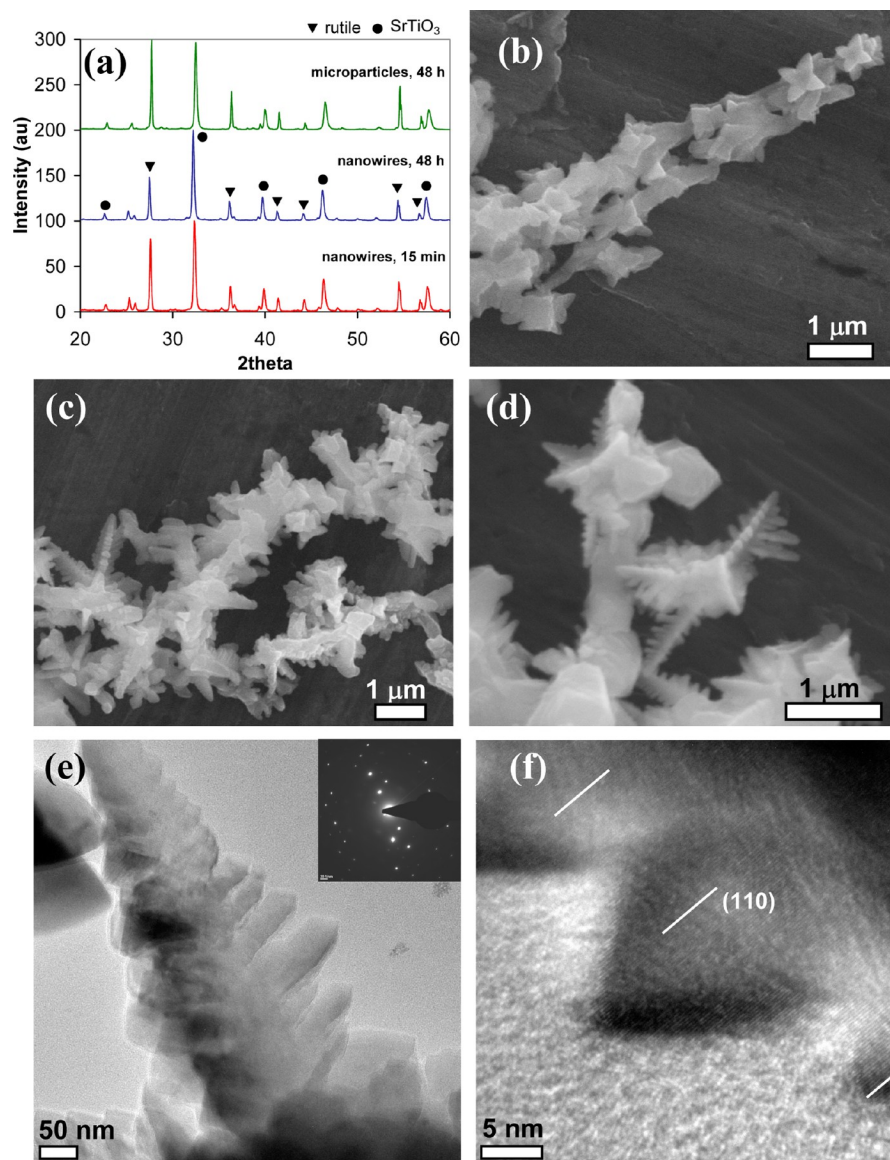


**Figure 7.** (a) XRD patterns of reaction products after hydrothermal reaction of rutile precursors at 200 °C in mixed solvent. (b–d) Morphology (SEM) of SrTiO<sub>3</sub> dendritic particles grown on (b) rutile NWs after 15 min, (c) rutile NWs after 48 h, and (d) rutile microparticles after 15 min. (e, f) HRTEM images of a dendritic SrTiO<sub>3</sub> crystal grown after 15 min on a rutile NW. The inset of part (e) shows the ED pattern.

parent phase or very close to it. This means that both the transport of soluble titanium species originated by precursor dissolution and the crystallization of SrTiO<sub>3</sub> are confined in a relatively narrow region near the precursor surface. The localization of the reaction in the interface region is determined by different factors. First, it should be considered that stagnant fluid conditions prevail during most of the time because the hydrothermal vessel is not stirred and long-range convective transport during the non-isothermal transient is minimized due to the low heating rate (1 °C/min). Second, the low solubility of the crystalline precursors (Figure 1) will strongly reduce the

supply of titanium aqueous species at the reaction front, whereas Sr<sup>2+</sup>(aq) is readily available in the solution because of the high solubility of Sr(OH)<sub>2</sub> as confirmed by thermodynamic calculations (Figure 3). The fact that the product directly grows on the substrate surface suggests that the dissolution rate is rather low and, when small enough, can become the rate-controlling step of the overall reaction. Therefore, despite the high calculated supersaturation (Figure 2) in principle would justify homogeneous nucleation in the bulk of solution, the bulk of solution remains undersaturated.

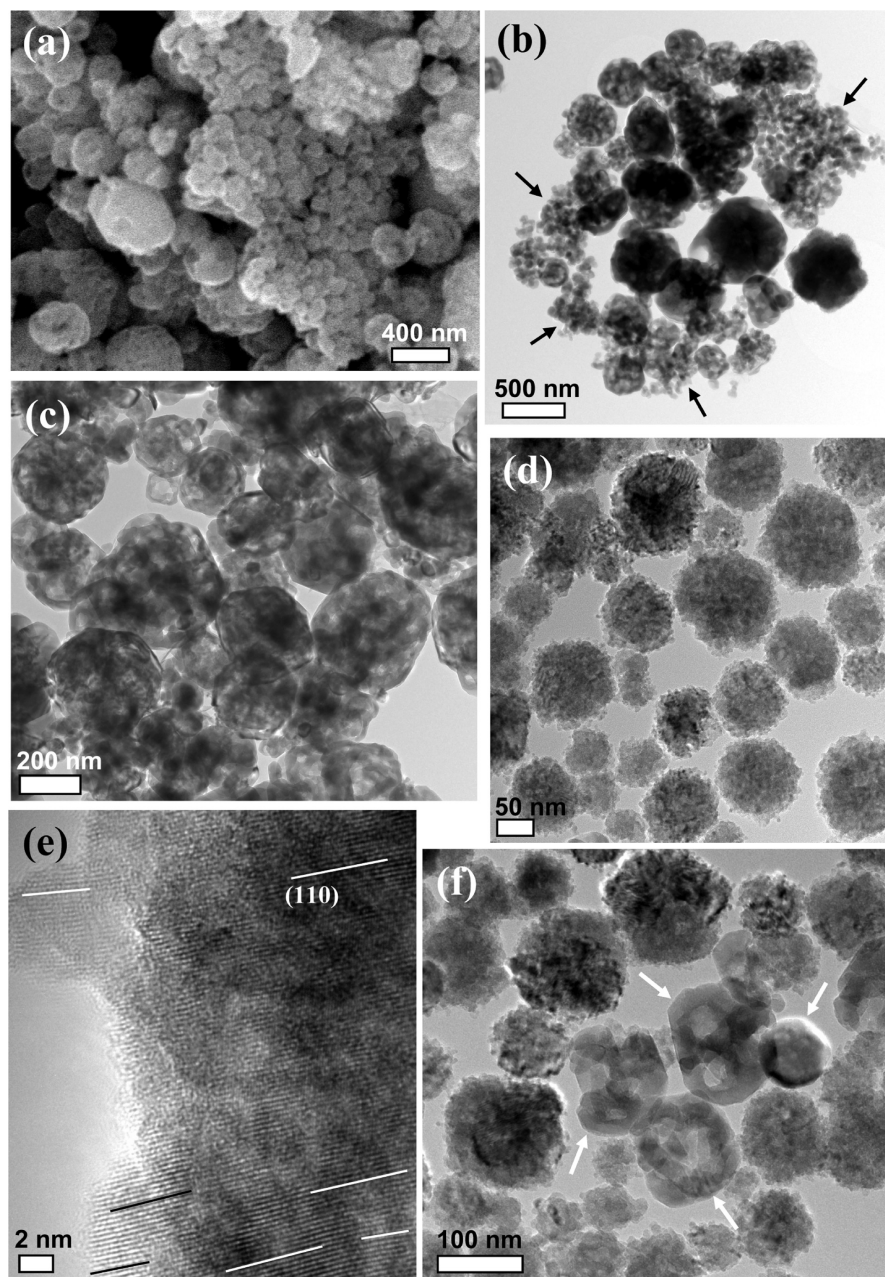


**Figure 8.** Morphology of  $\text{SrTiO}_3$  particles obtained by hydrothermal reaction of a  $\text{TiOCl}_2$  gel at 200 °C for 13 h in (a–c) mixed solvent. (d–f) water. (a) SEM (b–f) TEM/HRTEM. The solid lines in (e) indicate the existence of small misalignments between the primary nanocrystals. The white arrows in (f) indicate partially recrystallized porous particles.

If the dissolution rate is the controlling step, even the effective supersaturation in the interfacial layer could be much lower than that estimated by the thermodynamic calculations and, consequently, the substrate surface will play a significant role in the nucleation as well as on the crystallographic order and orientation of the new phase. Anyway, even a very sluggish

dissolution can supersaturate a very thin interfacial fluid layer. The incomplete surface coverage observed for rutile (Figure 7b,c) and hydrogen titanate (Figure 6a) provides strong evidence that after the early instants the heterogeneous nucleation rate is strongly depressed and mainly growth occurs with these precursors. Crystallization of  $\text{SrTiO}_3$  is not expected



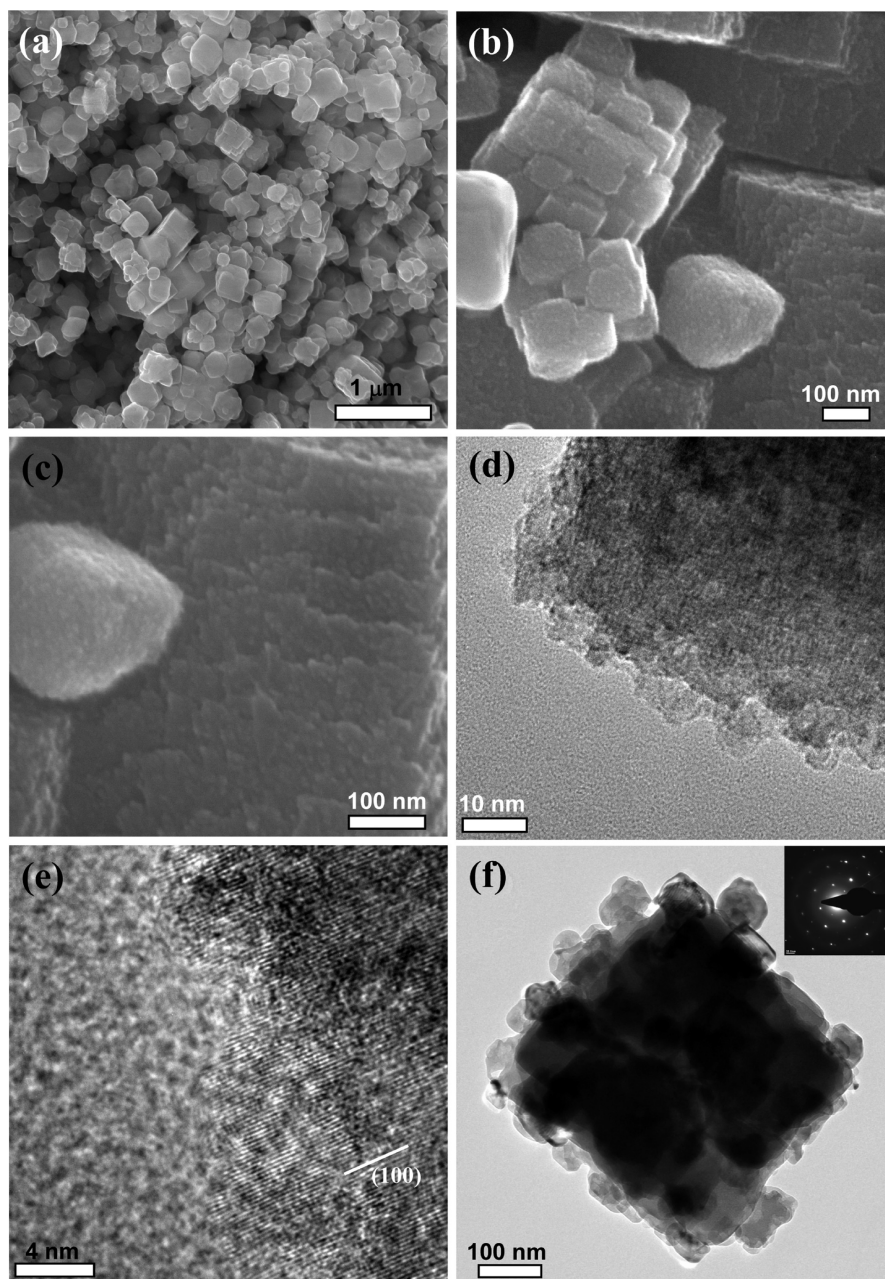


**Figure 9.** Morphology of SrTiO<sub>3</sub> particles obtained by hydrothermal reaction of a Ti(OBut)<sub>4</sub> gel at 200 °C for 13 h in (a–e) mixed solvent and (f) water. (a–c) SEM-FEG. (d–f) HRTEM. The inset of part (f) shows the ED pattern.

to be rate-controlling since in that case formation of the new phase would occur over a much longer distance because a thicker fluid layer around the substrate could supersaturate. In any case, irrespective of the rate-controlling process, the localization of the reaction in the interface region and the properties of the interface will largely determine the morphological evolution of the reaction product.

When there is a high degree of structural matching between precursor and product as in the case of anatase, the perovskite will grow epitaxially on the substrate (Figure 4). Since the crystallographic orientation of the substrate is largely transferred to the product phase, the reaction can be considered as a topochemical transformation. When the substrate/product compatibility is reduced, a polycrystalline product will be

formed as happens with sodium titanate (Figure 5) even though during the initial reaction stage formation of aligned perovskite nanocubes is also observed. In both cases, the parent phase is replaced by the product, a process known by mineralogists as pseudomorphic transformation; i.e., a different compound takes the place of the parent mineral while preserving the original crystal morphology.<sup>59,60</sup> Consequently the precursor crystals can be used as templates for the synthesis of SrTiO<sub>3</sub> particles with controlled shape.

Complete surface coverage of the new phase is required for the replacement reaction. If this is not realized, the morphology evolution will be completely different, as exemplified by the behavior of the H<sub>2</sub>Ti<sub>3</sub>O<sub>7</sub> NWs (Figure 6). In such a case, the new phase mainly grows as isolated particles with random orientation and a significant fraction of the precursor surface remains uncovered even after 24 h reaction (Figure 6a, inset). This indicates that nucleation is more difficult in comparison to other substrates. Consequently, the precursor morphology is not inherited by the perovskite, and the product particles are initially held together only by the residual precursor core.

As soon as complete surface coverage of the parent phase by the perovskite layer is attained the reaction will be strongly suppressed (but not stopped) considering that dissolution and transport of the precursor could only occur via channels, pores, and cracks existing in the product layer, as reported in different dissolution–precipitation experiments.<sup>60–62</sup> The existence of these defects, especially in the edge regions, is likely because the volume of SrTiO<sub>3</sub> formed per unit volume of parent phase is >1 (1.7 for anatase, 1.9 for rutile, 1.2 for Na<sub>2</sub>Ti<sub>3</sub>O<sub>7</sub>). There is some evidence that the transport of soluble species, including titanium hydroxocomplexes, during replacement reactions can occur along pores and channels at grain boundaries and other extended defects.<sup>59,60,63,64</sup> Complete overgrowth is already observed after 15 min for anatase and sodium titanate (Figures 4 and 5). For rutile, the attainment of surface coverage is not easily detected due to the complex morphology (Figure 7). A significant amount of the precursor phase still survives after 24/48 h in the case of anatase and rutile (see Figures S4 and 7a).

The formation of SrTiO<sub>3</sub> on the surface of rutile occurs by dendritic growth irrespective of the precursor nature, NWs or micrometric rounded particles (Figure 7). Formation of dendrites is usually observed under diffusion control because of the instability of the growth front and the tendency of the new phase to grow faster in the edge region. According to Fick's first law, the diffusion flux is proportional to the diffusivity and to the concentration gradient. Hence dendritic growth can be enhanced by a strong suppression of diffusivity as experimentally observed from crystallization experiments carried out in inert gel media<sup>65,66</sup> as well as predicted by Monte Carlo simulations<sup>67,68</sup> or by reducing the concentration gradient. The lower solubility of rutile in comparison to other precursors will result in a smaller gradient and, consequently, in a restricted supply of the titanium soluble species to the growth front, the main ingredient for dendritic growth. The intricate morphology determined by the dendritic growth has hampered a more detailed investigation of the crystallographic orientation of the perovskite dendrites. Considering that the heteroepitaxial growth of SrTiO<sub>3</sub> occurs on (100) and (110) rutile surfaces with several orientation relationships,<sup>69</sup> the oriented growth of the dendrites on the substrate is likely.

In conclusion, we can refer to the formation mechanism of SrTiO<sub>3</sub> from poorly soluble crystalline titanium precursors in stagnant conditions as an interface-driven dissolution and

crystallization process. The interface has an active role on the substrate dissolution as well as on nucleation and crystallographic order of the new phase. It is worth noting that, despite several attempts, the topochemical transformation of sodium and hydrogen titanate NWs in strontium titanate by ion exchange could not be obtained. This suggests that the exchange reaction, reported as an effective template-assisted synthesis method for the preparation of single crystal BaTiO<sub>3</sub> and SrTiO<sub>3</sub> NWs<sup>70–75</sup> only occurs in a rather narrow window of experimental conditions and is incompatible with an interface-driven dissolution and crystallization process.

The results reported by Maxim et al.<sup>40</sup> for the hydrothermal synthesis of BaTiO<sub>3</sub> from Na<sub>2.5</sub>H<sub>4</sub>Ti<sub>2</sub>O<sub>5</sub> nanotubes in stagnant hydrothermal conditions also pointed out that 1D titania-based precursors do not act as templates in a wide range of experimental conditions: formation of dendrites was always observed. The dendrites nucleated on the nanotube surface but, according to the TEM investigation (Figure 10 of ref 40), most of the nanotubes showed no evidence of dendrites. This suggests that nucleation was difficult and the effective supersaturation close to the precursor surface quite low, a situation similar to that observed with hydrogen titanate and rutile NWs in the present study. The stagnant conditions can be the limiting factor and synthesis in a well stirred reactor is likely to produce a different result. Indeed, topochemical transformation of hydrogen titanate platelets in different perovskites was attained by Feng et al. in stirred vessels.<sup>70,74,75</sup>

When well-defined interfaces are missing, the reaction pathway will be deeply altered. In fact, as evident from Figures 8 and 9, the use of ATH gel precursors promotes nanoparticle mediated nonclassical crystallization of SrTiO<sub>3</sub>. As many other gels, the gelatinous ATH precursor obtained by rapid hydrolysis of soluble titanium compounds such as TiOCl<sub>2</sub> and Ti(OBut)<sub>4</sub> has an amorphous polymeric network structure with pore and channels with a size from a few nanometers to a few tens of nanometers filled by the solvent.<sup>76,77</sup> Alkaline-earth ions do not take part into the formation of the network and remain in solution. The solution completely permeates the gel, and there are not well-defined solid/liquid interfaces to couple dissolution and crystallization as in the case of crystalline substrates. The huge contact area of the gel network with the solvent and the relatively higher solubility of Ti(OH)<sub>4</sub> in comparison to other precursors (Figure 1) will determine a higher supersaturation (Figure 2), and a very large number of small nanocrystals will readily nucleate within the whole gel volume and grow to a limited extent, up to about 5 nm as inferred from Figures 8 and 9. Since the diffusion of the nanocrystals is strongly depressed by the gel network, these nano building units will have enough time to reorient under the influence of the interaction potentials and align along a preferred crystallographic direction leading to the formation of mesocrystals rather than random aggregates. Reorientation is a fundamental step to remove the free energy barrier to aggregation.<sup>78</sup> In general, gels are well suited for the generation of mesocrystals.<sup>79,80</sup>

The size, the morphology (spherical or cubic), and the internal structure (porous or compact) of the final mesocrystals are very sensitive to the starting soluble titanium compound, TiOCl<sub>2</sub> or Ti(OBut)<sub>4</sub> and the solvent (Figures 8 and 9) because of the influence of these parameters on the structure of the polymeric network, the solubility of the gel, and the possible interactions of the gel with the mesocrystals and the nano building units. This suggests that an effective control on

the morphology of the SrTiO<sub>3</sub> mesocrystals can be achieved by tuning different parameters.

Mesocrystals are, by definition, metastable moieties, and consequently they have the tendency to transform in single crystals by crystallographic fusion of the primary nanocrystals and/or recrystallization processes like Ostwald ripening.<sup>79–81</sup> Recrystallization can determine the formation of particles with an intermediate structure between mesocrystals and single crystals as revealed, for example, by the morphology observed after hydrothermal synthesis from the Ti(OBut)<sub>4</sub> gel in water (Figure 9f). In this case the size of the cubic subunits (50–100 nm) is much larger than the typical size (5 nm) of the primary nanocrystals observed in SrTiO<sub>3</sub> mesocrystals (Figures 6 and 7). The recrystallization of the SrTiO<sub>3</sub> mesocrystals with formation of intermediate morphologies similar to that reported in Figure 7f was well documented by Park et al.<sup>82</sup> whereas multiple growth stages were identified by Zhan et al.<sup>83</sup> Although not observed in the present experiments, recrystallization and coarsening of the reaction products obtained from the crystalline precursors could become important if the size of the parent particles were reduced to a few tens of nanometers.

## 5. SUMMARY AND CONCLUSIONS

The hydrothermal crystallization of SrTiO<sub>3</sub> from six different titanium precursors, four crystalline titania/titanate phases and two freshly prepared amorphous titanium hydroxide gel suspensions, has been investigated for times of 0.25–48 h at 200 °C. The reaction occurs in a solution of Sr(OH)<sub>2</sub> (0.06–0.2 mol/L) and NaOH (0.83 mol/L) under stagnant conditions, i.e., without stirring and convective fluid motion. According to thermodynamic calculations and limited literature data, the solubility of the crystalline precursors is rather small (orders of magnitude lower than strontium concentration), whereas that of the gel precursors was moderate (on the order of 10<sup>–2</sup>–10<sup>–3</sup> mol/L). All the crystalline precursors (anatase, rutile, sodium titanate Na<sub>2</sub>Ti<sub>3</sub>O<sub>7</sub>, and hydrogen titanate H<sub>2</sub>Ti<sub>3</sub>O<sub>7</sub>) corresponded to single crystal nanowires with the same morphology as they were synthesized starting from the sodium titanate NWs by a series of topochemical transformations. This approach should minimize the impact of precursor morphology and crystallographic order on the reaction. Several conclusions can be drawn on the basis of the obtained results.

In the case of crystalline precursors, the formation of SrTiO<sub>3</sub> occurs by an interface-driven dissolution and crystallization process. The morphology evolution is largely determined by the substrate surface as the reaction is confined in a narrow region around the original crystals, whereas the bulk of solution remains undersaturated. If the product can easily nucleate and grow on the substrate, the parent phase will be gradually replaced by the product that will inherit the morphology of the precursor resulting in a pseudomorphic transformation. Depending on the crystallographic matching, the single parent crystal can either transform in a mesocrystal via a topochemical reaction as happens with anatase or in a polycrystalline product as observed with sodium titanate. For the replacement of the parent phase, surface coverage by the new phase is required. If nucleation is difficult and the product grows on the substrate in the form of noninteracting isolated particles, as in the case of hydrogen titanate precursor, surface coverage will not be realized and the new compound will not inherit the wire-like morphology of the precursor. The incomplete surface coverage indicates that even in the interfacial layer the supersaturation is

much lower than that resulting from thermodynamic calculations.

The importance of interfaces is made clear by the completely different crystallization pathway observed when well-defined phase boundaries are missing as in the case of ATH gel precursors. The higher solubility of ATH and the huge contact area of the amorphous polymeric network of the gel which is completely permeated by the solution favors the rapid nucleation and limited growth of a large number of SrTiO<sub>3</sub> nanocrystals. These nanocrystals are the building blocks for the formation of mesocrystals by self-assembly. In contrast, the mesocrystals observed after reaction of anatase NWs result from the heteroepitaxial growth of the perovskite on the substrate surface.

Besides the alkaline-earth titanates, manganites, chromates, niobates, and tantalates can be synthesized from solid precursors, usually binary oxides.<sup>84–90</sup> We propose that the foregoing conclusions are rather general and apply to the hydrothermal synthesis of other perovskites provided that the reaction occurs in stagnant or laminar flow conditions and involves a solid precursor with relatively low solubility. Clearly, the solubility of the parent phase must be higher than that of the product; otherwise no reaction will occur. The macroscopic morphological differences between product particles obtained from different precursors will tend to disappear when using small (<100 nm) equiaxed particles of the parent phases due to the small number of nuclei for each particle and the presence of recrystallization processes. Therefore, if very fine SrTiO<sub>3</sub> particles are required, anatase nanopowders are preferred as precursor.

Different applications can be considered depending on the final morphology. The mesocrystals synthesized from the anatase NWs could be used as templates for the preparation of textured ferroelectric and piezoelectric ceramics via templated grain growth. The porous particles obtained from the TiOCl<sub>2</sub> gel are of potential interest as catalyst or photocatalyst and can be impregnated or decorated with other nanoparticles to improve their catalytic efficiency and selectivity. The hydrogen titanate/SrTiO<sub>3</sub> heterostructures obtained at short reaction times could also be tested in photocatalysis.

## ■ ASSOCIATED CONTENT

### Supporting Information

The Supporting Information is available free of charge on the ACS Publications website at DOI: 10.1021/acs.cgd.5b00770.

Figures S1–S3. Morphology and XRD patterns of titania/titanate crystalline precursors. Figures S4–S8. XRD patterns of reaction products obtained by hydrothermal treatment of different titanium precursors in a Sr(OH)<sub>2</sub>/NaOH solution at 200 °C (PDF)

## ■ AUTHOR INFORMATION

### Corresponding Author

\*Tel. +39-010-6475708. Fax. +39-010-6475700. E-mail: v.buscaglia@ge.ieni.cnr.it.

### Present Address

<sup>†</sup>Department of Chemistry, Indian Institute of Technology, Bombay, Powai 400076, India.

### Notes

The authors declare no competing financial interest.



## ■ REFERENCES

- (1) Pithan, C.; Hennings, D.; Waser, R. *Int. J. Appl. Ceram. Technol.* **2005**, *2*, 1–14.
- (2) Kishi, H.; Mizuno, Y.; Chazono, H. *Jpn. J. Appl. Phys.* **2003**, *42*, 1–15.
- (3) Bednorz, J. G.; Müller, K. A. *Phys. Rev. Lett.* **1984**, *52*, 2289.
- (4) Ang, C.; Yu, Z.; Vilarinho, P. M.; Baptista, J. L. *Phys. Rev. B: Condens. Matter Mater. Phys.* **1998**, *57*, 7403–7406.
- (5) Itoh, M.; Wang, R.; Inaguma, Y.; Yamaguchi, T.; Shan, Y. J.; Nakamura, T. *Phys. Rev. Lett.* **1999**, *82*, 3540.
- (6) Haeni, J. H.; Irvin, P.; Chang, W.; Uecker, R.; Reiche, P.; Li, Y. L.; Choudhury, S.; Tian, W.; Hawley, M. E.; Craigo, B.; Tagantsev, A. K.; Pan, X. Q.; Streiffer, S. K.; Chen, L. Q.; Kirchhofer, S. W.; Levy, J.; Schlom, D. G. *Nature* **2004**, *430*, 758–761.
- (7) Tagantsev, A. K.; Sherman, V. O.; Astafiev, K. F.; Venkatesh, J.; Setter, N. *J. Electroceram.* **2003**, *11*, 5–66.
- (8) Müller, K. A.; Burkard, H. *Phys. Rev. B: Condens. Matter Mater. Phys.* **1979**, *19*, 3593. (b) Denk, I.; Munch, W.; Maier, J. *J. Am. Ceram. Soc.* **1995**, *78*, 3265–72.
- (9) Rothschild, A.; Menesklou, W.; Tuller, H. L.; Ivers-Tiffée, E. *Chem. Mater.* **2006**, *18*, 3651.
- (10) Ohta, H. *Mater. Today* **2007**, *10*, 49.
- (11) Fergus, J. W. *J. Eur. Ceram. Soc.* **2012**, *32*, S25–S40.
- (12) Peña, M. A.; Fierro, J. L. G. *Chem. Rev.* **2001**, *101*, 1981–2017.
- (13) Kato, H.; Kudo, A. *J. Phys. Chem. B* **2002**, *106*, S029–S034.
- (14) Konta, R.; Ishii, T.; Kato, H.; Kudo, A. *J. Phys. Chem. B* **2004**, *108*, 8992–8995.
- (15) Miyauchi, M.; Nakajima, A.; Fujishima, A.; Hashimoto, K.; Watanabe, T. *Chem. Mater.* **2000**, *12*, 3–5.
- (16) Luo, J.; Maggard, P. A. *Adv. Mater.* **2006**, *18*, S14.
- (17) Enterkin, J. A.; Setthapun, W.; Elam, J. W.; Christensen, S. T.; Rabuffetti, F. A.; Marks, L. D.; Stair, P. C.; Poeppelmeier, K. R.; Marshall, C. L. *ACS Catal.* **2011**, *1*, 629.
- (18) Ahuja, S.; Kutty, T. R. N. *J. Photochem. Photobiol., A* **1996**, *97*, 99.
- (19) Kao, C.-F.; Yang, W.-D. *Mater. Sci. Eng., B* **1996**, *38*, 127.
- (20) Kumar, V. *J. Am. Ceram. Soc.* **1999**, *82*, 2580.
- (21) Roeder, R. K.; Slamovich, E. B. *J. Am. Ceram. Soc.* **1999**, *82*, 1665.
- (22) Um, M.-H.; Kumazawa, H. *J. Mater. Sci.* **2000**, *35*, 1295.
- (23) Chen, D.; Jiao, X.; Zhang, M. *J. Eur. Ceram. Soc.* **2000**, *20*, 1261.
- (24) Zhang, S.; Liu, J.; Han, Y.; Chen, B.; Li, X. *Mater. Sci. Eng., B* **2004**, *110*, 11.
- (25) Calderone, V. R.; Testino, A.; Buscaglia, M. T.; Bassoli, M.; Bottino, C.; Viviani, M.; Buscaglia, V.; Nanni, P. *Chem. Mater.* **2006**, *18*, 1627–1633.
- (26) Wei, X.; Xu, G.; Ren, Z. H.; Wang, Y. G.; Shen, G.; Han, G. R. *J. Am. Ceram. Soc.* **2008**, *91*, 299.
- (27) Rabuffetti, F. A.; Kim, H.-S.; Enterkin, J. A.; Wang, Y.; Lanier, C. H.; Marks, L. D.; Poeppelmeier, K. R.; Stair, P. C. *Chem. Mater.* **2008**, *20*, 5628.
- (28) Fuentes, S.; Zarate, R. A.; Chavez, E.; Munoz, P.; Diaz-Droguett, D.; Leyton, P. *J. Mater. Sci.* **2010**, *45*, 1448.
- (29) da Silva, L. F.; Avansi, W., Jr.; Andres, J.; Ribeiro, C.; Moreira, M. L.; Longo, E.; Mastelaro, V. R. *Phys. Chem. Chem. Phys.* **2013**, *15*, 12386.
- (30) Lencka, M. M.; Riman, R. E. *Chem. Mater.* **1995**, *7*, 18–25.
- (31) Lencka, M. M.; Riman, R. E. *Ferroelectrics* **1994**, *151*, 159.
- (32) Modeshia, D. R.; Walton, R. I. *Chem. Soc. Rev.* **2010**, *39*, 4303.
- (33) Hertl, W. *J. Am. Ceram. Soc.* **1988**, *71*, 879.
- (34) Walton, R. I.; Millange, F.; Smith, R. I.; Hansen, T. C.; O'Hare, D. *J. Am. Ceram. Soc.* **2001**, *123*, 12547.
- (35) Moon, J.; Suvaci, E.; Morrone, A.; Costantino, S. A.; Adair, J. H. *J. Eur. Ceram. Soc.* **2003**, *23*, 2153.
- (36) Viviani, M.; Buscaglia, M. T.; Testino, A.; Buscaglia, V.; Bowen, P.; Nanni, P. *J. Eur. Ceram. Soc.* **2003**, *23*, 1383–1390.
- (37) Testino, A.; Buscaglia, M. T.; Buscaglia, V.; Viviani, M.; Bottino, C.; Nanni, P. *Chem. Mater.* **2004**, *16*, 1536.
- (38) Testino, A.; Buscaglia, V.; Buscaglia, M. T.; Viviani, M.; Nanni, P. *Chem. Mater.* **2005**, *17*, S346–S356.
- (39) Marchisio, D. *Chem. Eng. Sci.* **2009**, *64*, 697.
- (40) Maxim, F.; Vilarinho, P. M.; Ferreira, P.; Reaney, I. M.; Levin, I. *Cryst. Growth Des.* **2011**, *11*, 3358.
- (41) Zhan, H. Q.; Yang, X. F.; Wang, C. M.; Chen, J.; Wen, Y. P.; Liang, C. L.; Greer, H. F.; Wu, M. M.; Zhou, W. Z. *Cryst. Growth Des.* **2012**, *12*, 1247–1253.
- (42) Eckert, J. O., Jr.; Hung-Houston, C. C.; Gersten, B. L.; Lencka, M. M.; Riman, R. E. *J. Am. Ceram. Soc.* **1996**, *79*, 2929.
- (43) Choi, J. Y.; Kim, C. H.; Kim, D. K. *J. Am. Ceram. Soc.* **1998**, *81*, 1353.
- (44) Hu, M.Z.-C.; Kurian, V.; Payzant, A. E.; Rawn, C. J.; Hunt, R. D. *Powder Technol.* **2000**, *110*, 2.
- (45) Wang, Y.; Xu, H.; Wang, X.; Zhang, X.; Jia, H.; Zhang, L.; Qiu, J. *J. Phys. Chem. B* **2006**, *110*, 13835.
- (46) Demirörs, A. F.; Imhof, A. *Chem. Mater.* **2009**, *21*, 3002–3007.
- (47) Kalyani, V.; Vasile, B. S.; Ianculescu, A.; Buscaglia, M. T.; Buscaglia, V.; Nanni, P. *Cryst. Growth Des.* **2012**, *12* (12), 4450.
- (48) Lencka, M. M.; Riman, R. E. *Chem. Mater.* **1993**, *5*, 61.
- (49) Wang, P.; Anderko, A.; Young, R. D. *Fluid Phase Equilib.* **2002**, *203*, 141.
- (50) Kosinski, J. J.; Wang, P.; Springer, R. D.; Anderko, A. *Fluid Phase Equilib.* **2007**, *256*, 34.
- (51) Wang, P.; Kosinski, J. J.; Anderko, A.; Springer, R. D.; Lencka, M. M.; Liu, J. P. *Ind. Eng. Chem. Res.* **2013**, *52*, 15968.
- (52) OLI Systems, Inc., Cedar Knolls, NJ, USA.
- (53) Knauss, K. G.; Dibley, M. J.; Bourcier, W. L.; Shaw, H. F. *Appl. Geochem.* **2001**, *16*, 1115.
- (54) Schmidt, J.; Vogelsberger, W. *J. Solution Chem.* **2009**, *38*, 1267–1282.
- (55) Sugimoto, T.; Zhou, X.; Muramatsu, A. *J. Colloid Interface Sci.* **2002**, *252*, 339.
- (56) Kostrikin, A. V.; Spiridonov, F. M.; Lin'ko, I. V.; Zaitsev, B. E.; Kosenkova, O. V.; Tarasova, S. V.; Komissarova, L. N. *Russ. J. Inorg. Chem.* **2011**, *56*, 928.
- (57) Pujol, P.; Bowen, P.; Stadelmann, A.; Hofmann, H. *J. Phys. Chem. B* **2004**, *108*, 13128.
- (58) Cölfen, H.; Antonietti, M. *Angew. Chem., Int. Ed.* **2005**, *44*, 5576.
- (59) Putnis, A. *Science* **2014**, *343*, 1441–1442.
- (60) Ruiz-Agudo, E.; Putnis, C. V.; Putnis, A. *Chem. Geol.* **2014**, *383*, 132–146.
- (61) Cubillas, P.; Kohler, S.; Prieto, M.; Causserand, C.; Oelkers, E. H. *Geochim. Cosmochim. Acta* **2005**, *69*, S459–S476.
- (62) Zhao, J.; Brugger, J.; Ngathai, Y.; Pring, A. *Am. Mineral.* **2014**, *99*, 2389–2397.
- (63) Lucassen, F.; Franz, G.; Wirth, R.; Weise, M.; Hertwig, A. *Am. Mineral.* **2012**, *97*, 828–839.
- (64) Jonas, L.; John, T.; King, H. E.; Geisler, T.; Putnis, A. *Earth Planet. Sci. Lett.* **2014**, *386*, 64–74.
- (65) Oaki, Y.; Imai, H. *Cryst. Growth Des.* **2003**, *3*, 711.
- (66) Yang, D.; Qi, L. M.; Ma, J. M. *Chem. Commun.* **2003**, 1180.
- (67) Saito, Y.; Ueta, T. *Phys. Rev. A: At, Mol, Opt. Phys.* **1989**, *40*, 3408.
- (68) Bogoyavlenskii, V. A.; Chernova, N. A. *Phys. Rev. E: Stat. Phys., Plasmas, Fluids, Relat. Interdiscip. Top.* **2000**, *61*, 1629.
- (69) Lotnyk, A.; Senz, S.; Hesse, D. *J. Phys. Chem. C* **2007**, *111*, 6372.
- (70) Feng, Q.; Hirasawa, M.; Yanagisawa, K. *Chem. Mater.* **2001**, *13*, 290–296.
- (71) Bao, N. Z.; Shen, L. M.; Srinivasan, G.; Yanagisawa, K.; Gupta, A. *J. Phys. Chem. C* **2008**, *112*, 8634.
- (72) Kang, S.-O.; Park, B. H.; Kim, Y.-I. *Cryst. Growth Des.* **2008**, *8*, 3180.
- (73) Tang, H. X.; Lin, Y. R.; Sodano, H. A. *Adv. Energy Mater.* **2013**, *3*, 451.
- (74) Hu, D. W.; Luo, X.; Kong, X. G.; Wang, Y.; Tanaka, Y.; Feng, Q. *CrystEngComm* **2015**, *17*, 1758.
- (75) Kong, X. G.; Hu, D. W.; Ishikawa, Y.; Tanaka, Y.; Feng, Q. *Chem. Mater.* **2011**, *23*, 3978.

- (76) Hennings, D.; Rosenstein, G.; Schreinemacher, H. *J. Eur. Ceram. Soc.* **1991**, *8*, 107–115.
- (77) MacLaren, I.; Ponton, C. B. *J. Eur. Ceram. Soc.* **2000**, *20*, 1267–1275.
- (78) Spagnoli, D.; Banfield, J. F.; Parker, S. C. *J. Phys. Chem. C* **2008**, *112*, 14731.
- (79) Meldrum, F. C.; Cölfen, H. *Chem. Rev.* **2008**, *108*, 4332.
- (80) Song, R.-Q.; Cölfen, H. *Adv. Mater.* **2010**, *22*, 1301.
- (81) Donnet, M.; Aimable, A.; Lemaitre, J.; Bowen, P. *J. Phys. Chem. B* **2010**, *114*, 12058–12067.
- (82) Park, N.-H.; Wang, Y. F.; Seo, W.-S.; Dang, F.; Wan, C. L.; Koumoto, K. *CrystEngComm* **2013**, *15*, 679.
- (83) Zhan, H. Q.; Chen, Z. G.; Zhuang, J. L.; Yang, X. F.; Wu, Q. L.; Jiang, X. P.; Liang, C. L.; Wu, M. M.; Zou, J. *J. Phys. Chem. C* **2015**, *119*, 3530–3537.
- (84) Chen, Y.; Yuan, H.; Tian, G.; Zhang, G. H.; Feng, S. H. *J. Solid State Chem.* **2007**, *180*, 1340–1346.
- (85) Stampler, E. S.; Sheets, W. C.; Prellier, W.; Marks, T. J.; Poeppelmeier, K. R. *J. Mater. Chem.* **2009**, *19*, 4375–4381.
- (86) Zheng, W. J.; Pang, W. Q.; Meng, G. Y.; Peng, D. K. *J. Mater. Chem.* **1999**, *9*, 2833–2836.
- (87) Magrez, A.; Vasco, E.; Seo, J. W.; Dieker, C.; Setter, N.; Forró, L. *J. Phys. Chem. B* **2006**, *110*, 58–61.
- (88) Wang, G. Z.; Selbach, S. M.; Yu, Y. D.; Zhang, X. T.; Grande, T.; Einarsrud, M.-A. *CrystEngComm* **2009**, *11*, 1958–1963.
- (89) Suyal, G.; Colla, E.; Gysel, R.; Cantoni, M.; Setter, N. *Nano Lett.* **2004**, *4*, 1339–1342.
- (90) Hu, Y. M.; Gu, H. H.; Hu, Z. L.; Di, W. N.; Yuan, Y.; You, J.; Cao, W. Q.; Wang, Y.; Chan, H. L. W. *Cryst. Growth Des.* **2008**, *8*, 832–837.





# List of Publications

## First author journal articles

5. Mohammed\*, Ahmed S.A., **Agnese Carino\***, Andrea Testino, Mohammad Reza Andalibi, Christian Ludwig, and Antonio Cervellino. 'In-situ liquid WAXS and SAXS studies on the early stage of amorphous calcium carbonate (ACC) formation.' In: *In preparation* (2018)
4. **Carino, Agnese**, Andrea Testino, Elisabeth Mueller, Antonio Cervellino, and Christian Ludwig. 'Formation and Transformation of octacalcium phosphate (OCP) under biologically relevant conditions: experiments and modelling'. In: *Acta Biomaterialia*, *in press* (2018)
3. **Carino, Agnese** and Andrea Testino. 'Method for biomimetic growth of calcium phosphates ceramics on metal implants'. PTC International Patent Application n. 18159860.8. Oct. 20, 2017
2. **Carino, Agnese**, Andrea Testino, Mohammad Reza Andalibi, Frank Pilger, Paul Bowen, and Christian Ludwig. 'Thermodynamic-Kinetic Precipitation Modeling. A Case Study: The Amorphous Calcium Carbonate (ACC) Precipitation Pathway Unravelling'. In: *Crystal Growth & Design* 17.4 (Mar. 2017), pp. 2006–2015
1. **Carino, Agnese**, Aurelie Walter, Andrea Testino, and Heinrich Hofmann. 'Continuous Synthesis of Gold Nanoparticles Using the Segmented Flow Tubular Reactor (SFTR)'. in: *CHIMIA International Journal for Chemistry* 70.6 (June 2016), pp. 457–457

## Co-author journal articles

4. Pilger, Frank, Andrea Testino, **Agnese Carino**, and Davide Ferri. 'ASAXS study of the incorporation-segregation mechanism of Pt-clusters on CeO<sub>2</sub> NPs'. In: *in preparation* (2018)
3. Pilger, Frank, Andrea Testino, Ivo Alxneit, **Agnese Carino**, Mohammed Tarik, Elisabeth Mueller, Antonio Cervellino, and Christian Ludwig. 'One-Pot synthesis and thermal behaviour of pure and Pt-doped Ceria-Zirconia solid solutions'. In: *Under submission* (2018)
2. Pilger, Frank, Andrea Testino, **Agnese Carino**, Christian Proff, Anastasios Kambolis, Antonio Cervellino, and Christian Ludwig. 'Size Control of Pt Clusters on CeO<sub>2</sub> Nanoparticles via an Incorporation-Segregation Mechanism and Study of Segregation Kinetics'. In: *ACS Catalysis* 6.6 (May 2016), pp. 3688–3699
1. Kalyani, Vishwanath, Bogdan S. Vasile, Adelina Ianculescu, Andrea Testino, **Agnese Carino**, Maria Teresa Buscaglia, Vincenzo Buscaglia, and Paolo Nanni. 'Hydrothermal Synthesis of SrTiO<sub>3</sub>: Role of Interfaces'. In: *Crystal Growth & Design* 15.12 (Nov. 2015), pp. 5712–5725

---

\*Both authors contributed equally.



# CARINO AGNESE

## PhD. student

✉ agnese.carino@psi.ch

✉ OVGA/119, PSI, 5323 CH

📍 Villigen PSI, AG

🌐 [linkedin.com/in/agneseclarino](https://www.linkedin.com/in/agneseclarino)

🔗 [orcid.org/0000-0002-6136-4348](https://orcid.org/0000-0002-6136-4348)



## EDUCATION

### Ph.D. in Material Science and Engineering

#### EPFL (Ecole polytechnique fédérale de Lausanne)

📅 April 2014 – Ongoing

📍 Villigen-PSI, Switzerland

- Dissertation: Unravelling the precipitation pathway of biorelevant minerals: from fundamental studies to biomedical applications
- Advisor: Prof. Christian Ludwig
- Paul Scherrer Institut (PSI), Switzerland

### M.Sc. in Chemical sciences

#### Università degli Studi di Genova

📅 Nov 2010 – Dec 2012

📍 Genova, Italy

- M.Sc. Thesis: Synthesis and characterization of multi-layer magnetic sensors for transport of drugs
- Advisor: Prof. Fabio Canepa

### B.Sc. in Chemistry and chemical technologies

#### Università degli Studi di Genova

📅 Oct.2007 – Nov.2010

📍 Genova, Italy

- B.Sc. Thesis: Synthesis and formation of an innovative catalyst obtained through eco-sustainable processes
- Advisor: Prof. Adriana Saccone

### Maturità classica

#### Liceo scientifico E.Amaldi, Novi Ligure - Alessandria

📅 Sept. 2002 – June 2007

📍 Novi Ligure, Italy

## CERTIFICATES

### European School

#### ESRF-DESY

📅 March 2016 – April 2016

📍 Grenoble - Hamburg

- HERCULES, Higher European Research Course for Users of Large Experimental Systems

### Teaching Workshop

#### EPFL-CAPE

📅 May 2016 – June 2016

📍 Lausanne

- Teaching Toolkit I & II

### Workshops

#### PSI-Akademie

📅 October 2017 – November 2017

📍 Villigen

- Entrepreneurship, the 3rd way
- Basic of Project Management

## TEACHING



### Teaching Assistant

Analyse des polluants dans l'environnement ENV-300



### Teaching Assistant

Inorganic Particle Synthesis by Precipitation: From Nanoparticles to Self Organized Mesocrystals and from Theory to Practice, MSE-653 CCMX Advanced course

## STRENGTHS

Hard-working

Motivator & Leader

MS Office & Origin

LaTeX & Gnuplot

OLI & tiamo & GIMP

## PROJECTS

### CerInk Project

#### Swiss Nanoscience Institut (SNI)/ FHNW Basel-PSI-Medicoat AG

📅 Jan.2016 – Dec.2017

- Biomimetic ceramic scaffolds with density gradient and improved mechanical stability fabricated by Binder-into-Bed 3D-printing and ceramic Nanolnk

### NanoCoat Project

#### Swiss Nanoscience Institut (SNI)/ FHNW Basel-PSI-Medicoat AG-Atheros Medical AG - Meisinger

📅 Jan.2018 – Ongoing

- Biomimetic growth of calcium phosphates ceramics on Ti implants

## LANGUAGES

English

Italian

French

German



## INTERESTS

Reading & Playing music & Theater

Yoga & Hiking & Education

## PUBLICATIONS

---

### Journal Articles

- Carino, Agnese, Andrea Testino, Elisabeth Mueller, et al. (2018). "Formation and Transformation of octacalcium phosphate (OCP) under biologically relevant conditions: experiments and modelling". In: *Acta Biomaterialia*, in press.
- Carino, Agnese, Andrea Testino, Mohammad Reza Andalibi, et al. (Mar. 2017). "Thermodynamic-Kinetic Precipitation Modeling. A Case Study: The Amorphous Calcium Carbonate (ACC) Precipitation Pathway Unravelling". In: *Crystal Growth & Design* 17.4, pp. 2006–2015. DOI: 10.1021/acs.cgd.7b00006.
- Carino, Agnese, Aurelie Walter, et al. (June 2016). "Continuous Synthesis of Gold Nanoparticles Using the Segmented Flow Tubular Reactor (SFTR)". in: *CHIMIA International Journal for Chemistry* 70.6, pp. 457–457. DOI: 10.2533/chimia.2016.457.
- Pilger, Frank et al. (May 2016). "Size Control of Pt Clusters on CeO<sub>2</sub> Nanoparticles via an Incorporation-Segregation Mechanism and Study of Segregation Kinetics". In: *ACS Catalysis* 6.6, pp. 3688–3699. DOI: 10.1021/acscatal.6b00934.
- Kalyani, Vishwanath et al. (Nov. 2015). "Hydrothermal Synthesis of SrTiO<sub>3</sub>: Role of Interfaces". In: *Crystal Growth & Design* 15.12, pp. 5712–5725. DOI: 10.1021/acs.cgd.5b00770.

### Patent

- Carino, Agnese and Andrea Testino (Oct. 20, 2017). "Method for biomimetic growth of calcium phosphates ceramics on metal implants". PTC International Patent Application n. 18159860.8.

## REFEREES

---

### Prof Christian Ludwig

@ EPFL, ENAC IIE GR-LUD, Paul Scherrer Institut

✉ christian.ludwig@psi.ch

OVGA/111

Villigen-PSI, 5232 CH

-----

### Dr Andrea Testino

@ Paul Scherrer Institut

✉ andrea.testino@psi.ch

OVGA/116

Villigen-PSI, 5232 CH

# Bibliography

- [1] A.E. Nielsen. *Kinetics of Precipitation*. International series of monographs in analytical chemistry. Pergamon Press; [distributed in the Western Hemisphere by Macmillan, New York], 1964.
- [2] Helmut Cölfen and Markus Antonietti. 'Mesocrystals: Inorganic Superstructures Made by Highly Parallel Crystallization and Controlled Alignment'. In: *Angewandte Chemie International Edition* 44.35 (Sept. 2005), pp. 5576–5591.
- [3] Markus Niederberger and Helmut Cölfen. 'Oriented attachment and mesocrystals: non-classical crystallization mechanisms based on nanoparticle assembly'. In: *Phys. Chem. Chem. Phys.* 8.28 (2006), pp. 3271–3287.
- [4] Helmut Cölfen and Markus Antonietti. *Mesocrystals and Nonclassical Crystallization*. Wiley, 2008. URL: <https://www.amazon.com/Mesocrystals-Nonclassical-Crystallization-Helmut-elfen/dp/0470029811?SubscriptionId=0JYN1NVW651KCA56C102&tag=techkie-20&linkCode=xm2&camp=2025&creative=165953&creativeASIN=0470029811>.
- [5] F. C. Meldrum and R. P. Sear. 'Now you see them'. In: *Science* 322.5909 (Dec. 2008), pp. 1802–1803.
- [6] D. Gebauer, A. Volkel, and H. Cölfen. 'Stable Prenucleation Calcium Carbonate Clusters'. In: *Science* 322.5909 (2008), pp. 1819–1822.
- [7] T. F. Kazmierczak, Tomson M. B., and Nancollas G.H. 'Crystal growth of calcium carbonate. A controlled composition kinetic study.' In: *J. Phys. Chem.* 86 (1982), pp. 103–107.
- [8] M. B. Tomson and G. H. Nancollas. 'Mineralization kinetics: a constant composition approach'. In: *Science* 200.4345 (June 1978), pp. 1059–1060.
- [9] Inc. OLI Systems. *OLI Product-line*. Ed. by Inc. OLI Systems. OLI System, Inc.: Morris Plains, NJ. 2015. URL: <https://www.olisystems.com/product-line>.

## Bibliography

---

- [10] Andrea Testino, Vincenzo Buscaglia, Maria Teresa Buscaglia, Massimo Viviani, and Paolo Nanni. 'Kinetic modeling of aqueous and hydrothermal synthesis of barium titanate (BaTiO<sub>3</sub>)'. In: *Chemistry of Materials* 17.21 (2005), pp. 5346–5356.
- [11] Stevanovic S. and Chavanne P. 'Improvement of Mechanical Properties of 3d Printed Hydroxyapatite Scaffolds by Polymeric Infiltration'. In: *Bioceramics Development and Applications* 3 (2013).
- [12] Rohner AM. 'Postprocessing of 3D printed ceramic scaffolds for bone replacement.' In: *RTejournal* (2014). URL: <https://www.rtejournal.de/ausgabe11/3962>.
- [13] M. Faatz, F. Gröhn, and G. Wegner. 'Mineralization of calcium carbonate by controlled release of carbonate in aqueous solution'. In: *Materials Science and Engineering: C* 25.2 (2005). NATO Advanced Study Institute (ASI on Learning from Nature How to design New Implantable Biomaterials: From Biomineralization Fundamentals to Biomimetic Materials and Processing Routes), pp. 153–159. URL: <http://www.sciencedirect.com/science/article/pii/S0928493105000159>.
- [14] Donnet M., Aimable A., Lemaitre J., and Bowen P. 'Contribution of Aggregation to the Growth Mechanism of Seeded Calcium Carbonate Precipitation in the Presence of Polyacrylic Acid'. In: *J. Phys. Chem. B* 114.37 (Sept. 2010), p. 12058.
- [15] J. Franke and A. Mersmann. 'The influence of the operational conditions on the precipitation process'. In: *Chemical Engineering Science* 50.11 (June 1995), pp. 1737–1753.
- [16] Kanichi Kamiya, Sumio Sakka, and Katsuyuki Terada. 'Aragonite formation through precipitation of calcium carbonate monohydrate'. In: *Materials Research Bulletin* 12.11 (Nov. 1977), pp. 1095–1102.
- [17] Marcel Donnet, Paul Bowen, Nathalie Jongen, Jacques Lemaitre, and Heinrich Hofmann. 'Use of Seeds to Control Precipitation of Calcium Carbonate and Determination of Seed Nature'. In: *Langmuir* 21.1 (Jan. 2005), pp. 100–108.
- [18] Linghao He, Rui Xue, and Rui Song. 'Formation of calcium carbonate films on chitosan substrates in the presence of polyacrylic acid'. In: *Journal of Solid State Chemistry* 182.5 (May 2009), pp. 1082–1087.
- [19] Takeshi Ogino, Toshio Suzuki, and Kiyoshi Sawada. 'The rate and mechanism of polymorphic transformation of calcium carbonate in water'. In: *Journal of Crystal Growth* 100.1-2 (Feb. 1990), pp. 159–167.

- 
- [20] Debasish Chakraborty and Suresh K. Bhatia. 'Formation and Aggregation of Polymorphs in Continuous Precipitation. 1. Mathematical Modeling'. In: *Industrial & Engineering Chemistry Research* 35.6 (Jan. 1996), pp. 1985–1994.
- [21] Debasish Chakraborty and Suresh K. Bhatia. 'Formation and Aggregation of Polymorphs in Continuous Precipitation. 2. Kinetics of  $\text{CaCO}_3$  Precipitation'. In: *Industrial & Engineering Chemistry Research* 35.6 (Jan. 1996), pp. 1995–2006.
- [22] Zhaodong Nan, Xiangna Chen, Qianqian Yang, and Zhiying Chen. 'Transitions of calcium carbonate crystals controlled by self-assembly supermolecule of -cyclodextrin and sodium dodecyl benzene sulfonate'. In: *Materials Research Bulletin* 45.6 (2010), pp. 722–726. URL: <http://www.sciencedirect.com/science/article/pii/S0025540810000590>.
- [23] Lijun Wang and George H. Nancollas. 'Calcium orthophosphates: crystallization and dissolution'. In: *Chemical Reviews* 108.11 (Nov. 2008), pp. 4628–4669.
- [24] Helmut Cölfen and Limin Qi. 'A Systematic Examination of the Morphogenesis of Calcium Carbonate in the Presence of a Double-Hydrophilic Block Copolymer'. In: *Chemistry* 7.1 (Jan. 2001), pp. 106–116.
- [25] J. Rieger, J. Thieme, and C. Schmidt. 'Study of precipitation reactions by X-ray microscopy:  $\text{CaCO}_3$  precipitation and the effect of polycarboxylates'. In: *Langmuir* 16.22 (Oct. 2000), pp. 8300–8305.
- [26] Jianing Liu, Jens Rieger, and Klaus Huber. 'Analysis of the nucleation and growth of amorphous  $\text{CaCO}_3$  by means of time-resolved static light scattering'. In: *Langmuir* 24.15 (Aug. 2008), pp. 8262–8271.
- [27] E. M. Pouget, P. H. H. Bomans, J. A. C. M. Goos, P. M. Frederik, G. de With, and N. A. J. M. Sommerdijk. 'The initial stages of template-controlled  $\text{CaCO}_3$  formation revealed by Cryo-TEM'. In: *Science* 323.5920 (2009), pp. 1455–1458.
- [28] Shuxia Li, Li Yu, Fei Geng, Lijuan Shi, Liqiang Zheng, and Shiling Yuan. 'Facile preparation of diversified patterns of calcium carbonate in the presence of DTAB'. In: *Journal of Crystal Growth* 312.10 (May 2010), pp. 1766–1773.
- [29] Peng Wan, Yu Zhao, Hua Tong, Ziyang Yang, Zhihong Zhu, Xinyu Shen, and Jiming Hu. 'The inducing effect of lecithin liposome organic template on the nucleation and crystal growth of calcium carbonate'. In: *Materials Science and Engineering: C* 29.1 (Jan. 2009), pp. 222–227.
-

## Bibliography

---

- [30] Pieter Bots, Liane G. Benning, Juan-Diego Rodriguez-Blanco, Teresa Roncal-Herrero, and Samuel Shaw. 'Mechanistic Insights into the Crystallization of Amorphous Calcium Carbonate (ACC)'. In: *Crystal Growth & Design* 12.7 (May 2012), pp. 3806–3814.
- [31] Andreas Verch, Markus Antonietti, and Helmut Colfen. 'Mixed calcium-magnesium pre-nucleation clusters enrich calcium'. In: *Zeitschrift fur Kristallographie - Crystalline Materials* 227.11 (Nov. 2012), pp. 718–722.
- [32] D.A. Kulik, V.L. Vinograd, N. Paulsen, and B. Winkler. '(Ca,Sr)CO<sub>3</sub> aqueous–solid solution systems: From atomistic simulations to thermodynamic modelling'. In: *Physics and Chemistry of the Earth, Parts A/B/C* 35.6 (Jan. 2010). MIGRATION 2009, 12th International Conference on the Chemistry and Migration Behaviour of Actinides and Fission Products in the Geosphere, pp. 217–232. URL: <http://www.sciencedirect.com/science/article/pii/S1474706510000768>.
- [33] Dionisis Katsikopoulos, Angeles Fernandez-Gonzalez, and Manuel Prieto. 'Precipitation and mixing properties of the “disordered” (Mn,Ca)CO<sub>3</sub> solid solution'. In: *Geochimica et Cosmochimica Acta* 73.20 (Oct. 2009), pp. 6147–6161.
- [34] Adriana Bigi, Elisa Boanini, Chiara Capuccini, and Massimo Gazzano. 'Strontium-substituted hydroxyapatite nanocrystals'. In: *Inorganica Chimica Acta* 360.3 (Feb. 2007), pp. 1009–1016.
- [35] H. J. M. Heijligers, F. C. M. Driessens, and R. M. H. Verbeeck. 'Lattice parameters and cation distribution of solid solutions of calcium and strontium hydroxyapatite'. In: *Calcified Tissue International* 29.1 (Dec. 1979), pp. 127–131.
- [36] C. D. Bird and N. J. Emery. 'Insightful problem solving and creative tool modification by captive nontool-using rooks'. In: *Proceedings of the National Academy of Sciences* 106.25 (May 2009), pp. 10370–10375.
- [37] Arghavan Farzadi, Farhad Bakhshi, Mehran Solati-Hashjin, Mitra Asadi-Eydivand, and Noor Azuan abu Osman. 'Magnesium incorporated hydroxyapatite: Synthesis and structural properties characterization'. In: *Ceramics International* 40.4 (May 2014), pp. 6021–6029.
- [38] Chun-Wei Chen, Charles S. Oakes, Kullaiah Byrappa, Richard E. Riman, Kelly Brown, Kevor S. TenHuisen, and Victor F. Janas. 'Synthesis, characterization, and dispersion properties of hydroxyapatite prepared by mechanochemical–hydrothermal methods'. In: *J. Mater. Chem.* 14.15 (2004), pp. 2425–2432.



- [39] Wojciech L. Suchanek, Kullaiah Byrappa, Pavel Shuk, Richard E. Riman, Victor F. Janas, and Kevor S. TenHuisen. 'Preparation of magnesium-substituted hydroxyapatite powders by the mechanochemical–hydrothermal method'. In: *Biomaterials* 25.19 (Aug. 2004), pp. 4647–4657.
- [40] Walter E Brown, James R Lehr, James P Smith, and A William Frazier. 'Crystallography of octacalcium phosphate'. In: *Journal of the American Chemical Society* 79.19 (1957), pp. 5318–5319.
- [41] Walter E. Brown. 'Octacalcium Phosphate and Hydroxyapatite: Crystal Structure of Octacalcium Phosphate'. In: *Nature* 196.4859 (Dec. 1962), pp. 1048–1050.
- [42] W. E. Brown. *A mechanism for growth of apatite crystals*. In: *Tooth enamel II*. Ed. by M. V. Stack. Ed. by R. W. Fearnhead. Bristol: John Wright Ltd., 1965, p. 11.
- [43] W E Brown. 'Crystal growth of bone mineral.' In: *Clinical orthopaedics and related research* 44 (1966), pp. 205–220.
- [44] Marc Bohner. 'Resorbable biomaterials as bone graft substitutes'. In: *Materials Today* 13.1-2 (Jan. 2010), pp. 24–30.
- [45] Racquel Zapanta LeGeros. 'Properties of osteoconductive biomaterials: calcium phosphates'. In: *Clinical Orthopaedics and Related Research* 395 (Feb. 2002), pp. 81–98.
- [46] Peiming Wang, Andrzej Anderko, Ronald D. Springer, Jerzy J. Kosinski, and Malgorzata M. Lencka. 'Modeling chemical and phase equilibria in geochemical systems using a speciation-based model'. In: *Journal of Geochemical Exploration* 106.1-3 (July 2010), pp. 219–225.
- [47] Wilhelm Ostwald. 'Studien über die bildung und umwandlung fester körper'. In: *Zeitschrift für physikalische Chemie* 22.1 (1897), pp. 289–330.
- [48] R. A. Van Santen. 'The Ostwald step rule'. In: *The Journal of Physical Chemistry* 88.24 (Nov. 1984), pp. 5768–5769.
- [49] Aaron S. Posner and Foster Betts. 'Synthetic amorphous calcium phosphate and its relation to bone mineral structure'. In: *Accounts of Chemical Research* 8.8 (Aug. 1975), pp. 273–281.
- [50] Y.-W. Wang, Y.-Y. Kim, C. J. Stephens, F. C. Meldrum, and H. K. Christenson. 'In situ study of the precipitation and crystallization of amorphous calcium carbonate (ACC)'. In: *Crystal Growth & Design* 12.3 (Jan. 2012), pp. 1212–1217.

## Bibliography

---

- [51] Lijun Wang and George H. Nancollas. 'Pathways to biomineralization and biodemineralization of calcium phosphates: the thermodynamic and kinetic controls'. In: *Dalton Transactions* 15 (2009), p. 2665.
- [52] Sha Bian, Lin-Wei Du, Yu-Xi Gao, Jian Huang, Bao-Di Gou, Xiuhong Li, Yi Liu, Tian-Lan Zhang, and Kui Wang. 'Crystallization in Aggregates of Calcium Phosphate Nanocrystals: A Logistic Model for Kinetics of Fractal Structure Development'. In: *Crystal Growth & Design* 12.7 (June 2012), pp. 3481–3488.
- [53] Marion D. Francis and Ned C. Webb. 'Hydroxyapatite formation from a hydrated calcium monohydrogen phosphate precursor'. In: *Calcified Tissue Research* 6.1 (Dec. 1970), pp. 335–342. URL: <https://doi.org/10.1007/BF02196214>.
- [54] Metrohm Schweiz AG. *www-Metrohm*. 2010. URL: <https://www.metrohm.com>.
- [55] Andrea Testino, Maria Teresa Buscaglia, Vincenzo Buscaglia, Massimo Viviani, Carlo Bottino, and Paolo Nanni. 'Kinetics and mechanism of aqueous chemical synthesis of BaTiO<sub>3</sub> particles'. In: *Chemistry of Materials* 16.8 (Apr. 2004), pp. 1536–1543.
- [56] James O. Eckert, Catherine C. Hung-Houston, Bonnie L. Gersten, Malgorzata M. Lencka, and Richard E. Riman. 'Kinetics and Mechanisms of Hydrothermal Synthesis of Barium Titanate'. In: *Journal of the American Ceramic Society* 79.11 (Nov. 1996), pp. 2929–2939.
- [57] Jooho Moon, Ender Suvaci, Augusto Morrone, Stephen A. Costantino, and James H. Adair. 'Formation mechanisms and morphological changes during the hydrothermal synthesis of BaTiO<sub>3</sub> particles from a chemically modified, amorphous titanium (hydrous) oxide precursor'. In: *Journal of the European Ceramic Society* 23.12 (Nov. 2003), pp. 2153–2161.
- [58] I. MacLaren and C.B. Ponton. 'A TEM and HREM study of particle formation during barium titanate synthesis in aqueous solution'. In: *Journal of the European Ceramic Society* 20.9 (Aug. 2000), pp. 1267–1275.
- [59] G. M. Anderson. *Thermodynamics of Natural Systems*. Cambridge University Press, 2005.
- [60] A. F. Wallace, L. O. Hedges, A. Fernandez-Martinez, P. Raiteri, J. D. Gale, G. A. Waychunas, S. Whitlam, J. F. Banfield, and J. J. De Yoreo. 'Microscopic Evidence for Liquid-Liquid Separation in Supersaturated CaCO<sub>3</sub> Solutions'. In: *Science* 341.6148 (Aug. 2013), pp. 885–889.

- [61] J.O.M. Bockris, J.O.M. Bockris, and A.K.N. Reddy. *Volume 1: Modern Electrochemistry: Ionics*. Modern Electrochemistry. Springer US, 1998. URL: [https://books.google.ch/books?id=KGr%5C\\_UFSw9b8C](https://books.google.ch/books?id=KGr%5C_UFSw9b8C).
- [62] J.J. Moré, B.S. Garbow, and K.E. Hillstom. *User Guide for MINPACK-1*. Report ANL-80-74. National Laboratory, 1970.
- [63] M. J. D. Powell. 'A hybrid method for nonlinear equations'. In: *Numerical Methods for Nonlinear Algebraic Equations* (1970). URL: <https://ci.nii.ac.jp/naid/10006528967/en/>.
- [64] Jacob Kielland. 'Individual Activity Coefficients of Ions in Aqueous Solutions'. In: *Journal of the American Chemical Society* 59.9 (1937), pp. 1675–1678. eprint: <https://doi.org/10.1021/ja01288a032>. URL: <https://doi.org/10.1021/ja01288a032>.
- [65] Weast. *Handbook of Chemistry and Physics [64th. Edition, 1983-1984]*. CRC Press, 1984. URL: <https://www.amazon.com/Handbook-Chemistry-Physics-64th-1983-1984/dp/B000Z9R3BA?SubscriptionId=0JYN1NVW651KCA56C102&tag=techkie-20&linkCode=xm2&camp=2025&creative=165953&creativeASIN=B000Z9R3BA>.
- [66] Alan C Hindmarsh. 'ODEPACK, a systematized collection of ODE solvers'. In: *Scientific computing* (1983), pp. 55–64.
- [67] Edgard C. Moreno, Thomas M. Gregory, and Walter E. Brown. 'Solubility of  $\text{CaHPO}_4 \cdot 2\text{H}_2\text{O}$  and formation of ion pairs in the system  $\text{Ca}(\text{OH})_2 - \text{H}_3\text{PO}_4 - \text{H}_2\text{O}$  at  $37.5^\circ\text{C}$ '. In: *Journal of Research of the National Bureau of Standards Sec. A: Phys. Ch.* 70A.6 (1966), p. 545.
- [68] MS Tung, N Eidelman, B Sieck, and WE Brown. 'Octacalcium phosphate solubility product from 4 to  $37^\circ\text{C}$ '. In: *J Res Nat Bur Stand* 93.5 (1988), pp. 613–624.
- [69] H. McDowell, T. M. Gregory, and W. E. Brown. 'Solubility of  $\text{C}_5(\text{P}_{04})_3\text{OH}$  in the System  $\text{Ca}(\text{OH})_2 - \text{H}_3\text{P}_{04} - \text{H}_{20}$  at 5, 15, 25, and  $37^\circ\text{C}$ '. In: 81A (1977), p. 273.
- [70] Söhnle, O., and J. Garside. *Precipitation: Basic Principles and Industrial Applications*. Butterworth-Heinemann, 1992. URL: <https://books.google.ch/books?id=aDRRAAAAMAAJ>.

## Bibliography

---

- [71] L. Cristina Soare, Paul Bowen, Jacques Lemaitre, and Heinrich Hofmann. 'Precipitation of nanostructured copper oxalate: substructure and growth mechanism'. In: *The Journal of Physical Chemistry B* 110.36 (Sept. 2006), pp. 17763–17771.
- [72] Paul Bowen, Ollivier Pujol, Nathalie Jongen, Jacques Lemaitre, Alke Fink, Pierre Stadlerman, and Heinrich Hofmann. 'Control of morphology and nanostructure of copper and cobalt oxalates: Effect of complexing ions, polymeric additives and molecular weight'. In: *Nanoscale* 2.11 (2010), p. 2470.
- [73] S. Karthika, T. K. Radhakrishnan, and P. Kalaichelvi. 'A review of classical and nonclassical nucleation theories'. In: *Crystal Growth & Design* 16.11 (Oct. 2016), pp. 6663–6681.
- [74] Nathalie Jongen, Paul Bowen, Jacques Lemaitre, Jean-Christophe Valmalette, and Heinrich Hofmann. 'Precipitation of Self-Organized Copper Oxalate Polycrystalline Particles in the Presence of Hydroxypropylmethylcellulose (HPMC): Control of Morphology'. In: *Journal of Colloid and Interface Science* 226.2 (June 2000), pp. 189–198.
- [75] R. Lee Penn and Jillian F Banfield. 'Morphology development and crystal growth in nanocrystalline aggregates under hydrothermal conditions: insights from titania'. In: *Geochimica et Cosmochimica Acta* 63.10 (May 1999), pp. 1549–1557.
- [76] Wouter J. E. M. Habraken, Jinhui Tao, Laura J. Brylka, Heiner Friedrich, Luca Bertinetti, Anna S. Schenk, Andreas Verch, Vladimir Dmitrovic, Paul H. H. Bomans, Peter M. Frederik, Jozua Laven, Paul van der Schoot, Barbara Aichmayer, Gijsbertus de With, James J. DeYoreo, and Nico A. J. M. Sommerdijk. 'Ion-association complexes unite classical and non-classical theories for the biomimetic nucleation of calcium phosphate'. In: *Nature Communications* 4 (2013), p. 1507.
- [77] Raffaella Demichelis, Paolo Raiteri, Julian D. Gale, David Quigley, and Denis Gebauer. 'Stable prenucleation mineral clusters are liquid-like ionic polymers'. In: *Nature Communications* 2 (Dec. 2011), p. 590.
- [78] Denis Gebauer, Matthias Kellermeier, Julian D. Gale, Lennart Bergström, and Helmut Cölfen. 'Pre-nucleation clusters as solute precursors in crystallisation'. In: *Chem. Soc. Rev.* 43.7 (2014), pp. 2348–2371.

- [79] Archan Dey, Paul H. H. Bomans, Frank A. Müller, Julia Will, Peter M. Frederik, Gijsbertus de With, and Nico A. J. M. Sommerdijk. 'The role of prenucleation clusters in surface-induced calcium phosphate crystallization'. In: *Nature Materials* 9.12 (Nov. 2010), pp. 1010–1014.
- [80] Van Driessche, A.E.S., Kellermeier, M., Benning, L.G., and Gebauer D. *New Perspectives on Mineral Nucleation and Growth: From Solution Precursors to Solid Materials*. Springer International Publishing, 2016. URL: [https://books.google.ch/books?id=VP%5C\\_FDQAAQBAJ](https://books.google.ch/books?id=VP%5C_FDQAAQBAJ).
- [81] A. Navrotsky. 'Energetic clues to pathways to biomineralization: precursors, clusters, and nanoparticles'. In: *Proceedings of the National Academy of Sciences* 101.33 (Aug. 2004), pp. 12096–12101.
- [82] Q. Hu, M. H. Nielsen, C. L. Freeman, L. M. Hamm, J. Tao, J. R. I. Lee, T. Y. J. Han, U. Becker, J. H. Harding, P. M. Dove, and J. J. De Yoreo. 'The thermodynamics of calcite nucleation at organic interfaces: Classical vs. non-classical pathways'. In: *Faraday Discuss.* 159 (0 2012), pp. 509–523. URL: <http://dx.doi.org/10.1039/C2FD20124K>.
- [83] Jonathan R. I. Lee, T. Yong-Jin Han, Trevor M. Willey, Dongbo Wang, Robert W. Meulenberg, Joakim Nilsson, Patricia M. Dove, Louis J. Terminello, Tony van Buuren, and James J. De Yoreo. 'Structural development of mercaptophenol self-assembled monolayers and the overlying mineral phase during templated CaCO<sub>3</sub> crystallization from a transient amorphous film'. In: *Journal of the American Chemical Society* 129.34 (Aug. 2007), pp. 10370–10381.
- [84] Fiona C. Meldrum and Helmut Cölfen. 'Controlling mineral morphologies and structures in biological and synthetic systems'. In: *Chemical Reviews* 108.11 (Nov. 2008), pp. 4332–4432.
- [85] H. Cölfen and M. Antonietti. 'Mesocrystals and Nonclassical Crystallization'. In: *Mesocrystals and Nonclassical Crystallization*. John Wiley & Sons, Ltd, 2008, pp. 1–6.
- [86] J. Seto, Y. Ma, S. A. Davis, F. Meldrum, A. Gourrier, Y.-Y. Kim, U. Schilde, M. Sztucki, M. Burghammer, S. Maltsev, C. Jäger, and H. Cölfen. 'Structure-property relationships of a biological mesocrystal in the adult sea urchin spine'. In: *Proceedings of the National Academy of Sciences* 109.10 (Feb. 2012), pp. 3699–3704.

## Bibliography

---

- [87] D. Li, M. H. Nielsen, J. R. I. Lee, C. Frandsen, J. F. Banfield, and J. J. De Yoreo. 'Direction-specific interactions control crystal growth by oriented attachment'. In: *Science* 336.6084 (May 2012), pp. 1014–1018.
- [88] J. J. De Yoreo, P. U. P. A. Gilbert, N. A. J. M. Sommerdijk, R. L. Penn, S. Whitelam, D. Joester, H. Zhang, J. D. Rimer, A. Navrotsky, J. F. Banfield, A. F. Wallace, F. M. Michel, F. C. Meldrum, H. Cölfen, and P. M. Dove. 'Crystallization by particle attachment in synthetic, biogenic, and geologic environments'. In: *Science* 349.6247 (2015), aaa6760–aaa6760.
- [89] Elia Beniash, Rebecca A. Metzler, Raymond S.K. Lam, and P.U.P.A. Gilbert. 'Transient amorphous calcium phosphate in forming enamel'. In: *Journal of Structural Biology* 166.2 (May 2009), pp. 133–143.
- [90] Laurie B Gower and Damian J Odom. 'Deposition of calcium carbonate films by a polymer-induced liquid-precursor (PILP) process'. In: *Journal of Crystal Growth* 210.4 (Mar. 2000), pp. 719–734.
- [91] John W. Cahn and John E. Hilliard. 'Free Energy of a Nonuniform System. III. Nucleation in a Two-Component Incompressible Fluid'. In: *The Journal of Chemical Physics* 31.3 (Sept. 1959), pp. 688–699.
- [92] M.A. Larson and John Garside. 'Solute clustering and interfacial tension'. In: *Journal of Crystal Growth* 76.1 (July 1986), pp. 88–92.
- [93] J W Mullin. *Crystallization, Fourth Edition*. Butterworth-Heinemann, 2001. URL: <https://www.amazon.com/Crystallization-Fourth-J-W-Mullin/dp/0750648333?SubscriptionId=0JYN1NVW651KCA56C102&tag=techkie-20&linkCode=xm2&camp=2025&creative=165953&creativeASIN=0750648333>.
- [94] George Kaptay. 'The Gibbs Equation versus the Kelvin and the Gibbs-Thomson Equations to Describe Nucleation and Equilibrium of Nano-Materials'. In: *Journal of Nanoscience and Nanotechnology* 12.3 (Mar. 2012), pp. 2625–2633.
- [95] Johannes Ihli, Wai Ching Wong, Elizabeth H. Noel, Yi-Yeoun Kim, Alexander N. Kulak, Hugo K. Christenson, Melinda J. Duer, and Fiona C. Meldrum. 'Dehydration and crystallization of amorphous calcium carbonate in solution and in air'. In: *Nature Communications* 5 (Jan. 2014), p. 3169.
- [96] M. H. Nielsen, S. Aloni, and J. J. De Yoreo. 'In situ TEM imaging of CaCO<sub>3</sub> nucleation reveals coexistence of direct and indirect pathways'. In: *Science* 345.6201 (Sept. 2014), pp. 1158–1162.

- 
- [97] Agnese Carino, Andrea Testino, Mohammad Reza Andalibi, Frank Pilger, Paul Bowen, and Christian Ludwig. 'Thermodynamic-Kinetic Precipitation Modeling. A Case Study: The Amorphous Calcium Carbonate (ACC) Precipitation Pathway Unravelled'. In: *Crystal Growth & Design* 17.4 (Mar. 2017), pp. 2006–2015.
- [98] Jim De Yoreo. 'More than one pathway'. In: *Nature Materials* 12.4 (Apr. 2013), pp. 284–285.
- [99] W.N. Al Nasser, A. Shaikh, C. Morriss, M.J. Hounslow, and A.D. Salman. 'Determining kinetics of calcium carbonate precipitation by inline technique'. In: *Chemical Engineering Science* 63.5 (Mar. 2008), pp. 1381–1389.
- [100] N. Abdel-Aal, K. Satoh, and K. Sawada. 'Study of the adhesion mechanism of  $\text{CaCO}_3$  using a combined bulk chemistry/QCM technique'. In: *J. Cryst. Growth* 245 (2002), p. 87.
- [101] B. B. Schroeder, D. D. Harris, S. T. Smith, and D. O. Lignell. 'Theoretical framework for multiple-polymorph particle precipitation in highly supersaturated systems'. In: *Crystal Growth & Design* 14.4 (Mar. 2014), pp. 1756–1770.
- [102] J. Bolze, B. Peng, N. Dingenouts, P. Panine, T. Narayanan, and M. Ballauff. 'Formation and Growth of Amorphous Colloidal  $\text{CaCO}_3$  Precursor Particles as Detected by Time-Resolved SAXS'. In: *Langmuir* 18.22 (Oct. 2002), pp. 8364–8369.
- [103] A. V. Radha, T. Z. Forbes, C. E. Killian, P. U. P. A. Gilbert, and A. Navrotsky. 'Transformation and crystallization energetics of synthetic and biogenic amorphous calcium carbonate'. In: *Proceedings of the National Academy of Sciences* 107.38 (Sept. 2010), pp. 16438–16443.
- [104] W. N. Al Nasser and F. H. Al Salhi. 'Kinetics determination of calcium carbonate precipitation behavior by inline techniques'. In: *Powder Technology* 270 (Jan. 2015), pp. 548–560.
- [105] Johannes Ihli, Yi-Yeoun Kim, Elizabeth H. Noel, and Fiona C. Meldrum. 'The effect of additives on amorphous calcium carbonate (ACC): janus behavior in solution and the solid state'. In: *Advanced Functional Materials* 23.12 (Oct. 2012), pp. 1575–1585.
- [106] Gebauer Denis. 'A novel view on the early stage of crystallization.' PhD thesis. Potsdam University, Apr. 14, 2008. URL: [https://publishup.uni-potsdam.de/opus4-ubp/frontdoor/deliver/index/docId/1815/file/gebauer\\_diss.pdf](https://publishup.uni-potsdam.de/opus4-ubp/frontdoor/deliver/index/docId/1815/file/gebauer_diss.pdf).
-

## Bibliography

---

- [107] M. Kellermeier, P. Raiteri, J. K. Berg, A. Kempter, J. D. Gale, and D. Gebauer. 'Entropy drives calcium carbonate ion association'. In: *ChemPhysChem* 17 (2016), p. 3535.
- [108] Z Alexandrowicz. 'Nucleation theory versus cluster aggregation'. In: *Journal of Physics A: Mathematical and General* 26.15 (1993), p. L655. URL: <http://stacks.iop.org/0305-4470/26/i=15/a=007>.
- [109] Dima Kashchiev. *Nucleation*. Butterworth-Heinemann, 2000. URL: <https://www.elsevier.com/books/nucleation/kashchiev/978-0-7506-4682-6>.
- [110] L.Niel Plummer and Eurybiades Busenberg. 'The solubilities of calcite, aragonite and vaterite in CO<sub>2</sub>-H<sub>2</sub>O solutions between 0 and 90°C, and an evaluation of the aqueous model for the system CaCO<sub>3</sub>-CO<sub>2</sub>-H<sub>2</sub>O'. In: *Geochimica et Cosmochimica Acta* 46.6 (June 1982), pp. 1011–1040.
- [111] Stephan E. Wolf, Lars Müller, Raul Barrea, Christopher J. Kampf, Jork Leitterer, Ulrich Panne, Thorsten Hoffmann, Franziska Emmerling, and Wolfgang Tremel. 'Carbonate-coordinated metal complexes precede the formation of liquid amorphous mineral emulsions of divalent metal carbonates'. In: *Nanoscale* 3.3 (2011), p. 1158.
- [112] Denis Gebauer, Philips N. Gunawidjaja, J. Y. Peter Ko, Zoltán Bacsik, Baroz Aziz, Lijia Liu, Yongfeng Hu, Lennart Bergström, Cheuk-Wai Tai, Tsun-Kong Sham, Mattias Edén, and Niklas Hedin. 'Proto-Calcite and Proto-Vaterite in Amorphous Calcium Carbonates'. In: *Angewandte Chemie International Edition* 49.47 (Oct. 2010), pp. 8889–8891.
- [113] Masoud Farhadi-Khouzani, Daniel M. Chevrier, Peng Zhang, Niklas Hedin, and Denis Gebauer. 'Water as the Key to Proto-Aragonite Amorphous CaCO<sub>3</sub>'. In: *Angewandte Chemie International Edition* 55.28 (June 2016), pp. 8117–8120.
- [114] Marcel Donnet, Paul Bowen, and Jacques Lemaitre. 'A thermodynamic solution model for calcium carbonate: Towards an understanding of multi-equilibria precipitation pathways'. In: *Journal of Colloid and Interface Science* 340.2 (Dec. 2009), pp. 218–224.
- [115] Otakar Söhnel. 'Electrolyte crystal-aqueous solution interfacial tensions from crystallization data'. In: *Journal of Crystal Growth* 57.1 (Mar. 1982), pp. 101–108.



- [116] Daniele L. Marchisio and Rodney O. Fox. 'Solution of population balance equations using the direct quadrature method of moments'. In: *Journal of Aerosol Science* 36.1 (Jan. 2005), pp. 43–73.
- [117] R.O. Fox. 'Bivariate direct quadrature method of moments for coagulation and sintering of particle populations'. In: *Journal of Aerosol Science* 37.11 (Nov. 2006), pp. 1562–1580.
- [118] Agnese Carino, Andrea Testino, Elisabeth Mueller, Antonio Cervellino, and Christian Ludwig. 'Formation and Transformation of octacalcium phosphate (OCP) under biologically relevant conditions: experiments and modelling'. In: *Acta Biomaterialia*, in press (2018).
- [119] Paul Ducheyne, David W Grainger, Kevin E Healy, Dietmar W Hutmacher, and C J Kirkpatrick. *Comprehensive Biomaterials II, Second Edition. Second Edition*. English. Ed. by Paul Ducheyne. II. 6 vols. Elsevier, June 2, 2017, p. 4858.
- [120] C. Liu and H. He. *Developments and applications of calcium phosphate bone cements*. Springer Series in Biomaterials Science and Engineering. Springer Singapore, 2017. URL: <https://books.google.ch/books?id=uTY7DwAAQBAJ>.
- [121] Laurence C Chow and Edward D Eanes. *Octacalcium phosphate*. 2001.
- [122] E. D. Eanes and J. L. Meyer. 'The maturation of crystalline calcium phosphates in aqueous suspensions at physiologic pH'. In: *Calcified Tissue Research* 23.1 (Dec. 1977), pp. 259–269. URL: <https://doi.org/10.1007/BF02012795>.
- [123] Patricia Bodier-Houllé, Pierre Steuer, Jean-Claude Voegel, and Frédéric J. G. Cuisinier. 'First Experimental Evidence for Human Dentine Crystal Formation Involving Conversion of Octacalcium Phosphate to Hydroxyapatite'. In: *Acta Crystallographica Section D Biological Crystallography* 54.6 (Nov. 1998), pp. 1377–1381.
- [124] Osamu Suzuki, Masanori Nakamura, Yoshinori Mizasaka, Manubu Kagayama, and Minoru Sakurai. 'Bone formation on synthetic precursors of hydroxyapatite'. In: *The Tohoku Journal of Experimental Medicine* 164.1 (1991), pp. 37–50.
- [125] Osamu Suzuki, Masanori Nakamura, Yoshinori Miyasaka, Manabu Kagayama, and Minoru Sakurai. 'Maclura pomifera agglutinin-binding glycoconjugates on converted apatite from synthetic octacalcium phosphate implanted into subperiosteal region of mouse calvaria'. In: *Bone and Mineral* 20.2 (Feb. 1993), pp. 151–166.

## Bibliography

---

- [126] Osamu Suzuki. 'Octacalcium phosphate (OCP)-based bone substitute materials'. In: *Japanese Dental Science Review* 49.2 (May 2013), pp. 58–71.
- [127] O. Suzuki. 'Octacalcium phosphate: Osteoconductivity and crystal chemistry'. In: *Acta Biomaterialia* 6.9 (2010), pp. 3379–3387. URL: <http://www.sciencedirect.com/science/article/pii/S1742706110001807>.
- [128] Mayumi Iijima and Yutaka Moriwaki. 'Lengthwise and oriented growth of octacalcium phosphate on cation selective membrane in a model system of enamel formation'. In: *Journal of Crystal Growth* 112.2-3 (June 1991), pp. 571–579.
- [129] Kazuo Onuma and Atsuo Ito. 'Cluster Growth Model for Hydroxyapatite'. In: *Chemistry of Materials* 10.11 (Nov. 1998), pp. 3346–3351.
- [130] J. Mahamid, A. Sharir, L. Addadi, and S. Weiner. 'Amorphous calcium phosphate is a major component of the forming fin bones of zebrafish: Indications for an amorphous precursor phase'. In: *Proceedings of the National Academy of Sciences* 105.35 (Aug. 2008), pp. 12748–12753.
- [131] Nicole J. Crane, Victoria Popescu, Michael D. Morris, Pieter Steenhuis, and Michael A. Ignelzi. 'Raman spectroscopic evidence for octacalcium phosphate and other transient mineral species deposited during intramembranous mineralization'. In: *Bone* 39.3 (Sept. 2006), pp. 434–442.
- [132] J. Mahamid, B. Aichmayer, E. Shimon, R. Ziblat, C. Li, S. Siegel, O. Paris, P. Fratzl, S. Weiner, and L. Addadi. 'Mapping amorphous calcium phosphate transformation into crystalline mineral from the cell to the bone in zebrafish fin rays'. In: *Proceedings of the National Academy of Sciences* 107.14 (Mar. 2010), pp. 6316–6321.
- [133] Katja Henzler, Evgenii O. Fetisov, Mirza Galib, Marcel D. Baer, Benjamin A. Legg, Camelia Borca, Jacinta M. Xto, Sonia Pin, John L. Fulton, Gregory K. Schenter, Niranjana Govind, J. Ilja Siepmann, Christopher J. Mundy, Thomas Huthwelker, and James J. De Yoreo. 'Supersaturated calcium carbonate solutions are classical'. In: *Science Advances* 4.1 (Jan. 2018), eaao6283.
- [134] Botond Szilágyi, Norbert Muntean, Réka Barabás, Oana Ponta, and Béla G. Lakatos. 'Reaction precipitation of amorphous calcium phosphate: Population balance modelling and kinetics'. In: *Chemical Engineering Research and Design* 93 (Jan. 2015), pp. 278–286.

- [135] P.J. Andersen. '1.1 Metals for Use in Medicine'. In: *Comprehensive Biomaterials II*. Elsevier, 2017, pp. 1–18.
- [136] Mayumi Iijima, Hideo Kamemizu, Nobukazu Wakamatsu, Takayasu Goto, Yutaka Doi, and Yutaka Moriwaki. 'Effects of Ca addition on the formation of octacalcium phosphate and apatite in solution at pH 7.4 and at 37°C'. In: *Journal of Crystal Growth* 193.1-2 (Sept. 1998), pp. 182–188.
- [137] Carlo Meneghini, Maria Chiara Dalconi, Stefania Nuzzo, Settimio Mobilio, and Rudy H. Wenk. 'Rietveld refinement on X-Ray diffraction patterns of bioapatite in human fetal bones'. In: *Biophysical Journal* 84.3 (Mar. 2003), pp. 2021–2029.
- [138] P.G. Koutsoukos and G.H. Nancollas. 'The morphology of hydroxyapatite crystals grown in aqueous solution at 37°C'. In: *Journal of Crystal Growth* 55.2 (Nov. 1981), pp. 369–375.
- [139] Christophe Drouet. 'Apatite Formation: Why It May Not Work as Planned, and How to Conclusively Identify Apatite Compounds'. In: *BioMed Research International* 2013 (2013), pp. 1–12.
- [140] H. Tohda, M. Yamada, Y. Yamaguchi, and T. Yanagisawa. 'High-resolution electron microscopical observations of initial enamel crystals'. In: *Journal of Electron Microscopy* 46.1 (Jan. 1997), pp. 97–101.
- [141] M. Kakei, T. Sakae, and M. Yoshikawa. 'Electron microscopy of octacalcium phosphate in the dental calculus'. In: *Journal of Electron Microscopy* 58.6 (June 2009), pp. 393–398.
- [142] M S Johnsson and G H Nancollas. 'The role of brushite and octacalcium phosphate in apatite formation.' In: *Critical reviews in oral biology and medicine : an official publication of the American Association of Oral Biologists* 3 (1-2 1992), pp. 61–82.
- [143] E. D. Eanes and A. S. Posner. 'Division of biophysics: kinetics and mechanism of conversion of noncrystalline calcium phosphate to crystalline hydroxyapatite'. In: *Transactions of the New York Academy of Sciences* 28.2 Series II (Dec. 1965), pp. 233–241.
- [144] E. D. Eanes, I. H. Gillessen, and A. S. Posner. 'Intermediate States in the Precipitation of Hydroxyapatite'. In: *Nature* 208.5008 (Oct. 1965), pp. 365–367.

## Bibliography

---

- [145] Roy E. Wuthier, Gregory S. Rice, James E. B. Wallace, Robert L. Weaver, Racquel Z. LeGeros, and E. David Eanes. 'In vitro precipitation of calcium phosphate under intracellular conditions: formation of brushite from an amorphous precursor in the absence of ATP'. In: *Calcified Tissue International* 37.4 (July 1985), pp. 401–410.
- [146] R. A. Young and W. E. Brown. 'Structures of biological minerals'. In: *Biological Mineralization and Demineralization*. Springer Berlin Heidelberg, 1982, pp. 101–141.
- [147] M. Clara F. Magalhes, Paula A. A. P. Marques, and Rui N. Correia. 'Calcium and magnesium phosphates: normal and pathological mineralization'. In: *Biom mineralization– Medical Aspects of Solubility*. John Wiley & Sons, Ltd, 2007, pp. 71–123.
- [148] Ruikang Tang, Zachary J. Henneman, and George H. Nancollas. 'Constant composition kinetics study of carbonated apatite dissolution'. In: *Journal of Crystal Growth* 249.3-4 (Mar. 2003), pp. 614–624.
- [149] H.G. McCann. 'The solubility of fluorapatite and its relationship to that of calcium fluoride'. In: *Archives of Oral Biology* 13.8 (Aug. 1968), pp. 987–1001.
- [150] R Hawkins, D Locker, J Noble, and E J Kay. 'Prevention. Part 7: Professionally applied topical fluorides for caries prevention'. In: *British Dental Journal* 195.6 (Sept. 2003), pp. 313–317.
- [151] Edward A Tavss, James R Mellberg, Marilou Joziak, Robert J Gambogi, and Steven W Fisher. 'Relationship between dentifrice fluoride concentration and clinical caries reduction.' In: *American journal of dentistry* 16 (6 Dec. 2003), pp. 369–374.
- [152] Racquel Z. LeGeros and John P. LeGeros. 'Phosphate minerals in human tissues'. In: *Phosphate Minerals*. Springer Berlin Heidelberg, 1984, pp. 351–385.
- [153] H. Okumura, H. Nakagaki, K. Kato, F. Ito, J.A. Weatherell, and C. Robinson. 'Distribution of fluoride in human dental calculus'. In: *Caries Research* 27.4 (1993), pp. 271–276.
- [154] ME Fernández, JA Ascencio, C Zorrilla-Cangas, R García, and J Reyes-Gasga. 'Theoretical study of octacalcium phosphate-hydroxiapatite (OCP-HA) interface model'. In: *Revista Latinoamericana de Metalurgia y Materiales* 22.1 (2002), pp. 52–56.

- [155] M. Reza Andalibi, Abhishek Kumar, Bhuvanesh Srinivasan, Paul Bowen, Karen Scrivener, Christian Ludwig, and Andrea Testino. 'On the mesoscale mechanism of synthetic calcium–silicate–hydrate precipitation: a population balance modeling approach'. In: *Journal of Materials Chemistry A* 6.2 (2018), pp. 363–373.
- [156] Stephan E. Wolf, Jork Leiterer, Michael Kappl, Franziska Emmerling, and Wolfgang Tremel. 'Early Homogenous Amorphous Precursor Stages of Calcium Carbonate and Subsequent Crystal Growth in Levitated Droplets'. In: *Journal of the American Chemical Society* 130.37 (2008). PMID: 18717561, pp. 12342–12347. eprint: <https://doi.org/10.1021/ja800984y>. URL: <https://doi.org/10.1021/ja800984y>.
- [157] Tao Li, Andrew J. Senesi, and Byeongdu Lee. 'Small Angle X-ray Scattering for Nanoparticle Research'. In: *Chemical Reviews* 116.18 (2016). PMID: 27054962, pp. 11128–11180. eprint: <https://doi.org/10.1021/acs.chemrev.5b00690>. URL: <https://doi.org/10.1021/acs.chemrev.5b00690>.
- [158] Y. Mori, M. Furukawa, T. Hayashi, and K. Nakamura. 'Size Distribution of Gold Nanoparticles Used by Small Angle X-ray Scattering'. In: *Particulate Science and Technology* 24.1 (2006), pp. 97–103. eprint: <https://doi.org/10.1080/02726350500403215>. URL: <https://doi.org/10.1080/02726350500403215>.
- [159] Jörg Polte, T. Torsten Ahner, Friedmar Delissen, Sergey Sokolov, Franziska Emmerling, Andreas F. Thünemann, and Ralph Kraehnert. 'Mechanism of Gold Nanoparticle Formation in the Classical Citrate Synthesis Method Derived from Coupled In Situ XANES and SAXS Evaluation'. In: *Journal of the American Chemical Society* 132.4 (2010). PMID: 20102229, pp. 1296–1301. eprint: <https://doi.org/10.1021/ja906506j>. URL: <https://doi.org/10.1021/ja906506j>.
- [160] Jörg Polte, Robert Erler, Andreas F. Thünemann, Sergey Sokolov, T. Torsten Ahner, Klaus Rademann, Franziska Emmerling, and Ralph Kraehnert. 'Nucleation and Growth of Gold Nanoparticles Studied via in situ Small Angle X-ray Scattering at Millisecond Time Resolution'. In: *ACS Nano* 4.2 (2010). PMID: 20088602, pp. 1076–1082. eprint: <https://doi.org/10.1021/nn901499c>. URL: <https://doi.org/10.1021/nn901499c>.
- [161] Jörg Polte, Robert Erler, Andreas F. Thünemann, Franziska Emmerling, and Ralph Kraehnert. 'SAXS in combination with a free liquid jet for improved time-resolved in situ studies of the nucleation and growth of nanoparticles'.

## Bibliography

---

- In: *Chem. Commun.* 46 (48 2010), pp. 9209–9211. URL: <http://dx.doi.org/10.1039/C0CC03238G>.
- [162] P. R. Willmott, D. Meister, S. J. Leake, M. Lange, A. Bergamaschi, M. Böge, M. Calvi, C. Cancellieri, N. Casati, A. Cervellino, Q. Chen, C. David, U. Flechsig, F. Gozzo, B. Henrich, S. Jäggi-Spielmann, B. Jakob, I. Kalichava, P. Karvinen, J. Krempasky, A. Lüdeke, R. Lüscher, S. Maag, C. Quitmann, M. L. Reinle-Schmitt, T. Schmidt, B. Schmitt, A. Streun, I. Vartiainen, M. Vitins, X. Wang, and R. Wulschleger. ‘The Materials Science beamline upgrade at the Swiss Light Source’. In: *Journal of Synchrotron Radiation* 20.5 (July 2013), pp. 667–682.
- [163] Anna Bergamaschi, Antonio Cervellino, Roberto Dinapoli, Fabia Gozzo, Beat Henrich, Ian Johnson, Philipp Kraft, Aldo Mozzanica, Bernd Schmitt, and Xintian Shi. ‘The MYTHEN detector for X-ray powder diffraction experiments at the Swiss Light Source’. In: *Journal of Synchrotron Radiation* 17.5 (July 2010), pp. 653–668.
- [164] Agnese Carino, Aurelie Walter, Andrea Testino, and Heinrich Hofmann. ‘Continuous Synthesis of Gold Nanoparticles Using the Segmented Flow Tubular Reactor (SFTR)’. In: *CHIMIA International Journal for Chemistry* 70.6 (June 2016), pp. 457–457.
- [165] A. Agbabiaka, M. Wiltfong, and C. Park. ‘Small Angle X-Ray Scattering Technique for the Particle Size Distribution of Nonporous Nanoparticles’. In: *Journal of Nanoparticles* 2013 (2013), pp. 1–11.
- [166] L B Kiss, J Söderlund, G A Niklasson, and C G Granqvist. ‘New approach to the origin of lognormal size distributions of nanoparticles’. In: *Nanotechnology* 10.1 (1999), p. 25. URL: <http://stacks.iop.org/0957-4484/10/i=1/a=006>.
- [167] Wyn Brown. *Dynamic Light Scattering: The Method and Some Applications (Monographs on the Physics and Chemistry of Materials)*. Ed. by Wyn Brown. Clarendon Press, 1993. URL: <https://www.amazon.com/Dynamic-Light-Scattering-Applications-Monographs/dp/0198539428?SubscriptionId=0JYN1NVW651KCA56C102&tag=techkie-20&linkCode=xm2&camp=2025&creative=165953&creativeASIN=0198539428>.
- [168] Brian H. Toby. ‘EXPGUI, a graphical user interface for GSAS’. In: *Journal of Applied Crystallography* 34.2 (Apr. 2001), pp. 210–213.
- [169] H. M. Rietveld. ‘A profile refinement method for nuclear and magnetic structures’. In: *Journal of Applied Crystallography* 2.2 (June 1969), pp. 65–71.

- 
- [170] Ingrid Pilz, Otto Glatter, and Otto Kratky. 'Small-angle x-ray scattering'. In: *Enzyme Structure Part H*. Elsevier, 1979, pp. 148–249.
- [171] Bruce O. Fowler, Milenko Markovic, and Walter E. Brown. 'Octacalcium phosphate. 3. Infrared and Raman vibrational spectra'. In: *Chemistry of Materials* 5.10 (Oct. 1993), pp. 1417–1423.
- [172] S. Koutsopoulos. 'Synthesis and characterization of hydroxyapatite crystals: A review study on the analytical methods'. In: *Journal of Biomedical Materials Research* 62.4 (Sept. 2002), pp. 600–612.
- [173] I.A. Karampas and C.G. Kontoyannis. 'Characterization of calcium phosphates mixtures'. In: *Vibrational Spectroscopy* 64 (Jan. 2013), pp. 126–133.
- [174] A. Carino, A. Testino, R. Schumacher, N. Matter, and P. Gruner. *Project A11.01 CerInk: Biomimetic ceramic scaffolds with density gradient fabricated by Binder-into-Bed 3D-printing and ceramic NanoInk*. Annual Report. Swiss Nanoscience Institute, Mar. 1, 2018. URL: [https://script.nanoscience.unibas.ch/media-pdf/2017\\_supplement\\_final\\_klein.pdf](https://script.nanoscience.unibas.ch/media-pdf/2017_supplement_final_klein.pdf).
- [175] A.M. Rohner, R. Schumacher, N. Matter, A. Testino, A. Carino, and P. Gruner. *Project A11.01 CerInk: Biomimetic ceramic scaffolds with density gradient fabricated by Binder-into-Bed 3D-printing and ceramic NanoInk*. Annual Report. Swiss Nanoscience Institute, Mar. 1, 2017. URL: [https://nanoscience.ch/sni/wp-content/uploads/sites/8/2017/04/ar\\_2016\\_supplement\\_klein.pdf](https://nanoscience.ch/sni/wp-content/uploads/sites/8/2017/04/ar_2016_supplement_klein.pdf).
- [176] Nina Matter, Adrian Michael Rohner, Agnese Carino, Philipp Gruner, Andrea Testino, and Ralf Schumacher. 'Use of ceramic nano-particles as binder material to improve mechanical stability.' In: *Rapid.Tech – International Trade Show & Conference for Additive Manufacturing*. Carl Hanser Verlag GmbH & Co. KG, June 2017, pp. 38–50.
- [177] Agnese Carino and Andrea Testino. 'Method for biomimetic growth of calcium phosphates ceramics on metal implants'. 17 197 488.4. Oct. 20, 2017.
- [178] Tadashi Kokubo and Seiji Yamaguchi. 'Bioactive Ti Metal and its Alloys Prepared by Chemical Treatments: State-of-the-Art and Future Trends'. In: *Advanced Engineering Materials* 12.11 (Nov. 2010), B579–B591.
- [179] J. Lemaitre, N. Jongen, R. Vacassy, and P. Bowen. 'Production of Powders'. WO 98/02237. 1997.
-

## Bibliography

---

- [180] M. Donnet, N. Jongen, J. Lemaitre, and P. Bowen. 'New morphology of calcium oxalate trihydrate precipitated in a segmented flow tubular reactor'. In: *Journal of Materials Science Letters* 19.9 (2000), pp. 749–750.
- [181] N. Jongen, M. Donnet, P. Bowen, J. Lemaitre, H. Hofmann, R. Schenk, C. Hofmann, M. Aoun-Habbache, S. Guillemet-Fritsch, J. Sarrias, A. Rousset, M. Viviani, M.T. Buscaglia, V. Buscaglia, P. Nanni, A. Testino, and J.R. Herguijuela. 'Development of a Continuous Segmented Flow Tubular Reactor and the "Scale-out" Concept – In Search of Perfect Powders'. In: *Chemical Engineering & Technology* 26.3 (Mar. 2003), pp. 303–305.
- [182] A. Aimable, N. Jongen, A. Testino, M. Donnet, J. Lemaitre, H. Hofmann, and P. Bowen. 'Precipitation of nanosized and nanostructured powders: process intensification and scale-out using a segmented flow tubular reactor (SFTR)'. In: *Chemical Engineering & Technology* 34.3 (Dec. 2011), pp. 344–352.
- [183] Mattia Alberto Lucchini, Andrea Testino, Christian Ludwig, Anastasios Kambolis, Mario El-Kazzi, Antonio Cervellino, Paola Riani, and Fabio Canepa. 'Continuous synthesis of nickel nanopowders: Characterization, process optimization, and catalytic properties'. In: *Applied Catalysis B: Environmental* 156–157 (Sept. 2014), pp. 404–415.
- [184] Jose Enrico Q. Quinsaat, Andrea Testino, Sonia Pin, Thomas Huthwelker, Frank A. Nüesch, Paul Bowen, Heinrich Hofmann, Christian Ludwig, and Dorina M. Opris. 'Continuous production of tailored silver nanoparticles by polyol synthesis and reaction yield measured by X-ray absorption spectroscopy: toward a growth mechanism'. In: *The Journal of Physical Chemistry C* 118.20 (May 2014), pp. 11093–11103.
- [185] Andrea Testino, Frank Pilger, Mattia Lucchini, Jose Quinsaat, Christoph Stähli, and Paul Bowen. 'Continuous Polyol Synthesis of Metal and Metal Oxide Nanoparticles Using a Segmented Flow Tubular Reactor (SFTR)'. In: *Molecules* 20.6 (June 2015), pp. 10566–10581.
- [186] CCMX Materials Challenges programme. *NanoScreen project*. 2014. URL: <http://www.ccmx.ch/projects-partners/materialschallenges/nanoscreen-reliable-and-rapid-in-vitro-safety-assessment-of-nanomaterials/>.
- [187] Frank Pilger, Andrea Testino, Agnese Carino, Christian Proff, Anastasios Kambolis, Antonio Cervellino, and Christian Ludwig. 'Size Control of Pt Clusters on



- CeO<sub>2</sub> Nanoparticles via an Incorporation-Segregation Mechanism and Study of Segregation Kinetics'. In: *ACS Catalysis* 6.6 (May 2016), pp. 3688–3699.
- [188] Vishwanath Kalyani, Bogdan S. Vasile, Adelina Ianculescu, Andrea Testino, Agnese Carino, Maria Teresa Buscaglia, Vincenzo Buscaglia, and Paolo Nanni. 'Hydrothermal Synthesis of SrTiO<sub>3</sub>: Role of Interfaces'. In: *Crystal Growth & Design* 15.12 (Nov. 2015), pp. 5712–5725.



# Acronyms

**AFM** Atomic Force Microscopy

**ACC** Amorphous calcium carbonate

**ACP** Amorphous calcium phosphate

**AUC** Analytical Ultracentrifugation

**BSE** Backscattered electrons

**CaCs** Calcium carbonate system

**CaPs** Calcium phosphate system

**CNT** Classical Nucleation Theory

**DCPD** Dicalcium phosphate dihydrated, Brushite

**DFT** density functional theory

**ED** Electron diffraction

**EDX** Energy-Dispersive X-ray Spectroscopy

**EM** Electron Microscopy

**ESRF** European Synchrotron Radiation Facility (Grenoble, France)

**EELS** Electron Energy-Loss Spectroscopy

**EXAFS** Extended X-ray Absorption Fine Structure

**FE-SEM** Field-Emission Scanning Electron Microscopy

**FWHM** Full Width at Half Maximum

## Acronyms

---

**FHNW** Fachhochschule Nordwestschweiz

**FIB** Focused Ion Beam

**ICP** Inductively Coupled Plasma

**HA** Hydroxyapatite

**HAADF** High-Angle Annular Dark Field

**IR** Infrared

**IS** Ionic Strength

**HPLC** High Performance Liquid Chromatography

**HR-TEM** High-Resolution Transmission Electron Microscopy

**LBK** Bioenergy and Catalysis Laboratory (Labor für Bioenergie und Katalyse)

**MD** Molecular dynamics

**MS** Mass Spectrometry

**NCNT** Non Classical Nucleation Theory

**NPs** Nanoparticles

**OCP** Octacalcium phosphate

**PSD** Particle Size Distribution

**PSI** Paul Scherrer Institut

**RT** Room Temperature

**SDTA** Scanning Differential Thermal Analysis

**S** Saturation

**SE** Secondary core-level Electrons

**SEM** Scanning Electron Microscopy

**SFTR** Segmented Flow Tubular Reactor

**SLS** Swiss Light Source (PSI, Switzerland)

**SDC** Small Dense Clusters

**STEM** Scanning Transmission Electron Microscopy

**TEM** Transmission Electron Microscopy

**TGA** Termogravimetric Analysis

**TT** Termally Treated

**WP** Work Package

**XANES** X-ray Absorption Near Edge Structure

**XAS** X-ray Absorption Spectroscopy

**XRD** X-ray Diffraction

**SAXS** Small Angle X-ray Scattering

**WAXS** Wide Angle X-ray Scattering